



# Infrared Remote Sensing of Peroxyacetyl Nitrate in the Upper Troposphere

[Link to publication record in Manchester Research Explorer](#)

## Citation for published version (APA):

Allen, G. (2005). *Infrared Remote Sensing of Peroxyacetyl Nitrate in the Upper Troposphere*. University of Leicester.

## Citing this paper

Please note that where the full-text provided on Manchester Research Explorer is the Author Accepted Manuscript or Proof version this may differ from the final Published version. If citing, it is advised that you check and use the publisher's definitive version.

## General rights

Copyright and moral rights for the publications made accessible in the Research Explorer are retained by the authors and/or other copyright owners and it is a condition of accessing publications that users recognise and abide by the legal requirements associated with these rights.

## Takedown policy

If you believe that this document breaches copyright please refer to the University of Manchester's Takedown Procedures [<http://man.ac.uk/04Y6Bo>] or contact [uml.scholarlycommunications@manchester.ac.uk](mailto:uml.scholarlycommunications@manchester.ac.uk) providing relevant details, so we can investigate your claim.



# **The Infrared Remote Sensing of Peroxyacetyl Nitrate in the Upper Troposphere**

Thesis submitted to the University of Leicester for the degree of  
Doctor of Philosophy

by

Grant Allen MPhys

Department of Physics and Astronomy

University of Leicester

May 2005

# **Declaration**

I hereby declare that no part of this thesis has been submitted to this or any other University as part of the requirements for a higher degree. The work described here was conducted by the undersigned except for the contributions of colleagues indicated in the text.

Grant Allen

May 2005

# The Infrared Remote Sensing of Peroxyacetyl Nitrate in the Upper Troposphere

Grant Allen, May 2005

## Abstract

In this thesis, the potential for the detection and retrieval of concentration data for peroxyacetyl nitrate (PAN) in the Upper Troposphere (UT) from atmospheric infrared limb-sounding spectrometers is assessed.

PAN is an important compound in UT chemistry both through its direct influence on the oxidising power of the atmosphere and also through its indirect role as a reservoir species for active nitrogen. It is also a super greenhouse gas in its own right. Current measurements of PAN are limited to *in situ* sampling during specialised campaigns, with uncertainties to the order of 30% at typical UT concentrations. The launch of satellite instruments able to probe the UT could provide a more global view of this important compound.

In this thesis, atmospheric limb-emission spectra measured by two Michelson Interferometer for Passive Atmospheric Sounding (MIPAS) instruments, the MIPAS balloon-borne version 2 (MIPAS-B2) and MIPAS on Envisat (MIPAS-E), have been used to successfully detect PAN in the UT by virtue of its characteristic infrared spectral signature for the first time.

This is achieved using new infrared laboratory reference cross-sections for PAN also obtained in this thesis. This spectral reference dataset represents improved room temperature cross-sections ( $< 4\%$  uncertainty at the 95% confidence level) for PAN in the spectral range  $550\text{--}2200\text{ cm}^{-1}$  and the measurement of low temperature (down to 250 K) and nitrogen broadened (up to 300 mb) cross-sections appropriate to the UT for the first time.

Analysis of spectra measured by the MIPAS-B2 instrument over the Mediterranean Sea region in April 1998 and May 1999 has yielded PAN concentrations as high as 350 parts per trillion by volume (pptv) in the UT using an iterative spectral fitting and residual analysis method developed in this thesis.

The detection of PAN was also achieved using this method for spectra measured by the MIPAS-E instrument during April 2003 for the Mediterranean Sea and East China Sea regions. Back trajectories of airmasses observed by MIPAS-E indicate that very high PAN concentrations (up to 668 pptv) detected over the East China Sea may be indicative of pollution outflow from Asia. Limits of detection for PAN in the UT are estimated to be as low as 40 pptv.

The results of this thesis demonstrate that PAN can be detected and retrieved in the UT at typical concentrations from high spectral resolution infrared atmospheric spectra measured from space.

# Acknowledgements

This project has been a journey of discovery in every sense. And now, I owe a debt of thanks to a great many people who have helped me in the completion of this work, both directly and indirectly by saving my sanity

Firstly, thank you to my supervisor John Remedios for giving me the opportunity to undertake this PhD project and for all his help in guiding me throughout the past few years. Thanks also to Paul Monks, David Newnham and Kevin Smith for their input (and blood!) into this thesis and helping me make “gaseous dynamite”. It was PAN-tastic!

Thanks to all the good friends I’ve made in Leicester, both those still here and those who managed to escape, for giving me the best years of my life. I’ve been lucky to meet such good people and thanks to Dominic for putting up with me whilst writing up.

Thanks also to all members of the Earth Observation Science Group, especially Lizzie, Dave, Roland and Alison, for all their support in making the “research rollercoaster” rideable and for providing me with a source of income whilst writing up by continuing to play me at poker. When’s the next game?

Above all I want to thank parents and family for their help in getting me here and for always giving me support in all that I do.

Thanks also to NERC for funding this work and for three of the most memorable years of my life.

## List of Publications

Allen, G., Remedios, J. J., Newnham, D. A., Smith, K. M., and Monks, P. S.: Improved mid-infrared cross-sections for peroxyacetyl nitrate (PAN) vapour, *Atmos. Chem. Phys.*, 5, 47-56, 2005. (See Chapter 4)

# Contents

<b>1</b>	<b>Introduction</b>	<b>1</b>
1.1	Chemistry and Dynamics of the Upper Troposphere .....	3
1.1.1	Dynamics of the Upper Troposphere .....	4
1.1.2	Chemistry of the Upper Troposphere.....	5
1.1.2.1	HO <sub>x</sub> and NO <sub>x</sub> Chemistry.....	6
1.1.3	Organic Compounds .....	8
1.1.3.1	Alkanes and Alkenes .....	9
1.1.3.2	Aldehydes and PANs.....	11
1.2	The Role of Peroxyacetyl Nitrate in the Troposphere .....	12
1.2.1	Sources and Sinks of PAN .....	13
1.2.2	Global Distribution .....	15
1.2.3	Measuring PAN in the Atmosphere .....	19
1.3	Summary .....	22
<b>2</b>	<b>Infrared Limb Sounding of the Atmosphere</b>	<b>24</b>
2.1	Limb Sounding.....	25
2.2	Radiative Transfer.....	27
2.3	Measurement Inversion.....	29
2.4	Infrared Spectroscopy .....	31
2.4.1	Theory .....	31
2.4.1.1	Rotation of Molecules .....	32
2.4.1.2	Molecular Vibrations .....	33
2.4.1.3	Vibration-Rotation Bands.....	34
2.4.1.4	Line Intensities.....	35
2.4.1.5	Line Widths.....	36
2.4.1.6	Heavy Molecules .....	37

2.4.2	Previous PAN Measurements.....	39
2.5	Fourier Transform Spectroscopy .....	43
2.5.1	The Michelson Interferometer.....	44
2.5.2	Calculation of the Spectrum .....	47
2.5.2.1	Aliasing .....	47
2.5.2.2	Zero-filling.....	48
2.5.3	Resolution Limitations in FTS .....	49
2.5.3.1	Finite Path Difference.....	49
2.5.3.2	Finite Aperture .....	50
2.5.4	Sources of Error in FTS.....	51
2.5.4.1	Phase Error.....	51
2.5.4.2	Channelling.....	53
2.5.4.3	Detector Non-linearity.....	53
2.5.4.4	Thermal Emission.....	55
2.6	Summary .....	55

### **3 Laboratory Measurement of PAN 57**

3.1	Spectral Measurement Requirements.....	57
3.1.1	Measurement Limitations .....	58
3.2	Experimental Overview .....	59
3.2.1	The NERC Molecular Spectroscopy Facility .....	59
3.2.2	Spectrometer Configuration .....	60
3.2.3	The Sample Cell and Temperature Monitoring .....	65
3.2.4	Gas Handling and Vacuum Line .....	68
3.2.5	Pressure Monitoring.....	70
3.3	Sample Preparation and Purity .....	71
3.3.1	Synthesis of PAN.....	72
3.3.2	Preparation of PAN Vapour Samples .....	74
3.3.3	Sample Purity.....	75
3.3.3.1	PAN Decomposition.....	76
3.3.3.2	Contamination During PAN Synthesis .....	77
3.3.3.3	Other Sample Contamination .....	78
3.4	General Measurement Procedure.....	78



3.5	Measurement Parameters .....	79
3.6	Summary .....	81
<b>4</b>	<b>Analysis of PAN Laboratory Spectra</b>	<b>82</b>
4.1	Quality of Spectra .....	83
4.1.1	Detector Non-linearity .....	83
4.1.2	Thermal and Aperture Artefacts .....	85
4.1.3	Phase Errors .....	86
4.1.4	Wavenumber Calibration.....	86
4.2	Quality of Sample .....	87
4.2.1	Sample Degradation.....	87
4.2.2	Static Contaminants .....	89
4.2.2.1	Contaminant Retrieval Method for CO <sub>2</sub> and H <sub>2</sub> O .....	90
4.2.2.2	Acetone Contamination .....	94
4.3	Summary of Errors.....	97
4.4	Data Analysis of Measured Spectra .....	98
4.4.1	PAN Infrared Absorptivities.....	99
4.4.2	Reference Absorption Cross-sections .....	102
4.4.2.1	Nitrogen Broadening .....	105
4.4.3	Integrated PAN Band Intensities .....	106
4.5	Comparison to Previous Work .....	110
4.5.1	Comparison of Infrared Absorptivities .....	110
4.5.2	Comparison of Integrated Intensities .....	111
4.5.3	Comparison of Cross-sections.....	113
4.6	Conclusions .....	115
<b>5</b>	<b>Detection of PAN in MIPAS-B2 Spectra</b>	<b>117</b>
5.1	The MIPAS-B2 Instrument.....	117
5.1.1	Data Processing.....	119
5.1.2	Flight Details and Performance .....	120
5.1.2.1	Spectral Noise .....	123
5.1.2.2	Field of View and Instrument Lineshape .....	125
5.2	Detection of PAN.....	126



6.3.3	Simulated Spectra .....	186
6.3.4	Comparison to Measured Spectra .....	188
6.3.4.1	Mediterranean Sea, Spectral Band A .....	190
6.3.4.2	Mediterranean Sea, Spectral Band AB .....	197
6.3.4.3	East China Sea, Spectral Band A .....	200
6.3.4.4	East China Sea, Spectral Band AB .....	206
6.4	Detection of Formic Acid .....	209
6.5	Retrieval Accuracy.....	211
6.5.1	Fit Sensitivity .....	212
6.5.2	Limit of Detection.....	214
6.6	Back Trajectory Analysis.....	214
6.7	Conclusions .....	218
<b>7</b>	<b>Conclusions and Further Work</b>	<b>221</b>
7.1	New Laboratory Cross-sections for PAN.....	222
7.2	PAN Detection in MIPAS-B2 Spectral Data .....	223
7.3	PAN Detection in MIPAS-E Spectral Data.....	224
7.4	Future Work .....	226
7.4.1	Laboratory Measurements .....	226
7.4.2	PAN Detection and Retrieval at High Spectral Resolution.....	227
7.4.3	PAN Detection and Retrieval at Lower Spectral Resolution .....	228
7.4.4	Validation.....	231
7.4.5	Other Organic Compounds.....	231
	<b>Bibliography</b>	<b>232</b>

# List of Figures

Figure 1.1 The thermal structure of the Earth's atmosphere .....	2
Figure 1.2 Simplified oxidative tropospheric chemistry of organic compounds.....	9
Figure 1.3 Chemical pathways of PAN .....	14
Figure 1.4 MOZART modelled zonal average PAN concentrations for the year 2000 .....	16
Figure 1.5 Monthly averaged PAN concentrations from TOMCAT for May 2000. ....	18
Figure 1.6 Composite PAN concentration measurements by aircraft.....	20
Figure 2.1 Satellite limb-viewing geometry .....	26
Figure 2.2 Cross-section calculated for PAN by Hanst and Hanst [1993]. ....	41
Figure 2.3 The Classic Michelson Interferometer .....	44
Figure 3.1 Saturation vapour pressure of PAN.....	59
Figure 3.2 Digital photograph of the MSF main laboratory.....	60
Figure 3.3 Optical schematic of the Bruker IFS 120 HR spectrometer .....	61
Figure 3.4 Spectral windows allowed by optical filters used in PAN measurements .....	63
Figure 3.5 A schematic of the 26.0 cm gas absorption cell.....	65
Figure 3.6 Thermistor temperature logs.....	67
Figure 3.7 Schematic of the gas handling and vacuum line apparatus .....	69
Figure 3.8 Absorption cell pressure log .....	71
Figure 3.9 100ml 3-necked flask for PAN synthesis.....	73
Figure 4.1. A Comparison of the 100% transmittance baselines of four recorded spectra ..	84
Figure 4.2 A ratio of initial and final measurements of pure PAN transmission spectra .....	88
Figure 4.3 Spectral fits and residuals for H <sub>2</sub> O and CO <sub>2</sub> in a contaminated sample .....	94
Figure 4.4 Acetone contamination .....	96
Figure 4.5 Effect of acetone contamination on the X-filter region .....	97

Figure 4.6. Infrared absorbance for five strongest PAN bands as a function of temperature .....	101
Figure 4.7 PAN mid-infrared (550-2200 $\text{cm}^{-1}$ ) absorption cross-sections as a function of temperature .....	103
Figure 4.8 A close-up of the 794, 1163 and 1741 $\text{cm}^{-1}$ PAN cross-sectional bands showing temperature dependence at 295 K, 273 K and 250 K .....	105
Figure 4.9 Comparison of cross-sections determined for pure PAN (blue) and PAN+400 mb dry nitrogen gas (black) at 295 K for the a) 1741 $\text{cm}^{-1}$ and b) 794 $\text{cm}^{-1}$ PAN absorption bands.....	106
Figure 4.10 Integrated band areas as a function of PAN pressure and temperature for each of the five strongest PAN absorption bands.....	108
Figure 4.11 A comparison of PAN cross-section with Hanst and Hanst [1993].....	114
Figure 5.1 An illustrative schematic of the MIPAS-B2 spectrometer .....	118
Figure 5.2 Tangent points of the MIPAS-B2 flights 6 and 8 over the Mediterranean Sea	121
Figure 5.3 Absolute NESR spectrum for a typical blackbody measurement for channel 2 during flight 8.....	124
Figure 5.4 Standard deviation spectra derived from 4 coadded scans for MIPAS-B2.....	124
Figure 5.5 Field of view of the MIPAS-B2 instrument .....	126
Figure 5.6 Simulated atmospheric limb-emission spectrum for MIPAS-B2 at 10.7 km ...	128
Figure 5.7 Simulated PAN radiance contribution spectrum for a typical PAN profile.....	129
Figure 5.8 Initial gas concentration profiles for acetone, aerosol, $\text{CCl}_4$ , $\text{CH}_3\text{Cl}$ , $\text{CH}_4$ , $\text{CO}_2$ , F12 and F22 included in simulated atmospheres .....	133
Figure 5.9 Initial gas concentration profiles for $\text{HNO}_4$ , $\text{H}_2\text{O}$ , $\text{HNO}_3$ , $\text{N}_2\text{O}_5$ , $\text{NO}_2$ , $\text{C}_2\text{ClF}_5$ , $\text{C}_2\text{Cl}_2\text{F}_4$ and $\text{C}_2\text{Cl}_3\text{F}_3$ included in simulated atmospheres. ....	134
Figure 5.10 Initial gas concentration profiles for $\text{CClF}_3$ , $\text{C}_2\text{H}_2$ , $\text{COF}_2$ , F11, $\text{SO}_2$ , F14, $\text{C}_2\text{H}_6$ and $\text{NH}_3$ included in simulated atmospheres .....	135
Figure 5.11 Initial gas concentration profiles for $\text{ClO}$ , $\text{ClONO}_2$ , $\text{H}_2\text{O}_2$ , $\text{OCS}$ , $\text{O}_3$ , PAN and profiles for pressure and temperature included in simulated atmospheres.....	136

Figure 5.12 Simulated contributed radiance for: PAN, aerosol, acetone, ethane, ethyne, ozone, CCl <sub>4</sub> and CH <sub>3</sub> Cl, to total limb-emission spectrum at 10.4 km simulated for MIPAS-B2- channel 1 .....	139
Figure 5.13 Simulated contributed radiance for: ClO, ClONO <sub>2</sub> , CO <sub>2</sub> , F11, F113, F22, H <sub>2</sub> O and HCN, to total limb-emission spectrum at 10.4 km simulated for MIPAS-B2- channel 1 .....	140
Figure 5.14 Simulated contributed radiance for: HNO <sub>3</sub> , HNO <sub>4</sub> , NH <sub>3</sub> , COF <sub>2</sub> , NO <sub>2</sub> and OCS, to total limb-emission spectrum at 10.4 km simulated for MIPAS-B2- channel 1 .....	141
Figure 5.15 Simulated contributed radiance for: PAN, acetone, ethyne, methane, ClONO <sub>2</sub> , CO <sub>2</sub> , COF <sub>2</sub> and F113 to total limb-emission spectrum at 10.4 km simulated for MIPAS-B2- channel 1 .....	142
Figure 5.16 Simulated contributed radiance for: F114, F115, F12, F13, F14, F22, H <sub>2</sub> O and H <sub>2</sub> O <sub>2</sub> , to total limb-emission spectrum at 10.4 km simulated for MIPAS-B2- channel 2 .....	143
Figure 5.17 Simulated contributed radiance for: HOCl, N <sub>2</sub> O, N <sub>2</sub> O <sub>5</sub> , NH <sub>3</sub> , O <sub>3</sub> , SO <sub>2</sub> and aerosol, to total limb-emission spectrum at 10.4 km simulated for MIPAS-B2- channel 2 .....	144
Figure 5.18 An example of initial residual spectra for MIPAS-B2 flight 8 in channel 2 ...	146
Figure 5.19 Simulated PAN residual spectrum for flight 8 channel 2 with and without an applied wavenumber shift .....	146
Figure 5.20 Comparison of simulated total and measured spectra for channel 1 of Flight 6 at 13.5 km tangent altitude .....	148
Figure 5.21 Comparison of simulated total and measured spectra for channel 1 of Flight 6 at 10.4 km tangent altitude .....	149
Figure 5.22 Comparison of simulated total and measured spectra for channel 1 of Flight 6 at 8.5 km tangent altitude .....	150
Figure 5.23 PAN profile used to obtain the best simulated fit to MIPAS-B2 Flight 6 data .....	152

Figure 5.24 Jacobian perturbation spectra at 10.5 km for aerosol, pressure and temperature .....	153
Figure 5.25 Comparison of simulated total and measured spectra for channel 2 of flight 8 at 13.5 km tangent altitude .....	155
Figure 5.26 Comparison of simulated total and measured spectra for channel 2 of flight 8 at 10.4 km tangent altitude. ....	156
Figure 5.27 Comparison of simulated total and measured spectra for channel 2 of flight 8 at 10.4 km tangent altitude .....	157
Figure 5.28 Comparison of simulated total and measured spectra for channel 2 of flight 8 at 13.7 km tangent altitude. ....	159
Figure 5.29 Comparison of simulated total and measured spectra for channel 2 of flight 8 at 11.7 km tangent altitude. ....	160
Figure 5.30 Comparison of simulated total and measured spectra for channel 2 of flight 8 at 10.7 km tangent altitude. ....	160
Figure 5.31 Comparison of simulated total and measured spectra for channel 2 of flight 8 at 9.6 km tangent altitude .....	160
Figure 5.32 Comparison of simulated total and measured spectra for channel 2 of flight 8 at 8.5 km tangent altitude .....	161
Figure 5.33 PAN profile used to obtain the best simulated fit to MIPAS-B2 flight 8 data	161
Figure 5.34 Spectral difference plots between 11.7 and 10.4 km .....	164
Figure 6.1 An illustration of the ENVISAT satellite .....	170
Figure 6.2 A component overview schematic of the MIPAS-E instrument .....	171
Figure 6.3 An illustrative schematic of the MIPAS-E interferometer .....	172
Figure 6.4 Viewing geometry of the MIPAS-E instrument .....	174
Figure 6.5 NESR characterisation for MIPAS-E orbit 02081, July 24 <sup>th</sup> , 2002.....	176
Figure 6.6 Data processing structure for MIPAS-E.....	178
Figure 6.7 Valid and cloud-free Level 2 profiles of MIPAS-E data for: H <sub>2</sub> O, O <sub>3</sub> , HNO <sub>3</sub> and CH <sub>4</sub> , selected for the Mediterranean Sea in April 2003 .....	182

Figure 6.8 Valid and cloud-free Level 2 profiles of MIPAS-E data for: N <sub>2</sub> O, NO <sub>2</sub> , pressure and temperature, selected for the Mediterranean Sea in April 2003.....	183
Figure 6.9 Valid and cloud-free Level 2 profiles of MIPAS-E data for: H <sub>2</sub> O, O <sub>3</sub> , HNO <sub>3</sub> and CH <sub>4</sub> selected for the East China Sea in April 2003.....	184
Figure 6.10 Valid and cloud-free Level 2 profiles of MIPAS-E data for: : N <sub>2</sub> O, NO <sub>2</sub> , pressure and temperature, selected for the East China Sea in April 2003.....	185
Figure 6.11 Simulated atmospheric spectra and PAN at a tangent altitude of 11.4 km .....	188
Figure 6.12 Comparison of MIPAS-E band A and simulated spectra at 7.8 km tangent altitude .....	192
Figure 6.13 Comparison of MIPAS-E band A and simulated spectra at 9.1 km tangent altitude .....	193
Figure 6.14 Comparison of MIPAS-E band A and simulated spectra at 10.8 km tangent altitude .....	194
Figure 6.15 Comparison of MIPAS-E band A and simulated spectra at 11.9 km tangent altitude .....	195
Figure 6.16 Comparison of MIPAS-E band A and simulated spectra at 13.8 km tangent altitude .....	196
Figure 6.17 Comparison of MIPAS-E band AB and simulated spectra at 9.1 km tangent altitude .....	198
Figure 6.18 Comparison of MIPAS-E band AB and simulated spectra at 11.9 km tangent altitude .....	199
Figure 6.19 Comparison of MIPAS-E band A and simulated spectra at 9.0 km tangent altitude .....	201
Figure 6.20 Comparison of MIPAS-E band A and simulated spectra at 11.2 km tangent altitude .....	202
Figure 6.21 Comparison of MIPAS-E band A and simulated spectra at 11.2 km tangent altitude .....	203
Figure 6.22 Comparison of MIPAS-E band A and simulated spectra at 12.1 km tangent altitude .....	204



Figure 6.23 Comparison of MIPAS-E band A and simulated spectra at 13.9 km tangent altitude .....	205
Figure 6.24 Comparison of MIPAS-E band AB and simulated spectra at 9.1 km tangent altitude .....	207
Figure 6.25 Comparison of MIPAS-E band AB and simulated spectra at 12.1 km tangent altitude .....	208
Figure 6.26 Comparison of residual spectra for MIPAS-E and simulated residual for formic acid.....	210
Figure 6.27 Fitted PAN concentrations between 11 and 12 km for April 2003 in the Mediterranean Sea and East China Sea .....	216
Figure 6.28 72-hour HYSPLIT single-particle back trajectories at 11.2, 8.2 and 3.0 km originating from nominal geolocation for MIPAS-E sweep TID: 103814901, 11.2 km on 16/04/2003 .....	217
Figure 6.29 72-hour HYSPLIT single-particle back trajectories at 10.0, 4.0 and 1.0 km originating from nominal geolocation for MIPAS-E sweep TID: 10316519, 12.4 km on 09/04/2003.....	218
Figure 7.1 Comparison of spectral fits between fitted simulated PAN residual and MIPAS-E measured residual at spectral resolutions of $0.025\text{ cm}^{-1}$ and MIPAS-E data degraded to $0.1\text{ cm}^{-1}$ .....	229
Figure 7.2 A close up between $775\text{-}810\text{ cm}^{-1}$ comparing of spectral fits between fitted simulated PAN residual and MIPAS-E measured residual spectra at spectral resolutions of $0.025\text{ cm}^{-1}$ and MIPAS-E data degraded to $0.1\text{ cm}^{-1}$ unapodised. ...	230

# List of Tables

Table 1.1 Major aircraft campaigns to have measured PAN between 1985-1999. ....	19
Table 2.1 High-resolution limb sounding spectrometers capable of measuring infrared radiance of the upper troposphere. ....	25
Table 2.2 Mid-infrared band assignments for gaseous PAN. ....	40
Table 2.3 Previously reported infrared absorptivities for gaseous PAN. ....	42
Table 2.4 Previously reported infrared integrated intensities of five strongest PAN bands ....	42
Table 3.1 Configuration of the Bruker IFS120HR spectrometer for PAN measurements...	61
Table 3.2 Allowed spectral pass band of optical filters used for PAN measurements. ....	63
Table 3.3 Summary of measurement parameters for PAN spectra recorded at the NERC MSF ....	80
Table 4.1 Spectral fitting ranges for retrieval of contaminant gas concentrations ....	92
Table 4.2 Retrieved contaminant partial pressures and corrected PAN sample pressures for contaminated measurements ....	93
Table 4.3 Source and magnitude of typical errors assigned to PAN measurements ....	98
Table 4.4 Infrared absorptivities for PAN calculated for nine principal PAN bands at 295, 273 and 250 K. ....	102
Table 4.5 Peak cross-section at 295, 273 and 250 K for nine strongest PAN absorption bands in the mid-infrared. ....	104
Table 4.6 Spectral ranges used to calculate integrated band areas for the nine PAN absorption bands studied. ....	107
Table 4.7 Infrared integrated intensities of nine PAN bands ....	109
Table 4.8 Infrared absorptivities for gaseous PAN with a comparison to previously reported data. ....	111
Table 4.9 Infrared integrated intensities of nine PAN bands with comparison to previously reported data. ....	112

Table 4.10 Relative integrated absorption intensities normalised to the 794 cm <sup>-1</sup> band intensity.....	113
Table 5.1 Pass bands and averaged NESR values for MIPAS-B2 flight 6 Level 1B dataset .....	121
Table 5.2 Elevation angles and corresponding tangent point altitudes of MIPAS-B2 flight 6 spectra. ....	122
Table 5.3. Elevation angles and corresponding tangent heights of MIPAS-B2 flight 8 recorded .....	123
Table 5.4 Spectral regions chosen for the detection of the 794.0 cm <sup>-1</sup> and 1163.0 cm <sup>-1</sup> bands of PAN in MIPAS-B2 channels 1 and 2 .....	129
Table 5.5 Gases known to have spectral influence in the spectral windows of interest to PAN detection. ....	130
Table 5.6 Source list for first guess concentration, pressure and temperature profiles of contaminant gases for input to simulation of true atmosphere .....	132
Table 5.7 Summary of fitted PAN concentrations for MIPAS-B2 spectra.....	165
Table 5.8 Sensitivity of fitted PAN concentration (pptv) in channel 1 to perturbations in otherwise optimised profiles of temperature, pressure, aerosol, water vapour and CCl <sub>4</sub> .....	166
Table 6.1 Nominal pass bands of MIPAS-E spectral channels allowed by the combination of detectors in each output port. ....	174
Table 6.2 Pre-flight NESR (spectral noise) maxima for MIPAS-E measurement channels .....	176
Table 6.3 Reference lines and spectral windows used for spectral calibration and ILS retrieval .....	177
Table 6.4 Geo-location selection criteria for MIPAS-E data .....	180
Table 6.5 Spectral range of simulated spectra appropriate for detection of PAN in MIPAS-E channels A and AB. ....	187
Table 6.6 Fitted PAN concentrations for MIPAS-E profiles studied in this thesis with uncertainty due to spectroscopic error .....	211

Table 6.7 Sensitivity of fitted PAN concentration (pptv) to perturbations in otherwise optimised profiles of temperature, pressure, aerosol and CCl <sub>4</sub> .....	213
Table 6.8 Theoretical limits of detection for PAN (pptv) in measurement bands A and AB for MIPAS-E at nominal altitudes of 9 and 12 km.....	214

# Chapter 1

## 1 Introduction

Over the last decades, terms such as “global warming” and “climate change” have become household expressions. We see this as evidence for growing public concern regarding human impacts on the climate system and the effects thereof.

The changing composition of the atmosphere is an aspect of the climate system that is of special interest as the abundances of many minor constituents (trace gases) can affect the Earth’s radiation balance, potentially leading to an increased greenhouse effect and therefore to increased average surface temperatures. In addition there is the potential for many other local, regional and global effects, such as an increased frequency of extreme weather events, flooding and drought [IPCC, 2001].

The atmosphere is categorised into layers defined by the local vertical temperature gradient (see Figure 1.1). The troposphere (0 to 18 km at the tropics) extends from the Earth’s surface to the tropopause; a point defined by the transition from a decreasing to an increasing temperature gradient, and absorbs a significant fraction of the total infrared (IR) radiation emitted from the Earth’s surface (with the remainder absorbed at higher altitude or radiated to space). The resulting decreasing vertical temperature gradient gives rise to strong convective dynamics and the associated instability of this layer causes most tropospheric processes to occur on the timescale of days.

The region above the tropopause, known as the stratosphere, is heated by the absorption of solar ultraviolet (UV) radiation by ozone and characterised by an increasing vertical temperature gradient and consequent slow vertical mixing. Vertical transport typically takes place on the timescale of years rather than days and exchanges with the troposphere are slow due to the temperature inversion at the tropopause. The higher layers of the Earth’s atmosphere, above the stratosphere, have little impact on the

upper troposphere (the region of interest in this thesis) and are therefore not considered further in this work.

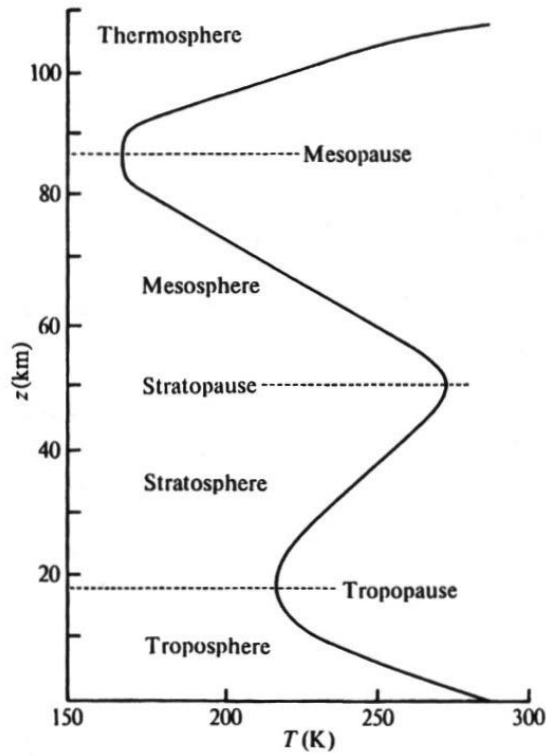


**Figure 1.1** The thermal structure of the Earth's atmosphere. The curve shown represents typical mean temperature at 40° North for June. Taken from Wayne [1991].

The Upper Troposphere (UT) is an intermediate region of the atmosphere between the rest of the troposphere below and the stratosphere above. Its uppermost limit is defined as a region of minimum temperature gradient between the warmer regions above and below and is generally defined to be between 8 and 12 km altitude at mid-latitudes [Jaegle *et al.*, 1999a]. It also defines a dividing layer between the differing transport and chemical regimes of the surrounding atmosphere. Furthermore, it is seen to be the coldest part of the lower atmosphere with temperatures reaching as low as 190 K in the tropical tropopause layer [Newell and Gould-Stewart, 1981].

The UT is known to have a potentially significant impact on the radiation balance of the atmosphere due to changes in its chemical constituents. In addition to the most prominent greenhouse gases such as carbon dioxide and methane, there are many lesser-characterised and variable trace gases that may have impacts on the climate system through direct radiative forcing or indirect impacts on the chemistry of

tropospheric ozone, for example. In addition, such trace gases may also affect the lifetimes of other molecules such as methane and the hydrochlorofluorocarbons (HCFCs) by affecting the oxidising potential of the atmosphere.

Recent aircraft campaigns to study UT chemistry have revealed high concentrations of many oxygenated organic compounds such as acetone, formaldehyde and peroxyacetyl nitrate [e. g. Heald *et al.*, 2003; Holzinger *et al.*, 2005]. The chemical roles of such organic compounds in the UT are manifold and poorly understood.

Compared with the surrounding regions of the atmosphere, observations and understanding of processes in the UT have been limited until relatively recently. However, new satellite instruments able to probe this region as well as many aircraft campaigns, are helping to increase the body of data and scientific interest in the chemistry and dynamics of the UT is high as a result.

New infrared remote sensing instruments on satellite platforms represent a new opportunity for studying the global chemical composition of the atmosphere from space. These have the capability to record high-resolution infrared spectra of the Earth's atmosphere, from which vertical concentration profiles for many trace gases may be retrieved.

The motivation for this thesis is to assess the potential for the retrieval of organic compounds in the UT, specifically the chemically important compound peroxyacetyl nitrate (PAN). In the remainder of this introduction, the chemistry and dynamics of the UT are first discussed, the role of PAN in the UT is examined and previous atmospheric measurements of PAN are reviewed.

## **1.1 Chemistry and Dynamics of the Upper Troposphere**

The chemistry and dynamics of the UT are complex. *In situ* chemistry coupled with transport from the chemically distinct stratosphere above and the remainder of the troposphere below, as well as direct emissions from aircraft, make this a highly variable chemical environment. This section describes the physical and chemical processes of the UT and their relation to the surrounding atmosphere.

### 1.1.1 Dynamics of the Upper Troposphere

Tropospheric dynamics are dominated by convective transport and associated large-scale pressure systems, and frontal activity. This convection is driven by radiative heating of air at the surface and a decreasing temperature gradient with height. The advection of airmasses from the lower troposphere by such processes (which may carry large amounts of anthropogenic pollution) can perturb the chemistry of the UT, causing changes to its equilibrium state.

The influence of vertical transport events that lift polluted planetary boundary layer air high into the UT can lead to an enhancement of species usually seen to have high volume mixing ratios at surface pollution sites such as SO<sub>2</sub>, NO<sub>2</sub>, HNO<sub>3</sub> and PAN. Depending on the meteorological history of a UT airmass, its composition can be quite different. For example, highly soluble species may experience removal by washout and rainout. Other airmasses may be characteristically photochemically aged or relatively clean due to the uplift of air from a remote ocean environment.

These vertical transport events are associated with large-scale convection of moist airmasses in the tropics and also with pressure systems in the mid-latitudes. The ascent of tropical air in cumulonimbus columns allows boundary layer air to reach high into the UT due to the large latent heat associated with such airmasses [Kritz *et al.*, 1991; Kelly *et al.*, 1993].

In the mid-latitudes, cyclonic pressure systems and associated surface cold fronts have been observed to lift boundary layer pollution high into the UT as they pass across polluted surface environments [e.g. Arnold *et al.*, 1997]. These so-called *warm conveyor belts* described by Stohl [2001] are associated with the convective uplift of warm surface air as cold frontal air passes; and represent a major mechanism for the transport of pollutants into the UT in the mid-latitudes. In addition, strong biomass burning plumes have also been observed to reach the UT, carrying large amounts of carbon based molecules and aerosol with them [Andreae and Merlet, 2001].

The tropopause acts as an efficient boundary, preventing large-scale mixing of the layers above and below due to the inversion of the temperature gradient at this point, thus essentially halting dry convection. However, transport of gases (e.g. ozone) from the lower stratosphere (LS) into the UT can also affect the chemistry of the region. The LS is characterised by slow vertical transport and a positive temperature gradient. It is rich in ozone and poor in water vapour, with a chemistry dominated by catalytic



destruction cycles. This interaction between the UT and the LS is important for both regions.

The so-called *Stratosphere-Troposphere Exchange* (STE) described by Holton [1995] is also important, as this is the route by which anthropogenic ozone depleting substances reach, and are removed from, the stratospheric ozone layer. Reactive species such as ozone are also enriched in the tropospheric chemical system in the reverse exchange. As well as the impact on chemistry, these inputs can also affect the local radiative flux of both regions. In addition, other smaller-scale transport mechanisms involve exchange through the tropopause such as diffusion.

The conventional thermal definition of the tropopause often obscures differing definitions that might include chemistry. A more convenient way to describe the tropopause defined by Holton [1995] is that the tropical tropopause corresponds roughly to a 380 K isentrope and that in the extra-tropics it is better defined by potential vorticity (PV), taking the 2 PVU surface (where PVU denotes the potential vorticity unit,  $1 \text{ PVU} = 10^{-6} \text{ m}^2 \text{ s}^{-1} \text{ K kg}^{-1}$ ). In general, the tropopause slopes downward and poleward, resulting in a differing definition of the height of the UT as a function of latitude.

The UT is therefore a key atmospheric region of interest; representing a region where chemically different airmasses above and below may intermix, thus affecting the chemical and radiative balance of the atmosphere around this region.

### **1.1.2 Chemistry of the Upper Troposphere**

The UT is low in ozone concentration relative to the stratosphere, with ozone formed primarily by  $\text{NO}_2$  photolysis amplified by  $\text{HO}_x$  chemistry (see Section 1.1.2.1). This  $\text{HO}_x$  chemistry is also modified by the presence of Volatile Organic Compounds (VOCs), which may be advected to the UT in polluted airmasses.

The major chemical questions in the UT concern possible trends in the concentrations of the major upper tropospheric oxidants,  $\text{O}_3$  and OH [Jacob, 2000], and the extent to which these changes are a function of atmospheric pollution in the boundary layer and aircraft emissions in the free troposphere [Bruhl *et al.*, 2000]. Any reduction in the oxidative power of the UT could lead to increased concentrations of VOCs and Non-Methyl HydroCarbons (NMHCs), thus affecting the radiative balance of the atmosphere because of their ability to attenuate radiation [Poisson *et al.*, 2000].

UT ozone is of concern not only because of its indirect effects on climate through its chemistry, but also because it is a potent greenhouse gas in its own right and an increasing trend in its concentration will further exacerbate the global warming problem. In addition, high surface ozone levels have been associated with adverse effects on human health such as those experienced in photochemical smog episodes regularly seen in large polluted cities.

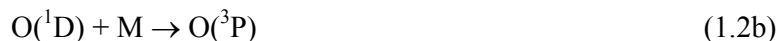
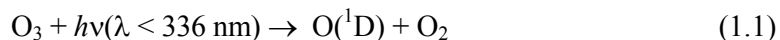
### 1.1.2.1 HO<sub>x</sub> and NO<sub>x</sub> Chemistry

The primary active radical species in UT chemistry are the active hydrogen and nitrogen species symbolised as HO<sub>x</sub> (OH + HO<sub>2</sub>) and NO<sub>x</sub> (NO + NO<sub>2</sub>) respectively. Together, these radical species act to control the oxidising potential of the atmosphere as well as the net production or loss of tropospheric ozone [Jaeglé *et al.*, 2000].

Major atmospheric oxidants in the UT are the hydroxyl radical (OH) and ozone (O<sub>3</sub>), with a contribution from the nitrate radical (NO<sub>3</sub>) at night. Together, these compounds serve to “clean” the atmosphere of tropospheric pollutants. In addition, HO<sub>2</sub> is responsible for the conversion of NO to NO<sub>2</sub>, which ultimately leads to ozone production.

The total nitrogen content of an air parcel is defined by the term NO<sub>y</sub> (NO<sub>x</sub> + Reservoirs) and clues to the origin, chemistry and evolution of an air parcel in the UT can be inferred from the partitioning between NO<sub>x</sub> and NO<sub>y</sub> [Wang *et al.*, 1997].

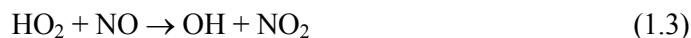
The major source of OH, first identified by Crutzen [1974] in remote areas is the photolysis of O<sub>3</sub> to electronically excited O(<sup>1</sup>D), followed by reaction with water vapour thus:



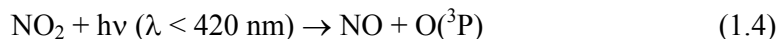
where M represents some stabilizing intermediary (usually N<sub>2</sub>). Only a small portion (1-10%) of the excited oxygen reacts with water to produce OH through Reaction 1.2a; the rest is deactivated through Reaction 1.2b and reacts with molecular oxygen to reform ozone.

In polluted UT airmasses, there are also additional sources of OH such as the photolysis of nitrous acid (HONO), hydrogen peroxide (H<sub>2</sub>O<sub>2</sub>), acetone (CH<sub>3</sub>C(O)CH<sub>3</sub>)

and formaldehyde (HCHO) [Folkins and Chatfield, 2000]; and in the presence of NO, sources of HO<sub>2</sub> can become sources of OH through the reaction:



The photolysis of NO<sub>2</sub> is a major source of UT ozone through the following reactions:



The products of Reaction 1.3 can also react with each other in the presence of a catalyst to remove OH from the system, terminating the catalytic cycle and generating one of the major *reservoir* compounds for NO<sub>2</sub>; HNO<sub>3</sub>:



This HNO<sub>3</sub> can either photolyse in the reverse of Reaction 1.6, but is also readily lost in the troposphere by both wet and dry deposition.

The stability of such reservoir compounds (including PAN, see following section), relative to active radical species, can allow NO<sub>x</sub> to be effectively transported across synoptic scales (> 100 km) or perhaps removed under certain conditions, for example by the efficient wet deposition of HNO<sub>3</sub>. Thus, HNO<sub>3</sub> can be considered a net atmospheric sink for NO<sub>2</sub> but can act as a local source under suitable conditions.

Hence we see the closely coupled nature of HO<sub>x</sub> and NO<sub>x</sub> chemistry in the UT and that high tropospheric ozone levels can be associated with elevated anthropogenic NO<sub>x</sub> concentrations [Crutzen, 1979]. Other smaller contributions to the production rate of tropospheric ozone, from natural sources of NO<sub>x</sub> and VOCs also exist and increase the rate of the reactions described above. Organic compounds also mediate the relative concentrations of HO<sub>x</sub> and NO<sub>x</sub>; acting as both net sources or sinks of active radicals or perhaps as reservoir species (e.g. PAN) under differing chemical and atmospheric environments.

### 1.1.3 Organic Compounds

The role of organic compounds in the UT is manifold. Oxygenated VOCs (or OVOCs) such as acetone, formaldehyde and formic acid can act as sources of  $\text{HO}_x$  radicals, but can also provide a sink or reservoir for reactive nitrogen ( $\text{NO}_x$ ) such as PAN (see Section 1.1.3.2). Sparse atmospheric measurement of such organic compounds, however, means that considerable uncertainty exists in their distribution and therefore their overall influence on the key chemical species of the UT:  $\text{HO}_x$ ,  $\text{NO}_x$  and ozone.

Hence, organic compounds can affect the oxidising potential of the atmosphere as well as tropospheric ozone concentrations. Organic reservoir species serve to mediate active chemistry, therefore acting as net local sources or sinks for active radicals.

Specific functional types of organic compounds are nominally defined as  $\text{RX}$  where X defines the functional group of chemical importance (e.g.  $\text{RO}_2$  defines the peroxy radical species). Figure 1.2 illustrates the role of such organic compounds in oxidative tropospheric chemistry and their coupling to  $\text{HO}_x$  and  $\text{NO}_x$  cycles. This figure also shows the production of ozone associated with such chemistry and the formation of carboxylic acids ( $\text{ROOH}$ ), which are easily removed from tropospheric air due to their high affinity for water vapour.

The oxidation chain and eventual removal of organic compounds in the troposphere is complex. There are multiple pathways available for such reactions to occur as well as varying wet and dry deposition rates and heterogeneous chemistry, but the net result is that oxidation leads to the formation of  $\text{HO}_2 + \text{RO}_2$  through radical reactions (where R refers to a hydrocarbon chain; e.g.  $\text{CH}_3$ ).

In the following sections we look at some of the important chemical mechanisms relevant to organic compounds in the troposphere. A full discussion of all atmospheric reactions is beyond the scope of this thesis, but the reader is referred to the reviews of Finlayson-Pitts [2000] and Baird [1999], upon which this discussion is largely based.

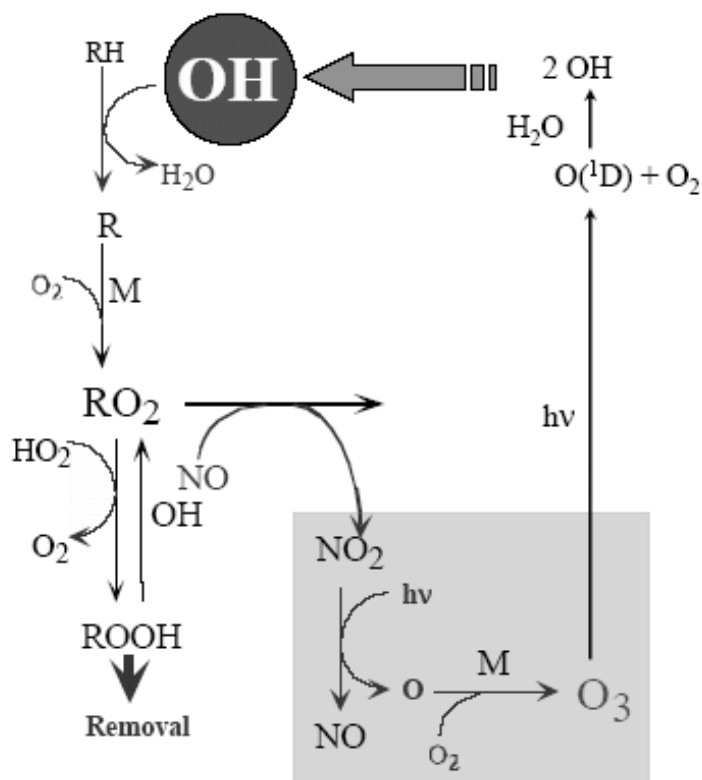


**Figure 1.2** Simplified oxidative tropospheric chemistry of organic compounds and their relationship to the chemistry of HO<sub>x</sub>, NO<sub>x</sub> and O<sub>3</sub>.

### 1.1.3.1 Alkanes and Alkenes

Alkanes and alkenes are compounds that are emitted from the surface layer both through anthropogenic and biogenic emission (e.g. methane) and are not formed by *in situ* chemistry. These molecules initiate a chain of numerous reactions, the most important of which are detailed below.

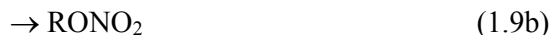
Alkanes react with OH and, at night-time, with NO<sub>3</sub> via the following reactions:



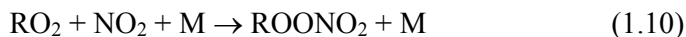
The resulting methyl radical reacts fast and only with O<sub>2</sub> to give the peroxyradical:



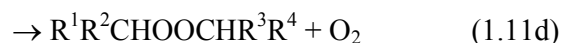
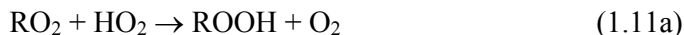
The peroxyradical has two pathways in the troposphere in the presence of NO to give NO<sub>2</sub> or a reservoir:



Reaction 1.9b is favoured with increasing pressure and decreasing temperature. The lower temperatures typical in the UT therefore increase the thermal lifetime of peroxyradicals allowing them to be transported over wide areas. In urban environments with increased NO<sub>2</sub> concentrations, peroxyalkyl nitrates can also be formed in the following way:



Other major reactions of the peroxyalkyl radical are with HO<sub>2</sub> and other RO<sub>2</sub> radicals forming organic acids, aldehydes and alcohols:

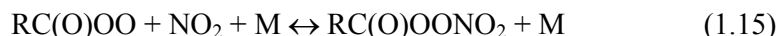
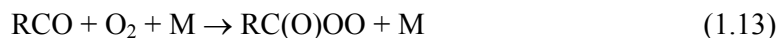


Each of these functional types has its own role in further reactions but an important point of note is that OVOCs can all act as sources of HO<sub>x</sub> by photolysis (e.g. formic acid, acetone, formaldehyde) and some act as reservoirs of NO<sub>x</sub> either directly (Reaction 1.10), or through the further oxidation of aldehydes and subsequent reaction with NO<sub>2</sub> to form peroxy acyl nitrates (PANs; see following section).

The reactions of alkenes can also follow other pathways including reaction with O<sub>3</sub> (ozonolysis), thus resulting in the formation of more OVOCs. The net result of such chemistry is complex, with the destruction of ozone by ozonolysis leading to further formation of HO<sub>x</sub> from the photolysis of resulting OVOCs.

### 1.1.3.2 Aldehydes and PANs

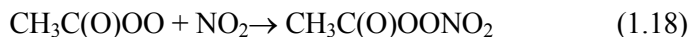
Aldehydes (RCHO) can undergo photolysis or react with OH or NO<sub>3</sub> in decreasing order of importance. The following reactions illustrate the oxidation of aldehydes and subsequent reactions, which lead to PAN (CH<sub>3</sub>C(O)OONO<sub>2</sub>) and its higher order analogues (RC(O)OONO<sub>2</sub>):



The rate of Reaction 1.14a is typically small compared with Reaction 1.15, although it can become competitive in high NO/NO<sub>2</sub> conditions [Jacobi *et al.*, 1999]. The rate of formation of PAN depends strongly on the relative amount of NO and NO<sub>2</sub> present as well as ambient pressure and temperature [Bridier *et al.*, 1991]. As already stated, it is this dependence on temperature that make PANs (RC(O)OONO<sub>2</sub>) efficient transporters of NO<sub>2</sub> in the upper troposphere.

The most important aldehyde in this mechanism is acetaldehyde (CH<sub>3</sub>CHO) both because of its abundance in the atmosphere and because of its main product, peroxyacetyl nitrate (PAN; CH<sub>3</sub>C(O)OONO<sub>2</sub>). PAN is by far the most abundant of the PANs and is more stable than higher order PANs by an order of magnitude. It is the nature of this varying thermal stability with pressure and temperature, as well as local NO/NO<sub>2</sub> partitioning, which makes PAN an efficient long-range transport species for NO<sub>2</sub>.

It has long been recognised that PAN is a product of the photochemical oxidation of non-methyl hydrocarbons (NMHCs) and subsequent reaction in the presence of nitrogen oxides [Stephens, 1969]. As much as half of *in situ* PAN formation in the UT has been found to be due to acetone photolysis in the northern mid-latitudes due to uplifted surface acetone [Arnold *et al.*, 1997] through the reactions:



Much of the remainder is formed by the oxidation of acetaldehyde in the presence of  $\text{NO}_2$  by Reactions 1.12 to 1.15; the small remainder of PAN formation is due to the various many other sources of the  $\text{CH}_3\text{CO}$  radical, with all reactions having to go through Reactions 1.17 and 1.18.

## 1.2 The Role of Peroxyacetyl Nitrate in the Troposphere

Peroxyacetyl nitrate (PAN,  $[\text{CH}_3\text{C}(\text{O})\text{OONO}_2]$ ) is ubiquitous in the troposphere and is a key reservoir species for  $\text{NO}_x$  [Singh and Hanst, 1981; Singh and Salas, 1983]. Both measurements [e.g. Singh *et al.*, 1994] and a three-dimensional Global Chemical and Transport Model (GCTM) study [Kashibatla *et al.*, 1993] have shown that in the free troposphere, PAN is a major component of  $\text{NO}_y$ . In some cases, for example where  $\text{HNO}_3$  has been “rained out”, it can become the dominant form of  $\text{NO}_y$ , albeit in a  $\text{NO}_y$  reduced airmass [McFadyen and Cape, 1999].

Despite its significance in UT chemistry described in the previous section, atmospheric measurements of PAN in the free and upper troposphere remain relatively sparse and there is a need for a greater body of data in order to understand the changing makeup and chemistry of the UT region. Such measurements of PAN in the atmosphere are limited to *in situ* detection methods using fixed instruments flown on specialised aircraft campaigns (see Emmons *et al.*, 1997, for a summary of such campaigns).

PAN is short-lived in the boundary layer (approximately two hours at 295 K) due to high rates of thermolysis [Senum *et al.*, 1986; Kirchener *et al.*, 1999]. However, this thermal decomposition rate decreases rapidly with altitude through the troposphere due to decreasing temperature and pressure, allowing PAN lifetimes against thermolysis of the order of months in the upper troposphere [Jacobi *et al.*, 1999]. Reaction with OH becomes dominant in this region [Talukdar *et al.*, 1995], although the long lifetime of PAN allows the transport of  $\text{NO}_x$  from polluted regions across thousands of kilometres, whereupon thermal dissociation may lead to the release of  $\text{NO}_2$  in subsiding UT airmasses [Singh, 1987]. This increase in  $\text{NO}_x$  in the lower troposphere, in otherwise



pristine locations, can lead to increased surface ozone levels in remote areas [e.g. Olszyna *et al.*, 1994; Kotchenruther *et al.*, 2001].

The limited sampling, quality and availability of PAN data in the troposphere given its chemical significance, make the requirement for more comprehensive measurement ability an important scientific concern. Little is known of the true average global concentrations of PAN in the UT or possible trends in its concentration with time. Localised concentrations, such as those seen in pollution events are also relatively poorly characterised and rely on specialised campaigns such as those discussed by Singh *et al.* [1990]. The launch of a number of remote sensing satellite platforms could further understanding of tropospheric chemistry and processes with greater certainty through their potential for global coverage. Further measurement capability could also allow greater confidence in chemistry and climate models that use such data [e.g. Moxim *et al.*, 1996; Levy II *et al.*, 1999].

### 1.2.1 Sources and Sinks of PAN

PAN was first identified in 1956 by Stephens *et al.* [1956] as a component of Los Angeles photochemical smog. The largest surface concentrations of PAN are typically found in photochemical smog episodes in large polluted cities. These cities act as primary source regions for both PAN and its precursors [Lelieveld *et al.*, 2002]. Extremely high-localised PAN concentrations (greater than 10 ppbv) have also been linked to adverse health effects and crop losses [Kleindienst, 1994]. PAN concentrations of up to several ppbv are commonly observed in Europe during spring due to long-range transport and local photochemical production [Penkett and Brice, 1986, Tsalkani *et al.*, 1991]. Lower temperatures at high latitudes stabilise PAN, preventing thermal decay and permitting long-range transport [Orlando *et al.*, 1992]. Episodes of Arctic outflow of PAN-rich air can bring concentrations of PAN in the region of 200 to 500 pptv to mid-latitudes [Singh *et al.*, 1992a; 1992b]. Conversely much lower concentrations are advected in flows from the South due to thermal depletion of PAN and termination reactions of precursors.

As already discussed in Section 1.1.3.2, as much as half of *in situ* PAN formation in the UT has been found to be due to acetone photolysis in the northern mid-latitudes. Global sources of acetone, and hence much of PAN, are estimated by Jacob *et al.* [2001] to be due to atmospheric oxidation of precursor hydrocarbons (51%), direct

emission from biomass burning (26%) and primary anthropogenic emission (23%). Figure 1.3 shows the complex chemistry of PAN, its precursors and dissociative products.

Hence, PAN can be created in large quantities in photochemically polluted environments where the abundance of precursor hydrocarbons including isoprene (an abundant biogenic hydrocarbon), NO<sub>2</sub> and solar radiation are largest [Trainer *et al.* 1991]. Although the rate coefficient for PAN formation (see Reaction 1.18) is large ( $k_1 = 9.6 \times 10^{-12} \text{ cm}^3 \text{ s}^{-1}$  at 298 K [Bridier *et al.*, 1991]), the lifetime of PAN at the surface is limited by the thermal decomposition rate ( $k_2 = 4.6 \times 10^{-4} \text{ s}^{-1}$  at 298 K). However, if transported into the free and upper troposphere this lifetime increases by two orders of magnitude or more ( $k_2 = 1.1 \times 10^{-6} \text{ s}^{-1}$  at 263 K, [Bridier *et al.*, 1991]). A detailed review of the atmospheric chemistry of organic nitrates by Roberts [1990] showed that other chemical loss rates from photolysis and reaction with OH ( $k = 3 \times 10^{-14} \text{ cm}^3 \text{ molecule}^{-1} \text{ s}^{-1}$ , [Talukdar *et al.*, 1995]) become dominant only when the thermal lifetime of PAN exceeds one hundred days such as in the cold temperatures of the UT. Compared with the timescale of tropospheric processes (typically only a few days), we see that the atmospheric role of PAN is therefore ultimately determined by its thermal decomposition properties.

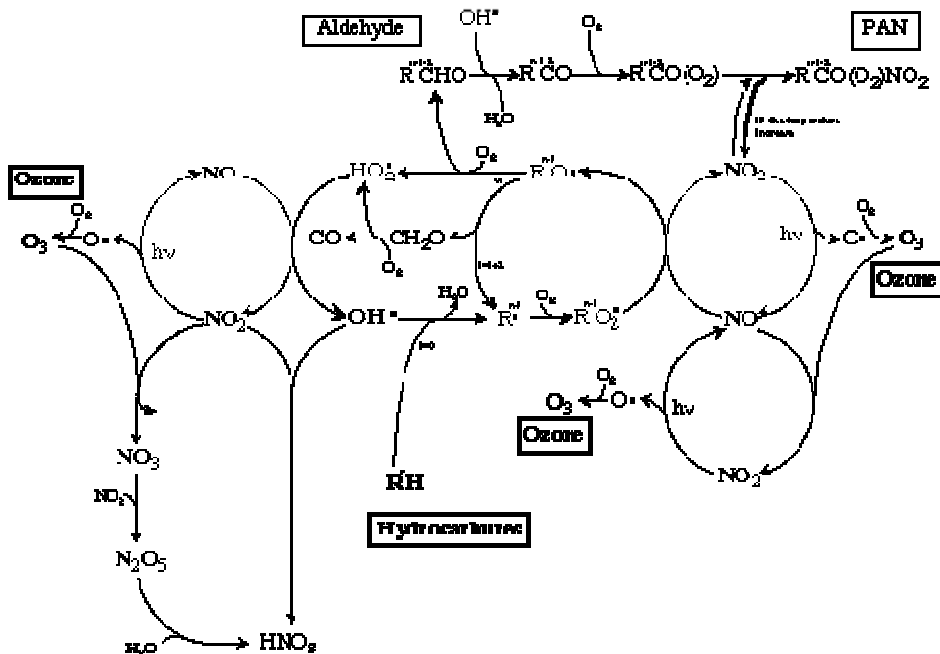


**Figure 1.3** Schematic showing available chemical pathways available for PAN production and loss and the role of OH and NO<sub>2</sub> chemistry. Figure courtesy of A.B.Haurie ([http://ecolunfo.unige.ch/~haurie/mutate/Mutate\\_final/Lectures/Lect\\_1\\_5\\_3/Image212.gif](http://ecolunfo.unige.ch/~haurie/mutate/Mutate_final/Lectures/Lect_1_5_3/Image212.gif)).

Several experimental and theoretical studies have demonstrated that PAN can be transported from polluted continental sites into the upper troposphere by fast, deep convection [e.g. Singh *et al.*, 1996; Jaffe *et al.*, 1997]. More recently, studies undertaken as part of the TRANsport and Chemical Evolution over the Pacific (TRACE-P) aircraft campaign [see Jacob *et al.*, 2003] have shown that cold frontal activity and associated warm conveyor belts can also lift boundary layer pollutants high into the troposphere at mid-latitudes.

Thus, PAN can be used as a specific indicator of anthropogenic photochemical air pollution in remote air masses. This can affect the NO<sub>x</sub> balance of those regions in the troposphere that are not directly influenced by long-range transport of NO<sub>x</sub> from continental sources due to the short chemical lifetime of NO<sub>x</sub> of 1 to 2 days under typical tropospheric conditions [Liu *et al.*, 1987]. This transport of active nitrogen to remote environments influences the production of surface ozone, which would otherwise be NO<sub>x</sub> limited [Carroll and Thompson, 1990].

Other non-chemical loss rates of PAN from the atmosphere are by wet and dry deposition and the removal of PAN by heterogeneous processes. Surface deposition velocities are poorly studied and highly variable with limited results showing variations between 0.2 and 0.8 cm s<sup>-1</sup> [Schrimpf *et al.*, 1996]. Such deposition is considered to be an important sink for PAN in the boundary layer although further work is required to better characterise this loss rate in surface chemistry models. The removal of PAN by “rainout” is negligible however because of its small Henry’s law coefficient ( $H = 9.04 \times \exp[(6513)/T]$  M atm<sup>-1</sup>) [Kames *et al.*, 1991]. This property makes it very different to HNO<sub>3</sub> (the other major reservoir of NO<sub>x</sub> in the troposphere), which is easily sequestered onto cloud droplets and subsequently removed from the atmosphere.

## 1.2.2 Global Distribution

The only information on global distributions of PAN concentrations are, as yet, simulated results from global chemical transport models (GCTMs, e.g. Singh *et al.*, 1986; Moxim *et al.*, 1996]. Some models are validated with the increasing dataset from *in situ* measurements during aircraft campaigns and at surface sites [e.g. Emmons *et al.*, 1997; Jacobi *et al.*, 1999; Kothchenruther *et al.* 2001; Heald, 2003]. However, in the UT, measurements of PAN are currently only possible using aircraft and given the high altitude of the UT, even these measurements are sparse.

Figure 1.4 shows simulated monthly and zonally averaged PAN concentrations for the year 2000 using the Model for OZone And Related Tracers (MOZART) described by Horowitz *et al.* [2003]. Such simulations can provide useful diagnostics of the general qualitative distribution of PAN.

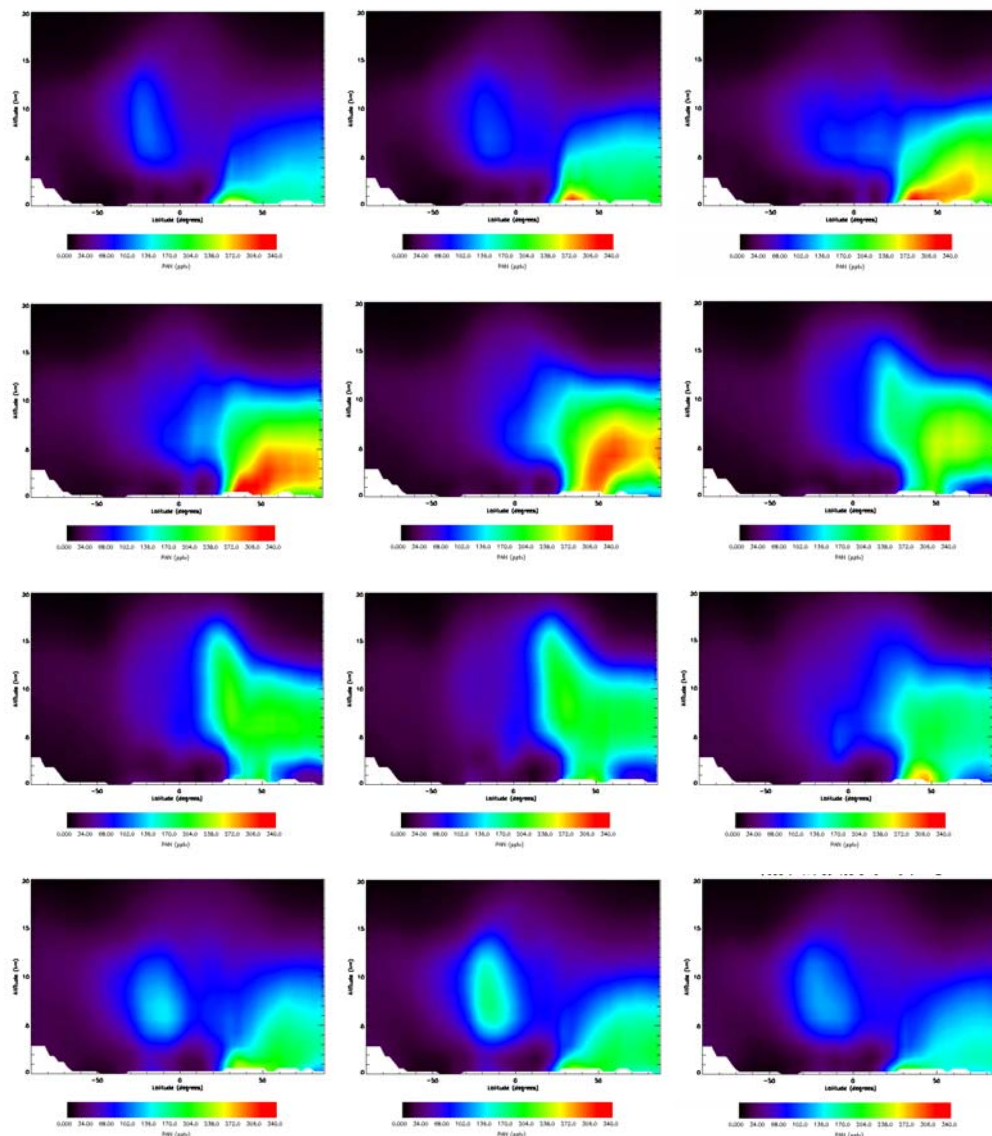


**Figure 1.4** Global zonally averaged PAN concentrations as a function of latitude and altitude for Jan – Dec 2000 in 1 month time steps plotted from simulated output by the MOZART chemical transport model [Hauglustaine *et al.* 1998].

Figure 1.4 clearly shows the predominance of PAN in the Northern Hemisphere. This is expected due to the abundance of precursor source sites such as large cities and industry. In the atmospheric boundary layer, PAN is concentrated over the continental

sites of NO<sub>x</sub> emissions, primarily the mid-latitudes of the Northern Hemisphere. The Southern Hemisphere is simulated to have much lower PAN concentrations due to the lack of anthropogenic precursor sources [Moxim *et al.*, 1996].

The more complicated seasonal variability is not only a function of changing atmospheric dynamics, but also of the changing ambient conditions, in particular the temperature structure of the troposphere and the availability of solar radiation for photolytic reactions. This is why we see a peak in April and May, when Northern Hemisphere lower troposphere temperatures are sufficiently low to permit a long lifetime for PAN whilst photolytic reactions can occur with sufficient rate to enhance production. The cause of simulated increased PAN concentrations, between 5 and 10 km in the Southern extra-tropics in November, is unexplained.

Similar distributions are also seen in the globally gridded output from the Tropospheric Ozone Model of Chemistry and Tracers (TOMCAT) shown in Figure 1.5. For a full description of the model and the assumed chemistry scheme of the TOMCAT model, see Chipperfield *et al.* [1999].

At surface levels (1011 mb), it is possible to see the influence of individual PAN source regions in Europe, China and the Eastern United States. In the free troposphere (501 mb), PAN is more zonally uniform with the highest values in the Polar Regions. And in the upper troposphere (181 mb) this distribution is more zonally uniform, with evidence to suggest that convective outflow from the Eastern United States can give enhanced PAN concentrations in the Atlantic, an event that has been observed in many aircraft campaigns [Jacobi *et al.*, 1999, Emmons *et al.*, 1997, Jaegle *et al.*, 1999a, 1999b].

Localised time series of NO<sub>x</sub> and PAN show that mean mixing ratios in remote surface regions are composed of numerous short-term (1 to 2 days) and large magnitude events [Olszyna *et al.*, 1994]. These episodes are large enough to result in ozone production even when background monthly mean NO<sub>x</sub> values are in the net ozone destruction range. PAN also induces high NO<sub>x</sub> episodes over the remote extra-tropical oceans by transport of polluted UT air from mid-latitudes that sink anticyclonically equatorward, releasing NO<sub>x</sub> from the PAN molecule in the warmer air.

Therefore, PAN, by nature of its temperature sensitivity, provides the efficient redistribution of NO<sub>x</sub> far from its source regions [Moxim *et al.*, 1996] and has been found to increase monthly mean NO<sub>x</sub> concentrations in the remote lower troposphere by up to a factor of five from background concentrations of around 100 pptv [Sillman *et*

*al.*, 1990]. Such increases are simulated to have the largest relative effect in the North Atlantic and North Pacific oceans [Levy II *et al.*, 1999; Jacobi *et al.*, 1999].

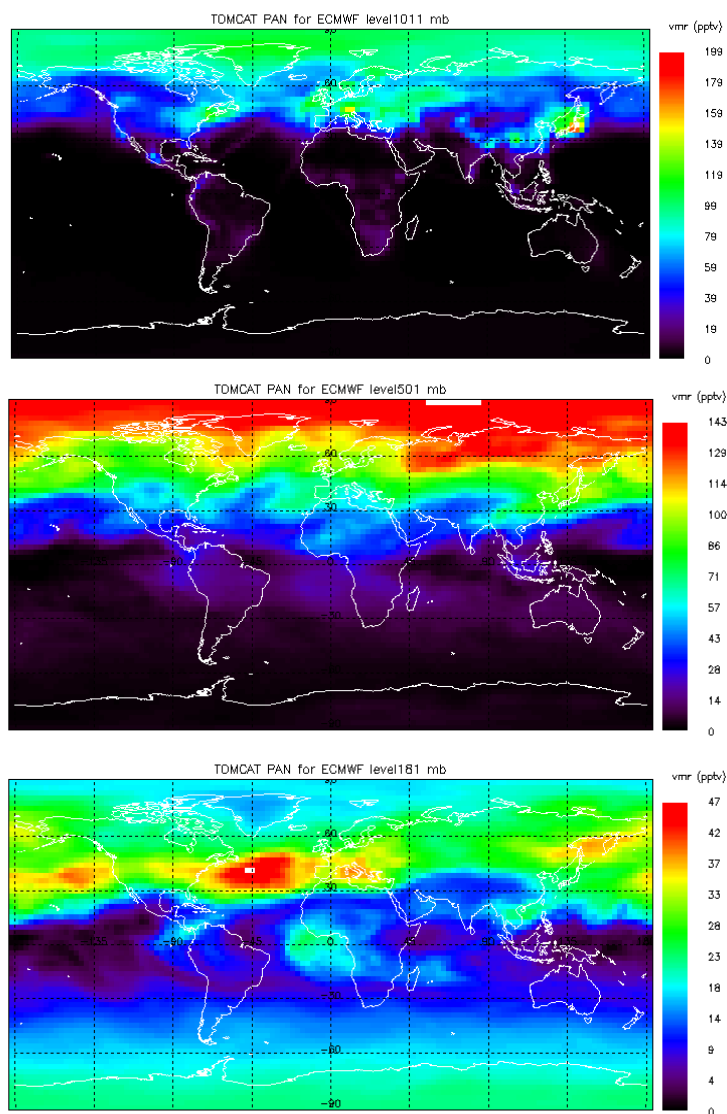


**Figure 1.5** Monthly averaged gridded ( $2.8^\circ \times 2.8^\circ$ ) output of PAN concentration from TOMCAT for May 2000 at 1011, 501 and 181 mb pressure level respectively.

In addition, PAN is expected to influence  $\text{NO}_x$  levels in the upper troposphere. Modelling studies by Moxim *et al.* [1996], Krause *et al.* [1996] and later by Penner *et al.* [1998] have shown that  $\text{NO}_x$  levels in the UT are modified by  $\pm 10\%$  with the inclusion of PAN chemistry; caused by the increased photolysis rate of PAN in the UT.

Future projections of the global distribution of PAN, based on chemistry-climate models that include future gaseous emission scenarios predict that the background concentration of PAN in the free and upper troposphere could increase by up to 50% on year 2000 levels over the next fifty years [Lawrence, 2004]. This is due to the expected increase in anthropogenic precursors in Inter-Governmental Panel on Climate Change (IPCC) emissions scenarios [IPCC, 2001]. Such increases in PAN concentration in the UT will further increase the redistribution of NO<sub>x</sub> to remote locations, affecting boundary layer chemistry but also affecting the oxidising power and radiative balance of the atmosphere.

### 1.2.3 Measuring PAN in the Atmosphere

In the free and upper troposphere, PAN is usually measured *in situ* as part of specialised atmospheric chemistry campaigns using aircraft. Such campaigns typically measure a range of key tropospheric species simultaneously such as NO<sub>x</sub>, ozone, other OVOCs and hydrocarbons in specified areas of the globe for the purpose of process studies. These measurements are very important for such studies but are limited by their accuracy and sampling for monitoring trends and global patterns. PAN and many other NO<sub>y</sub> compounds are studied *in situ* on aircraft, but with poor limits of detection and accuracy (e.g. 30% at 50 pptv for PAN; Tanimoto *et al.*, 1999). Such poor accuracy and sampling limits understanding of PAN in such process studies and the atmosphere as a whole. An example of some aircraft measured data for PAN between 6-12 km is plotted in Figure 1.6. This data is taken from a large number of aircraft campaigns (see Table 1.1) that have measured PAN between 1985 and 1999 [Emmons *et al.*, 2000].

Campaign	Dates
CITE-2	Aug-Sept 1986
ABLE-2B	Apr-May 1987
ABLE-3A	Jul-Aug 1988
TROPOZ-2	Jan-Feb 1991
PEM-West-A	Sept-Oct 1991
TRACE-A	Sept-Oct 1992
PEM-West-B	Feb-Mar 1994
PEM-Tropics-A	Aug-Oct 1996
ACSOE	1996-1998
PEM-Tropics-B	Mar-Apr 1999

**Table 1.1** Some major aircraft campaigns to have measured PAN between 1985-1999.  
Adapted from Emmons *et al.* [2000].

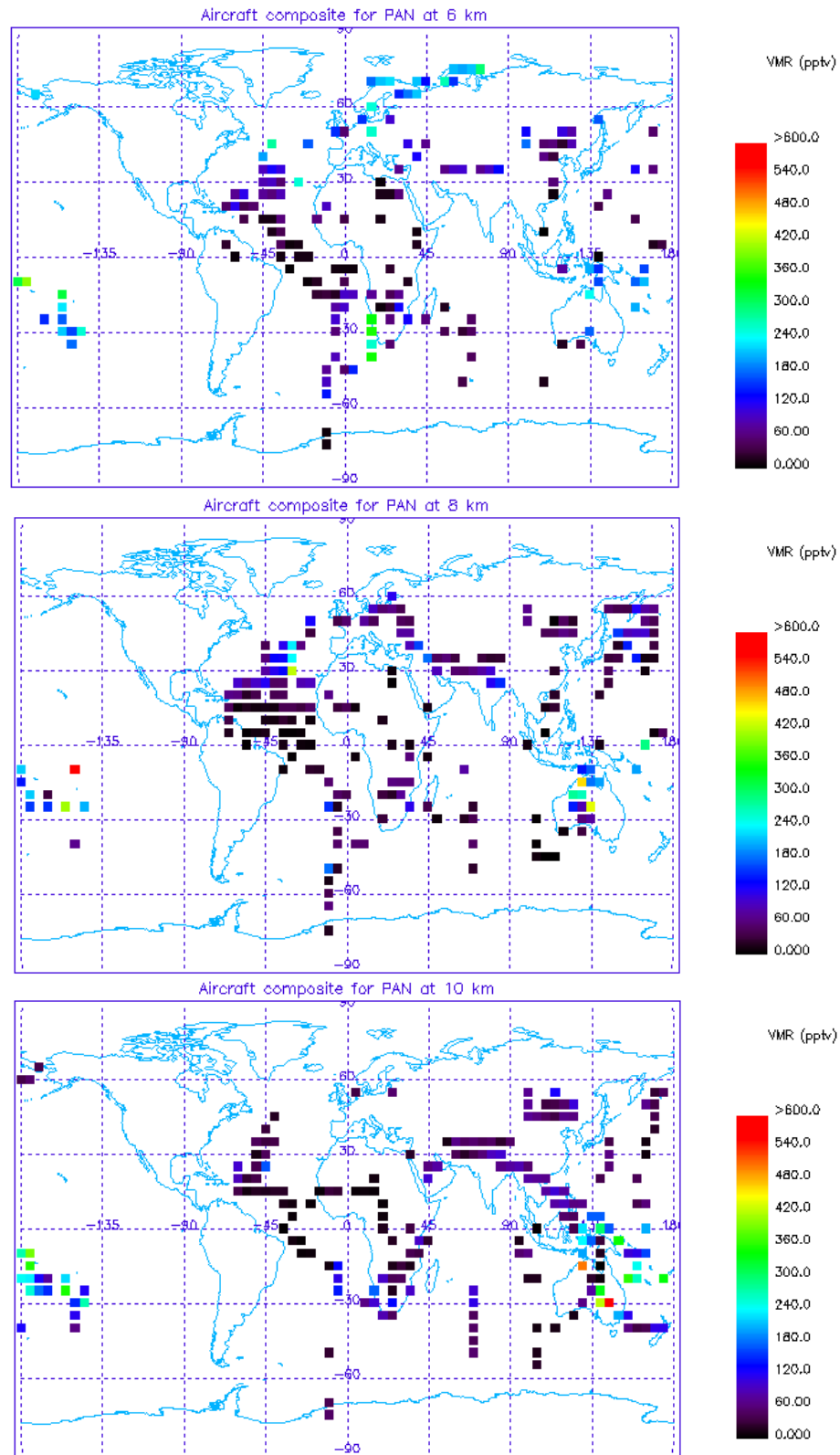


**Figure 1.6** Composite aircraft measured data for PAN from a number of aircraft campaigns between 1983-2000 at a) 6 km; b) 8 km; c) 10 km.



Figure 1.6 illustrates the relatively sparse coverage of data for PAN over this large timescale but the data available support some of the general model predictions for the global distribution of PAN. As can be seen, PAN concentrations in the UT are highly variable, with a fairly low background (around 60 pptv) and evidence for some enhancement near source regions such as the major cities of Australia. There is a clear lack of data however, in the northern mid-latitudes, a region where PAN concentrations are expected to be high and significant in terms of understanding climate impacts on population centres.

A common method used for the measurement of PAN in aircraft campaigns is Gas Chromatography Electron Capture Detection (GC-ECD), used for example by Gaffney *et al.* [1989] and Roberts [2004]. However, GC-ECD is limited both in accuracy and its ability to detect very low PAN concentrations with typical concentration errors of 30% (at 50 pptv) and a limit of detection of 15 pptv [Tanimoto *et al.*, 1999]. Such inaccuracy limits the ability to reliably make conclusions about detailed chemistry and also makes measurement difficult in very “clean” UT environments such as the West Pacific where PAN levels can be extremely low (< 20 pptv; Moxim *et al.*, 1996).

At surface sites, larger instruments that may not be suitable for aircraft campaigns have been employed in order to achieve higher limits of detection (<15 pptv) and better accuracy ( $\pm 15\%$  at 50 pptv). These instruments described by Tanimoto *et al.* [1999] use the Gas Chromatography/negative ion chemical ionisation mass spectrometry (GC/NICI MS) method and require an integration time of up to ten minutes to achieve such accuracy.

The measurement of PAN in the boundary layer has also been attempted using Fourier Transform InfraRed (FTIR) remote sensing instruments on the ground [Grutter, personal communication] with variable results. These measurements can be more useful for localised studies and have the advantage that they can measure concentrations of many infrared active compounds simultaneously from a single measurement. FTIR also has the advantage of being able to make routine measurements over a long time series in one location and the method can be used to monitor surface concentrations of pollutants. However, the accuracy of such measurement is limited not only by the instrument, but also by the accuracy of reference absorption cross-sections that are used to calculate concentration data from measured spectra.

Remote sensing from space offers many potential advantages over other techniques. A recent investigation of the potential for detecting PAN from space using infrared nadir sounders concluded that limits of detection using such a method could be as high as 5 ppbv [Clerbaux *et al.*, 2003], far in excess of typical UT PAN concentrations. However, FTIR instruments, such as the Michelson Interferometer for Passive Atmospheric Sounding (MIPAS) launched on Envisat in March 2002, is capable of recording infrared limb emission spectra with high spectral resolution ( $0.025\text{ cm}^{-1}$  unapodised) with a repeat reference orbit of thirty-five days (see Chapter 6.1). Such measurement has the potential to allow the retrieval of profile information down to the free troposphere (6 km) in cloud-free conditions. Whether or not PAN is detectable using FTIR remote-sounders, is the subject of later chapters in this thesis.

### 1.3 Summary

The role of organic compounds in the troposphere is key to our understanding of current and future trends in tropospheric ozone and atmospheric oxidising potential. PAN is an important compound in upper tropospheric chemistry through its role as an efficient transport species for  $\text{NO}_x$  and hence its indirect ability to substantially influence tropospheric ozone production in the remote environment. High surface levels of PAN and concomitant ozone are also associated with acute health risks and crop losses; and precursor sources of PAN are likely to increase in current emission scenarios. PAN may also be a potent greenhouse gas in its own right, although this remains to be studied.

PAN originates primarily from photochemically polluted continental sites in the Northern Hemisphere and the highest surface levels are observed in such locations. Convective transport and synoptic scale weather systems coupled with the thermal stability of PAN make it a ubiquitous compound in the free and upper troposphere. Model studies have shown that background PAN levels in the upper troposphere may increase by as much as 50% on 2000 levels by 2050.

Current measurements of PAN throughout the atmosphere are severely limited by their sampling and accuracy. *In situ* measurements from aircraft campaigns and limited surface-site monitoring mean that scientific interest in global studies of the compound remains high. New possibilities for remote sensing, and hence global coverage of trace gas concentrations by their infrared signature, have recently been

made available by the launch of MIPAS on Envisat and also by the new Tropospheric Emission Spectrometer (TES) on NASA's EOS-AURA satellite.

The retrieval of trace gas information from atmospheric spectra requires accurate laboratory reference absorption cross-sections in order to achieve the best possible information retrieval within the performance limits of the instrument. This thesis aims to assess the potential of using FTIR instruments to detect upper tropospheric PAN through the application of new, high quality PAN laboratory reference data.

## Chapter 2

# 2 Infrared Limb Sounding of the Atmosphere

Remote sensing of the atmosphere is one of many existing techniques for the measurement of trace gas concentrations. In contrast to *in situ* methods, where measurement relies on the direct sampling of air parcels, remote sensing retrieves information about the state of the atmosphere from information conveyed by electromagnetic radiation, such as atmospheric radiances. Along with balloon and aircraft based remote sensing instruments, space-based platforms offer the potential for global coverage of many trace species, as well as profiles of pressure and temperature; a significant advantage over the more limited spatial coverage of *in situ* methods.

In this thesis, the use of remotely sensed infrared spectra of the upper troposphere to detect PAN is considered. The motivation for such an investigation is the many recent launches of high-resolution limb-sounding spectrometers on various satellites, capable of recording vertical profiles of infrared spectra from the mesosphere down to the mid-troposphere. A number of important limb-sounding instruments are described in Table 2.1.

All molecules emit and absorb radiation at discrete characteristic frequencies. This spectral “fingerprint” can be used to obtain information on the concentration of such molecules in the atmosphere. Current remote sensing methods measure radiation from ultraviolet to microwave frequencies. The high-resolution instruments detailed in Table 2.1 cover the mid-infrared spectral region, which includes spectral bands of a large number of atmospheric gases (including many organic compounds), allowing the simultaneous measurement of information about such species.

The detection and potential retrieval of organic compound information by virtue of their characteristic influence on remotely measured infrared atmospheric radiances could allow the novel determination of global and seasonal distributions of such gases.

Instrument	Platform	Measurement	Launch date
MIPAS	ENVISAT (ESA)	Atmospheric Emission (4.15-14.6 $\mu\text{m}$ )	March 2002
ACE	SCISAT (Canadian Space Agency)	Solar Occultation (2-13 $\mu\text{m}$ )	August 2003
TES	EOS-AURA (NASA)	Atmospheric Emission (3.2-15.4 $\mu\text{m}$ )	July 2004
ATMOS	NASA Space Shuttle	Solar Occultation	1985-1994
MIPAS-B2	Balloon (IMK)	Atmospheric Emission	1985-ongoing
MIPAS-STR	Aircraft (IMK)	Atmospheric Emission	1998-ongoing

**Table 2.1** Selected important high-resolution limb sounding spectrometers, capable of measuring infrared radiances down to the upper troposphere.

In this chapter, theory relating to the propagation of radiation through the atmosphere (radiative transfer) and the infrared spectroscopy of gases is described and the measurement inversion (retrieval theory) problem is reviewed.

## 2.1 Limb Sounding

Limb-sounding instruments view slices of the Earth's atmosphere at a tangent to the Earth's surface (the Earth's limb). They are particularly well suited to measurements of gases that exhibit only weak spectral signatures such as PAN because of the long atmospheric pathlength involved in tangent viewing geometry. Figure 2.1 shows this geometry, illustrating how an instrument at high altitude views the limb of the Earth's

atmosphere. Scanning of the limb also delivers the ability to obtain vertical profiles of trace gases. Instruments such as MIPAS observe this limb-view against the background of cold space, whilst so-called limb-occultation instruments, such as ATMOS and ACE, observe the absorption of solar radiation as it passes through the atmosphere.

Figure 2.1 shows the path taken by rays incident on the detector of an instrument within its Field Of View (FOV). The path taken by a ray of light varies with the viewing angle of the instrument such that the tangent path labelled “3” in the diagram traverses a greater distance from the tangent point to the instrument than that from the point labelled “1”. Due to the rapid decrease in atmospheric density with increasing altitude, the majority of observed radiation at the instrument, for a given viewing angle, originates from the tangent point (where the line of sight intersects a line of circumference centred on the Earth).

At lower tangent altitudes, the contribution from higher layers to the total measured signal increases. Hence, for tangent points in the upper troposphere, a large amount of the measured signal is due to radiation from higher layers along the tangent path. Conversely, limb geometry also shows that regions of the atmosphere below the FOV at the tangent point do not contribute to measured spectra (neglecting scattering), so removing the complication of emission from the surface and lower atmosphere.

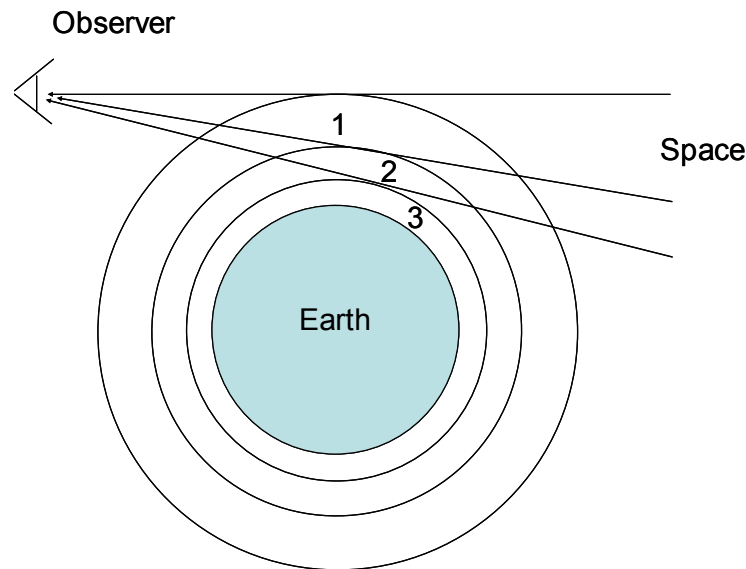


**Figure 2.1** The geometry of a high altitude limb-viewing instrument such as MIPAS (neglecting refraction along the path)

Vertical scanning by such instruments, gives good vertical resolution over altitudes ranging from the upper troposphere to the mesosphere, although horizontal resolution is poor due to the limited resolution along the line of sight of the instrument.

The varying density of the atmosphere further complicates the geometry of ray tracing in the atmosphere, producing a varying refractive index along the tangent path. This refractive index changes throughout the atmosphere as a function of local temperature, pressure and composition and is also wavelength dependent, meaning that the true path followed by any ray in the atmosphere is significantly curved from the simplified path shown in Figure 2.1. However, for a specified state of the atmosphere, the refracted path travelled by a beam of radiation can be calculated. To provide an accurate forward model of the radiation observed by any instrument, radiative transfer calculations must be performed over these refracted paths. These calculations are now described in the following section.

## 2.2 Radiative Transfer

The radiation arriving at a limb-viewing instrument is a combination of that entering the atmosphere in the FOV of the instrument and that emitted or scattered into the beam by atmospheric molecules (including aerosols and clouds) as it passes through the atmosphere.

The generalised equation of radiative transfer for a single ray path is described by the Schwarzschild Equation:

$$dI_\nu = -k_\nu \rho(s)(I_\nu - J_\nu)ds \quad (2.1)$$

where  $I_\nu$  is the intensity of radiation at some frequency  $\nu$ ,  $k_\nu$  is the mass extinction cross-section (due to both absorption and scattering out of the ray path),  $\rho(s)$  is the density of the medium as a function of the distance traveled  $s$  and  $J_\nu$  is some source function.

The observed intensity at some frequency at a particular point is then obtained by integrating Equation 2.1 over the complete path travelled by the radiation through the atmosphere.

$$I_\nu = I_{\nu 0} \exp(-\chi_{\nu 0}) + \int_0^{\chi_{\nu 0}} J_\nu \exp(-\chi_\nu) d\chi_\nu \quad (2.2)$$

where  $\chi_\nu$  is the optical thickness of the medium to radiation of frequency  $\nu$ , defined as

$$d\chi_\nu = -k_\nu \rho ds \quad (2.3)$$

Neglecting scattering and assuming local thermodynamic equilibrium, the source function in the Earth's atmosphere is given by the Planck Function

$$B_\nu(T) d\nu = \frac{2h\nu^3}{c^2 (\exp(h\nu/kT) - 1)} \quad (2.4)$$

which describes black body source radiation distribution as a function of frequency at some effective temperature  $T$ . The Planck Function describes the source function of a system in thermodynamic equilibrium and hence this source function is a suitable approximation for the troposphere and stratosphere where atmospheric density, and hence molecular collision frequency relative to the radiative lifetime of some state, remains high. This approximation is less valid in the upper layers of the atmosphere due to its low density and hence greater time between molecular collisions relative to radiative lifetime. However, as the uppermost layers have only a small influence on measured radiances for tangent points in the lower atmosphere, this approximation is suitable for the entire tangent path at lower pointing altitudes.

Further to this, for limb-sounding instruments such as MIPAS on Envisat, which views the atmosphere against the background of cold space, the first term in Equation 2.2 is negligible. Hence, the radiative transfer equation for limb-sounders of this type (neglecting scattering) can be written as

$$I_\nu = \int_0^{\chi_{\nu 0}} B_\nu \exp(-\chi_\nu) d\chi_\nu \quad (2.5)$$

showing that thermal radiation is attenuated by the extinction of the atmosphere along the tangent path, which is in turn determined by the characteristic interaction of radiation with all molecular species along such a path. This characteristic interaction is



described by the spectroscopic properties of atmospheric constituents and is discussed in the following section.

## 2.3 Measurement Inversion

The previous section describes the way in which a beam of radiation arriving at a detector is affected by the atmosphere through which it has passed. As such, these rays potentially contain information on atmospheric properties along the tangent path such as pressure, temperature and the concentrations of many atmospheric molecules. This information may be retrieved from a set of measurements by *measurement inversion*.

The fundamental principle of measurement inversion is the estimation of a desired set of state parameters (e.g. gas concentrations) from measurements of some other quantity or quantities (e.g. measured radiances) that are a function of the state.

In the most simple and idealised of cases, a linear relationship between a state parameter and a measurement allows direct inversion to obtain the true state so long as the dependence between state and measurement is known. The fact that a measurement may be subject to random or systematic error; and may also be a function of a number of other independent state parameters, complicates the inversion problem.

Furthermore, in many physical situations, the relationship between a number of measurements and states cannot be approximated as a simple linear response. This is true for many atmospheric applications, including limb sounding where a measured radiance is not only proportional to the concentration of a specific gas in the atmosphere, but is a simultaneous function of smooth and varying profiles of a number of gases, pressure and temperature. Given that the vertical resolution of limb-sounding measurements is finite (e.g. 3 km for MIPAS on Envisat), and that many gas profiles vary smoothly and greatly over such altitudes, it is not possible to retrieve a unique and exact solution by simple inversion of a set of measurements.

In this situation, an iterative approach using some forward model of the measurement response to changes in state parameters is required to find an *optimised* solution that fits the available measurements. The optimised solution (or state at convergence) is determined by a set of state parameters that minimises some cost function or achieves the best fit to measurements within some convergence criterion; judged for example by a chi-square goodness of fit test. A number of such iterative methods exist, chosen for their suitability to the specifics of the problem. A summary of

methods relevant to this thesis is given here. For a full discussion and formulation of such inversion methods appropriate to remote sounding instruments, the reader is referred to the excellent text of Rodgers [2000].

In general, optimal estimation techniques are based on an initial guess (either explicit or implicit) to the state of the system. Explicit methods use constrained *a priori* information in the estimation formalism, thus making use of prior information on the state of the atmosphere and reducing “noise” in the optimised solution. For example, a smoothly varying *a priori* profile of some gas concentration (assuming Gaussian statistics) may constrain the retrieved profile to be more smoothly varying and hence less noisy than implicit methods that do not make use of such information.

Implicit methods use an initial guess to the system that is inherent to the forward model. Here, the initial guess does not constrain the estimation and the result can be a more noisy retrieval (e.g. a “jagged” gas concentration profile) although the stability of convergence may be greater than for explicit methods.

Automated methods such as *global fitting* and *onion peeling* can be used to find optimised solutions. The global fitting method attempts to fit all measurements simultaneously and hence can be argued to make the best inherent use of the available information. This method is used in the operational retrieval algorithm employed for measurements made by MIPAS on Envisat, which retrieves volume-mixing ratio profiles of six trace gases ( $\text{H}_2\text{O}$ ,  $\text{CH}_4$ ,  $\text{O}_3$ ,  $\text{NO}_2$ ,  $\text{HNO}_3$  and  $\text{N}_2\text{O}$ ) as well as pressure and temperature from a series of limb spectra (see Chapter 6.2).

The onion peeling method is especially suited to the limb-sounding inversion problem. For the limb-sounding case, an optimised fit to measurements is made at high altitude and subsequently used as an initial guess for the state of that altitude level for forward calculations of radiances measured at successively lower altitudes, thus peeling away layers of the atmosphere.

These methods work well for retrieval of information from small spectral ranges appropriate, for example, to strong spectral line emission from gases such as water vapour. However, an automated method becomes increasingly complex and computationally expensive (with poor convergence stability) for simultaneous fitting of large spectral ranges and retrieval of information for gases exhibiting weak spectral signals; of which PAN is one example. In this case, a more tailored approach is necessary. In this thesis, the detection and estimation of PAN concentrations from measured data (see Chapters 5 and 6) is based on a combination of the global fitting and

onion peeling methods performed iteratively using a forward model with goodness of fit determined by the visual analysis of spectral residuals.

## 2.4 Infrared Spectroscopy

The retrieval of atmospheric state parameters from a set of measured infrared spectral radiances such as those described in the previous section, requires the use of accurate reference spectral data for use in any forward model. Infrared spectral parameters (e.g. line strengths and line widths) derived from laboratory spectra are necessary in order to accurately model radiative transfer through the atmosphere. Since even fundamental parameters such as line splitting and line widths depend on pressure and temperature, it is necessary to obtain accurate spectral data for constituent atmospheric gases, recorded under ambient conditions as near as possible to those of the atmospheric region of interest. This is even more important for gases such as carbon dioxide, where pressure and temperature profiles are determined from measured line parameters in the atmosphere.

As is often the case, the measured infrared radiance over even very small spectral ranges is a function of spectral influence from multiple gases. Therefore, accurate and appropriate reference spectra are usually required for many gases in the forward model to obtain the best possible retrieval of such parameters. Any inaccuracy in the reference data for one gas may consequently cause error in the retrieval for other gases.

The following sections describe the theory of infrared spectroscopy relevant to the target gas of interest in this thesis, peroxyacetyl nitrate (PAN).

### 2.4.1 Theory

The discrete energy exchanged in any transition between quantum states of a molecule is accompanied by the emission or absorption of photons of electromagnetic radiation. For the mid-infrared (the spectral region of interest in this thesis), photon energies involved in such transitions correspond mainly to simultaneous molecular vibrational and rotational transitions. For all molecules, the energy exchanged in changes of vibrational quantum number obeys  $\Delta E = h\nu$ . For vibrational quantum transition energies

this corresponds to infrared frequencies, whilst the energies associated with changes in rotational quantum number are much smaller.

In practice, both vibrational and rotational transitions occur simultaneously, giving rise to infrared *bands* centred on some vibrational transition frequency, adding detailed lines or *rotational fine structure* to the appearance of the band. Although all transitions involve quantised energy, various physical mechanisms can cause the broadening and possible overlap of spectral lines, such as molecular collisions and Doppler effects. Coupled with the finite resolution of spectrometers, such infrared bands may sometimes be observed as a quasi-continuum. The following sections describe the further theory and spectroscopy relevant to heavy molecular species such as PAN.

#### 2.4.1.1 Rotation of Molecules

All molecules can be categorised according to their moments of inertia around three mutually perpendicular axes. By convention, the inertia around each of the axes A, B and C are labelled  $I_A$ ,  $I_B$  and  $I_C$  respectively, with the axes defined such that  $I_A \leq I_B \leq I_C$ . Depending on the rotational symmetry around these axes, all molecules fall into one of the following four categories:

- Linear molecules; have one moment of inertia equal to zero with the other two equal ( $I_A = 0$ ,  $I_B = I_C$ ), e.g. carbon dioxide.
- Symmetric top; e.g. ethane, are sometimes also called rotor molecules, these have two equal moments of inertia with the other different but non-zero. Depending on which two moments of inertia are equal, this category is subdivided into the prolate symmetric top ( $I_A \leq I_B = I_C$ ) and oblate symmetric top ( $I_A = I_B \leq I_C$ ).
- Spherical top; have all three moments of inertia equal ( $I_A = I_B = I_C$ ); e.g. methane.
- Asymmetric top; are those where all three moments of inertia are finite and different ( $I_A \neq I_B \neq I_C$ ). The majority of molecules belong to this class; including PAN.

The energy of a purely rotational transition typically lies in the microwave region of the spectrum. In theory, the energy of such transitions can be calculated from the

Schrödinger equation and quantum number selection rules can be determined. Selection rules are different for the different classes of molecule described above and can be found in standard textbooks on molecular spectroscopy [e.g. Duxbury, 1999].

### 2.4.1.2 Molecular Vibrations

The number of fundamental vibrations of a molecule is determined from the number of degrees of freedom the molecule has and hence is related to the number of atoms in the molecule. A molecule containing  $N$  atoms has  $3N$  degrees of freedom in total. Translational motion of the molecule requires three degrees of freedom with a further three required for rotational translation for non-symmetric molecules. Rotational motion requires only two vectors for linear molecules. The remaining degrees of freedom are all due to fundamental vibrations and hence we see that non-linear molecules possess  $3N-6$  such vibrations, whilst linear molecules possess  $3N-5$ .

As mentioned earlier, transitions between vibrational states involves the exchange of infrared quanta. If a molecule is assumed to be a simple harmonic oscillator, then the energy of vibrational states can be described by:

$$E_v(\nu) = \hbar c(\nu + 1/2)\tilde{\nu} \quad (2.6)$$

where  $\tilde{\nu}$  is the wavenumber (reciprocal wavelength) of the normal vibrational mode and  $\nu$  is the vibration quantum number (an integer greater than or equal to zero). The selection rule for vibrational transitions of this type is  $\Delta\nu = \pm 1$  (corresponding to absorption or emission respectively), except for the ground state where only the positive transition (absorption) is allowed.

The strongest band is typically observed to occur for the transition between the ground state ( $\nu = 0$ ) and  $\nu = 1$ , with weaker bands seen for transitions from higher vibrational quantum states, known as the fundamental bands. This decrease in intensity of higher energy bands is explained by the Boltzmann distribution, which describes the population of energy states of molecules as a function of temperature (assuming thermodynamic equilibrium). The population,  $N_\nu$ , of higher vibrational states relative to the ground state,  $N_0$ , at some temperature,  $T$ , is defined by the Boltzmann factor:

$$\frac{N_v}{N_0} = \exp\left(-\frac{E_v}{kT}\right) \quad (2.7)$$

As the spacing between vibrational energy levels is typically large, the majority of molecules occupy the ground state at normal atmospheric temperatures. As temperature increases, the population of higher energy states increases, allowing transitions ( $\Delta v = \pm 1$ ) between higher vibrational states ( $v > 0$ ). Such bands are known as *hot* bands. Furthermore, each vibrational state may have additional harmonics or *overtones*, such that  $\Delta v = \pm 2, 3, 4, \dots$ . Transitions between these states and different fundamental modes can lead to the presence of *combination* bands (e.g.  $\nu_1 + \nu_3$ ) and *difference* bands (e.g.  $\nu_3 - \nu_1$ ), which may also be seen in the mid-infrared region.

In addition to this simplified description, departures from the simple harmonic oscillator approximation may occur due to electrical and mechanical anharmonicity. Electrical anharmonicity arises because of small higher-order terms present in the expression of the molecular electric dipole. Mechanical anharmonicity relates to the nature of molecular bond elasticity; atoms do not obey Hooke's law and hence are not subject to symmetric potential energy curves. In both cases, this has the potential to also allow transitions where  $\Delta v = \pm 2, \pm 3, \dots$ , leading to *overtone* bands.

There exists the possibility that some of these bands may have very similar energies. In this case of *accidental degeneracy*, bands may be subject to a resonance phenomenon, which allows energy to be exchanged between the degenerate modes, also leading to a shift in the band frequency. A specific case of such resonance where a fundamental mode is degenerate with an overtone band is called Fermi resonance and can lead to a significant increase in the intensity of otherwise weak overtone or combination bands.

### 2.4.1.3 Vibration-Rotation Bands

Vibrational energy levels in a rotating molecule are split into rotational energy levels according to the Born-Oppenheimer approximation, which assumes that the energy associated with vibrational, rotational, electronic and nuclear states are independent. Furthermore, in this assumption, the total energy of a molecule is the sum of energies due to each type of motion (vibration and rotation). Interactions between the two

motions can be significant, however, meaning that this approximation does not hold exactly.

Since rotational transitions involve much smaller amounts of energy than vibrational transitions, they typically occur simultaneously with vibrational transitions as noted earlier in Section 2.4.1.

The selection rules for vibration-rotation bands differ for different types of molecule, depending on whether vibration causes a change in the electric dipole moment parallel, or perpendicular, to the rotational axis of symmetry. Essentially, bands exhibit branched structure, which obey the selection rules  $\Delta J = 0, \pm 1$  or in some cases, only  $\Delta J = \pm 1$ , where  $J = 0, 1, 2, \dots$  denotes the rotational quantum number. Branches corresponding to the selection rules  $\Delta J = -1$ ,  $\Delta J = 0$ ,  $\Delta J = +1$  are known as P, Q and R branches respectively. The P branch is observed at lower frequency with respect to the Q branch, whilst R branches are observed at higher frequency. The band centre corresponds to the purely vibrational transition energy.

#### 2.4.1.4 Line Intensities

As well as the positions of spectral lines it is also important to know the *line intensity*,  $S$ , where

$$S = \int k(\tilde{\nu}) d\tilde{\nu} \quad (2.8)$$

integrated over the spectral line, and  $k(\tilde{\nu})$  is the absorption coefficient. These can be derived using the Einstein coefficient for induced absorption and stimulated emission, and will depend on the population of the states between which the transition takes place (governed by the Boltzmann distribution) in conjunction with the transition probability. For a vibration-rotation line for a transition from some state  $i$  to a state  $j$ , the line intensity for a single molecule is given by

$$S_{line} = \frac{8\pi^3 \tilde{\nu}_{ji}}{4\pi\epsilon_0 3hcQ} \exp\left(\frac{-E_i}{kT}\right) \left(1 - \exp\left(\frac{-hc\tilde{\nu}_{ij}}{kT}\right)\right) S_{ij} \quad (2.9)$$

where  $Q$  is the partition function,  $E_i$  is the energy of the lower state and  $S_{ij}$  is the line strength, which is defined as the square of the transition moment relative to an axis fixed in space.

#### **2.4.1.5 Line Widths**

Various physical mechanisms can cause the broadening of quantised spectral lines. A detailed formalism of such mechanisms is beyond the scope of this thesis, although the significance of such broadening is discussed in the context of the forward modelling of rays in the atmosphere described in Section 2.2. A detailed discussion of broadening mechanisms can be found in most introductory literature on infrared spectroscopy such as Hollas [1997].

Natural, Doppler and collisional broadening all affect the intensity and width of a spectral line. Natural broadening is a fundamental process induced by the nature of the Heisenberg Uncertainty Principle, which states that the energy of a state cannot be measured exactly. Other larger effects include Doppler broadening, manifest as a frequency shift caused by particles moving toward or away from the point of measurement with a Boltzmann distribution of thermal speeds; and also collisional broadening which relates to the change in vibrational-rotational state induced by loss of translational energy in molecular collisions. Collisional (or pressure) broadening is the most important line-broadening mechanism in the atmosphere below 30 km.

The varying influence of these broadening mechanisms in different regions of the atmosphere requires thought in the forward modelling of atmospheric spectra and can be parameterised using *line shapes* that can be applied to spectral lines for atmospheric species.

#### **The Voigt Lineshape**

In the atmosphere, the widths of spectral lines are dominated by pressure broadening at low altitudes and Doppler broadening at higher altitudes due to decreasing pressure and density. In the mid-infrared, spectral line widths due to both mechanisms become equal at around 30 km. Any radiative transfer model must consider the spectral line shape of line sources originating from the surrounding altitudes in order to provide the most accurate representation of the true atmosphere. For atmospheric applications, this combined behaviour is often reasonably well described by the Voigt lineshape



(Armstrong [1967]). This provides a useful convolution of the Doppler and Lorentz (pressure-broadened) lineshapes described thus as:

$$k(\tilde{\nu}) = \frac{S}{\alpha_D \sqrt{\pi}} \frac{y}{\pi} \int_{-\infty}^{\infty} \frac{e^{-t^2}}{y^2 + (x-t)^2} dt \quad (2.10)$$

where  $k(\tilde{\nu})$  is the absorption coefficient at some wavenumber  $\tilde{\nu}$ .  $S$  is the line intensity at some reference line centre,  $\nu_0$  and  $t$  is the duration of emission with  $x$  and  $y$  defined as:

$$x = \frac{\alpha_L}{\alpha_D} \quad (2.11a)$$

$$y = \frac{\tilde{\nu} - \tilde{\nu}_0}{\alpha_D} \quad (2.11b)$$

where  $\alpha_L$  and  $\alpha_D$  are the Lorentz and Doppler half-widths respectively.

#### 2.4.1.6 Heavy Molecules

Relatively heavy molecules such as PAN (relative molecular mass of 121 atomic mass units) have a large moment of inertia, causing the energy and hence spectral spacing of rotational transition lines to be very small. The rotational constant,  $B$ , where

$$B = \frac{\hbar^2}{2I} \quad (2.12)$$

and  $I$  is the moment of inertia, is related to the spacing of rotational energy levels by

$$E_J = BJ(J+1) \quad (2.13)$$

where  $J$  is a positive integer and represents the rotational quantum number. Hence, for heavy molecules with a large moment of inertia the spacing of rotational energy levels decreases. Furthermore, even at the highest spectral resolutions possible, the lines within a typical band may still overlap with each other due to the physical processes

described in the Section 2.4.1.5. Such overlapping can give rise to *broadband* spectral features. In this case, measuring at very high spectral resolution will not yield significant additional information about individual line parameters. Rotational constants, and hence the expected spacing of rotational transition lines for PAN, have not been estimated, although such spacing is expected to be very small.

For lighter molecules, line parameters (line position, intensity, pressure and self-broadened half-widths are some examples) are typically stored in databases for use by the scientific community. The HITRAN and GEISA databases described by Rothman *et al.* [1998a] and Jacquinet-Husson *et al.* [1992] respectively are examples of two major international databases of such parameters. These databases provide reference data that can be used with radiative transfer models.

Given the complexity of spectra of heavy molecules, determination of line parameters for most heavy molecules has not been attempted and would in any case require a theoretical treatment beyond the scope of most current models. Instead, reference spectral data for heavy molecules are usually reported as absorption cross-sectional data, where the absorption cross-section per molecule is reported as a function of wavenumber. These absorption cross-sections are derived from the Beer-Lambert law; a solution to Equation 2.5, which applies to the absorption of radiation along a homogeneous path for negligible emission and scattering:

$$I(\nu) = I_0(\nu) \exp(-n\sigma(\nu)x) \quad (2.14)$$

where  $I_0(\nu)$  is the intensity of source radiation as a function of wavenumber,  $I(\nu)$  is the transmitted intensity of radiation through some sample of pathlength  $x$  with molecular number density, or concentration,  $n$ . The absorption cross-section per molecule,  $\sigma(\nu)$ , is conventionally given in units of  $\text{cm}^2 \text{ molecule}^{-1}$ .

Measurements of transmittance spectra  $[I(\nu)/I_0(\nu)]$  of a gas in the laboratory can then be used to calculate the absorption cross-section from Equation 2.14. Typically, the cross-section may also depend on temperature and total pressure, and therefore measurements of reference cross-sections over a range of conditions relevant to the atmosphere are needed for accurate calculations of spectra using forward models. The HITRAN database contains cross-sectional data for some molecules in addition to line parameter data as a special supplement.

## 2.4.2 Previous PAN Measurements

The PAN molecule [ $\text{CH}_3\text{C}(\text{O})\text{OONO}_2$ ] is an asymmetric top species, consisting of a methyl group, a carbonyl group ( $\text{C}=\text{O}$ ) and a peroxyxynitrate group ( $\text{O}-\text{O}-\text{NO}_2$ ). It has twenty-seven fundamental vibration modes, of which only nineteen are infrared active in the spectral range  $370\text{-}3022\text{ cm}^{-1}$ . Band assignments for PAN in the mid-infrared are listed in Table 2.2 and are compiled from those reported by Gaffney *et al.* [1984] and Bruckmann and Willner [1983].

In addition to this work, others to have observed these bands in the mid-infrared include Stephens [1969]; Bruckmann and Willner [1983]; Niki *et al.* [1985]; Tsalkani and Toupance [1989]; and Hanst and Hanst [1993]. These studies have performed spectral analyses of PAN at spectral resolutions of 5.00, 1.20, 0.06, 1.00 and  $0.25\text{ cm}^{-1}$  respectively, with much disagreement in the reported data between the datasets for integrated band strengths and peak absorptivities.

The nature of the PAN molecule makes it a very difficult species to study in the laboratory due predominantly to the peroxyxynitrate group, which makes the molecule thermally unstable. This instability makes the molecule very difficult to handle in its pure form, as it is known to be spontaneously explosive and shock sensitive at room temperature. It is also a toxic mutagen, carcinogen and a strong lachrymator. Furthermore, it is noted to be extremely reactive with many common surface materials. Such properties have limited previous attempts to comprehensively study the molecule and quantitative investigation is further complicated due to the associated difficulty in maintaining a pure sample for spectral measurement purposes.

For these reasons, PAN is not commercially available and requires a complicated and hazardous laboratory synthesis. Various methods have been proposed to produce PAN; including the nitration of peracetic acid described by Gaffney *et al.* [1984], and the ultraviolet photolysis of  $\text{NO}_2$  in the presence of acetaldehyde. The liquid phase nitration of peracetic acid is seen to be the preferred method employed in available literature studies of PAN and is also used later in this thesis (see Chapter 4).

Band Centre / $\text{cm}^{-1}$	Intensity	Mode	Assignment
3660	VW	$2\nu_4$	
3455	VW	$2\nu_5$	
3022	W	$\nu_2$	$\text{CH}_3$ assym. stretch
2590	VW	$\nu_3$	$\text{CH}_3$ sym. stretch
1842	S	$\nu_4$	$\text{C}=\text{O}$ stretch
1741	VS	$\nu_5$	$\text{NO}_2$ assym. Stretch
1653	VW	$\nu_6$	?
1430	W	$\nu_7$	$\text{CH}_3$ d-deform
1371	M	$\nu_8$	$\text{CH}_3$ s-deform
1302	S	$\nu_9$	$\text{NO}_2$ sym. Stretch
1162.5	S	$\nu_{10}$	$\text{C}-\text{O}$ stretch
1055	W	$\nu_{11}$	$\text{CH}_3$ rock
990	M	$\nu_{13}$	$\text{C}-\text{C}$ stretch
930	M	$\nu_{14}$	$\text{O}-\text{O}$ stretch
821	M	$\nu_{15}$	$\text{N}-\text{O}$ scissors
791.5	S	$\nu_{16}$	$\text{NO}_2$ stretch
716	W	$\nu_{17}$	$\text{NO}_2$ wag
604	M	$\nu_{18}$	$\text{C}-\text{O}$ bend
573	M	$\nu_{19}$	$\text{NO}_2$ stretch
488	W	$\nu_{20}$	?
370	VW	$\nu_{21}$	?

**Table 2.2** Mid-infrared band assignments for gaseous PAN compiled from data reported by Gaffney, [1984] and Bruckmann and Willner, [1983]. Where questioned, these band assignments have not been made. Note: VW=very weak, W=weak, M=medium, S=strong absorption.

The purity of the gas sample is of specific concern for spectroscopic studies of PAN. The short thermal lifetime (several minutes) of PAN at room temperature, coupled with decomposition in storage and synthesis, as well as surface reactions with the sample cell, make it very difficult to achieve a pure PAN sample for any length of time. All known previous studies have indicated the presence of water vapour and carbon dioxide (amongst others) impurities in samples; identified through either gas chromatography or by spectral influence or both. Such impurity inevitably leads to uncertainty in the quality of results calculated using those data unless it is well characterised.

It is also important to note that all previous studies of PAN have been made at room temperature and of these, the only known cross-section data for PAN in the mid-infrared are those recorded by Hanst and Hanst [1993] at a spectral resolution of 0.25

$\text{cm}^{-1}$ . The Hanst and Hanst [1993] cross-section is plotted in Figure 2.2 and clearly shows evidence of some poorly resolved spectral features such as an unusual straight edge to the PAN band at  $822\text{ cm}^{-1}$ , which includes some unrealistic negative values.

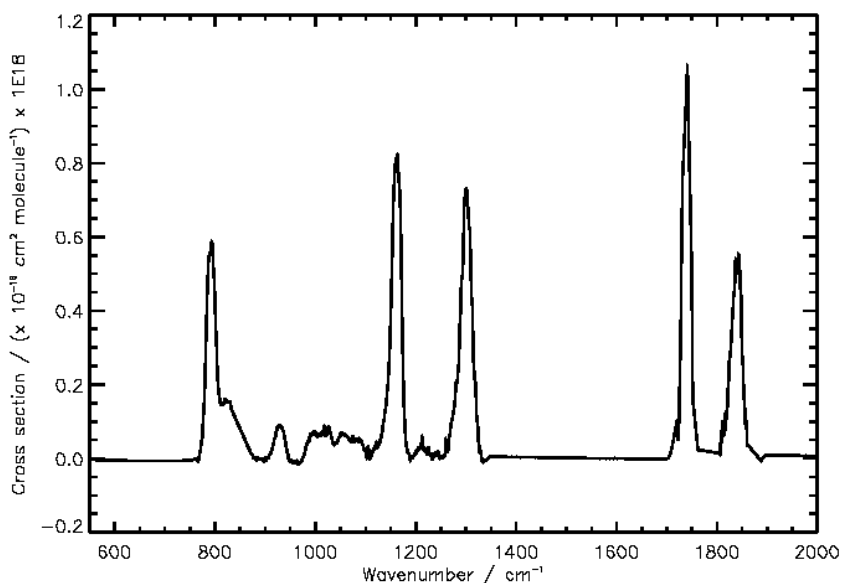


**Figure 2.2** Cross-section calculated for PAN by Hanst and Hanst [1993].

In addition to cross-sectional data, parameters such as peak infrared absorptivities and integrated band intensities are also useful for atmospheric applications. Infrared absorptivity defines the absorption at the nominal band centre for 1 ppmv of a target molecule at atmospheric temperature and pressure, whilst the integrated band intensity defines the band area ( $\text{cm}^{-2}\text{ molecule}^{-1}$ ) integrated over the full range of the nominal band for 1013.25 mb of pure gas at some temperature. Such data can be extrapolated from known intensities and absorptivities calculated at lower pressures. This is explained in more detail and performed for measurements of PAN in this thesis in Chapter 4.4.

To date, infrared absorptivities have been reported by Stephens [1964]; Bruckmann and Willner [1983]; Niki *et al.* [1985]; and Tsalkani and Toupance [1989]. The only known literature sources to quote integrated band intensities for PAN are those reported by Gaffney *et al.* [1984] and Tsalkani and Toupance [1989]. All such previous results are given in Table 2.3 and Table 2.4.

Band centre / $\text{cm}^{-1}$	Stephens, 1964. <sup>1</sup>	Bruckmann and Willner, 1983.	Niki <i>et al.</i> 1985	Tsalkani and Toupance, 1989
794	10.1	13.4	$11.5 \pm 0.6$	$12.2 \pm 0.4$
1163	14.3	15.8	$14.5 \pm 1.4$	$15.7 \pm 0.6$
1302	11.2	13.6	$11.3 \pm 1.2$	$11.9 \pm 0.4$
1741	23.6	32.6	$31.0 \pm 3.2$	$31.4 \pm 1.6$
1842	10.0	12.4	$10.2 \pm 1.0$	$10.9 \pm 0.4$

**Table 2.3** Infrared absorptivities for gaseous PAN (log to base 10; values refer to 1013.25 mb) for the five principal PAN absorption bands previously reported.

Band centre / $\text{cm}^{-1}$	Gaffney <i>et al.</i> , (1984)	Tsalkani and Toupance, (1989)
794	$247 \pm 6$	$239 \pm 4$
1163	$477 \pm 9$	$322 \pm 7$
1302	$405 \pm 20$	$270 \pm 2$
1741	$808 \pm 34$	$563 \pm 10$
1842	$322 \pm 9$	$262 \pm 4$

**Table 2.4** Previously reported infrared integrated intensities ( $\text{atm}^{-1}\text{cm}^{-2}$  to 3.s.f) of five strongest PAN bands Units refer to 1 atm pressure at ambient temperature 291 K.

In all cases, there is large disagreement between all previously reported data with differences in reported integrated intensity ranging from 4% (for the  $794 \text{ cm}^{-1}$  band) to 50% (for the  $1741 \text{ cm}^{-1}$  band). Differences in reported infrared absorptivities are little better.

Previous spectroscopy of PAN clearly suffers from a number of uncertainties. The potential errors for cross-section data are clearly large as evidenced by the spread of results for peak absorptivity and integrated intensity. Moreover, the spectral resolutions employed thus far have been limited to  $0.06 \text{ cm}^{-1}$ ; much poorer than that of current atmospheric spectrometers such as MIPAS on Envisat ( $0.025 \text{ cm}^{-1}$  unapodised). Furthermore, cross-sectional data have all been measured at room temperature (291 K) rather than at lower temperatures typical of the upper troposphere (as low as 190 K, see Section 1.1).

The aim of this thesis is to provide more accurate and appropriate reference spectral data in order to investigate the atmospheric detection and retrieval of PAN

through obtaining a set of accurate PAN cross-sections recorded at appropriate resolutions, temperatures and pressures.

## 2.5 Fourier Transform Spectroscopy

A particularly powerful technique for obtaining the requisite spectral data is provided by Fourier Transform Spectroscopy (FTS). Both the laboratory and atmospheric spectra discussed in the subsequent chapters of this thesis have been obtained from measurements by FTS instruments. These instruments offer many advantages for atmospheric infrared measurements over other spectrometers such as dispersive and laser methods.

One of the principal advantages of the FTS instrument is the *multiplex* advantage or the ability to measure the entire desired spectral range simultaneously, limited only by the source and the spectral response of the instrument. In practice, the spectral range of an FTS instrument is limited by a combination of the detector, beamsplitter and other optics (e.g. optical filters and sample cell windows).

For atmospheric measurements, such as those from satellite instruments, the use of an FTS is vital for obtaining high-resolution spectra over a very broad spectral range, leading to the possibility of retrieving information on multiple gas species from a single measurement. Moreover, this leads to a shorter measurement time relative to traditional dispersive spectrometers with a higher signal to noise for a given measurement period. Also, the same characteristic instrument lineshape form is generally applicable to the entire measured spectral range.

A further advantage relates to the increased throughput of radiation over dispersive spectrometers, the so-called Jacquinot advantage. In dispersive spectrometers, the spectral resolution is increased with a smaller grating width but at the expense of radiation throughput. In comparison, laser spectrometry such as the cavity-ringdown method described by Zalicki and Zare [1995], can provide much higher resolutions than conventional FTS instruments with higher signal to noise, however the spectral range of measurements is severely limited relative to FTS. Such laser instruments are therefore more suited to the laboratory study of line parameters over specific narrow frequency ranges.

This section details the theory relating to the measurement of spectra using FTS instruments and discusses some of the issues that require thought in the measurement of laboratory and atmospheric spectra using the method.

### 2.5.1 The Michelson Interferometer

FTS instruments are all based on some modified form of the classic Michelson Interferometer illustrated in Figure 2.3.

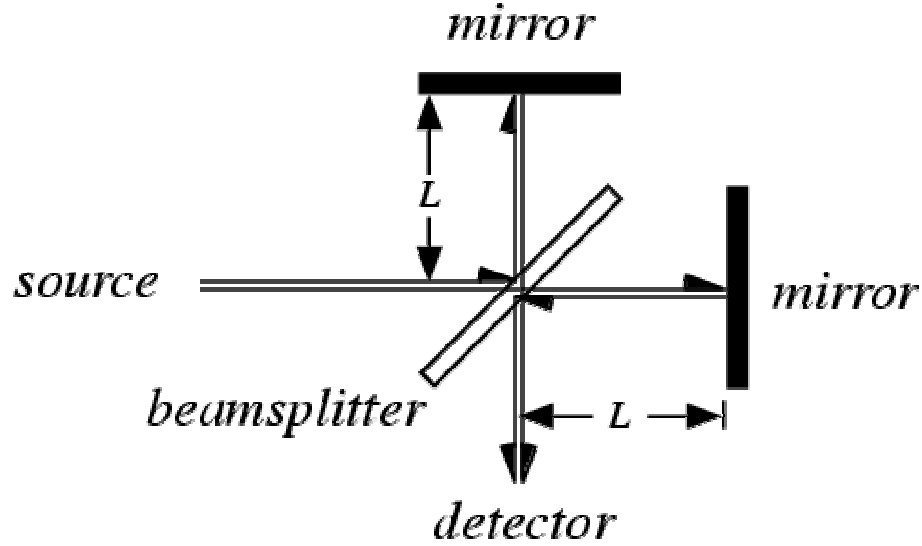


**Figure 2.3** The Classic Michelson Interferometer

In the idealised Michelson interferometer, source radiation is equally split by some beamsplitter with one beam allowed to pass through to a fixed mirror whilst the other is reflected in the direction of a second movable mirror. Assuming a monochromatic point source of radiation, of wavenumber  $\tilde{\nu}$ , at some distance  $x$  from the beamsplitter, the electric field,  $E$ , incident on the beamsplitter is given by

$$E(x, \tilde{\nu}) = E_0(\tilde{\nu}) \exp[i(\omega t - 2\pi x \tilde{\nu})] \quad (2.15)$$

where  $\omega$  is the angular frequency of radiation and  $t$  is time. The mirror-reflected beams are then recombined at the beamsplitter and divided again such that one beam is directed to an appropriate detector while the other is returned to the source. The difference in pathlength of the two rays through the beamsplitter is usually corrected by using a compensator plate of the same material placed in the path of one of the two



beams. The thickness of this compensator is simply equal to the difference in the optical path difference travelled by the two beams through the beamsplitter.

Any difference in the pathlength of the two beams introduced by the movement of one of the mirrors causes interference at the recombination point such that the beams will constructively or destructively interfere depending on the phase difference. The electric field at the detector is given as a function of mirror position by:

$$E(x_1, x_2, \tilde{\nu}) = rtE_0(\tilde{\nu})[\exp(i(\omega t - 2\pi x_1 \tilde{\nu})) + \exp(i(\omega t - 2\pi x_2 \tilde{\nu}))] \quad (2.16)$$

where  $x_1$  and  $x_2$  are the optical paths for each of the recombining beams and the beamsplitter reflectance and transmittance amplitudes are given by  $r$  and  $t$  respectively. Hence, as the path difference varies, the electric field at the detector varies sinusoidally, decaying to zero where the path difference is an integer multiple of  $2\pi\tilde{\nu}$ .

The intensity,  $I$ , of the detected radiation, recorded as a function of path difference,  $\delta$ , is called an *interferogram*. This interferogram is described thus as:

$$I(\delta) = \frac{1}{2} \epsilon_0 c |E(\delta)|^2 \quad (2.17)$$

$$= \frac{1}{2} \epsilon_0 c |rtE_0(\tilde{\nu})|^2 (2(1 + \cos(2\pi(x_1 - x_2)\tilde{\nu}))) \quad (2.17a)$$

$$= \frac{1}{2} I(0)(1 + \cos(2\pi\tilde{\nu}\delta)) \quad (2.17b)$$

Hence, as the optical path difference changes with movement of one of the mirrors, the recorded intensity for a monochromatic wave will display a cosine wave superimposed on a constant background.

If the source beam is passed through a sample cell containing a target gas, radiation is absorbed at different frequencies, meaning that the intensity of the modulated beam is also attenuated. The subsequent Fourier transformation of the interferogram gives the desired spectrum (absorption as a function of wavenumber).

In the ideal spectrometer, energy is conserved and there are in fact two output beams, each containing equal energy. In some real spectrometers, the optical arrangement is such that both the recombined beams are detected. This can be advantageous since the addition of both outputs gives the constant (DC) flux at the

detector, which can be used to correct for various problems such as optical imperfections and to subtract the constant term in Equation 2.17b. Some instruments described later in this thesis, however, use only one output beam and remove the effect of this constant term; the DC offset, using an electronic filter.

As is the case for most FTS instruments, the source will not be monochromatic and is chosen to give an output over the spectral range of interest to measurement. By superposition, the detected intensity will therefore be the sum of the contributions from each frequency. Hence the interferogram function becomes

$$I(\delta) = \frac{1}{2} \int_0^\infty B(\tilde{\nu}) d\tilde{\nu} + \frac{1}{2} \int_0^\infty B(\tilde{\nu}) \cos(2\pi\tilde{\nu}\delta) d\tilde{\nu} \quad (2.18)$$

where  $B(\tilde{\nu})d\tilde{\nu}$  is the spectral energy density of the source as a function of wavenumber. In the non-ideal interferometer, this source function is the signal recorded after modification by the non-idealised optics, the detector response and the electronics.

For any discrete frequency, constructive interference will occur when the path difference is equal to an integer multiple of the wavelength of source radiation ( $\delta = n\lambda$ ). It follows that source radiation of all frequencies will therefore constructively interfere at the point of zero optical path difference; sometimes called the *centre burst* or *zero path difference point* of the interferogram. Subsequent fringes of decreasing amplitude, tending to zero at high optical path differences, surround this bright central fringe.

The spectral resolution of the instrument is, in theory, only limited by the Maximum optical Path Difference (MPD) and is idealised to be equal to  $1/\text{MPD}$ . However, imperfections to the ideal interferometer usually reduce this resolution from the maximum resolution usually quoted by manufacturers.

From Equation 2.18, it can be seen that the interferogram is the cosine Fourier transform of the detected radiation spectrum. Hence the desired spectrum can be obtained by the inverse transform given (to within some constant multiplying factor) by

$$B(\tilde{\nu}) = \int_0^\infty I(\delta) \cos(2\pi\tilde{\nu}\delta) d\delta \quad (2.19)$$

Hence, we see that all frequencies can, in principle, be measured simultaneously and recovered from the interferogram.

## 2.5.2 Calculation of the Spectrum

In practice, the interferogram cannot be recorded continuously as a function of mirror displacement or changing optical path difference and is instead sampled at discrete intervals. In this case, a Fast Fourier Transform (FFT) is used to calculate the spectrum. The *sampling interval* is usually determined by use of a frequency-stabilised laser that travels the same optical path as the source radiation. This output is detected separately to the source radiation but also varies co-sinusoidally with optical path difference. Therefore, evenly spaced points can be sampled by selecting zero crossings of the laser interference pattern, provided that the laser frequency can be assumed to be stable.

### 2.5.2.1 Aliasing

The discrete sampling interval of the interferogram with optical path difference can be expressed as the multiplication of a continuous interferogram with a function consisting of periodically repeated Dirac delta functions known as a Dirac delta comb. Thus:

$$I_s(\delta) = I_c(\delta) d \sum_{n=-\infty}^{\infty} \delta'(\tilde{\nu} - nd) \quad (2.20)$$

where  $I_c(\delta)$  is the continuous interferogram and  $I_s(\delta)$  is the sampled interferogram.

The sample spacing is given by  $d$ . The Fourier Transform of such a spectrum is then simply another Dirac-delta comb, which leads to a periodic repetition of the spectrum with a period of  $1/d$  when convolved with the spectrum obtained from the continuous interferogram. This is the phenomenon known as spectral aliasing expressed by Equation 2.21 below.

$$B_s(\tilde{\nu}) = B_c(\tilde{\nu}) \sum_{n=-\infty}^{\infty} \delta\left(\tilde{\nu} - \frac{n}{d}\right) \quad (2.21a)$$

$$= \sum_{n=-\infty}^{\infty} B_c\left(\tilde{\nu} - \frac{n}{d}\right) \quad (2.21b)$$

In addition, Fourier Transform mathematics leads to the mirror image of the expected spectrum at negative frequencies. In order to prevent repeated spectra from overlapping

with one another, the distance between alias orders must therefore be at least twice the bandwidth of the input spectrum. Hence

$$d \leq \frac{1}{2(\tilde{\nu}_2 - \tilde{\nu}_1)} \quad (2.22)$$

where the upper and lower wavenumber limits ( $\tilde{\nu}_2$  and  $\tilde{\nu}_1$  respectively) are restricted by the need for the total bandwidth to fit between zero and the upper wavenumber limit by an integer factor,  $n$ , thus:

$$\frac{\tilde{\nu}_2}{\tilde{\nu}_2 - \tilde{\nu}_1} = n \quad (2.23)$$

If Equations 2.22 and 2.23 are not satisfied then repeated spectra overlap with one another, distorting the measured spectrum. In the spectrometers used in this thesis, electronic and sometimes optical filters are used to remove any detected signal lying outside the spectral region of interest to prevent such aliasing.

### 2.5.2.2 Zero-filling

In many cases, the length of the measured interferogram is artificially increased before transformation by a process known as *zero filling*. This process simply extends the number of samples in the interferogram and hence increases the number of points (sampling) of the resulting spectrum. The zero-filling factor is defined according to the requirement that the total number of points,  $m$ , in the interferogram must satisfy the condition  $m = 2n + 1$ , where  $n$  is an integer.

This increased number of points in the interferogram will accurately interpolate the output spectrum. This process does not increase the spectral resolution of the resulting spectrum since no further information content is added, although it does allow better sampling of spectral lines that would otherwise appear distorted due to lack of spectral definition.

### 2.5.3 Resolution Limitations in FTS

In reality, FTS instruments do not behave ideally due to various factors that have to be taken into account in the qualitative analysis of derived spectra. The most important of these limitations, relevant to the work subsequently described in this thesis, are discussed in this section.

The observed spectrum at the end of measurement is modified by the characteristics of the instrument as well as many other sources of error. The observed *instrument lineshape* (ILS), or observed output from a monochromatic source, is generally broadened from the expected delta function, to cover a range of frequencies.

Two unavoidable departures from the ideal instrument described in the previous section, are the need for a finite path difference and a finite stop aperture diameter in all real instruments. The effects of these limitations are described below.

#### 2.5.3.1 Finite Path Difference

The fact that the recorded interferogram can only be measured over a finite path difference can introduce perturbations to the true spectrum due to the mathematical limitations of performing a Fourier transform over finite space. This is equivalent to multiplying the continuous and infinite interferogram by a rectangular function where  $-L \leq \delta \leq +L$ . Thus

$$B(\tilde{\nu}) = \int_{-\infty}^{\infty} I(\delta) \cos(2\pi\tilde{\nu}\delta) \cdot \Pi(\delta/2L) d\tilde{\nu} \quad (2.24)$$

where the rectangular function is described by

$$\begin{aligned} \Pi(\delta/2L) &= 1 & \text{for } -L \leq \delta \leq +L \\ &= 0 & \text{otherwise} \end{aligned} \quad (2.25)$$

By the convolution theorem, the Fourier transform of two multiplied functions is the convolution of Fourier transforms of the two functions individually. Since the Fourier transform of a rectangular function is simply a sinc function, then the truncation of the interferogram is equivalent to convolving the true spectrum with such a sinc function. Hence:

$$B_{obs}(\tilde{\nu}) = B(\tilde{\nu}) \otimes 2L \text{sinc}(2\pi L \tilde{\nu}) \quad (2.26)$$

where the sinc function is described by

$$\text{sinc}(2\pi L \tilde{\nu}) = \frac{\sin(2\pi L \tilde{\nu})}{2\pi L \tilde{\nu}} \quad (2.27)$$

The observed spectrum therefore has a sinc function ILS giving rise to negative side lobes of spectral lines, an effect known as spectral *ringing*. This unwanted effect is usually suppressed by the process of apodisation, where the interferogram is multiplied by an appropriate function such that the interferogram is not truncated abruptly; instead the amplitude is reduced slowly, leading to a broadened spectral line, but with reduced side lobes. The choice of apodisation function is an optimised compromise between loss of effective spectral resolution and the presence of ringing and depends on the spectral resolution employed in the measurement. At the relatively high resolutions used in this thesis, the Norton-Beer strong apodisation function is used. This function is further described by Norton and Beer [1976] with subsequent correction by Norton and Beer [1977].

### 2.5.3.2 Finite Aperture

In order to achieve a reasonable signal to noise in measured spectra, the entrance aperture has a finite size. This leads to off-axis (or parallax) rays entering the interferometer with increasing aperture size. The path difference for such rays as a function of the off-axis angle,  $\alpha$ , relative to the principle optical path, is given by  $\delta \cos(\alpha)$  and the measured interferogram is therefore integrated over the full range of the solid angle,  $\Omega_M$ , subtended by such rays; where solid angle is defined as  $\Omega = \pi\alpha^2$ . Since such angles remain typically small and noting that  $\cos(\alpha) \approx 1 - \alpha^2/2$  for such angles, then the interferogram (Equation 3.10) can be rewritten to include off-axis rays such that

$$I(\delta) = \int_0^{\Omega_M} \int_0^\infty B(\tilde{\nu}) \cos\left(2\pi\tilde{\nu}\delta\left[1 - \frac{\Omega}{2\pi}\right]\right) d\tilde{\nu} d\Omega \quad (2.28)$$

$$= \Omega_M B(\tilde{\nu}) \text{sinc}\left(\frac{\tilde{\nu} \delta \Omega_M}{2}\right) \cos\left(2\pi \tilde{\nu} \delta \left[1 - \frac{\Omega_M}{4}\right]\right) \quad (2.29)$$

Hence the finite aperture affects the spectrum in two ways. Firstly, from Equation 2.29, we see that there is a shift toward lower wavenumber with increasing solid angle. We also see that the interferogram is multiplied by a sinc function, which again leads to broadening of spectral lines in the same manner described in the previous section.

## 2.5.4 Sources of Error in FTS

Where relevant, observed sources of error are discussed in relation to recorded spectra in Chapter 4, although their general effect on spectra is discussed in this section. A comprehensive discussion of all known error sources in FTS is given by Birch and Clarke [1995] and most other introductory texts on Fourier transform spectroscopy (e.g. Sakai [1983]; Guelachvili [1983]; and Beer [1992]).

Sources of error in FTS can lead to distortion of the instrument lineshape, a shift in the wavenumber scale or apparent spurious signals in the final spectrum. Such sources of error include: poor alignment of the optical path; the performance of optical components, detectors and amplifiers; the thermal and physical stability of the instrument, source and sample; anisotropic emission from the source; thermal emission from the instrument and sample and inaccurate knowledge of the path difference and hence incorrect sample spacing of the recorded interferogram. Hence knowledge of the measurement characteristics and limitations of individual instruments is important in assessing the quality of spectral data.

### 2.5.4.1 Phase Error

In a real instrument, the interferogram may deviate from the idealised symmetry around the point of zero path difference. This asymmetry derives from any difference in the assumed point of constructive interference for each wavenumber in the interferogram (i.e. when  $\delta = n\lambda$ ). These phase shifts potentially come from a range of sources, such as: an unaccounted difference in the optical path between the two beams (perhaps due to an imperfect match between the beamsplitter and compensator plate); and inaccurate knowledge of the path difference at the sampled point (i.e. if the position of the

movable mirror is not accurately known). Any unaccounted phase delay in the amplifier detector system may also introduce the same problem in the interferogram.

The asymmetry of the interferogram will not allow the calculation of a purely real spectrum and the computed spectrum will be complex. Hence:

$$B_c(\tilde{\nu}) = B_r(\tilde{\nu}) + iB_i(\tilde{\nu}) \quad (2.30)$$

$$= B(\tilde{\nu}) \exp(i\phi(\tilde{\nu})) \quad (2.31)$$

where the subscripts  $r$  and  $i$  denote the real and imaginary parts of the calculated spectrum respectively. The phase,  $\phi(\tilde{\nu})$ , can be found from

$$\phi(\tilde{\nu}) = \arctan\left(\frac{B_i(\tilde{\nu})}{B_r(\tilde{\nu})}\right) \quad (2.32)$$

The true spectrum can therefore be determined by taking the root sum of the real and imaginary terms squared by

$$B(\tilde{\nu}) = \sqrt{B_r(\tilde{\nu})^2 + B_i(\tilde{\nu})^2} \quad (2.33)$$

Hence, so long as the recorded interferogram is recorded as a double-sided function, then the true spectrum can be recovered easily using the equations above. The only disadvantage of this method is that any negative radiance, recorded as a result of noise around the zero baseline, will become positive and therefore may induce an effective positive baseline shift.

In the absence of a double-sided interferogram, phase correction cannot be applied. However, many spectrometers record single-sided interferograms only, at high resolution. The spectrometers used in this thesis record a short part of the double-sided interferogram such that a low-resolution phase spectrum is determined. Since phase typically varies slowly with wavenumber, this low-resolution phase spectrum is suitable for correction in high-resolution spectra and used in the phase correction procedures performed automatically in the instruments described later in this thesis.



#### **2.5.4.2 Channelling**

Unwanted reflections off any surfaces in the optical path such as from sample cell windows will lead to double or multi-modulated beams that will subsequently undergo interference on recombination and lead to the presence of secondary interferograms within the measurement. Such unwanted interferograms would be centred on the optical path difference between the reflecting surfaces. The Fourier transform of such a measured interferogram would result in observed periodic oscillations superimposed on the output spectrum.

This effect is greatly reduced by using surfaces such that any unwanted reflections are simply reflected out of the optical path. This can be performed using wedged optics such as wedge shaped sample windows. Such optics are used in the instrument configuration used in this thesis and described further in Chapter 3. The removal of characteristic peaks in the measured interferogram prior to transformation may also be used to partially remove this effect although care must be taken not to remove true data or to produce additional spectral artefacts. Such correction is not always possible for this reason.

#### **2.5.4.3 Detector Non-linearity**

A further source of distortion in the output spectrum relates to deviations in the linearity of the instrument response to source radiation. In this event, the output signal from the detector is not directly proportional to the flux of incident radiation. Common detectors used in FTS instruments such as the liquid nitrogen cooled MCT (Mercury-Cadmium Telluride) detector, and used in laboratory measurements of PAN in this thesis, are well known to exhibit significant non-linear responses to radiation reaching the detector (see Richardson *et al.*, [1998] and references therein for a detailed discussion of spectral artefacts caused by such detectors). In addition, the instrument electronics (amplifier-filter circuits) can also introduce a non-linear response to the photon flux even where the detector may behave linearly (Rahmelow, [1997]).

A common manifestation of such non-linearity is the observation of spectral artefacts outside of the spectral passband permitted by the source, detector and filter optics; where the measured signal should equal zero.

The non-linear measured interferogram,  $I_m(\delta)$ , can be represented in terms of the true interferogram,  $I_t(\delta)$  as a polynomial thus:

$$I_m(\delta) = aI_t(\delta) + bI_t^2(\delta) + cI_t^3(\delta) + \dots \quad (2.34)$$

where  $a$ ,  $b$  and  $c$  are constants. Thus, the measured spectrum can be written using the more general exponential form for the Fourier transform as

$$\begin{aligned} B_m(\tilde{\nu}) &= \alpha \int_{-\infty}^{\infty} I_t(\delta) \exp(-i2\pi\tilde{\nu}\delta) d\delta \\ &+ \beta \int_{-\infty}^{\infty} I_t^2(\delta) \exp(-i2\pi\tilde{\nu}\delta) d\delta \\ &+ \gamma \int_{-\infty}^{\infty} I_t^3(\delta) \exp(-i2\pi\tilde{\nu}\delta) d\delta + \dots \end{aligned} \quad (2.35)$$

By the convolution theorem, the product of multiplying the true interferogram with the Fourier transform is simply the convolution of the true spectrum with itself. Therefore the higher order terms in Equation 2.35 represent higher order convolutions of the spectrum. Hence

$$B_m(\tilde{\nu}) = \alpha B_t(\tilde{\nu}) + \beta B_t(\tilde{\nu}) \otimes B_t(\tilde{\nu}) + \gamma B_t(\tilde{\nu}) \otimes B_t(\tilde{\nu}) \otimes B_t(\tilde{\nu}) + \dots \quad (2.36)$$

Non-linearity will therefore lead to a frequency dependant perturbation of the baseline of derived spectra given by the higher order terms in Equation 2.36. The influence of the non-linear response is especially strong in the centre burst of the interferogram due to the large photon flux. This can affect the symmetry and consequently the phase of the recorded interferogram such that the phase correction described in Section 2.5.4.1 cannot be performed. If any such phase error is present, the use of phase correction further complicates the way the spectrum is influenced by non-linearity. Chase [1984] showed that the second order term in Equation 2.36 introduces a negative offset to the measured baseline in the absence of phase errors. However, if a phase error is included in the calculation, its effect may have a positive or a negative baseline influence. Although many methods exist for non-linear error correction such as those described by Offersgaard and Öjelund [2002], this correction cannot be accurately

applied in conjunction with phase correction. Therefore, since phase correction is used in this thesis, every attempt is made to reduce (rather than to correct for) non-linear responses through the use of appropriate electronic and optical filters to ensure that any detector operates in the linear regime.

Detector non-linearity can be greatly reduced by limiting the spectral range of measurements and the use of appropriate electronic filters. This is discussed further in Section 3.2.2.

#### **2.5.4.4 Thermal Emission**

Both the sample under analysis and components of the spectrometer itself may exhibit thermal emission, which affect the calculated spectrum through their effects on the recorded interferogram.

The effects of sample emission described by Ballard *et al.* [1992] are such that radiative heating of the sample may cause thermal emission, which is detected, thus adding to the measured intensity of radiation and artificially adding to the true transmission spectrum of the sample. Also, radiative heating of spectrometer components by source radiation, such as the stop aperture in some FTS instruments, may also result in thermal emission. Such emission may be different to that of the source and if modulated by the spectrometer, would affect the measured spectrum by also masking the true transmission spectrum of the sample [Johns, 1987].

The effects of thermal emission can be investigated, by recording spectra with source radiation switched on and off. It's impact can then be assessed in the context of measured spectra.

## **2.6 Summary**

In this chapter, the principles of atmospheric limb sounding and radiative transfer have been introduced. In addition, theory relating to the molecular spectroscopy of PAN has been discussed together with the principles and practice of Fourier transform spectroscopy. In addition, a summary of previous available spectroscopic measurements of PAN in the mid-infrared has been given, highlighting the need for new cross-sectional data for PAN of greater accuracy and higher spectral resolution. Further improvement is also required for the highly variable infrared absorptivities and

integrated band intensities reported to date. Furthermore, new spectral data for PAN are required for a range of temperatures and pressures appropriate (as closely as possible) to the measurement of PAN in the upper troposphere.

In the following chapters, experiments are described which attempt to improve on the currently available spectral data so that the possibility of atmospheric detection and retrieval of PAN will be enhanced.

## Chapter 3

### 3 Laboratory Measurement of PAN

The accurate determination of trace gas concentrations from measured atmospheric spectra requires the use of accurate reference spectroscopic data. Such reference data for PAN prior to this work are far from ideal, as noted in the discussion of previous PAN measurements in Section 2.4.2.

PAN is an extremely difficult and hazardous compound to handle and requires customised procedures for its production, handling, measurement and disposal. Such experiments therefore require considerable attention to be paid to chemical preparation and safety. This chapter describes PAN measurements required to obtain spectral reference data for use in remote sensing of the upper troposphere and details the procedure adopted for their acquisition in the laboratory.

#### 3.1 Spectral Measurement Requirements

As noted in Section 2.4.2, previously reported PAN spectral data exist only at room temperature (between 291 and 296 K) and only for pure PAN vapour at low sample pressures. Furthermore, such data are recorded at low spectral resolution ( $< 0.06 \text{ cm}^{-1}$ ) relative to most infrared remote sensing instruments (e.g.  $0.025 \text{ cm}^{-1}$  for MIPAS on Envisat) for the atmosphere.

For the best possible accuracy of information retrieval from measured spectra, cross-section data should reflect the ambient conditions (total pressure and temperature) under which the measurement was made as closely as possible. In addition, the spectral resolution of reference data should ideally be close to or greater than the spectral resolution of the remote sensing instrument.

For these reasons, the PAN reference dataset derived in this work is compiled to reflect the conditions encountered in the atmosphere where PAN is likely to be detected

by remote sensing methods. As discussed in Chapter 1, this region is the upper troposphere and the typical pressure and temperature profiles (see Figure 1.1) over this region can be used to define the requirements of the PAN reference dataset. The spectral resolution is also chosen to best match that of remote sensing instruments currently planned or already in use (i.e.  $0.025\text{ cm}^{-1}$ ). Furthermore, such reference data should take the form of absorption cross-sections due to the broadband nature of PAN absorption bands (see Section 2.4.1.6).

### 3.1.1 Measurement Limitations

The pressure and temperature range studied should satisfy the range of conditions expected in the atmosphere as closely as practicable. Ideally, it would be good to measure PAN spectra at temperatures as low as 190 K to reflect the lower limit of temperatures encountered in the upper troposphere. However, the allowed temperature and pressure ranges for measuring pure PAN spectra are limited by the thermodynamics of the PAN molecule, with lower limits set by the saturation vapour pressure relationship to temperature. This saturation vapour pressure curve for PAN as a function of temperature is calculated from data reported by Bruckmann and Willner [1983] and plotted in Figure 3.1. At lower temperatures, the saturation vapour pressure is extremely small (e.g. 0.02 mb at 220 K), making accurate spectral measurement difficult due to the limitations in accuracy of pressure monitoring equipment. Furthermore, at such low pressures, a very long sample pathlength would be required in order to observe significant absorption of source radiation. For these reasons, cold temperature measurements were limited in this thesis to a minimum of 250 K.

Near room temperature (291 K), saturation partial pressures of PAN reach 20 mb. However, the thermal decomposition rate of the molecule increases rapidly near this temperature and PAN becomes explosively unstable in its pure form above 310 K. The associated problems in determining PAN concentration over the course of a typical measurement due to thermal decomposition, together with the increased explosive risk, therefore place an upper limit on the temperature and pressure range measured in this work at 298 K. An intermediate temperature of 273 K was also chosen to increase sampling over the temperature range.

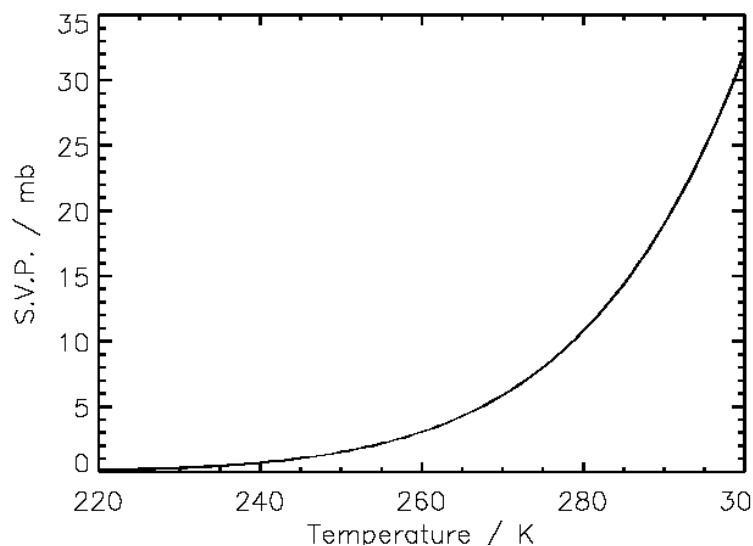


**Figure 3.1** Saturation vapour pressure (s.v.p.) of PAN (mb) as a function of temperature; calculated from data reported by Bruckmann and Willner [1983].

## 3.2 Experimental Overview

To achieve the measurement requirements listed in the previous section, the choice of laboratory apparatus and measurement technique must reflect the needs of the experiment. This section describes these laboratory apparatus and the operating procedure chosen for the spectral measurement of PAN.

### 3.2.1 The NERC Molecular Spectroscopy Facility

Laboratory measurements of infrared spectra of gaseous PAN under a variety of conditions were performed at the Natural Environment Research Council (NERC) Molecular Spectroscopy Facility (MSF), based at the Rutherford Appleton Laboratory. This facility is a world-class research laboratory with a number of state of the art spectrometers.

Two Fourier Transform Spectrometers, the Bruker IFS-120 HR and the Bruker IFS-66v, were used for measurements over three measurement periods between May 2002 and September 2003. The IFS-120 HR spectrometer was employed for all PAN spectral measurements described in this thesis, chosen for its high resolution and accuracy, whilst the lower resolution IFS-66v was used to perform spectral measurements of other possible PAN sample contaminant gases (see Section 3.3.3.3). A

summary of measurement parameters for spectra recorded in each measurement period is given later in Section 3.5.

A digital photograph of the IFS-120 HR spectrometer room showing the spectrometer itself and associated gas-handling apparatus, is shown in Figure 3.2.



**Figure 3.2** Digital photograph of the MSF main laboratory housing the Bruker IFS 120HR spectrometer and associated gas handling and cooling systems.

### 3.2.2 Spectrometer Configuration

A schematic of the optical path of the Bruker IFS-120 HR Fourier Transform Spectrometer instrument is shown in Figure 3.3. This spectrometer has a maximum optical path difference (MPD) that can be set to up to six metres, corresponding to a nominal spectral resolution of  $0.0015 \text{ cm}^{-1}$ . This nominal resolution is defined by the manufacturer to be  $0.9/\text{MPD}$ . In all subsequent definitions of spectral resolution in this and the following chapter, the nominal resolution refers to the unapodised spectral resolution of measurements made at the MSF.



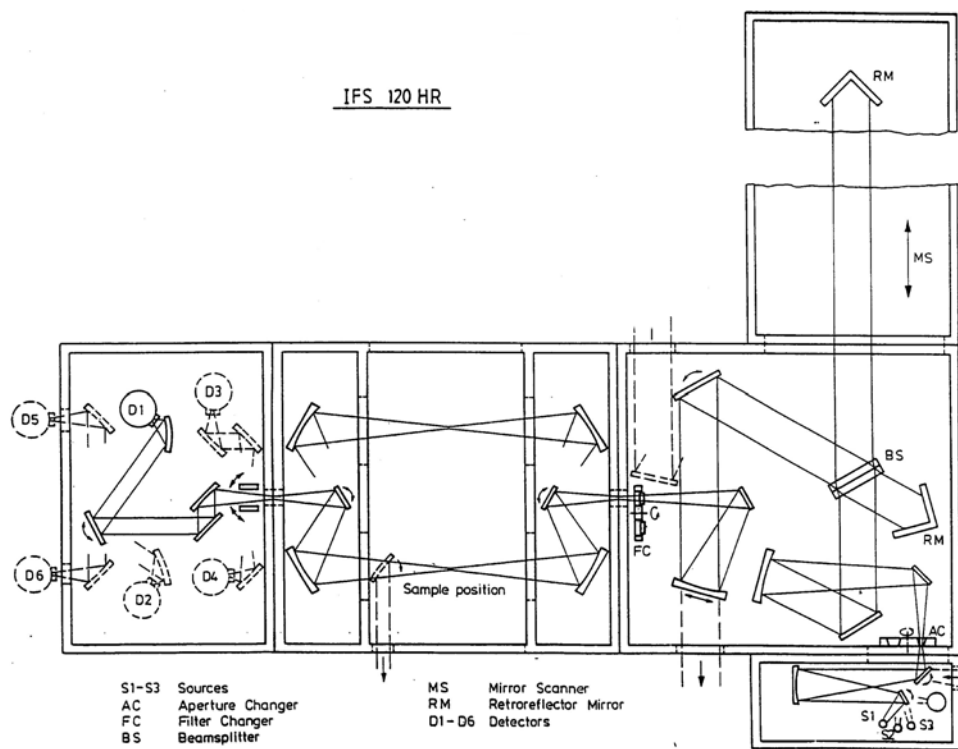


**Figure 3.3** Optical schematic of the Bruker IFS 120 HR spectrometer

To meet measurement requirements, the IFS-120 HR was configured to measure spectra in the mid-infrared using the equipment listed in Table 3.1.

Spectrometer Configuration	
Nominal resolution	0.03/0.25 $\text{cm}^{-1}$
Beamsplitter	Ge/KBr
FTIR input aperture	1.0 – 1.7 mm
Detectors	Broadband liquid nitrogen-cooled mercury cadmium telluride (MCT-D360)
Source	Room temperature DLaTGS
Gas cell	Globar
Cell windows	26.1 cm glass (evacuable)
	Wedged KBr

**Table 3.1** Configuration of the Bruker IFS120HR spectrometer for PAN measurements.

Measurements in this thesis were recorded at lower spectral resolutions (0.03 and 0.25  $\text{cm}^{-1}$ ) than the maximum capability of the spectrometer. No resolution of fine structure is expected at even the highest resolution of the spectrometer due to the high molecular

mass of PAN (121 atomic mass units, see Section 2.4.1.6). In addition, the highest resolutions require long integration times which were not possible with PAN due to its thermal instability. Lower resolution measurement does, however, allow shorter measurement times with a greater spectral signal to noise ratio.

The higher spectral resolution of  $0.03\text{ cm}^{-1}$  was employed initially with no resolution of fine structure in PAN absorption bands. Therefore, the resolution of subsequent measurements was reduced to  $0.25\text{ cm}^{-1}$  with no significant loss of spectral information. The advantage of reducing resolution meant that measurement time was further reduced so that thermal decomposition of PAN over the period of a single measurement was sufficiently small as to introduce little error in the recorded spectrum (estimated to be less than 0.1%, see Section 4.2.1).

The spectral range of measurements covered the mid-infrared spectral window between  $500$  and  $2200\text{ cm}^{-1}$  ( $4.55$  to  $20\text{ }\mu\text{m}$ ) and was chosen to cover all previously known mid-infrared absorption bands of PAN. This limit reflects the limitations of the DLaTGS detector cut-off near to  $450\text{ cm}^{-1}$  (the lower limit) and the use of an optical filter (the upper limit). The need for a restricted spectral range has been discussed in the context of Fourier transform techniques in Section 2.5.

High-resolution measurements ( $0.03\text{ cm}^{-1}$ ) were first recorded across the range  $550$  to  $1900\text{ cm}^{-1}$  with the use of a wideband optical filter and the MCT-D360 detector. This range was later deemed to be less suitable as the large spectral window of such a measurement gave rise to undesirable detector non-linearity (see Section 2.5.4.3).

For reasons of accuracy and the need to better measure the  $1841\text{ cm}^{-1}$  PAN band, subsequent measurements (mainly at the lower spectral resolution of  $0.25\text{ cm}^{-1}$ ) were recorded using a range of smaller-window optical filters together with high and low pass electronic filters. Optical filters were chosen to give overlapping spectral windows (see Table 3.2) and to completely cover the required spectral range of  $550$  to  $2200\text{ cm}^{-1}$ .

The label for each filter listed in Table 3.2 is arbitrary and is chosen here to easily identify the spectral region of corresponding measurements. Filter “A” corresponds to the wideband filter used in the majority of high-resolution measurements whilst the X, Y and Z filters are narrower but in combination cover the entire spectral range of interest for PAN. The W filter allows measurements of possible sample contaminants such as carbon dioxide (see Section 3.3.3).

Filter	Spectral range / $\text{cm}^{-1}$
A	550-1900
W	3200-4000
X	550-1400
Y	850-1700
Z	1550-2200

**Table 3.2** Allowed spectral pass band of optical filters used for PAN measurements.

Figure 3.4 illustrates the spectral pass band of each optical filter and the relative transmittance characteristics as a function of wavenumber for each of the filters listed in Table 3.2. This plot is derived from a number of successive background spectra recorded by the IFS 120 HR spectrometer at  $0.03 \text{ cm}^{-1}$  spectral resolution, with each filter in place. The effect of detector non-linearity using Filter A is clearly seen in the plotted black line, which corresponds to this wideband optical filter. An apparent detected signal below  $500 \text{ cm}^{-1}$  (beyond the detector cut-off) illustrates the problem. The reduction in non-linearity is immediately apparent using all other filters.

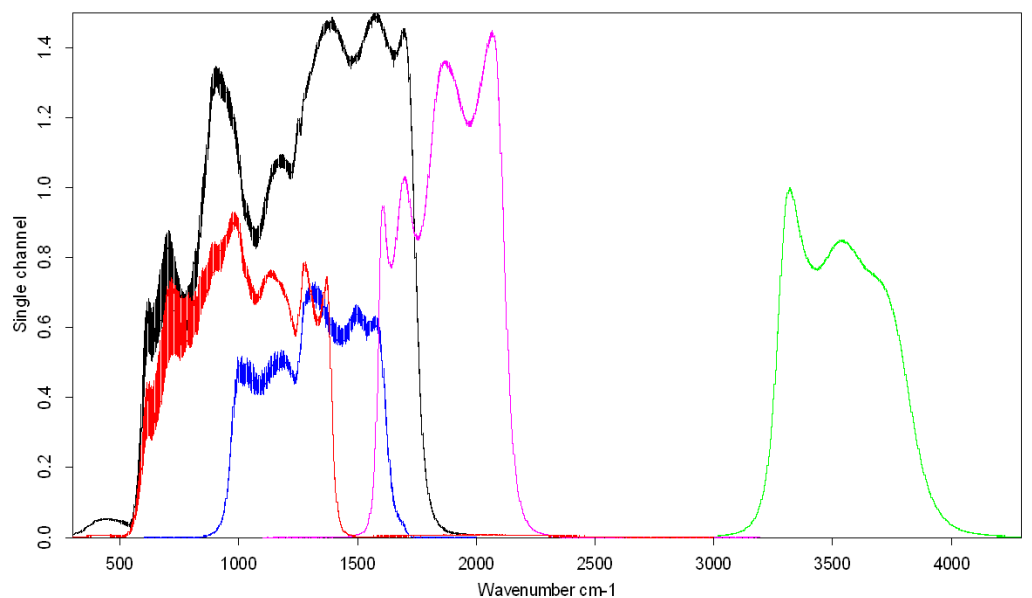


**Figure 3.4** Spectral windows allowed by the optical filters used in PAN measurements, where black = filter A, red = filter X, blue= filter Y, purple = filter Z and green = filter W. All background spectra were recorded at  $0.03 \text{ cm}^{-1}$  spectral resolution.

A limitation in using multiple optical filters was that measurement of all absorption bands over the full spectral range was not possible simultaneously. Furthermore, separate measurements with different optical filters could not be made for the same PAN sample due to a problem with the thermal equilibrium of the spectrometer optics; each time the optical filter was changed, it was noted that measured spectra showed artefacts similar to channelling. This is expected to be caused by the changing temperature of the optical filter as it reaches thermal equilibrium inside the spectrometer following exposure to source radiation. For this reason, a period of at least two hours was required after changing optical filters to allow thermal equilibrium to be achieved. Such a length of time renders any PAN sample useless due to thermal decomposition, meaning that the same sample cannot be used for different spectral windows. Hence different PAN samples were required for each measurement and for each spectral range of the spectral windows in Table 3.2. An unfortunate consequence of this requirement was that a far greater number of individual measurements was required and also that no observation of potential contamination in other spectral regions to that being measured, could be made. However, low quality spectra of alternate spectral windows made immediately after the desired measurement did not show any evidence of such contamination.

The width of the collimated infrared beam was restricted by the use of a stop aperture. The higher aperture diameter (1.7 mm) was used for the high-resolution measurements whilst the smaller size (1.0 mm) was used in the low-resolution mode. A larger diameter could have been used without adversely affecting the resolution of spectra, with an associated improvement in the signal to noise ratio. However, the chosen setting is a compromise between this improvement and the reduction in detector nonlinearity. The signal to noise at this smaller aperture was more than sufficient ( $S/N = 700$  at  $1740\text{ cm}^{-1}$ ) to yield precise measurements whilst no observable evidence of detector non-linearity was seen in measured background spectra.

All raw interferograms were apodised with the Norton-Beer Strong apodisation function [Norton and Beer, 1976; 1977], Mertz phase correction and a zero-filling factor of two.

### 3.2.3 The Sample Cell and Temperature Monitoring

A single-pass glass sample absorption cell with an optical path length of 26.0 cm was used for PAN measurements made with the IFS120 HR (see Figure 3.5). A glass cell was chosen in preference to available stainless steel cell because of the possibility of PAN adsorption and surface reaction with the metal. The cell was housed within the body of the sample compartment of the evacuated spectrometer and equipped with Young's tap fittings at either end of the cell in order to interface with a gas handling line.

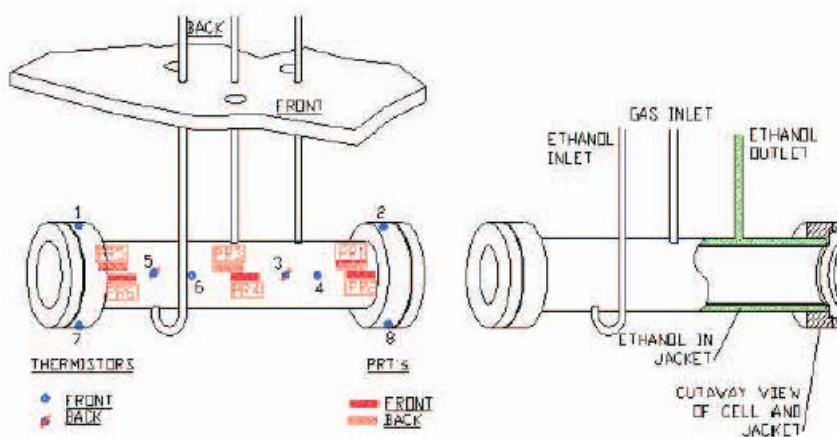


**Figure 3.5** A schematic of the 26.0 cm gas absorption cell showing locations of thermistors and cooling jacket.

Potassium bromide cell windows were chosen for their excellent transmission character across the spectral range of interest and their chemical inertness to PAN. Wedge shaped windows were used to prevent total internal reflection of source rays that would suffer multiple reflections, otherwise resulting in channelling.

For initial measurements of pure PAN, the sample cell was equipped with eight curve-matched thermistors suitable for measurements over the range 270 to 350 K with a quoted accuracy of  $\pm 0.2$  K over the range 270 to 350 K. These were placed in thermal contact at various positions to monitor overall cell temperature and possible differences in the temperature around the cell. The thermistors were later replaced with higher accuracy ( $\pm 0.1$  K), wider temperature range (70 to 350 K), but more expensive, platinum resistance thermistors (PRTs) for low temperature and nitrogen-broadened measurements. Circuitry for both types of thermistor was fed through to the sample compartment using an electrical vacuum-tight feed through socket. For the curve-

matched thermistors, output was recorded both manually (using an ohm-meter at two minute intervals throughout the course of a measurement) and logged automatically by a PC interface, whilst PRT output was recorded continuously using a SignalLogger PC interface manufactured by Laplace instruments.

The cell was also surrounded with a thermal jacket and cooling system installed for use with low temperature measurements. This system allows cooling of the sample cell down to temperatures as low as 214 K by the active circulation of ethanol through the jacket. The ethanol is cooled externally in an ethanol filled Dewar with a liquid nitrogen based heat exchanger and thermostat. A similar setup has been described by Smith *et al.* [1999] and is regularly used by users of the MSF.

For low temperature measurements (273 and 250 K), the cooling apparatus was set to the desired temperature and switched on at least three hours prior to measurement. This allowed sufficient time for the cell to stabilise at the required temperature. Temperature logging was made continuously throughout the day to ensure this.

In general, the temperature stability of the sample cell during a typical measurement was good (see Figure 3.6), with a deviation of less than 0.3 K between start and finish in all cases. Individual curve-matched and PRT thermistor readings typically had standard deviations better than  $\pm 0.07$  K. A systematically higher temperature was observed for thermistors placed on the two ends of the cell for lower temperature measurements. This is generally expected as the cooling jacket cannot completely cover the ends of the cell. The central thermistors showed little inter-variability, however, and no significant temperature gradient across the cell could be inferred from the measured temperatures at either end of the cell. The assignment of sample temperature was made by taking an average of the temperature recorded over the whole measurement and by all resistors. Associated error in this assignment is calculated as the maximum amplitude of the observed variability over the course of the measurement plus the quoted accuracy of the thermistors. Such error was calculated to be  $\pm 0.3$  K at worst for room temperature measurements using curved match thermistors.

A more noticeable periodic variability in temperature was noted to be due to the cooling cycle of the ethanol pump for measurements at low temperature and reflected in the temperature-time plot of Figure 3.6. This effect leads to the greatest uncertainty in the assigned temperatures for measurements at low temperature, giving error assignments of  $\pm 0.5$  K at 250 K. Again, this error is quoted as the sum of the maximum

observed variability in the cell and the nominal accuracy of the PRT thermistors. At room temperature, the air-conditioned laboratory is thermostated at 294 K with no such cyclic variability observed in the data, resulting in a greater accuracy of  $\pm 0.2$  K for measurements using PRTs at room temperature.

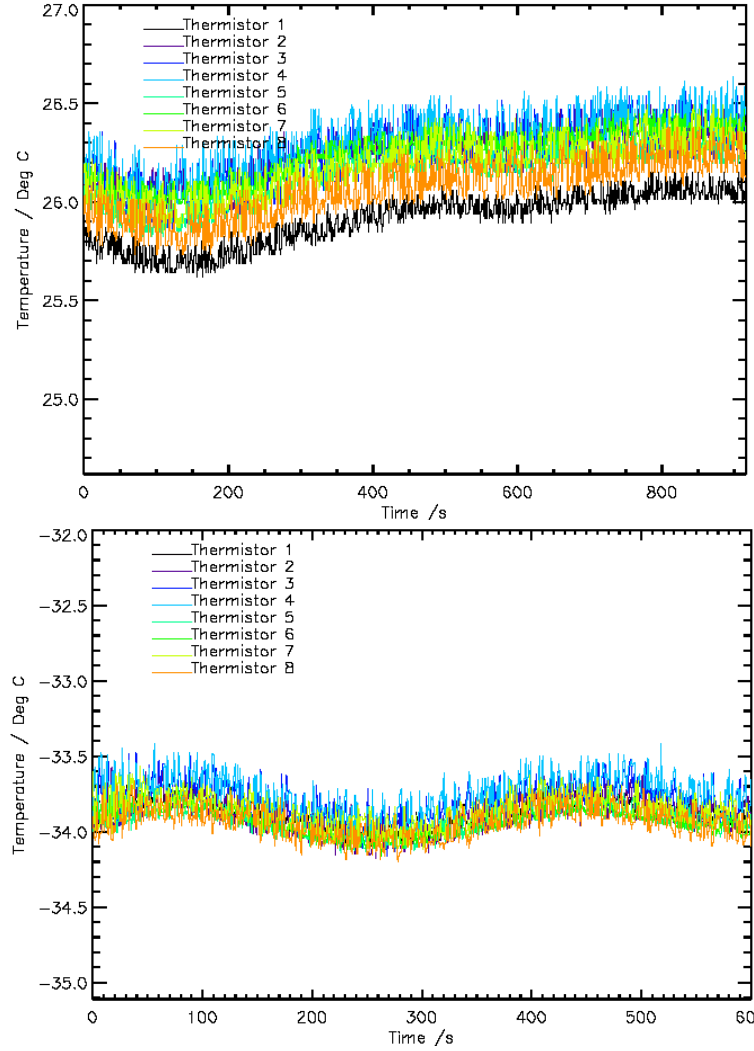


**Figure 3.6** Thermistor temperature logs recorded over the course of a typical a) room temperature measurement using curve-matched thermistors and b) a low temperature measurement showing cooling cycle periodicity using PRTs.

In addition to this direct temperature monitoring method, the accuracy of the assigned cell temperature was investigated using a retrieval of cell temperature from spectral lines of a calibration sample of carbon dioxide. An iterative Levenberg-Marquardt retrieval scheme was used together with reference line parameters for carbon

dioxide from HITRAN 2000 (Rothman *et al* [2003]). This retrieval scheme and its application to contaminant retrieval are described further in Section 4.2.2.1. A comparison of five spectra with recorded temperature data yielded temperature differences of less than 0.3 K. This is within the assigned uncertainty.

### 3.2.4 Gas Handling and Vacuum Line

The sample cell was securely interfaced with a gas handling line for sample preparation, cell injection and evacuation purposes. This gas handling system is shown in Figure 3.7. The line was custom-built from glass and equipped with Teflon sealed PTFE Young's tap fittings for manual gas flow control. A liquid nitrogen cold trap was used to trap any evacuated compounds, preventing potentially hazardous absorption into the oil of the vacuum pumps.

A rotary vacuum pump was used to evacuate the cell down to pressures of less than 0.5 mb and a switchable diffusion pump was used to further achieve very high vacuums of up to  $10^{-5}$  mb. This very small gas residual is negligible (0.1% at worst) relative to the lowest PAN pressure (0.22 mb) used in this work. The highest vacuum attainable is physically limited by the performance of the diffusion pump and also by the magnitude of any small ambient air leakage into the system. Such small leaks are typically unavoidable in such gas handling lines and every attempt was made to minimise such leaks through careful operating procedure and testing.

Over the typical timescales of measurement an acceptable leak rate limit of 0.01 mb per minute was set with the added criterion that initial pressure of the system prior to PAN handling must be better than 0.001 mb. This limit prevents any noticeable errors on the results from pressure broadening contributions for example and corrections can be made to the results by accurately measuring the leak rate into the system at regular intervals. Leak rate measurements were made at the start and end of each day and also prior to each measurement. No leak rates were found to exceed 0.01 mb per minute.

The gas line was also fitted with a Perspex screen to prevent the user from injury in the event of an explosion. In addition, a Perspex facemask, suede gloves and lab coat were worn at all times by the operator and personnel within a ten-metre radius of the apparatus.



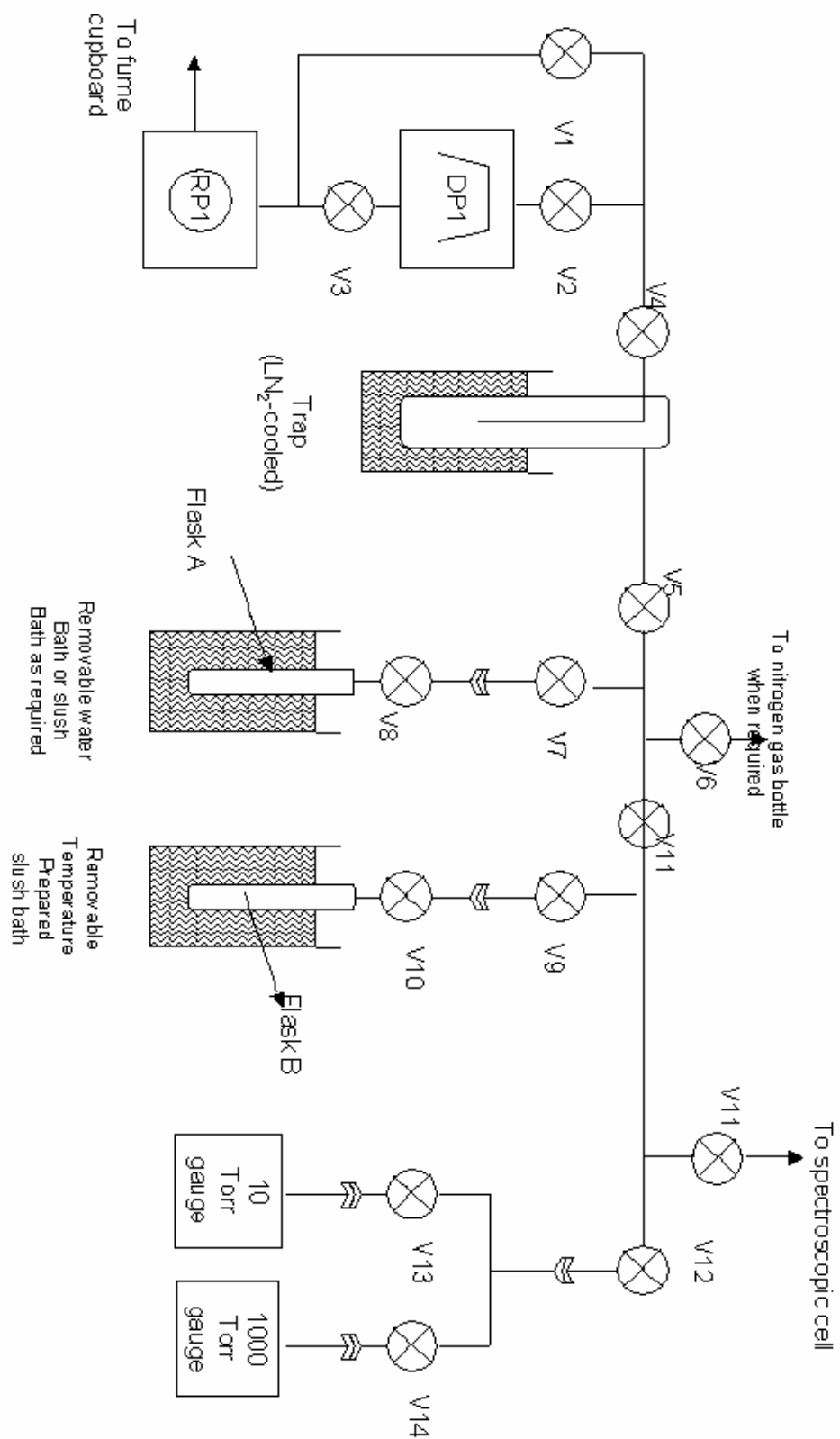


**Figure 3.7** Schematic of the gas handling and vacuum line apparatus. V denotes the various Young's tap fittings, whilst DP and RP represent the rotary pump and diffusion pump respectively.

### 3.2.5 Pressure Monitoring

Pressure was monitored throughout the measurements by 10 Torr and 1000 Torr MKS Baratron 390 pressure gauges (1 Torr = 1.33 mb). The two gauges were calibrated against each other at low pressure whilst the 1000 Torr head was first calibrated at ambient pressure using a recently certified aneroid manometer (Negretti type M2236A).

To avoid decomposition or detonation of the PAN sample, the Baratron gauges were operated at room temperature rather than at the normal 40°C thermostated operating temperature. At the air-conditioned laboratory temperature of  $295 \pm 1$  K, the uncertainty in the 10 Torr Baratron calibration was determined to be small (less than 0.7% of full scale) by cross-calibration between the thermostated and non-heated Baratron gauges. No observable drift was seen between the gauges over a period of two hours with a static nitrogen sample.

The 1000 Torr gauge head was used for coarse measurement of line pressure during evacuation and flushing whilst the 10 Torr gauge head was used for higher accuracy at low line pressure during sample injection and the final stages of line evacuation. The 10 Torr head was isolated from the line or switched off during periods of high line pressure to prevent damage.

Pressure was monitored continuously throughout the day, with tests for satisfactory leak rates made in the morning and afternoon. A typical pressure log from a room temperature measurement is shown in Figure 3.8. The figure shows the filling of the cell with pure PAN vapour prior to measurement. Immediately after the gas line is isolated from the cell, the cell pressure is seen to decrease. This is due to the unavoidable adsorption of PAN onto the walls of the cell. The pressure quickly stabilises and measurement is started as soon as possible after the pressure change is seen to be minimal. The pressure change over the course of the measurement is minimal with the only deviations (square shaped anomalies in Figure 3.8) being due to the rounding errors of the logged pressure (rounded to nearest 0.001 mb). Any change in the sample pressure due to the decomposition of PAN over the timescale of room temperature measurements is expected to be smaller than the rounding accuracy of the Signallogger (see Section 4.2.1).

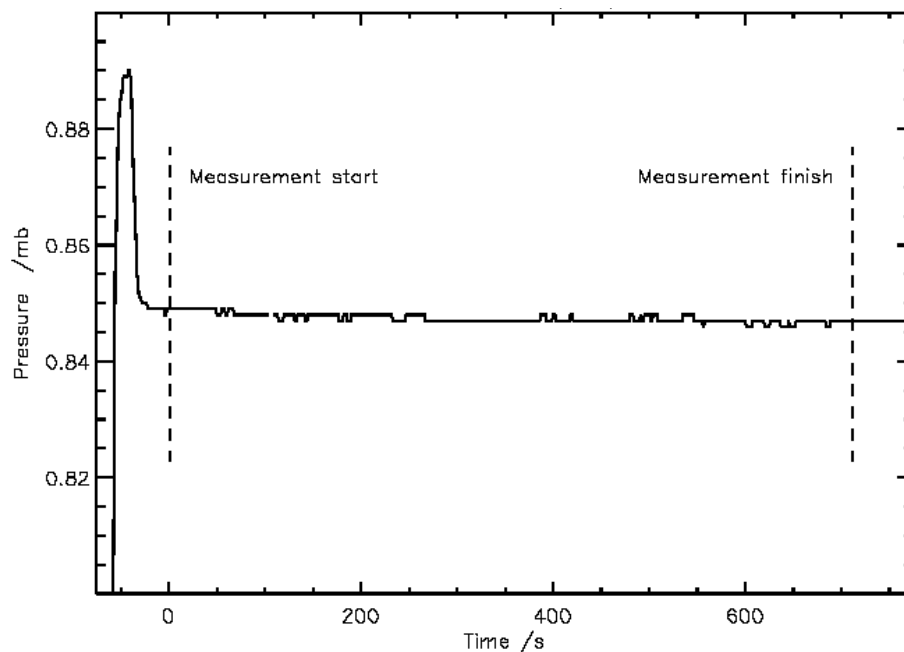


**Figure 3.8** Absorption cell pressure log over the course of a room temperature measurement made on 4<sup>th</sup> September 2003.

### 3.3 Sample Preparation and Purity

As previously noted, PAN is an extremely dangerous compound to study in its pure form. It is highly toxic, carcinogenic and mutagenic. In addition to these health risks, it is also physically dangerous, posing a risk of explosion in all forms. Solid and liquid state PAN samples are sensitive to sudden physical shock including rapid changes in pressure. The gaseous form is more stable to physical effects but can spontaneously detonate at temperatures in excess of 40°C. Exposure to high intensity ultraviolet radiation can also cause sudden decomposition. For these reasons, careful and customized procedures were devised for all stages involved in handling PAN from synthesis to disposal.

An accident in May 2002 during the purge of the vacuum line at the end of a measurement, led to an extensive safety review by MSF staff and the preparation of an extensive procedural and safety document before further measurements could be resumed. A report into the accident compiled by Newnham and Knight [2002], concluded that the most probable cause of the accident was an explosion, caused by the immediate compression of pure PAN following sudden failure of a Young's tap fitting

on the gas handling line. Existing procedures in place at the time of the accident prevented damage to the spectrometer optics by the routine isolation of the absorption cell from the handling line during this purging step.

The procedure adopted for preparing, handling and measuring PAN gas samples using the Bruker IFS 120 HR spectrometer are detailed in the remainder of this section.

### **3.3.1 Synthesis of PAN**

PAN samples cannot be purchased from known chemical suppliers and is produced instead from the nitration of the commercially available product, peracetic acid. The PAN product is dissolved and stored in an organic solvent. In this work dodecane was chosen for this purpose due to its low volatility and high solubility of PAN. The procedure detailed here is a customised synthesis, similar to that described by Gaffney *et al.* [1984] and Nielsen [1982].

Initially, PAN-dodecane samples were prepared at the University of Leicester chemistry department and frozen in carbon dioxide ice prior to transport to the MSF. However, the presence of contaminant gases observed in some spectra in initial measurements due to the breakdown of PAN during long periods of storage (up to three months), meant that a revised preparation procedure was employed for later measurements. Such PAN decomposition products are undesirable and can greatly contaminate measured spectra, requiring otherwise unnecessary correction increasing the uncertainty in PAN concentrations. The following procedure describes the procedure for PAN-dodecane synthesis in the MSF measurement period of September 2003, with the only difference relative to the earlier May 2002 procedure, being that samples were prepared at Leicester and stored for long periods in dry ice.

All elements of the synthesis were carried out in an active fume cupboard and a laboratory coat and safety goggles were worn at all times. The cleanliness of glassware was noted to be crucial to successful synthesis and all glassware was washed with Decon 90 and rinsed with distilled water and wash acetone before being placed in an autoclave oven overnight prior to PAN synthesis (performed in the morning of each measurement day, except during May 2002).

The reaction chamber, a 100 ml 3-necked flask, is supported by a clamp and stand and immersed in a water ice bath as illustrated in Figure 3.9.

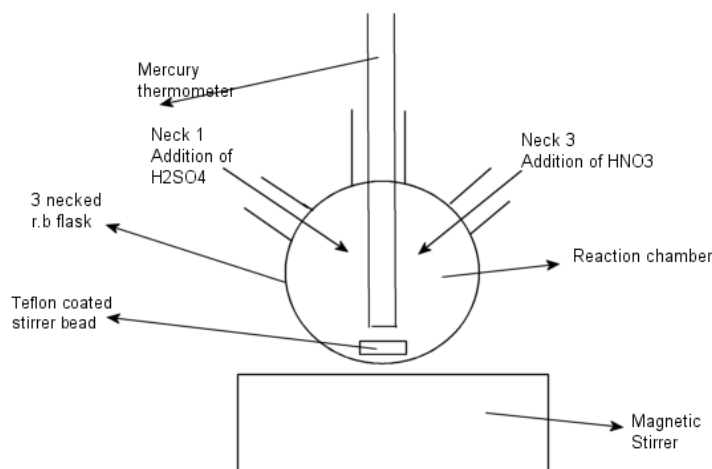


**Figure 3.9** 100ml 3-necked flask showing experimental setup

A constant nitrogen flow (100 ml/min) was maintained through the flask. In early preparations of PAN, the synthesis was carried out without this nitrogen flow and evidence of atmospheric contamination was seen. In later procedures this nitrogen flow was used to minimise contamination and also to prevent the build up of potentially hazardous PAN vapour in the reaction chamber.

Firstly, 25 ml of dodecane was added to the flask. The solvent was then cooled to between 1 and 3°C (measured by mercury thermometer) under permanent stirring using a Teflon coated magnetic stirrer bead and magnetic stirring table. Stirring was maintained throughout the synthesis and reduced as necessary to avoid formation of foam which may lead to dangerous local high concentrations of PAN in the form of bubbles.

In a single operation, 2.5 ml of peracetic acid (30% wt. vol. in acetic acid) was added by graduated pipette. Care was taken to ensure the initial temperature of the dodecane was no less than 1°C as peracetic acid may freeze when added to the flask at lower temperatures. Next, 2 ml of pure concentrated  $\text{H}_2\text{SO}_4$  (99.999% wt. vol.) was added in a single operation with a clean graduated pipette. Heavy-duty nylon gloves were worn when handling concentrated acids.

The reactants were again allowed to cool under continuous magnetic stirring whilst monitoring temperature. On obtaining a temperature of 1°C, 0.5 ml of concentrated red fuming  $\text{HNO}_3$  ( $\text{NO}_3^-$  saturated in  $\text{H}_2\text{O}$ ) was added by Pasteur pipette at a rate of one drop per minute and under strong magnetic stirring in order to emulsify the mixture, with care taken to prevent the formation of foam.

The quality and yield of PAN synthesized using this method depended strongly on never exceeding a maximum temperature of 5°C, which prevents the formation of PAN. The reaction was allowed to proceed for a further five minutes after the end of the acid addition whilst monitoring reaction temperature to maintain a temperature range of 1 to 3°C; crushed ice was added to the water bath as necessary.

The product was then transferred to a separating funnel containing 50 ml distilled water at 0°C. The mixture was stirred firmly with a glass stirring rod and left to separate for thirty seconds before draining off the lower aqueous phase into a 100 ml round bottomed flask containing universal indicator fluid. This operation was repeated as many times as necessary to obtain a pH of greater than 6 in the drained aqueous phase to ensure removal of excess acids used in the synthesis.

The resultant organic phase was then transferred to a conical flask containing magnesium sulphate granules in sufficient quantity such that at the end of this drying step, magnesium sulphate grains remained non-agglomerated at the bottom of the flask.

Solutions of PAN obtained at the end of this procedure are quoted to range from 0.005 to 0.05 molar, but are generally around 0.02 to 0.025 molar [Gaffney *et al.* 1989]. The organic phase was subsequently filtered through standard filter paper into a round-bottomed sample tube equipped with a PTFE/Teflon tap fitting. Samples stored in this manner were then ready for immediate use on the gas handling line. To prevent decay at times when samples were not immediately used, samples were frozen in dry ice (CO<sub>2</sub>) and placed in a chemical freezer.

### **3.3.2 Preparation of PAN Vapour Samples**

PAN vapour samples were prepared on the gas handling line. Frozen samples were immersed in dry ice and attached to the line by a Teflon flange interface at V8 (see Figure 3.7). The remaining gas was then evacuated from the volume above the sample in the storage flask and immersed in a thermally insulated Dewar containing liquid nitrogen.

Preparation of pure PAN gas from the dodecane solute was achieved using a freeze-pump thaw method between flasks A and B (see Figure 3.7). The dodecane sample, initially frozen, is warmed slowly to 273 K in a water ice bath, whilst flask B is immersed in a slush bath of Galden 100 cooled to 217 K using dry ice. Galden-100 is a commercially available refrigerant, which is liquid at room temperature and freezes at

213 K. The use of a slush bath at this temperature allows volatile gases to be pumped away whilst leaving PAN frozen in dodecane.

Other slush baths were also investigated including dry ice with acetone, purely liquid nitrogen and purely dry ice. The use of the Galden 100 with dry ice was chosen both for its temperature range (213 to 296 K) and for safety reasons as it is completely innocuous and inert; acetone poses a fire hazard in the event of an explosion; liquid nitrogen could cause the condensation of potentially dangerous liquid oxygen.

Flasks A and B were isolated from the rest of the line for the transfer process. As the dodecane solute in flask A melted, bubbles of gas containing PAN were released from the crystals and frozen out in the colder environment of flask B. Other gases that were present with partial pressures greater than their saturation vapour pressure at the temperature of flask B were also frozen out. Once melting was complete flask A was isolated and immersed again in the slush bath. Both flasks were then vacuum pumped to remove all remaining gases.

Nitrogen broadened experiments were carried out following the same method, except for the addition of dry nitrogen gas to the prepared PAN sample. Pure PAN samples were slowly mixed with dry nitrogen gas to the desired total cell pressure by adding nitrogen to the cell via V6 (see Figure 3.7). Measurements were then recorded after a ten-minute period to allow sufficient mixing of the PAN and nitrogen sample in the cell.

### **3.3.3 Sample Purity**

Accurate spectroscopic measurement of PAN clearly requires purity of sample. This section deals with the methods employed to ensure the best possible purity and discusses the nature of remaining contamination.

The success of the synthesis method in early samples was tested using a low-resolution bench top infrared spectrometer. Such tests aimed to demonstrate the successful production of PAN by identifying the presence of known infrared bands of PAN. This initial characterisation was carried out at the University of Leicester chemistry department.

In these experiments, the isolation of PAN from the solvent was attempted and the gas transferred on a vacuum line to a custom-made infrared gas cell, equipped with calcium fluoride windows. This was inserted into the sample compartment of a Perkin-

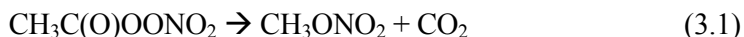
Elmer FTIR spectrometer and transmission spectra were recorded at 2.0 cm<sup>-1</sup> resolution over the 1000 to 3000 cm<sup>-1</sup> range with ten co-added scans.

The presence of PAN was confirmed by the observed strong broadband absorption features characteristic of PAN at 1302 cm<sup>-1</sup> and 1791 cm<sup>-1</sup>.

In addition, a Gas Chromatography-Mass Spectroscopy (GC-MS) analysis of the PAN-dodecane product was performed to test the purity of initial samples. This analysis confirmed the purity of freshly prepared sample (greater than 99%) with the possibility of some water vapour dissolved with PAN in the dodecane solvent.

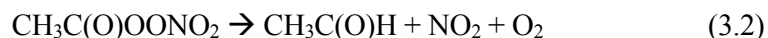
### 3.3.3.1 PAN Decomposition

PAN is not a chemically stable molecule. It is highly reactive and suffers from thermal and photolytic decomposition under ambient laboratory conditions [Von Ahsen and Willner, 2004]. Decomposition by any route introduces impurities into the sample. Such impurities can be produced slowly in storage or more rapidly during purification and gas handling. For example, carbon dioxide is produced in the slow decomposition of PAN during storage by the reaction:



The methyl nitrate product is not frozen out at the temperatures of the slush baths used in this work and is removed in the freeze-pump process. This is not true, however, for CO<sub>2</sub> and in early pure PAN experiments (where the samples used were up to one month old), CO<sub>2</sub> was observed in measured spectra by its spectral influence.

Nitrogen Dioxide was also observed in very small quantities and is produced by the photolysis of the PAN molecule described by Miller *et al.* [1999], thus:



The oxygen product is more volatile than PAN and is not frozen out by the slush bath of flask B and therefore is removed by the freeze-pump process. Conversely, acetaldehyde is significantly less volatile and therefore mostly remains dissolved in dodecane. The NO<sub>2</sub> product, however, is frozen out and cannot be removed easily from the sample. To minimise the concentration of NO<sub>2</sub> impurity, the rate of photolysis was reduced as



much as possible by shrouding the gas handling line with optically thick black cloth to protect the PAN vapour from ultraviolet light emitted by fluorescent lights in the laboratory.

Evidence of spectral absorption features for NO<sub>2</sub> were observed in two spectra used in this thesis. These spectra are later included in the data analysis (see Chapter 4.2) as it was possible to accurately remove spectral absorption due to NO<sub>2</sub> using spectral fitting and subtraction. The maximum amount of NO<sub>2</sub> contaminant found by this method was 0.5% at 1.8 mb. For other samples, no evidence of NO<sub>2</sub> was observed above the baseline noise. Calculation with a line by line model place an upper limit of NO<sub>2</sub> concentration in other “non-contaminated” samples of 0.03%; calculated such that NO<sub>2</sub> absorption at this concentration would not be visible above baseline noise.

### **3.3.3.2 Contamination During PAN Synthesis**

Water vapour was also noted to be present in small quantities because of the unavoidable solution of atmospheric water vapour into the organic phase during synthesis.

The freeze thaw purification process mostly removed water vapour. However, small quantities remained due to the absolute saturation vapour pressure of water vapour over ice at the temperatures used in the experiment. The maximum partial pressure of water vapour expected in any sample is determined by the Marti and Mauersberger [1993] relation:

$$\text{Log}_{10}(P_i) = -2663.5 / T + 12.537 \quad (3.3)$$

where pressure and temperature are in the normal units of Pascal and Kelvin respectively.

Quantities of water vapour calculated using this method indicate that relatively large partial pressures of water vapour are permitted to enter the cell should sufficient quantity exist in the dodecane solvent (e.g. 0.55 mb at 296 K). High concentrations were observed in early measurements (May 2002), but improved drying and leak proofing of the handling system resulted in negligible quantities in the September 2003 measurement period with no detectable trace in measured spectra. Derivations of contaminant concentrations are discussed in Section 4.2.

### 3.3.3.3 Other Sample Contamination

Tests for the possibility of other sample contaminants were also made during March 2003 using the Bruker IFS 66v spectrometer. This spectrometer has a maximum nominal resolution of  $0.12\text{ cm}^{-1}$  and was used here to test for the possibility of spectral signatures from other compounds that may have been dissolved in dodecane during synthesis, as well as dodecane itself.

Dodecane was measured to have a vapour pressure of 0.004 mb at 296 K, confirming values quoted in standard tables [e.g. Lide, 1996]. In any PAN sample measured at room temperature, this partial pressure of dodecane is expected to be present. Therefore a correction to the PAN concentration (determined from measured pressure) is made accordingly by subtracting the dodecane partial pressure from that measured for the sample. At lower temperatures (273 and 250 K), dodecane partial pressure was measured to be 0.003 and 0.001 mb respectively.

Dodecane was found to have a broad and unresolved absorption peak in the  $2550\text{ cm}^{-1}$  spectral region. As this is outside of the region of interest for PAN spectroscopy in the mid-infrared, no spectral interference from dodecane is expected in PAN measurements.

Although spectra of peracetic acid and hydrogen peroxide were recorded separately from standard laboratory reagents, no evidence of such spectral contamination was seen in prepared samples, confirming that both compounds had been successfully removed during the neutralisation step of the synthesis.

## 3.4 General Measurement Procedure

The general procedure for recording spectra was as follows:

- Where appropriate, the sample cell was cooled to the required temperature
- Leak rate tests and thermal equilibrium tests were carried out before measurement. Cell pressure and temperature were monitored throughout.
- Pure PAN samples were prepared by freeze-pump-thawing on the vacuum line whilst physically isolated from the absorption cell.

- An empty cell background spectrum was recorded, at the desired resolution of 0.03 or 0.25  $\text{cm}^{-1}$ , consisting of fifty coadded scans, lasting approximately fifteen minutes and six minutes respectively.
- PAN vapour was then injected into the sample cell and a spectrum recorded at the desired resolution, also using fifty coadded scans.
- The cell was then evacuated and a second empty background spectrum was recorded. The two background spectra were combined and ratioed with the measured spectrum to give a transmission spectrum. The use of two background spectra accounts for any linear temperature drift between the start and end of measurement. Where possible, this second background was used as an initial background for the following sample.
- Leak rate tests and PAN disposal procedures were carried out at the end of each day.

### 3.5 Measurement Parameters

PAN measurements were recorded over two main experimental periods in May 2002 and September 2003 with an additional measurement period in March 2003 allocated to refine measurement procedure and characterise sources of error. A summary of the experiments carried out in each period is given in Table 3.3. The first measurement period was used to develop procedures surrounding spectroscopic measurement and handling of PAN. In addition, three high-resolution ( $0.03 \text{ cm}^{-1}$ ) spectra of pure PAN vapour at room temperature (295 K) were recorded as well as related measurements for possible contaminant gases and calibration purposes. The second PAN measurement period (September 2003) was used to record final temperature dependant and nitrogen-broadened spectra at lower resolution ( $0.25 \text{ cm}^{-1}$ ) to complete a range of suitable measurements.

Cross-sectional data were calculated from multiple spectra for each of the sample conditions listed in Table 3.3. A total of eight spectra were used at room temperature for pure PAN vapour (three at  $0.03 \text{ cm}^{-1}$  and five at  $0.25 \text{ cm}^{-1}$  spectral resolution) over the pressure range 0.15 to 1.74 mb, covering the 550 to  $1400 \text{ cm}^{-1}$  spectral range. To cover the 1400 to  $2200 \text{ cm}^{-1}$  spectral range, a further five spectra were measured at  $0.25 \text{ cm}^{-1}$  resolution, covering the pressure range 0.29 to 1.42 mb. A

further three spectra were recorded at room temperature to investigate possible effects of nitrogen broadening, with gaseous nitrogen pressures added of 200, 300 and 400 mb. At 273 K, five spectra were recorded at 0.25 cm<sup>-1</sup> resolution, covering the 550 to 1400 cm<sup>-1</sup> region for a pressure range of 0.19 to 0.41 mb. A 200 mb pressure of nitrogen was also added for two such measurements.

Date	Temperature / K	Resolution / cm <sup>-1</sup>	Filter	PAN pres. / mb	N <sub>2</sub> pres. /mb
Mar 2002	295	0.03	A	0.31, 0.91, 1.74	-
Sep 2003	295	0.25	X, Y	0.48, 0.88, 0.89, 1.43, 1.72	-
	295	0.25	Z	0.29, 0.56, 0.69, 0.92, 1.42	-
	295	0.25	X	0.88, 1.72	200
	295	0.25	Z	0.56, 0.69	300
	295	0.25	Z	0.56, 0.69	400
Sep 2003	273	0.25	X, Y	0.19, 0.37, 0.38, 0.39, 0.41	-
	273	0.25	X	0.19, 0.41	200
Sep 2003	250	0.25	X, Y	0.34, 0.39, 0.40, 0.41, 0.41	-
	250	0.25	Z	0.48, 1.30	-
	250	0.25	X	0.40, 0.41	200
	250	0.25	Z	0.48, 1.30	200

**Table 3.3** Summary of measurement parameters for PAN spectra recorded at the NERC MSF

At 250 K, five spectra were recorded at 0.25 cm<sup>-1</sup> resolution in the 550 to 1400 cm<sup>-1</sup> spectral range across pressures of 0.34 to 0.41 mb, whilst two were recorded in the 1400 to 2200 cm<sup>-1</sup> region at 0.48 and 1.30 mb. Nitrogen pressures of 200 mb were added to two samples in each spectral range.

### 3.6 Summary

The range of temperature (250 to 296 K) and pressure (0.22 to 2.2 mb) measurements outlined in this chapter meet the requirements for a new spectral reference dataset for atmospheric applications of PAN detection as closely as possible within the limits of experimental apparatus used in this thesis.

This chapter has also laid out the complex and customised experimental procedure required for studying PAN in the laboratory using FTIR spectroscopy; the use of which is necessary for PAN due to its difficult and dangerous nature.

The accuracy of the monitoring of sample state parameters for measured spectra such as pressure and temperature has also been discussed. Assigned temperature accuracies are in the range  $\pm 0.3$  K at 296 K and  $\pm 0.5$  K at 250 K, whilst pressure measurement accuracy is in the range 0.01-0.1 mb.

Sources of sample contamination such as carbon dioxide, water vapour and nitrogen dioxide have also been identified and methods to reduce such contamination by the careful selection of slush bath temperature and synthesis procedure have been explained.

Measurements made using this methodology can now be assessed and a set of absorption cross-sections, integrated band intensities and infrared absorptivities for PAN are calculated and discussed in the following chapter.

# Chapter 4

## 4 Analysis of PAN Laboratory Spectra

This chapter discusses the quality of the infrared spectral data recorded at the MSF using the method described in Chapter 3 and presents the determination of a set of reference cross-sections for PAN applicable to infrared remote sensing of the compound in the atmosphere. These data are then discussed with reference to previously reported literature data for PAN band intensities and band centre absorptivities.

The steps involved in the production of this absorption cross-section dataset are listed below and described in further detail in the remainder of this chapter.

- Assessment of the quality of measured spectral data.
- Assignment of the mean temperatures and pressures for each sample measurement and the determination of associated errors.
- Calculation of transmittance spectra for all measurements.
- Correction for spectral and sample contamination (where required).
- Error assignment for each measurement.
- Calculation of peak absorptivities and integrated PAN band intensities.
- Calculation of cross-sections for each set of temperature and nitrogen-broadened measurements from Beer's law fitting, using all possible measurements
- Tabulation of cross-section data into RFM/HITRAN format for use in this thesis and for use in atmospheric applications by the remote sensing community.

## 4.1 Quality of Spectra

The quality of an FTIR instrument and the stability of measurements are reflected in the quality of the spectral baseline at the 100% and 0% transmittance levels. Thus, in spectral regions where there is no sample absorption, the ratio of a measurement to its corresponding background should yield a transmittance baseline of value unity. Furthermore, in saturated spectral regions where all source radiation is absorbed by the sample, the baseline should exact zero transmittance. The observed nature of the measured baseline can be used to infer the specific source and magnitude of deviations from this ideal case.

Sources of instrument error are manifold. This section discusses only the considerations relevant to this work. For a detailed discussion of all possible FTIR instrument error sources, see Birch and Clark [1995]. Detector non-linearity, thermal and aperture artefacts, phase correction and sampling error are examples of possible instrument-induced error (see Section 2.5.3) that are relevant and discussed in this section.

In addition to instrumental error, the stability of sample concentration and temperature are also reflected in the baseline as noted by Ballard *et al.* [2000]. Potential error due to small changes in these parameters is also discussed in this section.

Small baseline anomalies were observed in some of the spectra measured in this work, principally in those measured for pure PAN vapour at high spectral resolution. The sources of possible error and their magnitudes are now discussed.

### 4.1.1 Detector Non-linearity

Figure 4.1 shows a comparison between transmittance baselines for four spectra measured at high resolution ( $0.03\text{ cm}^{-1}$  without the use of optical filters); and improved baselines for spectra measured with optical and electronic filters. The improved instrument configuration uses a smaller aperture (1.0 mm), an optical filter with a smaller spectral pass band (Filter X, see Chapter 3.2.2) and electronic filters to constrain the measured signal (12 Hz to 2 KHz pass band). These improvements, all aimed at reducing detector non-linearity, confirm that such error is more significant when optical and electronic filters were not used. The effect of such non-linearity is manifest as a net

bias of the baseline (after averaging noise) from the 100% transmittance line (e.g. red trace in upper panel of Figure 4.1).

The observed sample pressure dependence in the magnitude of the deviation from the 100% transmittance level (and therefore increased non-linearity) is explained by a reduction in the intensity of source radiation reaching the detector for higher sample concentrations and hence a more linear detector response.

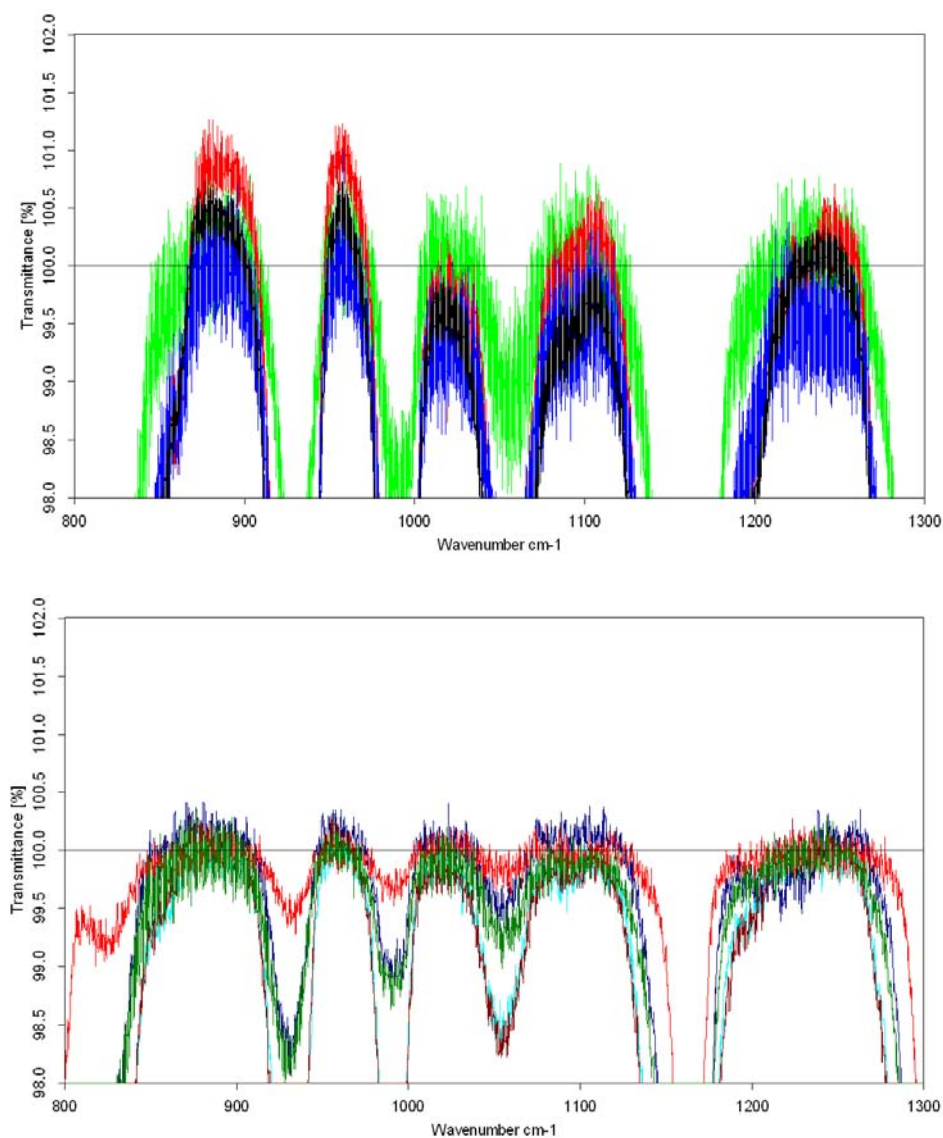


**Figure 4.1.** A Comparison of the 100% transmittance baselines of four spectra recorded with (lower panel) and without optical and electronic filters (top panel) showing the improvement in spectral baseline in using such filters. The baseline is seen here as the region in between the obvious PAN absorption bands.



In order to reliably utilise high-resolution measurements exhibiting detector non-linearity, in the calculation of cross-sectional data, some attempt must be made to correct or account for the observed error. As noted previously, non-linearity correction methods do not work in conjunction with Bruker electronic filters. A simple scaling factor for regions of no apparent spectral absorption was used by Waterfall [2003] to correct for such error. In this thesis, such a method is used only for error estimation. The non-linearity error in this work was calculated to be in the range of 1.5-2% of the total cross-section (at  $1740\text{ cm}^{-1}$ ) for pure PAN, measured at high resolution at room temperature, and zero for all other measurements.

This method of error calculation, by its nature, also accounts for small errors caused by small temperature fluctuations in the cell over the course of the measurement.

It should be stressed that no observable detector non-linearity was observed in measurements made using the optical filter and electronic filter configuration described in Chapter 3.5 and therefore no such cross-sectional error assignment is required for those spectra.

### 4.1.2 Thermal and Aperture Artefacts

The use of a small aperture (1.0 mm) to reduce detector non-linearity is a compromise between the slight inherent degradation in signal to noise and the uncertainty that would result from increased detector non-linearity and off-axis rays in using a larger aperture. For maximum signal to noise, Bruker (the manufacturer of the IFS 120 HR spectrometer) recommend an upper limit of a 4 mm aperture diameter at  $0.03\text{ cm}^{-1}$  spectral resolution and 12.5 mm at  $0.25\text{ cm}^{-1}$  resolution. In using a smaller aperture in this work, the signal to noise remains sufficiently high ( $>500:1$  at  $1741\text{ cm}^{-1}$ ), whilst no evidence of detector non-linearity is observable.

However, the use of a smaller aperture has been noted to increase the effect of the so-called “warm aperture problem” for some FTS instruments discussed by Johns [1987]. However, this effect is not expected for the IFS 120 HR due to the use of cube corner retro-reflectors and a second aperture after the interferometer, meaning that this extra source radiation is not modulated as noted by Johnson *et al.* [2002].

Of potentially greater importance is the potential effect of sample emission described by Ballard *et al.* [1992]. Sample emission for the IFS 120 HR was measured by Waterfall [2003] for the same spectrometer configuration for similar pressures of

acetone vapour as those measured here for PAN. In recording background spectra with the Globar source switched on and off at room temperature, sample emission was found to be negligible (below the baseline noise level of measurements).

### **4.1.3 Phase Errors**

All spectra were recorded as single-sided interferograms (with a short double-sided part) using a Mertz phase-correction provided by standard Bruker software. Phase errors are expected in saturated spectral regions where there is no signal from which to derive the phase. Since no spectra close to saturation ( $>30\%$  transmission) were used in the determination of PAN cross-sections in this thesis under any measurement conditions, no problem with phase determination was expected or observed.

### **4.1.4 Wavenumber Calibration**

The wavenumber calibration of measured spectra was seen to be excellent. This was determined using calibration measurements of carbon dioxide. Since line positions of carbon dioxide are well known, it is possible to measure any potential shift by analysing the difference in measured and known line positions. For pure spectra of carbon dioxide measured at  $0.03\text{ cm}^{-1}$  resolution in this work, no detectable shift was observed using this method, suggesting that any possible wavenumber shift must therefore be smaller than the sample spacing of the measured spectrum ( $0.03\text{ cm}^{-1}$ ).

Furthermore, this calibration was also performed for PAN spectra that were seen to be contaminated with carbon dioxide. By measuring the peak positions of PAN recorded in spectra where measured carbon dioxide lines were not shifted, it was possible to use these peak positions to assess possible wavenumber shift in subsequent spectra of pure PAN using the same PAN bands as reference points. No such shift was detectable in any of the spectra measured in this thesis. Since any wavenumber calibration error is therefore expected to be less than the sampling interval itself ( $0.03\text{ cm}^{-1}$ ), then such a small shift (if present) would have negligible consequence for atmospheric applications at similar spectral resolutions to these measurements.

## 4.2 Quality of Sample

Calculating a cross-section from measured spectra requires an accurate knowledge of the number density of the absorbing gas. Number density is derived from the pressure of the gas in the cell assuming ideal gas behaviour. Where present, the partial pressure of sample contaminants must first be subtracted from the cell pressure (as measured by the Baratron gauges) to give the correct partial pressure of the analyte; in this case, PAN. This section discusses sources of uncertainty in the calculated PAN sample concentration and efforts to correct such effects.

### 4.2.1 Sample Degradation

As noted earlier, PAN suffers from thermal decomposition at room temperature with rapidly decreasing importance at lower temperatures. Simple literature values for this rate constant are not sufficient to calculate additional concentration changes due to other factors such as adsorption or other chemical reaction pathways and such determination requires a more measurement-specific approach.

Sample degradation was determined in this work, by recording a series of successive spectra and a static PAN sample in order to obtain a time-resolved spectral dataset. By examining the change in the strength of PAN absorption bands over the course of such measurements, it is possible to calculate the concentration change and overall rate constant of PAN sample decomposition from the spectra themselves.

Time resolved analyses were made of six measurements each consisting of one hundred co-added scans at a resolution of  $0.25\text{ cm}^{-1}$ . These measurements were made with 1.5 mb of pure PAN vapour present in the cell. In this case, measurements were made without an optical filter in order to record data over the wider spectral range of  $400\text{--}4000\text{ cm}^{-1}$  thus allowing observation of other infrared-active species that may be formed by PAN decomposition. These six measurements required thirty-six minutes to complete, giving a time resolution between measurements of six minutes. By taking a ratio of start and final spectra, it is possible to identify decreases in some spectral features and increases in others. Figure 4.2 shows this spectral ratio.

Figure 4.2 shows an overall constant baseline of very near unity, showing that there is negligible drift in background between the times of the two spectra. The large deviation at  $500\text{ cm}^{-1}$  is due to the rapid decrease in signal to noise at the lower MCT

detector response cut-off. The positive bands (relative to the baseline) in the spectrum are all characteristic of PAN, indicating a small loss over the measurement period. In contrast, the negative spike at  $1600\text{ cm}^{-1}$  is due to an increase in  $\text{NO}_2$ , and other negative features are associated with carbon dioxide.

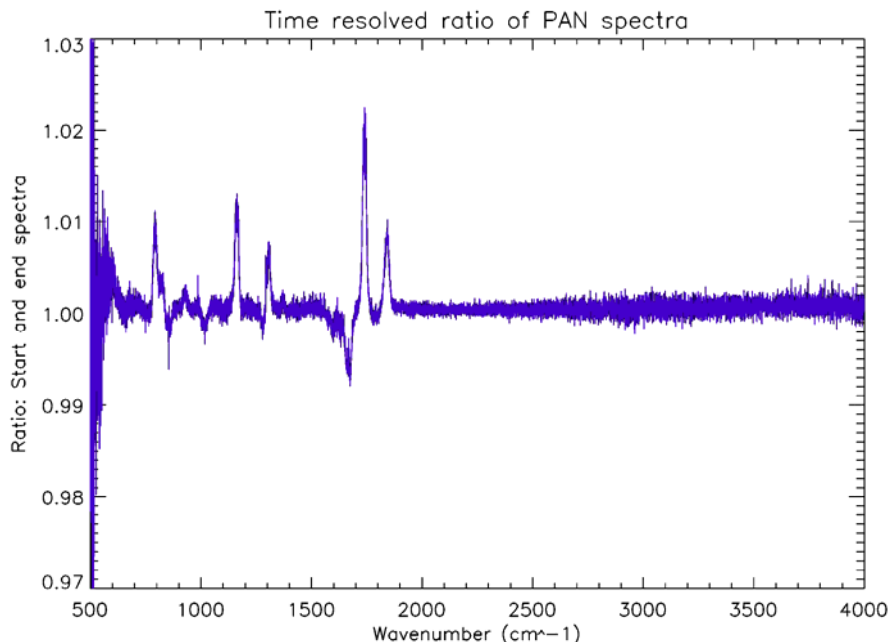
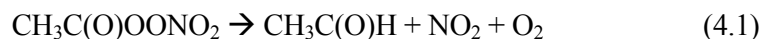


**Figure 4.2** A ratio of initial and final measurements of pure PAN transmission spectra recorded thirty-six minutes apart. Positive-going features are characteristic of compounds that have decreased in concentration over the time of measurement, with negative-going bands denote concentration increases.

Such products are expected from the thermolysis pathway described by the reaction:



Oxygen absorption features are not observed or expected in this spectral region at the concentrations and pressures of these experiments.

By taking a ratio ( $R$ ) of the absorbance  $[\log_{10}(T)]$  at the band centre at the start and end of the measurements, then it is possible to calculate the fractional change and hence the PAN partial pressure decrease ( $\Delta P$ ) using the Beer-Lambert law. Using values from the  $798\text{ cm}^{-1}$ ,  $1165\text{ cm}^{-1}$  and  $1741\text{ cm}^{-1}$  peaks and using the Beer Lambert law gives the fractional change in PAN sample pressure by the equation:

$$R = \frac{P}{\Delta P} \quad (4.2)$$

This method gives a fractional change in PAN concentration of 0.594% over the thirty-six minutes of this measurement, corresponding to an overall decrease of 0.089 mb. This gives an approximation of the total PAN loss rate constant at 295 K under the conditions of this experiment to be:

$$k_{-1, 295K} = 2.75 \times 10^{-6} \text{ s}^{-1} \quad (4.3)$$

This is approximately twice the reported rate ( $1.32 \times 10^{-6} \text{ s}^{-1}$ ) of thermal self-decomposition for PAN calculated by Senum *et al.* [1986] for a pure PAN vapour sample at 3.4 mb and 295 K. Since the rate calculated in Equation 4.3 includes all loss mechanisms in the cell, including adsorption, it is not possible to directly compare this rate constant to previous work. However, assuming the rate constant of Senum [1986] is accurate, it is possible to conclude that around 50% of the PAN lost in the course of a typical measurement is thermolysed to give the products in Equation 4.1. The other half is lost through other processes; the most likely of which is adsorption onto the walls of the cell. Given that most measurements are of the order of six minutes, the very small decrease in PAN pressure (<0.1% of sample) does not require any spectral correction. This small concentration change is, however, included in the error budget assigned to individual samples.

Similar time-resolved measurements at 273 K and 250 K showed no evidence of a change in PAN concentration over a thirty six minute period using this method and therefore no such error was assigned for low temperature measurements.

### 4.2.2 Static Contaminants

Small levels of sample contamination were observed by anomalous infrared absorption in two spectra used in this work, principally those measured in early samples at high resolution and at room temperature. Contaminants seen in these spectra were mostly carbon dioxide and water vapour and attempts were made to reduce their presence by adopting new sample preparation procedures with limited success. These spectra were deemed suitable for the purposes of calculating PAN cross-sections, however, as it was

possible to accurately quantify contaminant concentrations and remove their spectral absorption through a spectral fitting and retrieval method.

Other measurements showed evidence of contamination from acetone, which is thought to have been produced during PAN synthesis. These measurements were not included in the calculation of PAN cross-sections as acetone absorption is not easily removed from measured spectra and subtle interference with the  $1741\text{ cm}^{-1}$  PAN absorption band introduces an otherwise avoidable and significant uncertainty. The importance of acetone contamination is, however, discussed in this section as it may be of relevance to the accuracy of studies reported previously for PAN integrated band intensities and absorptivities.

All observed contaminants and their effect on the quality of the dataset are now reviewed.

#### **4.2.2.1 Contaminant Retrieval Method for $\text{CO}_2$ and $\text{H}_2\text{O}$**

Two spectra showing contamination from carbon dioxide and water vapour were included in this analysis, since it is possible to adequately correct for their presence by removing their infrared spectral features whilst simultaneously correcting for their concentration in the measured cell pressure.

Determining contaminant partial pressures from measured spectra is non-trivial, and requires the use of retrieval techniques similar to those employed in atmospheric remote sensing (see Chapter 2.3). In this work, a spectral fit to the measured data is made using optimal estimation with *Levenberg-Marquardt* convergence as described by Rodgers [2000]. This method combines the advantages of the *Gauss-Newton* and *gradient search* methods, which provide fast convergence from an initial guess close to or far away from some true state respectively. Hence, the Levenberg-Marquardt method allows fast convergence on an optimal solution from any initial guess, through the use of a tuneable parameter that weights the nature of the iteration in favour of either the Gauss-Newton or gradient search method as appropriate; chosen depending on the outcome of minimising some cost function in the preceding iterative step.

In this method, a set of *a priori* parameters,  $\mathbf{x}_a$ , constrained by their variance,  $\mathbf{S}_a$ , are used as an initial guess,  $\mathbf{x}_i$ , to the true state of the system for temperature, total pressure and contaminant partial pressure. Given some measurement,  $\mathbf{y}$ , also

constrained by the variance of associated measurement errors,  $\mathbf{S}_E$ , the Levenberg-Marquardt iterative scheme is described thus as:

$$\mathbf{x}_{i+1} = \mathbf{x}_i + (\mathbf{S}_a^{-1} + \mathbf{K}_i^T \mathbf{S}_E^{-1} \mathbf{K}_i + \gamma \mathbf{S}_a^{-1})^{-1} [\mathbf{K}_i^T \mathbf{S}_E^{-1} (\mathbf{y} - \mathbf{F}(\mathbf{x}_i)) - \mathbf{S}_a^{-1} (\mathbf{x}_i - \mathbf{x}_a)] \quad (2.14)$$

where  $\mathbf{x}_{i+1}$  are the updated state parameters at each step,  $\mathbf{F}(\mathbf{x}_i)$  represents the forward function (or expected relationship) between the state parameter and the measurement; and  $\mathbf{K}_i$  represents the *weighting function*; the differential of the forward function,  $\mathbf{F}(\mathbf{x}_i)$ , with respect to the state vector,  $\mathbf{x}$ . The  $\gamma$  term represents the tunable parameter, allowing the scheme to be weighted in favour of either the Gauss-Newton or gradient search method. A simple method for a suitable selection of  $\gamma$  in each iteration is proposed by Marquardt and discussed by Press, [2001]. In this method,  $\gamma$  is chosen by calculating the difference in a minimised cost function described by a chi square fit thus as:

$$\chi^2 = (\mathbf{y} - \mathbf{F}(\mathbf{x}))^T \mathbf{S}_E^{-1} (\mathbf{y} - \mathbf{F}(\mathbf{x})) + (\mathbf{x} - \mathbf{x}_a)^T \mathbf{S}_a^{-1} (\mathbf{x} - \mathbf{x}_a) \quad (2.13)$$

If the difference in successive chi square values is positive, then gamma is increased and the iteration repeated again with the same guess of the state vector ( $\mathbf{x}_i$ ). If the difference is negative, gamma is decreased and the new estimate of the state vector ( $\mathbf{x}_{i+1}$ ) is used in the next iteration. Hence we see that as the solution converges on the optimal guess of the true state, the iteration becomes more like that in the Gauss-Newton method.

The initial guess of sample pressure and temperature was set to equal the measured sample pressure and temperature and constrained with the absolute error of the measuring devices (see Section 4.3). As the concentration of contaminants is not well known, *a-priori* values for carbon dioxide and water vapour are poorly constrained in order to allow the retrieval process a wide margin. The constraints chosen were a  $2 \times 10^4$  ppmv  $\pm 1000\%$  concentration for water vapour and  $2 \times 10^5$  ppmv  $\pm 300\%$  for carbon dioxide.

The iteration is stopped when the cost function is minimised such that the ratio of successive chi-square values is less than  $1 \times 10^{-5}$  in difference. If this condition is not met, the retrieval is stopped after 100 iterations. A useful addition of this method is that an uncertainty on the retrieved value is provided automatically at convergence.

Forward modelling of absorption spectra was performed using the line-by-line Oxford Reference Forward Model (RFM; further details can be found at <http://www.atm.ox.ac.uk/RFM>) with existing reference spectral data for contaminant gases from the HITRAN 2000 spectral database [Rothman, 2003].

An appropriate spectral fitting window was chosen for contaminant retrieval that contains the most information on the target species. The spectral windows used in the retrieval are shown in Table 4.1.

Species	Window 1 range / $\text{cm}^{-1}$	Window 2 range / $\text{cm}^{-1}$	Window 3 range / $\text{cm}^{-1}$
CO <sub>2</sub>	643-697	2255-2385	3560-3750
H <sub>2</sub> O	1465-1575	1480-1625	

**Table 4.1** Spectral fitting ranges for retrieval of contaminant gas concentrations for carbon dioxide and water vapour in PAN samples from May 2003.

The accuracy of the retrieval of contaminant concentrations is excellent (better than 0.5% relative uncertainty) for two contaminated samples (see Table 4.2), with the same retrievals obtained when performed on independent spectral windows. However, there is a large uncertainty (1.6% and 11.6%) in the other two samples. One of these poorly fitted samples was also observed to suffer from spectral channelling, which is expected to reduce the accuracy of the retrieval method. For these reasons, these two poorly fitted spectra were not included in further quantitative analysis.

The general quality of the fitting and retrieval method for contaminated spectra is reflected by the quality of the spectral fit and corresponding residuals in Figure 4.3. This figure shows an example of the spectral fit and retrieval of contaminant state parameters for carbon dioxide and water vapour in the sample showing the heaviest contamination. This sample was not included in the calculation of the final cross-section as the level of contamination and corresponding retrieval uncertainty was deemed too poor for such a purpose. However, it does demonstrate very nicely, the quality of the fits achieved.

The residual to each spectral fit, shown in the bottom half of each panel in Figure 4.3, shows the excellent spectral fit to the measurement, with only one or two absorption lines remaining poorly fitted for each case. These lines are not evidence of additional contamination and are observed at known line positions for water vapour and



carbon dioxide. Therefore it is expected that the line parameters reported for these poorly fitted lines are likely to be in error in the HITRAN 2000 database. Much work continues in assigning the most accurate line parameters for water vapour in this spectral region, with further modifications made in the updated HITRAN 2004 database [Rothman *et al.*, 2004], although this update was not available at the time of analysis.

Sample	Measured pressure /mb	Retrieved CO <sub>2</sub> /ppmv	Retrieved H <sub>2</sub> O vapour / ppmv	Corrected PAN pressure /mb
1	1.178	$1.619 \times 10^5$	$5.712 \times 10^4$	$0.920 \pm 0.005$
2	0.298	$2.785 \times 10^4$	$1.167 \times 10^4$	$0.286 \pm 0.001$
3*	2.583	$5.674 \times 10^5$	$3.629 \times 10^3$	$1.108 \pm 0.018$
4*	1.980	$4.001 \times 10^5$	$7.836 \times 10^4$	$1.033 \pm 0.115$

**Table 4.2** Retrieved contaminant partial pressures and corrected PAN sample pressures for measurements exhibiting contamination from carbon dioxide and water vapour. Quoted error represents the 1-sigma uncertainty obtained at retrieval convergence. \*Not included in further analysis due to high retrieval uncertainty.

The retrieved contaminant concentrations (partial pressures) were then subtracted from the original measured pressures to obtain the correct PAN sample pressure whilst the spectral fit for the contaminant could also be subtracted from the measured spectrum to obtain the pure PAN spectrum.

No such retrieval or correction was performed on measurements with no obvious observable contamination, although an upper limit on the concentration of chemically produced contaminants was calculated by performing a simulation of the concentration required to observe spectral absorption by contaminants above a typical noise level. Limits for carbon dioxide and water vapour found in this way were  $2.5 \times 10^{-4}$  mb and  $4.2 \times 10^{-4}$  mb respectively (or 0.067% of total sample at 1 mb total pressure). This is included in the error analysis for individual samples.

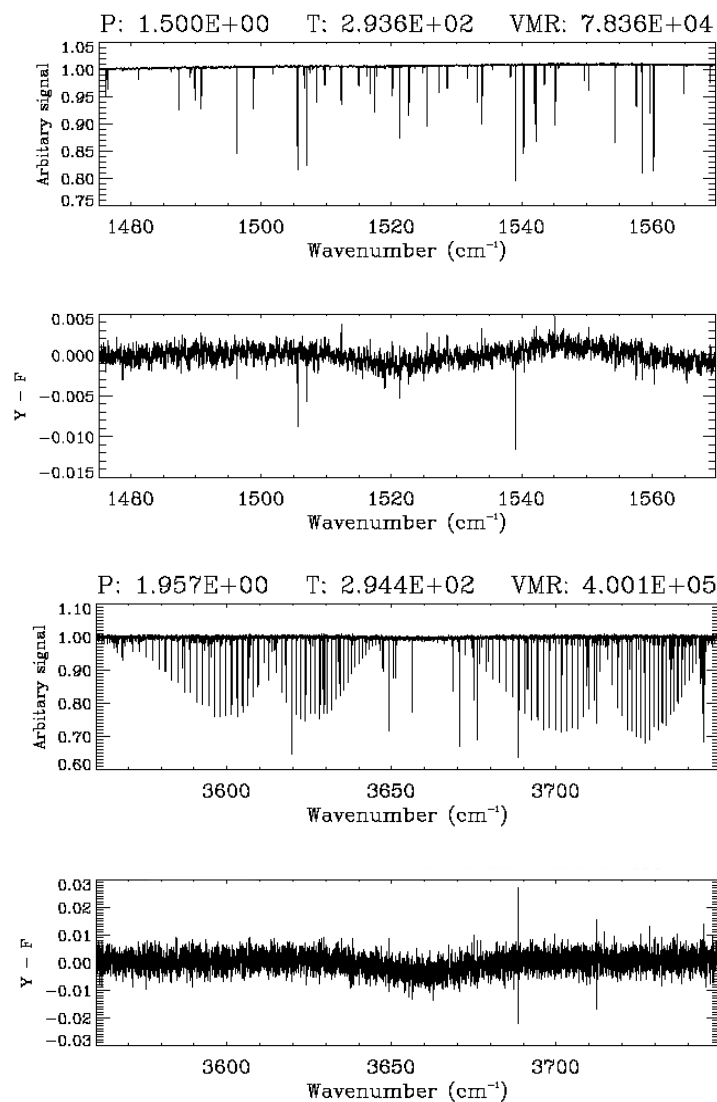


**Figure 4.3** Spectral fits and residuals for H<sub>2</sub>O (top) and CO<sub>2</sub> (bottom) for a contaminated sample. The retrieved sample pressure (mb), temperature (K) and contaminant concentration (ppmv) are also shown. The top half of each panel shows the spectral fit in the relevant retrieval window, whilst the lower half shows the spectral residual after spectral fitting and subtraction of the relevant contaminant.

#### 4.2.2.2 Acetone Contamination

As noted in the previous section, evidence of acetone contamination was seen in some measurements of pure PAN vapour at room temperature. Although these measurements were not included in the calculation of cross-sections, they are discussed in this section as they are believed to be relevant in the comparison with previously reported data for PAN, which may have suffered from acetone contamination.

Figure 4.4 shows evidence of acetone [ $\text{CH}_3\text{C}(\text{O})\text{CH}_3$ ] contamination in one such spectrum recorded at room temperature. The red trace in Figure 4.4a shows a clean pure PAN spectrum whilst the blue trace shows another contaminated with acetone vapour. The contaminated (blue) spectrum was normalised to match the absorbance of the  $1841\text{ cm}^{-1}$  PAN band, which is known not to suffer from acetone interference. This normalisation ensures that an equivalent sample concentration of PAN is represented in both spectra. The difference in the absorption of the  $1740\text{ cm}^{-1}$  band illustrates contamination with the additional absorption in the blue spectrum (relative to the red plot) being due to the acetone contaminant. In taking the difference of the two spectra in Figure 4.4a, we obtain the residual spectrum in Figure 4.4b, which fits well with a simulated pure acetone spectrum of 1.65 mb in the cell.

It is not possible to perform a similar optimal estimation of acetone concentration, such as that performed for  $\text{CO}_2$  and  $\text{H}_2\text{O}$ , as the acetone absorption feature is nowhere independent of PAN and would require simultaneous fitting of both acetone and PAN, which increases uncertainty. Although it may be possible to perform a spectral fit, by scaling to this acetone residual feature such correction was not performed as any uncertainty would greatly affect the calculated band intensity of the  $1741\text{ cm}^{-1}$  PAN band.

Although Figure 4.4 shows contamination in the spectral window of the Y optical filter, acetone contamination was also observed in the range studied using the X filter. Figure 4.5 shows the simulated absorption spectrum of acetone in the region of the X filter, using the fitted concentration to the residual acetone feature in Figure 4.4b. A contaminated spectrum in the X-filter region would resemble the black (pure PAN) trace plus the acetone (blue) trace. Such acetone contamination of this spectral region was observed in some spectra, which were again discarded due to the overlap of the  $1220\text{ cm}^{-1}$  and  $1370\text{ cm}^{-1}$  acetone band with the  $1163\text{ cm}^{-1}$  and  $1302\text{ cm}^{-1}$  PAN absorption bands respectively.

The origin of acetone contamination in some samples remains uncertain. Two pathways were identified for its presence in the sample cell. One such pathway may be that acetone was produced during synthesis by reduction of peracetic acid. Another possibility is the chemical reaction of PAN with other compounds in the liquid or gas phase of prepared samples. Interestingly, acetone was observed in vapour samples prepared from only two PAN-dodecane solute samples, indicating that the former

(production of acetone in synthesis) may be more probable. One would have expected contamination of more samples if the latter chemical process were true.

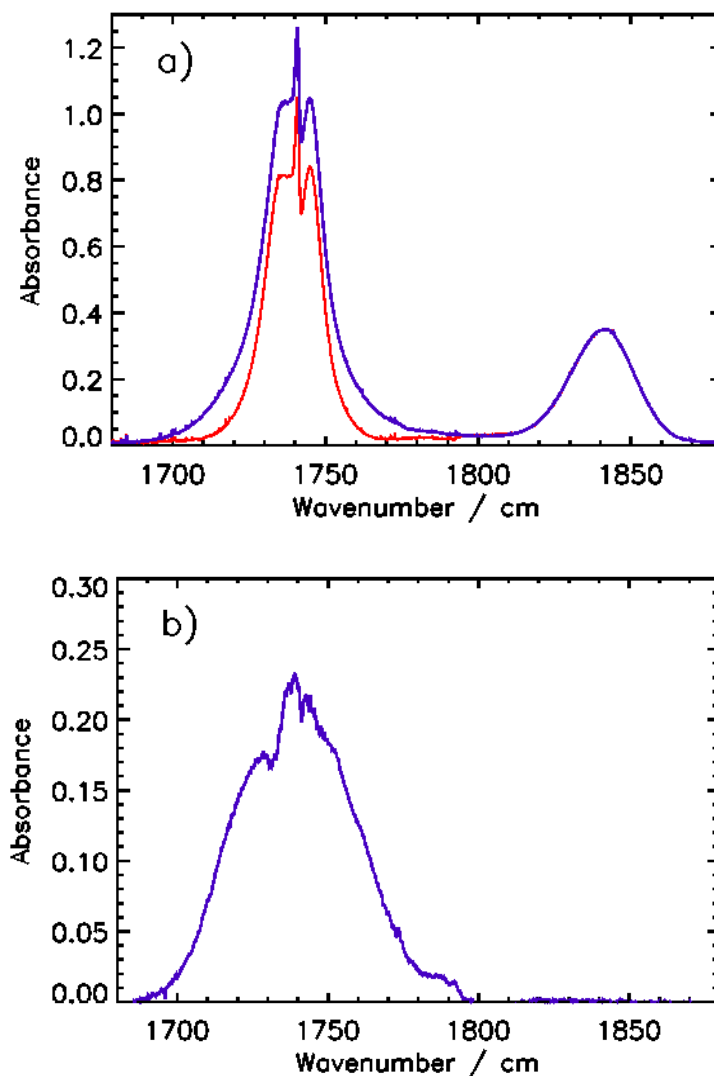


**Figure 4.4** A comparison of a pure PAN spectrum with another showing acetone contamination of the  $1740\text{ cm}^{-1}$  PAN band. a) The red line shows a clean PAN spectrum whilst the blue line shows a contaminated spectrum scaled to match the absorbance of the  $1841\text{ cm}^{-1}$  PAN band, showing evidence of contamination in the  $1741\text{ cm}^{-1}$  PAN band. b) The residual of the two spectra in a), showing the characteristic  $1740\text{ cm}^{-1}$  absorption band of acetone.

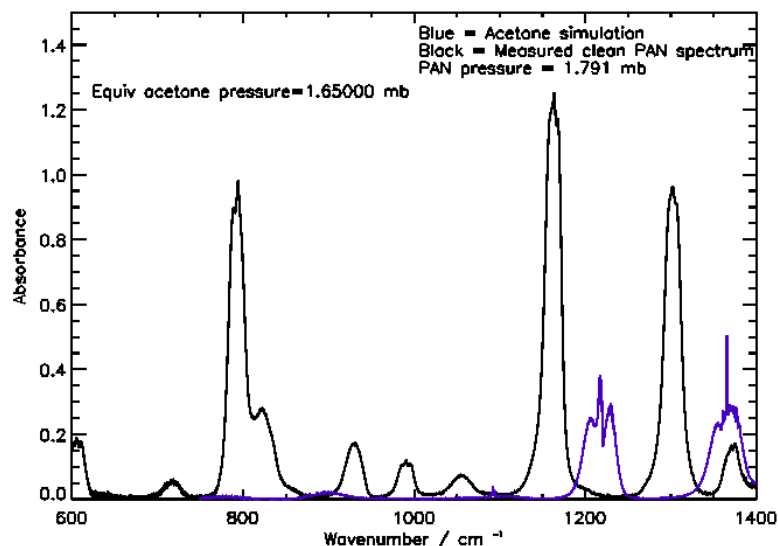


**Figure 4.5** An illustration of how acetone contamination (blue) would affect an otherwise pure PAN spectrum (black) in the spectral window studied using the X optical filter.

Acetone, and the subtleties of its presence due to it underlying the absorption bands of PAN, may be a cause of considerable uncertainty between previous independently reported data for PAN band intensities, especially for the  $1740\text{ cm}^{-1}$  band (c.f. Section 4.5.2). As contaminated spectra are discarded from cross-sectional work in this thesis, no such error is believed to affect the quality of the results reported herein.

### 4.3 Summary of Errors

A summary of the range of all errors identified and assigned to individual PAN spectra discussed in Chapter 4.1 and summarised in Table 4.3. The range of errors reflects the whole pressure and temperature range studied. Errors have been separated into their correspondent uncertainty in calculated PAN sample pressure and derived spectral absorbance.

The highest assigned errors are seen to be at the highest sample pressures and for 295 K measurements, where uncertainty due to contaminants and PAN decomposition are expected to be largest.

In summary, typical pressure uncertainties are around 5% with extremes of 2.2 and 10.2% (for one sample), whilst derived relative uncertainty in absorbance values range from 0.1-1.3% at the nominal band centres of the five strongest PAN bands.

Error Source	Sample pressure uncertainty /mb	Radiometric uncertainty (converted to absorbance units)
Cell leak	0.006 – 0.03	-
PAN adsorption in cell	0.010 – 0.035	-
PAN decomposition	0.005 – 0.02	-
Temperature drift	0.000 - 0.001	0.000 - 0.001
Pressure gauge uncertainty	0.010 – 0.150*	-
Sample contamination	0.001 – 0.100*	-
Instrumental noise	-	0.000 - 0.001
Detector non-linearity		0.000 - 0.020
Cell path-length knowledge uncertainty		+/- 0.004

**Table 4.3** Source and magnitude of typical errors assigned to measurements made in this study. The range in uncertainty reflects the range of error assigned for different samples.

\*For the highest PAN sample pressures (2.2 mb) at 295 K.

## 4.4 Data Analysis of Measured Spectra

Cross-sections are calculated from as many individual measurements as possible so as to reduce the uncertainty that may be present in any one sample. Between five and eight measurements were used from each spectral window allowed by the optical filters used after measured spectra were filtered for contamination (see Section 3.5)

Raw measurements were first converted to transmittance spectra by ratioing each sample spectrum with a corresponding evacuated cell background spectra described by Equation 4.6 below. This background was derived from the average of two background spectra recorded immediately before and after each sample measurement in order to minimise errors from any background drift due to source intensity or temperature.

In order to calculate absorption cross-sections, it is first necessary to know the concentration (number density),  $n$ , of PAN molecules in the sample. This is calculated assuming ideal gas behaviour from the equation of state:

$$P = N_A n R T \quad (4.6)$$

where  $P$  represents the corrected pressure of the sample (measured pressure corrected for contaminants and PAN thermolysis).  $N_A$  denotes Avogadro's number and  $T$  is the average of the cell temperature, determined from data recorded at the time of measurement (see Chapter 3.2.3).

Calculation of the absorption cross-section ( $\text{cm}^2 \text{ molecule}^{-1}$ ) as a function of wavenumber for a specified temperature is then possible by the Beer-Lambert law:

$$I(\tilde{\nu}, T) = I_0(\tilde{\nu}, T) e^{-n \sigma(\tilde{\nu}, T) x} \quad (4.7)$$

where  $I(\tilde{\nu}, T)$  is the signal intensity sample spectrum at the detector as a function of wavenumber,  $\tilde{\nu} (\text{cm}^{-1})$ , and temperature,  $T$  (K). The  $I_0(\tilde{\nu}, T)$  term represents the background signal intensity spectrum, whilst  $n$  is the number density ( $\text{molecules cm}^{-3}$ ) of the absorbing gas and  $\sigma(\tilde{\nu}, T)$  is the absorption cross-section. Also,  $x$  is the absorption pathlength (cm). The ratio  $\frac{I(\tilde{\nu}, T)}{I_0(\tilde{\nu}, T)}$  defines the transmission spectrum,  $T(\tilde{\nu}, T)$ .

#### 4.4.1 PAN Infrared Absorptivities

If the Beer-Lambert law is obeyed, a linear relationship is expected between the absorbance (equal to  $-\ln[T(\tilde{\nu}, T)]$ ) and the absorber amount (concentration  $\times$  pathlength; or pressure) at any given wavenumber. The slope of Beer's law fits calculated in this way can be used to determine the infrared absorptivities of peak absorbance for each of the major PAN bands.

Such linearity of Beer's law was indeed seen, as illustrated in Figure 4.6, which shows an error weighted least squares linear regression fit (forced to fit the origin) to data derived for the five strongest PAN absorption bands for each temperature studied. Such weighting takes account of varying errors between samples [Press *et al.*, 2001]. This error weighting method is chosen in preference to the method of using a

transmittance weighting, which would be an important consideration in bands that approach saturation. Chu *et al.* [1999] note that absorption bands with an optical density greater than 0.5 (corresponding to less than 31% transmission) begin to show significant deviations from Beer's law linearity. Since no PAN absorption band in the mid-infrared was observed to absorb radiation at greater than 30% in any measurement in this study, such deviation from linearity is not expected and consequently no other weighting method is required.

The linearity of the fit is seen to be best for the 295 K data ( $R^2$  goodness of fit of 0.97 at 1302  $\text{cm}^{-1}$ ) and less well, although by no means poorly, correlated at 250 K ( $R^2$  of 0.78 at 1740  $\text{cm}^{-1}$ ). The fitting statistics for each of the plots in Figure 4.6 are given in Table 4.4. The nature of this correlation is expected as more measurements were made at room temperature over a wider pressure range, whilst low temperature measurements were limited by the smaller saturation vapour pressure of PAN samples allowed at such temperatures (PAN vapour pressure = 1.41 mb at 250 K).

Sharpe *et al.* [2001] note that the residual to fits calculated in this way contains information about sample impurities as the deviation vector shows signatures that do not scale with sample pressure. No significant residual exists for fits to the 794, 1163 or 1302  $\text{cm}^{-1}$  bands although there may be evidence of a shift in the data at room temperature for the 1741 and 1842  $\text{cm}^{-1}$  bands; however, the significance of such curvature cannot be addressed given the error bars.

The slope of Beer's law fits for each band was used to determine the infrared peak absorptivities for pure PAN at the nominal band centre for each of the bands listed in Table 4.4. The errors quoted in the table define the two standard deviation (95% confidence level) uncertainty calculated from fit statistics for the error-weighted least squares fit to data for each of the nine major PAN band centres.



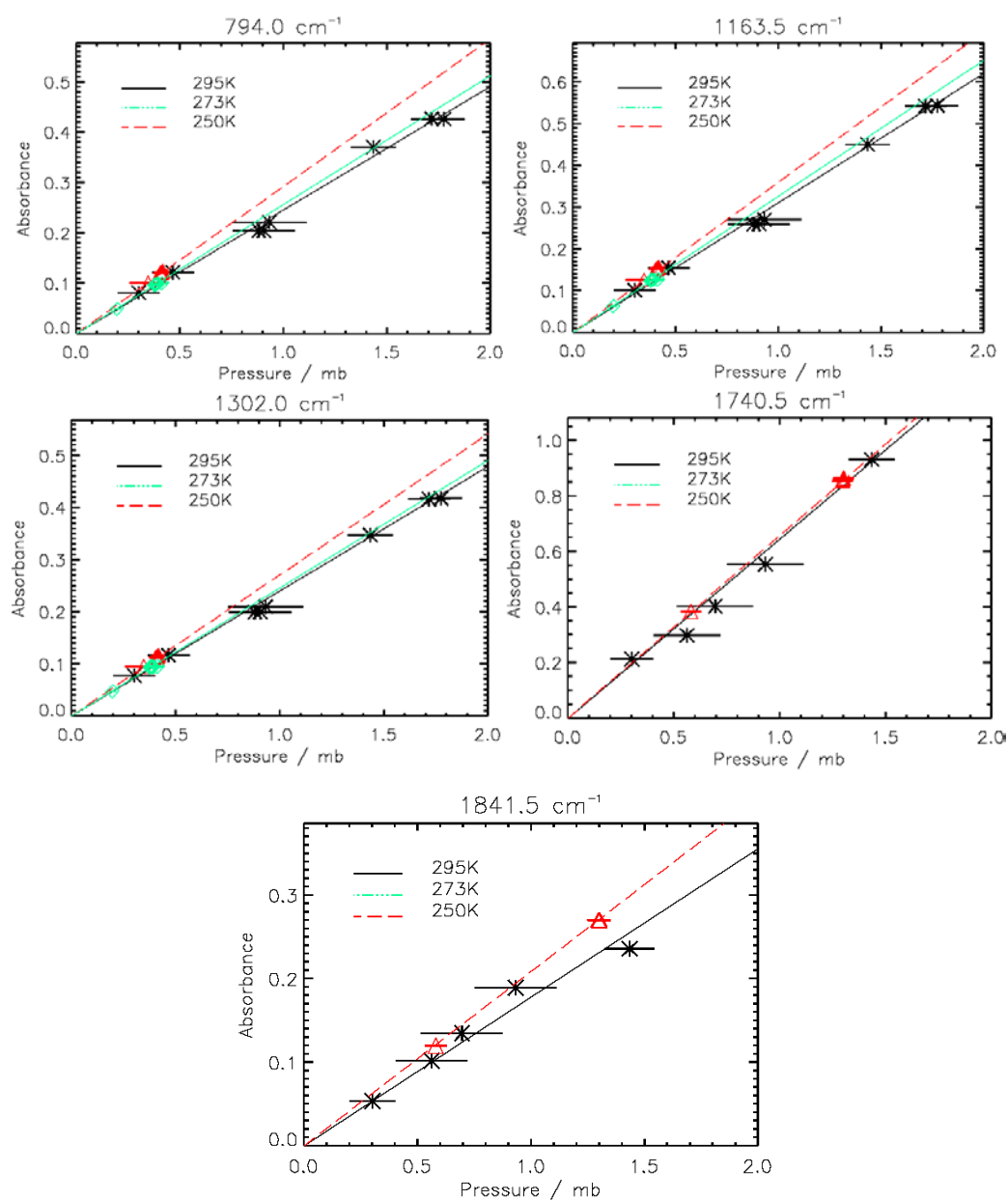


**Figure 4.6.** Infrared absorbance for the five strongest PAN absorption bands taken at the nominal band centre as a function of sample pressure at 295, 273 and 250 K. Plotted error bars represent the assigned error for each sample, calculated as the sum of all error contributions for each sample. Individual measurements are represented by: stars (295 K); diamonds (273 K) and triangles (250 K).

Band centre position /cm <sup>-1</sup>	Peak Infrared Absorptivity	X <sup>2</sup> Statistics
794	11.4 ± 0.8	0.57
1163	14.6 ± 1.0	0.60
1302	11.4 ± 0.8	0.43
1741	30.2 ± 3.0	0.67
1842	9.50 ± 1.2	0.48
606	1.55 ± 0.12	0.56
930	1.46 ± 0.12	0.62
991	1.03 ± 0.08	0.61
1055	0.62 ± 0.06	0.48

**Table 4.4** Infrared absorptivities for PAN vapour (10<sup>-1</sup> ppm<sup>-1</sup> m<sup>-1</sup>, natural logarithm, to 3 s.f. Values refer to 1013.25 mb), calculated for nine principal PAN bands at 295 K Errors quoted correspond to the two-sigma uncertainty (95% confidence level) of a weighted least squares fit to Beer's Law for each band. The chi-square fit statistics of the Beer's law fits used to calculate absorptivities are also shown.

#### 4.4.2 Reference Absorption Cross-sections

Reference cross-sections for PAN are also calculated from the slope of such Beer's law fits, determined at each spectral point. The wavenumber range of final cross-sections was reduced to 550-2200 cm<sup>-1</sup> to remove regions outside this range where there is little or no signal due to detector and optical filter limitations. These cross-sections are plotted in Figure 4.7.

At 291 K, eight spectra measured between 550 and 1450 cm<sup>-1</sup> and five between 1450 and 2200 cm<sup>-1</sup> were used to calculate the final cross-section. At 250 K, five samples were used in each spectral range, whilst six samples were used in the 550-1450 cm<sup>-1</sup> range at 273 K.

The peak cross-section determined for each of the nine major PAN absorption bands at all temperatures studied is also given in Table 4.5 together with a two standard deviation (95% confidence level) uncertainty calculated from error weighted least square fits at the nominal band centre. Cross-sectional data for the 1741 and 1842 cm<sup>-1</sup> bands at 273 K is absent as no measurements of the 1600-2200 cm<sup>-1</sup> spectral region could be made at this temperature due to the limited availability of measurement time at the MSF.

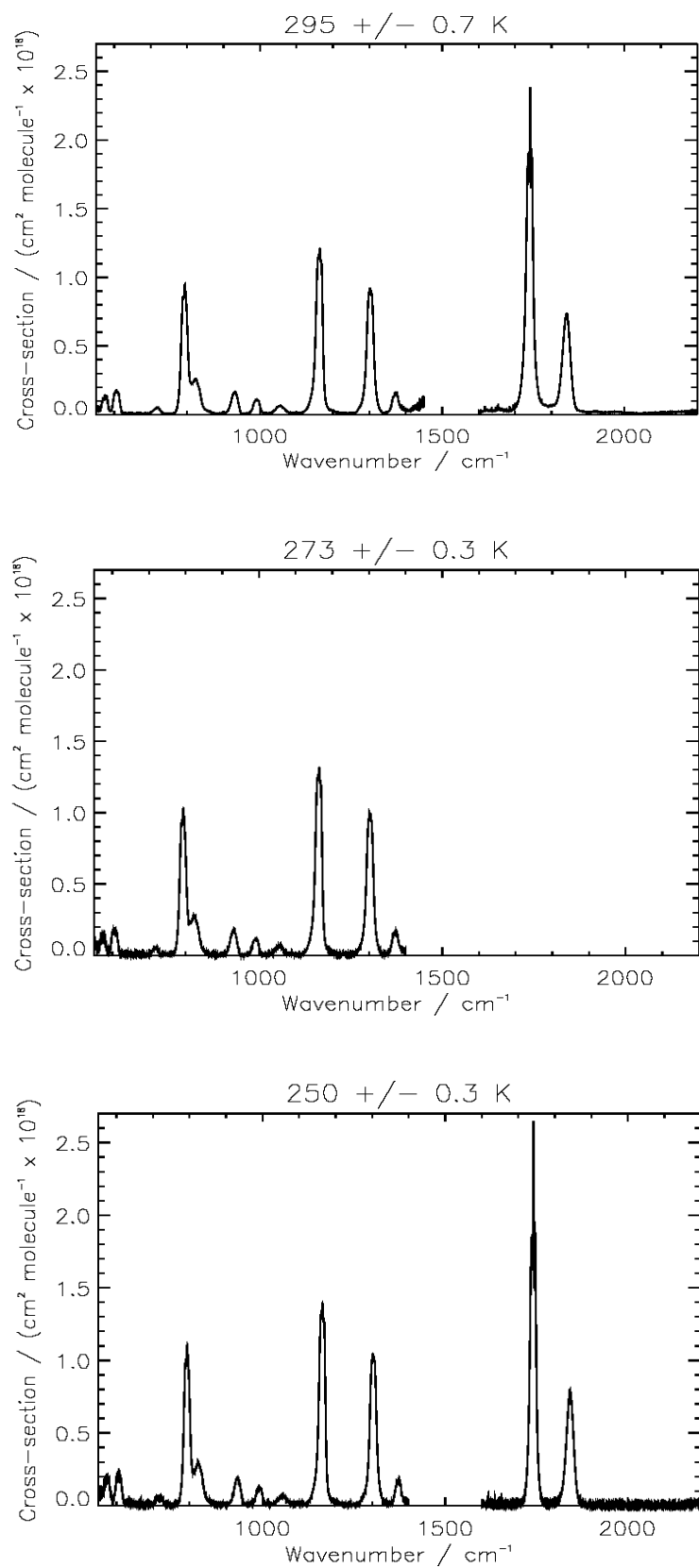


**Figure 4.7** PAN mid-infrared (550-2200  $\text{cm}^{-1}$ ) absorption cross-sections (0.25  $\text{cm}^{-1}$  resolution) at sample temperatures of a)  $295 \pm 0.7 \text{ K}$ , b)  $273 \text{ K}$ , and, c)  $250 \pm 0.3 \text{ K}$

Band centre position /cm <sup>-1</sup>	Peak cross-section / ( $\times 10^{18}$ cm <sup>2</sup> molecule <sup>-1</sup> )		
	295 K	273 K	250 K
794	0.95 $\pm$ 0.02	1.10 $\pm$ 0.07	1.12 $\pm$ 0.07
1163	1.21 $\pm$ 0.03	1.32 $\pm$ 0.08	1.39 $\pm$ 0.08
1302	0.92 $\pm$ 0.02	1.02 $\pm$ 0.06	1.05 $\pm$ 0.06
1741	2.39 $\pm$ 0.06	-	2.68 $\pm$ 0.13
1842	0.74 $\pm$ 0.03	-	0.79 $\pm$ 0.06
606	0.18 $\pm$ 0.02	0.21 $\pm$ 0.04	0.22 $\pm$ 0.04
930	0.17 $\pm$ 0.01	0.20 $\pm$ 0.03	0.21 $\pm$ 0.03
991	0.10 $\pm$ 0.01	0.12 $\pm$ 0.02	0.13 $\pm$ 0.02
1055	0.08 $\pm$ 0.01	0.09 $\pm$ 0.02	0.10 $\pm$ 0.02

**Table 4.5** Peak cross-section ( $\times 10^{18}$  cm<sup>2</sup> molecule<sup>-1</sup>) at 295, 273 and 250 K for nine strongest PAN absorption bands in the mid-infrared. Errors shown represent the two-sigma uncertainty calculated from a Beer's law fit at the nominal band centre.

In comparing the peak cross-sections calculated at each of the nine PAN band centres in Table 4.5 as a function of temperature, there is a clear systematic increase in cross-section with decreasing temperature for all bands. The increase between 294 and 250 K ranges from 17-25% for the 794.0 cm<sup>-1</sup> and 1055 cm<sup>-1</sup> bands respectively. This is also reflected in the increasing gradient with temperature of the Beer's law fits in Figure 4.6.

There is also evidence of some change in the structure of the 1163, 794 and 1742 cm<sup>-1</sup> bands with the increased definition of a likely Q-branch of the 1741 cm<sup>-1</sup> band with decreasing temperature. This can be seen in Figure 4.8, which shows a closer look at these bands. The full width at half maximum of the Q-branch of the 1741 cm<sup>-1</sup> band was measured to be 1.40 cm<sup>-1</sup> at 295 K and 1.11 cm<sup>-1</sup> at 250 K, with both peaks observed at 1740.80 cm<sup>-1</sup>. The behaviour of this sharp spectral feature of PAN may be of interest in infrared remote sensing of PAN in this spectral region.

For the 794 cm<sup>-1</sup> and 1163 cm<sup>-1</sup> PAN bands, used later in this thesis, the change in the intensity of these bands, requires that the relevant cross-section be used in the inversion of atmospheric data; corresponding to the ambient temperature of the atmospheric region of interest. For the upper troposphere, the most appropriate choice of reference cross-section is that derived at 250 K and this is used in the detection of PAN in the following chapter.

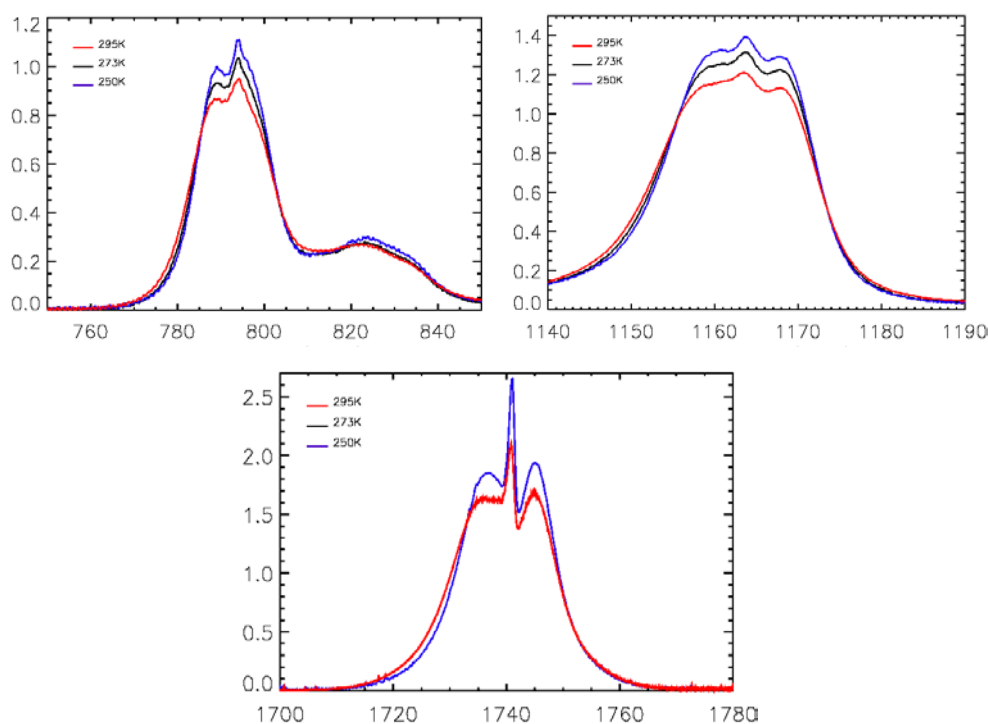


**Figure 4.8** A close-up of the a) 794, b) 1163 and c) 1741  $\text{cm}^{-1}$  PAN cross-sectional bands showing temperature dependence at 295 K (red), 273 K (black) and 250 K (blue). Note: y-axis refers to absorbance units.

#### 4.4.2.1 Nitrogen Broadening

In addition to the measurement of pure PAN spectra, measurements were also recorded with varying pressures of dry nitrogen gas added to the cell to test for the possible effect of nitrogen-broadening on PAN absorption bands. With pressures of up to 400 mb of nitrogen gas added to a PAN partial pressure of 1.0 mb, no observable broadening effect was observed for any of the PAN absorption bands.

Figure 4.9 shows a close-up of the 794 and 1741  $\text{cm}^{-1}$  PAN cross-sectional bands both with and without nitrogen added to the cell. Apart from a small amount of water vapour contamination (due to impurities in the nitrogen gas used) seen in the 1720  $\text{cm}^{-1}$  region (seen as sharp absorption lines), there is no significant difference (less than  $0.03 \text{ cm}^2 \text{ molecule}^{-1}$ ) in the nature of either band, nor any effect on the Q-branch of the 1740  $\text{cm}^{-1}$  band which was seen earlier to have a temperature dependence. No difference in the calculated peak cross-section was seen, meaning that the cross-sections

calculated for pure PAN are equally valid as reference data for conditions where PAN is present in trace quantities in nitrogen or air.

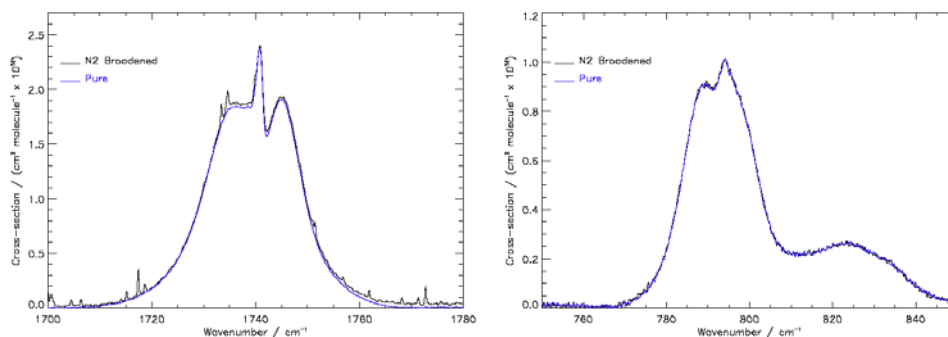


**Figure 4.9** Comparison of cross-sections determined for pure PAN (blue) and PAN+400 mb dry nitrogen gas (black) at 295 K for the a) 1741  $\text{cm}^{-1}$  and b) 794  $\text{cm}^{-1}$  PAN absorption bands.

### 4.4.3 Integrated PAN Band Intensities

The integrated intensity of the nine major PAN bands can also be calculated from the slope of fits made between PAN sample pressure and the integrated area of each absorption band calculated over a spectral range which encompasses the nominal band. This quantity, in principle, is not subject to resolution effects as the bandwidth considered is suitably large relative to the spectral resolution so long as there is no spectral saturation and no resolvable line structure present. Integrated band intensities, unlike peak absorptivities, are therefore a useful tool for comparing independent datasets recorded at differing spectral resolutions.

The integration ranges used for the purpose of calculating integrated band area for the nine principal PAN bands are listed in Table 4.6. In calculating integrated band areas it is important to account for any baseline offset that would otherwise positively bias the result. Since the baseline was seen to be effectively equal to zero in all measurements recorded for the purposes of this study, no such correction was required.

Figure 4.10 shows the integrated band area as a function of PAN pressure and temperature for the five strongest PAN bands. Again, between five and eight samples were recorded for each spectral range with five used for the 550-1400  $\text{cm}^{-1}$  and eight in the 1600-2200  $\text{cm}^{-1}$  region. It should be noted that six 250 K samples at similar

pressures are in fact represented in Figure 4.10 for the 1741 and 1842  $\text{cm}^{-1}$  bands, despite the overlap of plotting symbols.

Band centre position / $\text{cm}^{-1}$	Integration range / $\text{cm}^{-1}$
606	585.0-652.0
794	767.4-810.2
930	900.1-956.0
991	967.5-1008.1
1055	1035.0-1075.1
1163	1115.3-1210.2
1302	1260.7-1333.0
1740	1685.8-1780.0
1842	1802.0-1875.3

**Table 4.6** Spectral ranges used to calculate integrated band areas for the nine PAN absorption bands studied.

An increase in absorption in all but the 1302  $\text{cm}^{-1}$  band is seen with decreasing temperature, similar to that observed for peak absorptivities calculated in the previous section. The 1302  $\text{cm}^{-1}$  band shows a marginally smaller gradient at 250 K than at 273 K, although the two are consistent within the calculated two standard deviation uncertainty (see Table 4.7) associated with the line fits.

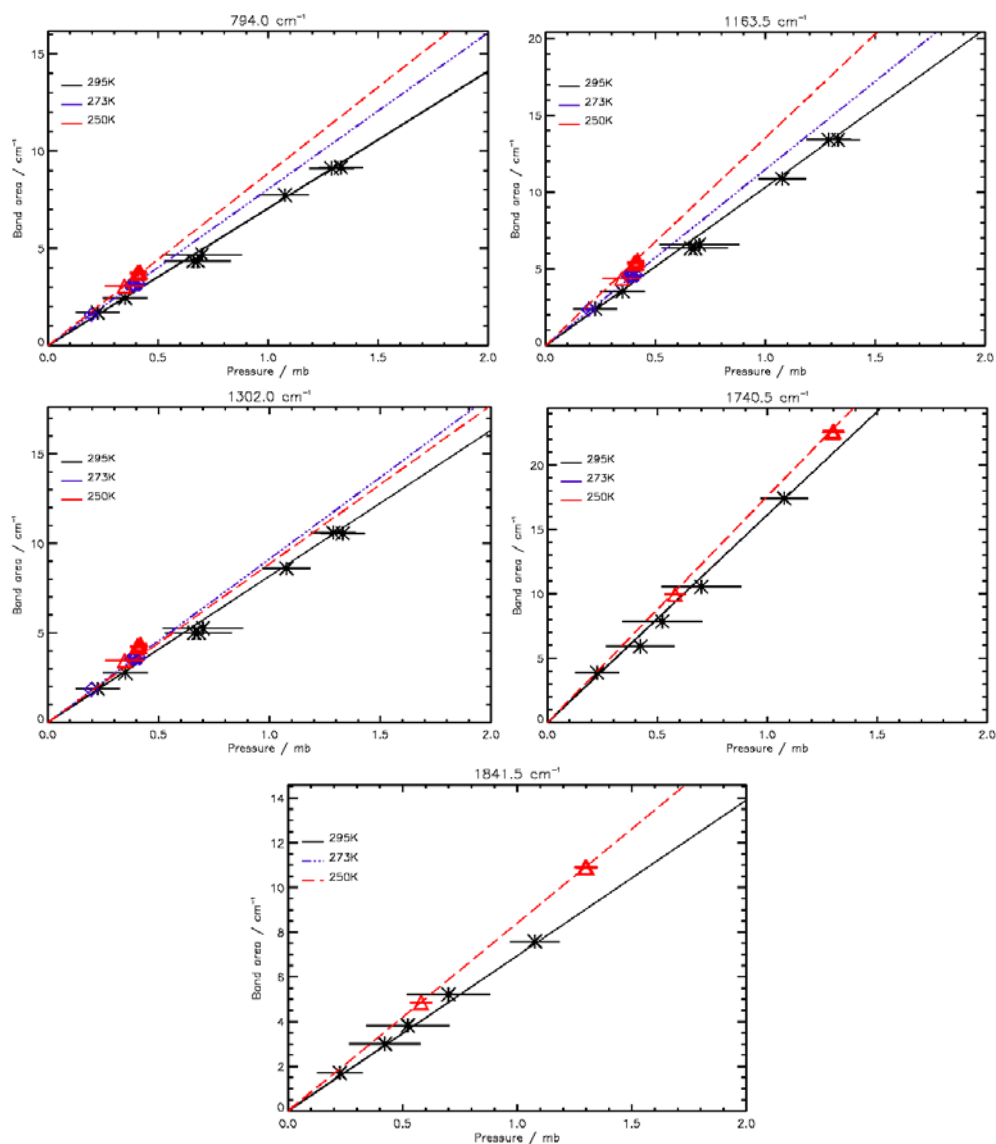


**Figure 4.10** Integrated band areas as a function of PAN pressure and temperature for each of the five strongest PAN absorption bands. Plotted errors represent the assigned error for each sample, calculated as the sum of all error contributions in each sample.



The slope of the error-weighted least squares fit to the data for each band is used to calculate the integrated band intensities ( $\text{atm}^{-1}\text{cm}^{-2}$ ) given in Table 4.7.

Band centre / $\text{cm}^{-1}$	Integrated band intensity / $\text{atm}^{-1}\text{cm}^{-2}$		
	250 K	273 K	295 K
606	39.0 $\pm$ 3.0	35.9 $\pm$ 2.6	34.2 $\pm$ 1.4
794	272 $\pm$ 11	252 $\pm$ 9	241 $\pm$ 6
930	36.2 $\pm$ 2.9	34.1 $\pm$ 2.5	32.2 $\pm$ 1.2
991	23.4 $\pm$ 2.1	21.5 $\pm$ 1.6	20.1 $\pm$ 0.8
1055	18.4 $\pm$ 1.4	16.9 $\pm$ 1.0	16.0 $\pm$ 0.8
1163	401 $\pm$ 20	370 $\pm$ 17	356 $\pm$ 8
1302	313 $\pm$ 16	315 $\pm$ 13	281 $\pm$ 6
1741	567 $\pm$ 9	-	537 $\pm$ 10
1842	289 $\pm$ 4	-	260 $\pm$ 6

**Table 4.7** Infrared integrated intensities ( $\text{atm}^{-1}\text{cm}^{-2}$  to 3.s.f) of nine PAN bands (Units refer to 1013.25 mb at ambient temperature 295, 273 and 250 K). Errors quoted represent a two standard deviation calculated from regression fits.

The largest errors quoted in Table 4.7 are seen for low temperature measurements of the 550-1400  $\text{cm}^{-1}$  region. This error reflects the limited range of pressures studied in this spectral region and hence the inherent uncertainty in extrapolating to integrated intensities at one atmosphere equivalent pressure of PAN. The measurement of only five samples (at 250 K for the 794, 1163 and 1302  $\text{cm}^{-1}$  bands) at less than 0.4 mb pressure, increases the corresponding uncertainty of the derived gradient. This uncertainty would be reduced with a greater number of measurements. However, the maximum 2-sigma uncertainty (95% confidence) corresponds to only a 4% relative uncertainty for the 794  $\text{cm}^{-1}$  band at 250 K.

There is a general moderate increase in the integrated band intensity with decreasing temperature for all bands except the 1302  $\text{cm}^{-1}$  band. Similar increases with decreasing temperature were reported for acetone by Wang *et al.* [2001] and noted to be attributable to the increased population of combination-difference bands at lower temperatures, which may overlap with other bands due to anharmonicities (see Section 2.4.1.3). This may also be the case for PAN although this has not been investigated further in this thesis.

## 4.5 Comparison to Previous Work

As noted in Section 2.4.2, infrared absorptivities for PAN at room temperature have been reported previously for the five major PAN absorption bands by four other groups. Furthermore, integrated PAN band intensities have also been reported by Tsalkani and Toupance [1989] and Gaffney *et al.* [1984]. The only known PAN reference cross-section (recorded at  $0.25\text{ cm}^{-1}$  spectral resolution) prior to this work is reported by Hanst and Hanst [1993]. In this section, results obtained in this study are discussed in comparison to those data previously reported.

### 4.5.1 Comparison of Infrared Absorptivities

A summary of all literature data for PAN peak absorptivities at room temperature is given in Table 4.8 together with those calculated in this study. Errors were not assigned for absorptivities reported by Stephens [1964], nor by Bruckmann and Willner [1983]. The nature of the assigned error for results reported by Tsalkani and Toupance [1989] is not known. The one-sigma uncertainty reported by Niki *et al.* [1985] has been modified to reflect a two-sigma uncertainty, in line with that reported for results calculated in this study.

There are significant differences seen between the datasets with the most important being the difference between the higher resolution studies (this work, Niki *et al.* [1985] and Tsalkani and Toupance [1989]) and those at lower spectral resolution made by Bruckmann and Willner [1983] and Stephens [1964]. There is excellent agreement in Table 4.8 for intensities calculated in this work for the 794, 1163 and 1302  $\text{cm}^{-1}$  bands with respect to work by Tsalkani and Toupance [1989] and by Niki *et al.* [1985]. However, a significant difference still exists between the datasets for the 1842  $\text{cm}^{-1}$  band with a 15% difference with the Tsalkani and Toupance [1989] result and 7% with that reported by Niki *et al.* [1985]. The reason for this difference is unclear and difficult to assess because of the lack of a detailed error assessment in the Tsalkani and Toupance [1989] data.

The higher absorptivities reported for the 1741  $\text{cm}^{-1}$  PAN band in earlier studies at lower resolutions could be subject to interference from a noted contaminant water vapour absorption line centred at 1739.850  $\text{cm}^{-1}$ . This contaminant absorption line would not be resolved from the 1741  $\text{cm}^{-1}$  PAN band centre at spectral resolutions

below  $0.5 \text{ cm}^{-1}$  such as those resolutions employed by all but Niki *et al.* [1985] and in this work. Some water vapour contamination was noted in those studies detailed in Table 4.8 and this could have resulted in a positive bias to related data at  $1741 \text{ cm}^{-1}$ .

Band centre / $\text{cm}^{-1}$	Stephens, 1964. Res.: >5.0 $\text{cm}^{-1}$	Bruckmann and Willner, 1983. Res.: 1.20 $\text{cm}^{-1}$	Niki <i>et al.</i> 1985 Res.: 0.06 $\text{cm}^{-1}$	Tsalkani and Toupance, 1989 Res.: 1.0 $\text{cm}^{-1}$	This Work Res.: 0.03 / 0.25 $\text{cm}^{-1}$
606	-	-	-	-	$1.55 \pm 0.12$
794	10.1	13.4	$11.5 \pm 0.6$	$12.2 \pm 0.4$	$11.4 \pm 0.8$
930	-	-	-	-	$1.46 \pm 0.12$
991	-	-	-	-	$1.03 \pm 0.08$
1055	-	-	-	-	$0.62 \pm 0.06$
1163	14.3	15.8	$14.5 \pm 1.4$	$15.7 \pm 0.6$	$14.6 \pm 1.0$
1302	11.2	13.6	$11.3 \pm 1.2$	$11.9 \pm 0.4$	$11.4 \pm 0.8$
1741	23.6	32.6	$31.0 \pm 3.2$	$31.4 \pm 1.6$	$30.2 \pm 3.0$
1842	10.0	12.4	$10.2 \pm 1.0$	$10.9 \pm 0.4$	$9.5 \pm 1.2$

**Table 4.8** Infrared absorptivities for gaseous PAN ( $10^{-1} \text{ ppm}^{-1}$ , log to base 10); values refer to 1013.25 mb at 295 K for nine PAN absorption bands with a comparison to previously reported data. Errors for previously reported data by Niki *et al.*, [1985], have been modified to reflect a two standard deviation, in line with those quoted for this work.

## 4.5.2 Comparison of Integrated Intensities

A detailed comparison could also be performed for integrated band intensities, which is not expected to be subject to the resolution effects discussed above for peak absorptivities. A summary of previously reported literature values for PAN integrated band intensities is given in Table 4.9 for studies at room temperature.

Integrated band absorption data calculated in this study compare well with those of Tsalkani and Toupance [1989] with a minimum 0.8% difference in the  $794 \text{ cm}^{-1}$  absorption band and a maximum 10.6% difference in the  $1163 \text{ cm}^{-1}$  band. Comparing data in this study with that originally reported by Gaffney *et al.* [1984], however, we see differences ranging from 2.5% for the  $794 \text{ cm}^{-1}$  band and 50.5% for the  $1741 \text{ cm}^{-1}$  band. Large differences were also reported by Tsalkani and Toupance [1989] in their

comparison with the Gaffney *et al.* [1984] data. The results from this work therefore support those of Tsalkani and Toupance [1989] rather than that of Gaffney *et al.* [1984].

Band centre / cm <sup>-1</sup>	Gaffney <i>et al.</i> [1984]	Tsalkani and Toupance [1989]	This Work
606	-	-	34.2 ± 1.4
794	247 ± 6	239 ± 4	241 ± 6
930	-	-	32.2 ± 1.2
991	-	-	20.1 ± 0.8
1055	-	-	16.0 ± 0.8
1163	477 ± 9	322 ± 7	356 ± 8
1302	405 ± 20	270 ± 2	281 ± 6
1741	808 ± 34	563 ± 10	537 ± 10
1842	322 ± 9	262 ± 4	260 ± 6

**Table 4.9** Infrared integrated intensities (atm<sup>-1</sup>cm<sup>-2</sup> to 3.s.f) of nine PAN bands with comparison to previously reported data.. (Units refer to 1 atm at ambient temperature 291 K unless otherwise stated). Errors quoted for this work represent a two standard deviation calculated from regression fits. The nature of errors from previously reported data is unknown.

In comparison to the favoured Tsalkani and Toupance [1989] data, this study has found a 4.8% lower intensity for the 1741 cm<sup>-1</sup> band as well as a significant difference in the 1163 cm<sup>-1</sup> (ν(C-O)) band intensity, found to be 10.6% higher. It should be noted that the spectral integration range used by previous groups for the purposes of calculating PAN integrated band intensities is not known; therefore, this potential cause of uncertainty cannot be assessed further in this thesis.

A constant relative difference between all bands would indicate a systematic error due to incorrect pressure measurements for example as noted by Tsalkani and Toupance [1989], who also noted that there may be impurities in the PAN sample contributing to some bands. Tsalkani and Toupance [1989] assert that their PAN samples were >98% pure as determined by gas chromatography and state that the only contaminants identified were carbon dioxide and water vapour. However, these contaminants are clearly seen in the Tsalkani and Toupance [1989] spectrum with water

lines visible in the 1600-1650  $\text{cm}^{-1}$  spectral region, even with a relatively low resolution of 1  $\text{cm}^{-1}$ .

An informative way to analyse the effects of contaminants is to consider the relative intensity of each band with respect to a band that shows the best internal consistency and is expected to be free from any contamination. The 794  $\text{cm}^{-1}$  absorption band was chosen for this purpose here since it shows the best agreement between all previous datasets; Tsalkani and Toupance [1989] employed the 1842  $\text{cm}^{-1}$  band for which some absolute intensity disagreements may still exist. The relative intensities for this work are calculated for each independent measurement and averaged to give the results shown in Table 4.10. In the table, the results of Tsalkani and Toupance [1989] together with their re-evaluation of the Gaffney *et al.* [1984] data are shown; the relative intensities originally reported by Gaffney *et al.* [1984] were noted to be incorrect in the Tsalkani and Toupance [1989] re-evaluation.

The largest differences in the relative ratios shown in Table 4.10 are seen for the 1741  $\text{cm}^{-1}$  band. It is possible on the basis of this result that measurement of the 1741  $\text{cm}^{-1}$  absorption band in earlier studies may have been affected by the same subtle contamination by acetone seen in spectra discarded in this study (see Section 4.2.2.2).

Band position / $\text{cm}^{-1}$	Re-evaluation of data reported by Gaffney <i>et al.</i> [1984]	Tsalkani and Toupance [1989]	This work
794	1.00	1.00	1.00
1163	1.33	1.39	1.47
1302	1.13	1.13	1.16
1741	2.11	2.36	2.23
1842	1.10	1.10	1.08

**Table 4.10** Relative integrated absorption intensities normalised to the 794  $\text{cm}^{-1}$  band intensity. The quoted data from Gaffney *et al.* [1984] are based on a re-evaluation of the Gaffney *et al.* [1984] results performed by Tsalkani and Toupance [1989].

### 4.5.3 Comparison of Cross-sections

A comparison of room temperature cross-sections in this work with those calculated by Hanst and Hanst [1993] reveals significant differences (See Figure 4.11). Most importantly, the five principal absorption bands are calculated to be much stronger than

those by Hanst and Hanst [1993]. This increase is not systematic however, with a difference of 133% in the 1741  $\text{cm}^{-1}$  band and only 17% in the 1842  $\text{cm}^{-1}$  band, indicating that there is more than simply a difference in the assumed number density when calculating cross-sections.

Furthermore, Hanst and Hanst [1993] appears not to have observed the 1371  $\text{cm}^{-1}$  ( $\text{CH}_3$  s-deform) PAN band and only very poorly resolves the weaker bands in the 900-1100  $\text{cm}^{-1}$  region. There also appears to be an unusual artefact on the shoulder of the 822  $\text{cm}^{-1}$  absorption band in the Hanst [1993] data, which appears to be an unrealistic “diagonal” side lobe of the 822  $\text{cm}^{-1}$  band.

This significantly weaker absorption means that integrated band intensities inferred from the Hanst and Hanst [1993] cross-section are much weaker than all those previously reported for the five principal absorption bands with a minimum 36% difference for the 1302  $\text{cm}^{-1}$  band relative to that reported by Tsalkani and Toupance [1989] and a 140 % difference in the 1741  $\text{cm}^{-1}$  band relative to this work.

The large differences in the Hanst and Hanst [1993] dataset relative to all previously reported data, as well as this work, make the accuracy of that dataset questionable. For these reasons, cross-sections calculated in this study are believed to be a significant improvement.

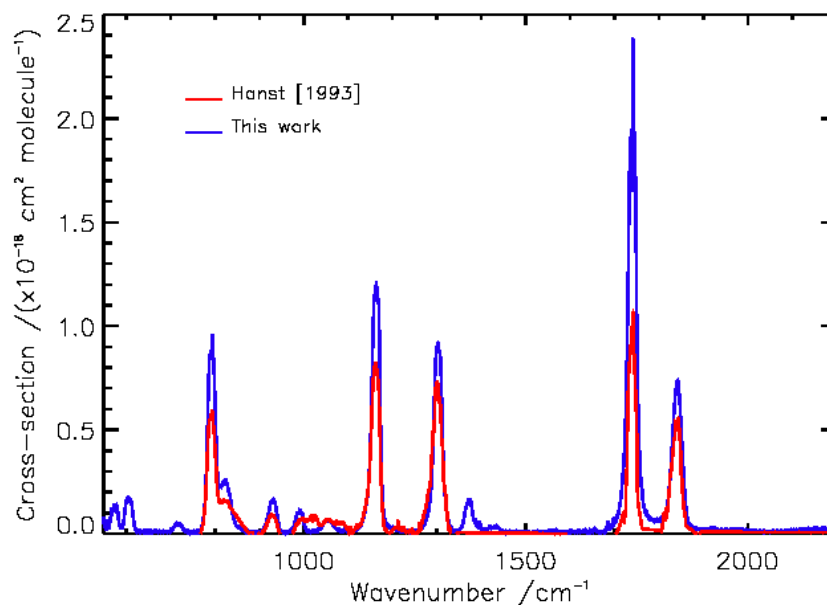


**Figure 4.11** A comparison between PAN cross-sections calculated in this work (blue) at 295 K, with those calculated by Hanst and Hanst [1993] (red).

## 4.6 Conclusions

Cross-sections for PAN vapour at spectral resolutions of  $0.03\text{ cm}^{-1}$  and  $0.25\text{ cm}^{-1}$  have been determined in the mid-infrared range of  $550\text{--}2200\text{ cm}^{-1}$  at 295 and 250 K with further cross-sections calculated at  $0.25\text{ cm}^{-1}$  resolution in the range  $550\text{--}1400\text{ cm}^{-1}$  at 273 K. No resolution of fine structure was observed at the spectral resolutions employed for these measurements.

Large and systematic differences were found relative to previously reported PAN data for the Hanst and Hanst [1993] PAN cross-section, questioning the accuracy of those data.

A general increase in nominal peak infrared absorptivity and integrated band intensities was observed with decreasing temperature. A minimum 6% difference was observed between 295 and 250 K in the band intensity of the  $1741\text{ cm}^{-1}$  PAN band, whilst a maximum 13% difference was observed for the  $1163\text{ cm}^{-1}$  band. No evidence of nitrogen induced broadening was observed in any of the PAN bands studied.

The  $794$  and  $1163\text{ cm}^{-1}$  PAN absorption band absorptivities are calculated with good accuracy at all temperatures in this study ( $<7\%$  relative error for both bands at the 95 % confidence level).

Integrated band intensities and band centre absorptivities have been reported for the first time in this work for the weak PAN absorption bands centred at  $606$ ,  $930$ ,  $990$ , and  $1055\text{ cm}^{-1}$ .

Integrated band intensities at room temperature for the five main bands of PAN are seen to be generally in good agreement with earlier work by Tsalkani and Toupance [1989] supporting these results rather than those of Gaffney *et al.* [1984]. The integrated intensity of the  $1741\text{ cm}^{-1}$  PAN band is noted to show the greatest inconsistency between all datasets.

The nature of a difference in the integrated intensity reported for the  $1741\text{ cm}^{-1}$  band in the datasets studied remains unresolved although it is proposed here that contamination by acetone in this band may be a source of error in previous measurements. Similar contamination may have resulted in an overestimation of the reported integrated intensity for the  $1741\text{ cm}^{-1}$  band in previously reported data.

In addition, the removal of probable contamination by water vapour and carbon dioxide was not considered in previous calculations of PAN data. Correction for, or an

accounting of, such contaminants in the Gaffney *et al.* [1984] and Tsalkani and Toupance [1989] datasets, would be required if these data are to be used in quantitative applications.

Most significantly, the requirement for remote sensing applications is the confirmation of absorption cross-sectional data together with estimated errors. This has been achieved for PAN at room temperature for the first time. Furthermore, cross-sections have also been derived at lower temperatures allowing a more accurate investigation of PAN at the cold temperatures of the upper troposphere. This is the subject of the following chapter.



# Chapter 5

## 5 Detection of PAN in MIPAS-B2

### Spectra

The measurement of new, high-resolution absorption cross-sections for PAN was undertaken with the aim of applying these new reference data in the retrieval of PAN concentrations from measurements of atmospheric spectra. In this chapter, spectra recorded by a balloon-borne infrared spectrometer, the Michelson Interferometer for Passive Atmospheric Sounding Balloon-borne version 2 (MIPAS-B2), are used to investigate the possibility of detecting PAN in the upper troposphere by its characteristic infrared signature.

The MIPAS-B2 instrument is chosen for such assessment because of its high performance (low spectral noise and high spectral resolution), with the intention to apply similar detection methods for PAN, should they prove successful, to space-based platforms such as the MIPAS instrument onboard Envisat (MIPAS-E), which has significantly higher spectral noise.

#### 5.1 The MIPAS-B2 Instrument

The MIPAS-B2 instrument is a cryogenically cooled FTIR spectrometer flown on stratospheric balloons. The B2 version, first flown in 1995, is one of a series of MIPAS instruments developed and operated by the Institut für Meteorologie und Limaforschung (IMK) based in Karlsruhe, Germany. Vertical trace gas profiles retrieved from MIPAS-B2 observations have been used in a number of validation campaigns for satellite instruments, such as for CLAES (Cryogenic Limb Array Etalon Spectrometer) and ILAS (Improved Limb Atmospheric Spectrometer). Furthermore, MIPAS-B2 is

currently being operated for the validation of retrievals for the MIPAS space-borne instrument on the European Space Agency's ENVISAT satellite launched in March 2001 [Fischer and Oelhaf, 1996]. The MIPAS-B2 instrument is therefore highly suited to the investigation of trace gases, such as those studied in this thesis, as it is a well-characterised instrument.

The MIPAS-B2 instrument, like its satellite counterpart, is a limb sounding spectrometer (see Section 2.1), recording mid-infrared emission spectra of the Earth's stratosphere and troposphere. A brief description of the design and characterisation of the MIPAS-B2 instrument is given here. For further details, see Friedl-Vallon *et al.* [2004]. A schematic of the instrument is shown in Figure 5.1, showing the optics, detector and a line of sight (LOS) stabilisation system.

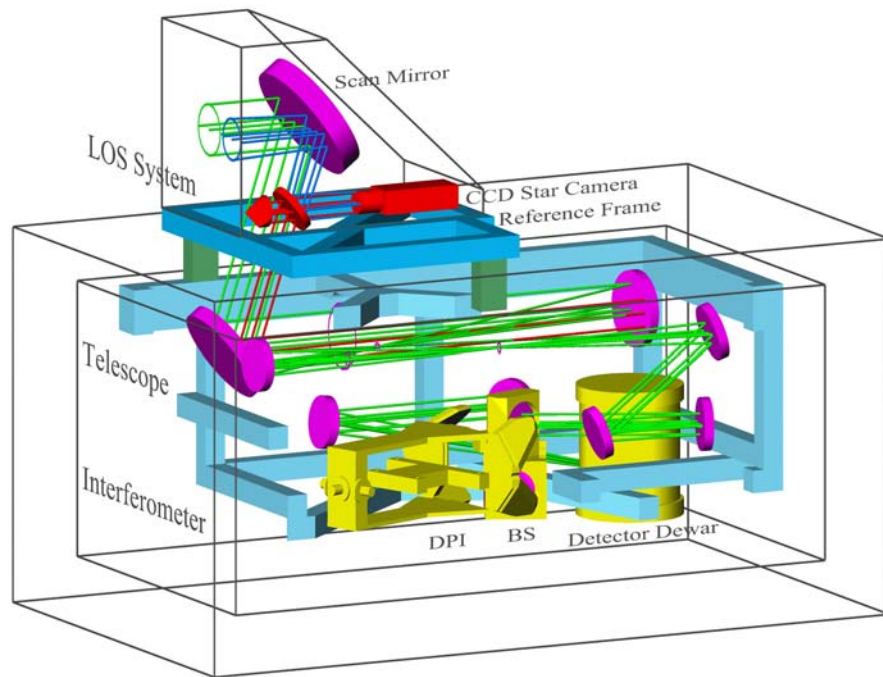


**Figure 5.1** An illustrative schematic of the MIPAS-B2 spectrometer

The instrument, together with its electronics and telemetry system are housed in a gondola attached to a stratospheric helium balloon ( $\sim 400,000 \text{ m}^3$  volume at nominal observing heights) operated by the French Space Agency (CNES), allowing the instrument to fly at observing altitudes between 29 and 39 km. The spectrometer unit itself consists of a three-mirror off-axis telescope, a Double Pendulum Interferometer (DPI) and a four-channel liquid-helium-cooled Silicon Arsenide-BIB detector. There is also an internal blackbody source (200 K) for instrumental gain and radiometric

calibration purposes. The DPI is a modification of the classical Michelson apparatus, using two cube-corner mirrors mounted on a rotating structure [Fischer and Oelhaf, 1996]. A two-sided interferogram is recorded with a maximum optical path difference (MPD) of 14.5 cm, corresponding to the unapodised resolution of  $0.0345 \text{ cm}^{-1}$  (slightly less than MIPAS-E) defined by  $1/(2 \times \text{MPD})$ . After apodisation with the Norton-Beer strong function (Norton and Beer, 1976; 1977), this resolution is decreased to approximately  $0.07 \text{ cm}^{-1}$ . The field of view of the telescope gives a vertical field of view of 5.0 mrad, corresponding to approximately 3 km in the upper troposphere with a decreasing field of view at higher altitudes.

The whole apparatus shown in Figure 5.1 is enclosed in an insulated container and cooled using frozen  $\text{CO}_2$  to an operating temperature of 210 K. The line of sight stabilisation system consists of an altitude and heading reference system (a miniaturised inertial navigation system and integrated GPS) as well as an azimuth and elevation stabilisation loop. These elements work together in an active feedback control system to keep the line of sight as stable as possible throughout the flight. The addition of a star camera or star reference system also allows post-flight calibration of the line of sight. The star camera records a CCD image of the night sky for each measured interferogram, allowing calculation of the line of sight to within an accuracy of 0.3 mrad (40-190 m depending on tangent altitude).

### 5.1.1 Data Processing

The raw interferograms recorded by the instrument (Level 0) are relayed to ground and stored for later processing. The processing of the raw data to geo-located apodised spectra (Level 1B) is performed routinely by the IMK team and is described in detail by Trieschmann [2000] and consists of the following summary steps:

- Correction to interferograms for non-linearity
- Phase correction of interferograms
- Apodisation
- Fast Fourier transformation of the interferograms
- Radiometric and spectral calibration
- Geo-location assignment

Radiometric calibration is performed using the instrumental gain and offset determined using the onboard blackbody reference source and that of cold space recorded during the flight. Here deep space is defined by a  $+20^{\circ}$  elevation viewing angle. Emission lines from molecules in the atmosphere above the balloon are “shaved” in the high-resolution spectrum to produce the required calibration curve. The resultant level 1B data product consists of these calibrated and geolocated spectra together with the associated instrument line shape (ILS) and noise equivalent spectral radiance (NESR) data.

### 5.1.2 Flight Details and Performance

The spectral dataset used in the work described in the following sections were recorded during flight campaigns 6 and 8 of MIPAS-B2 in the Northern mid-latitudes. The instrument was launched from Aire sur L’Adour in Southwest France for campaign 6 and 8 on 7<sup>th</sup>-8<sup>th</sup> May 1998 and 30<sup>th</sup> April 1999 respectively. The spectra used here were all measured between 02:17 – 03:17 UTC for both campaigns. Further details of this campaign are described by Friedl-Vallon [1999a]. Flight 6 (1998) took place as part of the EU-funded CHELOSBA (CHemistry of the LOwer Stratosphere investigated with Balloon) project and recorded limb spectra over the Western Mediterranean region. Additionally, data collected during flight 6 have been used for testing of on line processors being developed for the operational analysis of the MIPAS-Envisat (MIPAS-E) spectral dataset [Dinelli and Carloti, 2001]. Flight 8 took place two hours after local sunrise, measuring limb spectra between the Balearic Islands and Corsica. See Figure 5.2 for tangent point locations for both flights.

Although these campaigns studied the Western Mediterranean, its proximity to the Eastern Mediterranean region is especially interesting for pollution studies, with recent studies by Holzinger *et al.* [2005] and Lelieveld *et al.* [2002] revealing that European pollution can concentrate in the Eastern Mediterranean region. Furthermore, Holzinger *et al.* [2005] have reported greatly enhanced concentrations of organic compounds including PAN, acetone and acetonitrile in the Eastern Mediterranean in aged biomass burning plumes originating from the Southwest.

Flight 6 data specifications were chosen to match those of MIPAS-E as closely as possible by extending the spectral measurement channels (see Table 5.1) and choosing elevation angles to match the MIPAS-E nominal tangent altitudes between 7.5 and 37.9 km in steps of approximately 3 km (see Table 5.2).

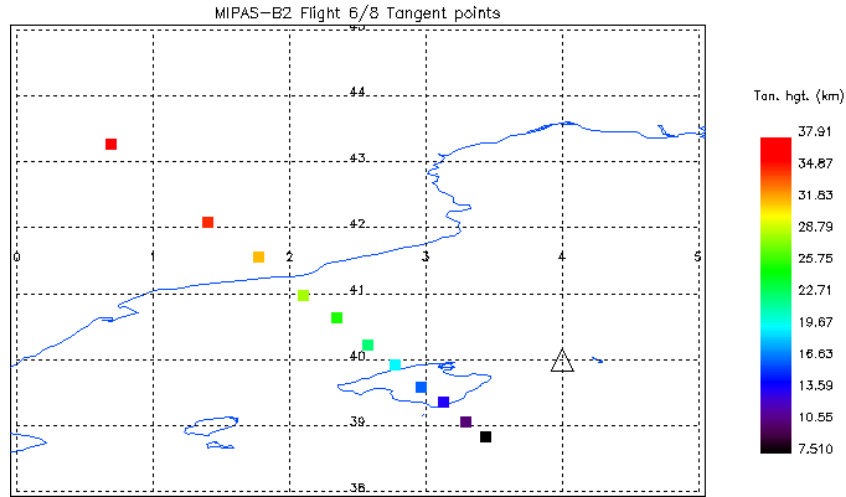


**Figure 5.2** Tangent points of the MIPAS-B2 flights 6 and 8 over the Mediterranean. Plot shows the East coast of Spain and the Balearic Islands (land borders are in blue). Triangular symbol denotes mean tangent point of the Flight 8 campaign whilst squares denote the Flight 6 campaign.

A new detector system was installed to provide the required spectral measurement channels. The upper and lower limits of the spectral pass bands were defined by the condition that they must have a NESR of twice the minimum NESR observed using the internal blackbody reference. The calculated average flight NESR value is derived from single blackbody measurements recorded during calibration sequences made before and after each measurement sequence. The spectral dataset provided for analysis in this work extends over the quoted nominal pass band.

Channel	Nominal pass band /cm <sup>-1</sup>	Typical NESR / W cm <sup>-2</sup> sr <sup>-1</sup> cm <sup>-1</sup>
1	685-970	$1.5 \times 10^{-8}$
2	1020-1500	$3.5 \times 10^{-9}$
3	1580-1750	$3.0 \times 10^{-8}$
4	1820-2410	$3.0 \times 10^{-9}$

**Table 5.1** Pass bands and averaged NESR values for MIPAS-B2 flight 6 Level 1B dataset, taken from Friedl-Vallon *et al.*, 1999a.

The geo-locations derived from the onboard Global Positioning System (GPS) for flight 6 and 8 are given in Table 5.2 and Table 5.3 respectively. Four atmospheric spectra

were provided for each tangent altitude as well as a standard deviation spectrum calculated from consecutive calibration spectra and used for noise characterisation (see following section). Each of these four spectra is also calculated from between five and ten coadded scans. The resulting four spectra were then averaged to further increase the signal to noise ratio.

All spectra were apodised with the Norton-Beer strong function [Norton and Beer, 1976, 1977] and interpolated to give a wavenumber spacing of  $0.025 \text{ cm}^{-1}$  using zero-filling of the recorded interferogram (see Section 2.5.2.2). The final apodised spectral resolution has been calculated to be  $0.068 \text{ cm}^{-1}$  [H. Oelhaf; private communication].

An updated version of the flight 6 spectral data was available for analysis, however significant differences were observed with the original data that were not easily explained [Waterfall, personal communication]. The updated data was not wavenumber calibrated and noise spectra displayed a variable offset and broad structured spectral features. For these reasons, the original flight 6 data product is used in this thesis.

Elevation Angle ( $^{\circ}$ )	Tangent Altitude (km)	Latitude ( $^{\circ}$ N)	Latitude ( $^{\circ}$ E)
-0.746	37.88	43.26	0.69
-1.927	34.76	42.07	1.40
-2.618	31.73	41.55	1.78
-3.156	28.55	40.97	2.10
-3.615	25.59	40.63	2.35
-4.014	22.53	40.21	2.58
-4.378	19.60	39.92	2.78
-4.719	16.44	39.57	2.97
-5.013	13.63	39.34	3.13
-5.306	10.42	39.05	3.30
-5.564	7.51	38.82	3.44

**Table 5.2** Elevation angles and corresponding tangent point altitudes of MIPAS-B2 flight 6 spectra.

Elevation Angle ( $^{\circ}$ )	Tangent hgt /km	Elevation Angle ( $^{\circ}$ )	Tangent hgt /km
-4.648	17.6	-5.418	9.6
-4.838	15.7	-5.508	8.5
-5.048	13.7	-5.588	7.5
-5.238	11.7	-5.678	6.4
-5.328	10.7	-5.769	5.2

**Table 5.3.** Elevation angles and corresponding tangent heights of MIPAS-B2 flight 8 recorded spectra for the upper troposphere and lower stratosphere. A number of higher and lower tangent point measurements were made in this campaign, but are not listed here.

Spectral data for flight 8 were not wavenumber calibrated. This is accounted for in this study by fitting a wavenumber shift in the spectral region of interest (see Section 5.2.5).

#### 5.1.2.1 Spectral Noise

Standard deviation spectra, provided with the level 1B data product reflect the typical NESR quoted in Table 5.1. An example of an NESR spectrum from a single blackbody measurement during flight 6 is shown for channel 2 in Figure 5.3, with characteristic rapid increases in noise seen at the edges of the pass band being due to tail off in detector response. The average noise in the region of the  $1163 \text{ cm}^{-1}$  PAN absorption band is better than  $3 \text{ nW cm}^{-2} \text{ sr}^{-1} \text{ cm}$ . However, noise does increase rapidly below  $1140 \text{ cm}^{-1}$  and although this should not interfere greatly with the lower wavenumber limit of this PAN absorption band ( $1125 \text{ cm}^{-1}$ ), it is important to note that some effect may be manifest in any resultant spectra analysed in this spectral region.

A more informative discussion of the noise contributions to the resulting coadded spectrum used in the analysis is to look at the standard deviation spectrum derived from an individual spectrum used in the co-adding. Figure 5.4 shows the calculated standard deviation spectra for channels 1 and 2 at selected altitudes. A significant decrease in variability is seen with increasing altitude and there is also evidence of unusual “structure” seen at 7.5 km.

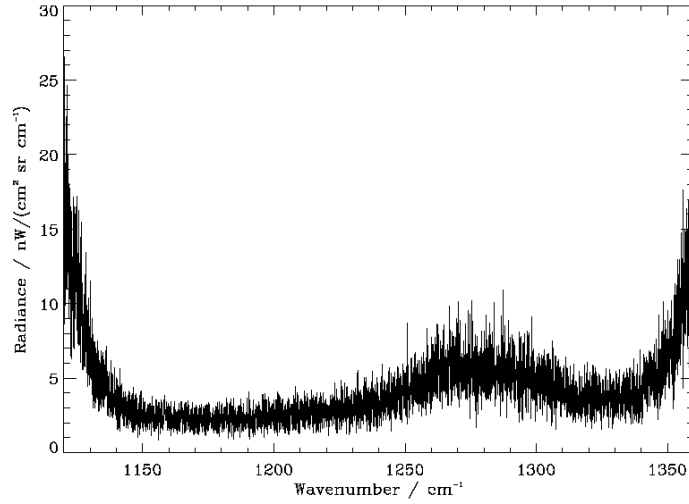


**Figure 5.3** Absolute NESR spectrum for a typical blackbody measurement for channel 2 during flight 8.

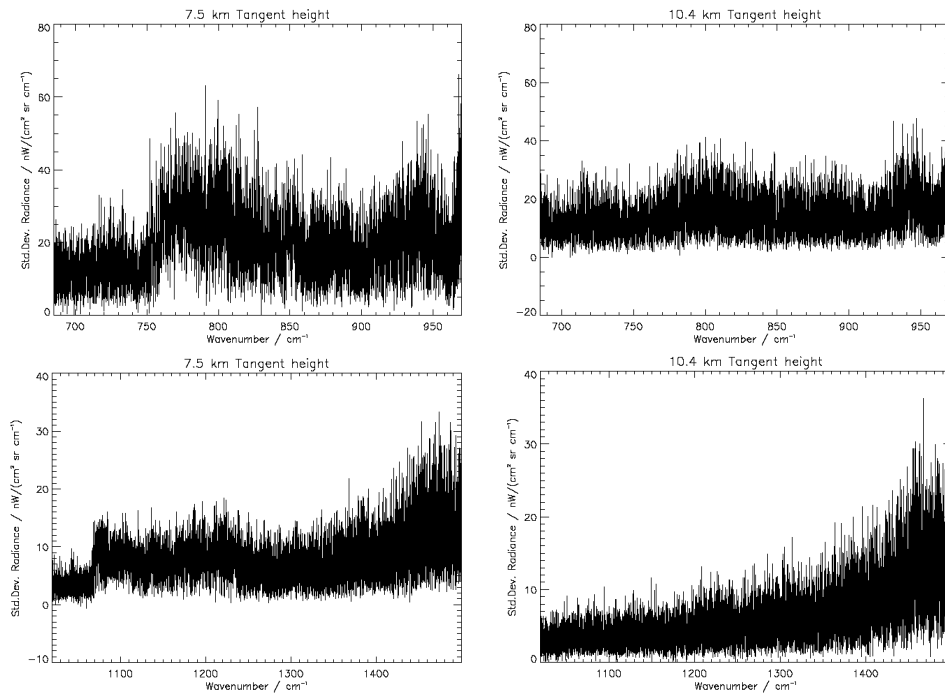


**Figure 5.4** Standard deviation spectra derived from 4 coadded scans for MIPAS-B2 flight 6 for a) Ch. 1, 7.5 km, b) Ch. 1, 10.4 km, c) Ch. 2, 7.5 km, d) Ch. 2, 10.4 km.

The reason for such structure is not explained in the flight reports by Friedl-Vallon [1999a, 1999b], although it is likely that this may be due to the optical properties of the instrument such as the variability with wavenumber of the optical filter transmission spectrum. Alternative sources of variability may be due to the presence of thin cloud or



scattering of light into the spectrometer at low altitude and potential radiometric calibration errors. Given that such error is relatively small ( $<1\%$  of total signal), this is not expected to significantly affect the work undertaken in this thesis, although it is necessary to note such error in any quantitative evaluation.

### **5.1.2.2 Field of View and Instrument Lineshape**

The instrument field of view (FOV) for each channel was measured by moving a modulated collimated infrared source horizontally and vertically through the field of view. These were averaged horizontally to provide an effective field of view, which was provided with the spectra, along with the calculated instrument lineshape (ILS). The ILS is approximated by the FOV distribution of the detector optics (the dominant factor of ILS broadening), rather than being retrieved from laboratory measurements. The mean intensity of the FOV on a circular plane as a function of off-axis angle is used to determine the ILS by convolution with the ideal ILS (a sinc function determined from the finite path difference effect on the interferogram; see Section 2.5.3.1).

The FOV and ILS for flight 6 described further by Friedl-Vallon [1999a] and provided with the Level 1B data product are assumed to be a reasonable approximation for both campaigns studied in this work, as there is no change in the instrument characteristics between each campaign.

Any difference in the simulated FOV compared with the true FOV would result in small inaccuracies in simulated spectra. Therefore, it is necessary to simulate this FOV as closely as possible to its true nature. The choice of this approximation is a compromise between the accuracy of the simulated FOV and the computing time required for simulations.

Coefficients for the polynomial expansion required to approximate the FOV were supplied by IMK. The FOV for both channels of MIPAS-B2 are shown in Figure 5.5. In this work, a twenty-one-point approximation to the FOV is used in simulations. Comparing this approximation with that of a forty-one point approximation (also plotted in Figure 5.5), it is clear that there is negligible improvement in the approximated FOV with an increased number of points. However a comparison with the seven-point approximation clearly shows that there would be a significant difference. The twenty-one-point approximation is therefore considered sufficient to

provide a realistic representation of the FOV whilst reducing the computation time of simulation from the forty-one-point case.

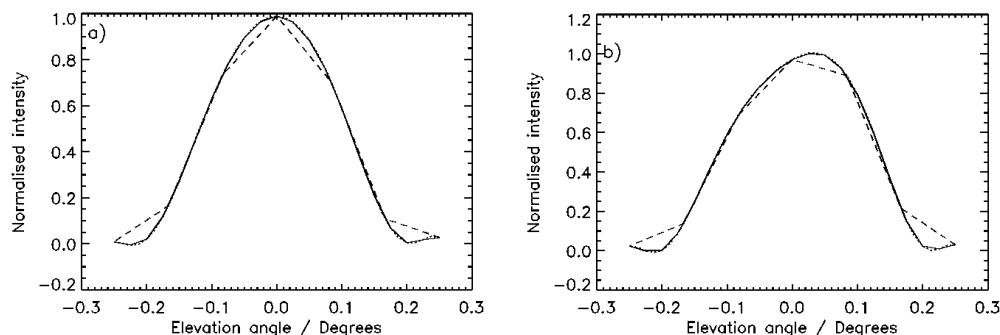


**Figure 5.5** Field of view of the MIPAS-B2 instrument calculated using a polynomial approximation for a) Channel 1, b) Channel 2. Solid lines are the field of view calculated with a 21-point approximation, whilst the dashed and dotted lines are 7 point and 41 point approximations respectively.

## 5.2 Detection of PAN

Spectra from the MIPAS-B2 instrument obtained during flight 6 and 8 have been used to attempt detection of the infrared signature of PAN. The typically low mixing ratios of PAN in the upper troposphere (<150 pptv) and the mainly structureless broadband cross-sectional absorption features of PAN (see Chapter 4) make its detection extremely complex.

In order to detect PAN, it is necessary to first isolate any spectral feature that would be associated with the presence of PAN in the atmosphere. The presence of many other gaseous species, exhibiting resolved line emission, as well as other cross-sectional compounds with spectral features completely or partially overlapping those of PAN, further complicate this problem. Detecting PAN therefore requires a good knowledge of these other “interfering” gases, both in terms of the quality of their own spectroscopy and their abundances in the atmosphere. The accuracy of this detection is further limited by the performance of the instrument (noise) and the accuracy of any numerical techniques (retrieval method and forward model) used in the determination of atmospheric profiles of temperature and pressure.

In the following sections, the method for the detection of PAN in limb-emission spectra is described and results are presented from the MIPAS-B2 flight 6 and 8 spectral datasets.

### **5.2.1 Forward Modelling with the Oxford RFM**

The retrieval of gas concentration information, as well pressure and temperature, requires an analysis of spectra simulated to represent the true atmosphere from which the measured spectra were recorded. The accuracy of fit between the measured and simulated spectra ultimately determines the accuracy of parameters used in the simulation, within the limitations of measurement error. The accuracy of the simulation and hence the accuracy of retrieved parameters is also limited by the accuracy of reference spectral data used for each gas included in the simulation. In addition, care must also be taken to simulate an atmosphere that includes all gases that are expected to influence the spectral region of interest.

In this study, simulated spectra were calculated with the Oxford Reference Forward Model (RFM). For further details of the RFM see [www.ox.ac.uk/rfm](http://www.ox.ac.uk/rfm). This line-by-line radiative transfer model allows the simulation of atmospheric spectra using input parameters of pressure, temperature and gas concentration profiles using a specified viewing geometry. It also includes the ability to simulate the instrument field of view and instrument line shape and to use a number of other spectral and numerical approximations in the forward model.

### **5.2.2 Candidate Spectral Regions for PAN detection**

The suitability of a PAN spectral band for detection purposes from atmospheric spectra is assessed on the following criteria:

- The entire band must fall within the nominal spectral pass band of a single spectral measurement channel.
- The simulated radiance contribution at the nominal band centre must exceed the NESR in the spectral region of such a band by at least a factor of two.

Infrared bands not meeting these criteria would not be distinguishable from instrumental noise with significant confidence.

A simulated mid-infrared atmospheric emission spectrum at 10.7 km tangent height is shown in Figure 5.6. The PAN concentration profile used in this simulation (see Figure 5.11) was set to values of 193 and 161 pptv at profile levels of 10 and 11 km respectively and is derived from results from the MOZART model [Hauglustaine *et al.* 1998] of zonally averaged PAN concentrations at 40° N for mid-February 2000. Simulated profiles for other gases (see Table 5.5) are taken from ACECHEM [2001].

For trace gas species with small contributions to the total observed infrared emission radiance, it is possible to linearly approximate the radiance contribution for a particular gas by calculating the difference between simulated spectra with and without the gas of interest in the simulated atmosphere. The simulated radiance contribution spectrum, calculated in this way for PAN is shown in Figure 5.7. Comparing this simulated radiance contribution spectrum of PAN for MIPAS-B2 at 10.7 km with the total simulated emission spectrum in Figure 5.6, we see that PAN is expected to contribute only a small amount to the total radiance observed. Even for the stronger PAN absorption bands (e.g. 794.0  $\text{cm}^{-1}$ ), there is only a 5% contribution to the total radiance at its peak.

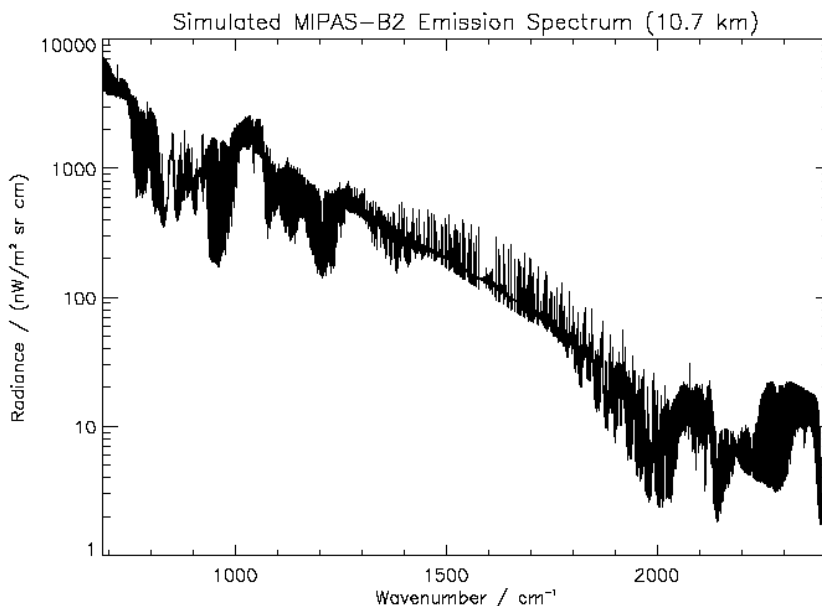


**Figure 5.6** Simulated atmospheric limb-emission spectrum for MIPAS-B2 at 10.7 km across the spectral region measured by the MIPAS-B2 instrument using reference atmosphere gas profiles from ACECHEM [2000].

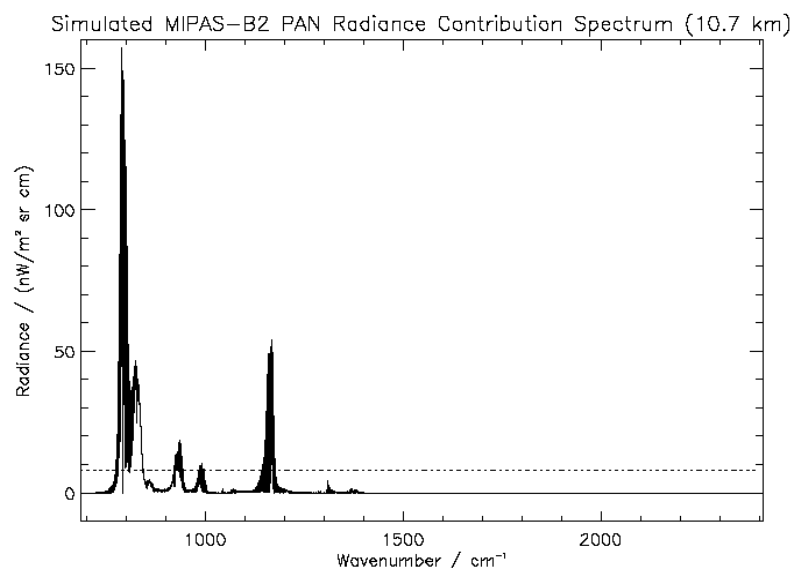


**Figure 5.7** Simulated PAN radiance contribution spectrum for a typical PAN profile across the spectral region covered by MIPAS-B2 measurements. The dashed line shows the typical NESR (7.5 nW) of MIPAS-B2 at 10.7 km.

Figure 5.7 also shows the suitability of the 794 and 1163  $\text{cm}^{-1}$  bands for detection purposes according to the criteria described earlier. Both these bands exceed the minimum criterion described earlier due to their large predicted signal to noise ratio and their complete envelopment by channels 1 and 2 respectively. We see here that the weaker bands of PAN (930 and 1055  $\text{cm}^{-1}$ ) are near the average noise level and that otherwise stronger PAN absorption bands at 1302 and 1841  $\text{cm}^{-1}$  have no contribution due to the saturation of the spectrum in these spectral regions by stronger contributing species such as water vapour at this altitude.

In order to detect the spectral signature of PAN in measured spectra, two spectral windows are chosen here (see Table 5.4) so as to completely encompass the PAN band of interest along with a sufficiently wide region on either side of the band to establish a reasonable baseline to distinguish the PAN feature from. These windows are determined from the simulated radiance contribution for PAN in Figure 5.7.

PAN band	Spectral Window ( $\text{cm}^{-1}$ )
794.0 $\text{cm}^{-1}$	750 - 850
1163.0 $\text{cm}^{-1}$	1120 – 1330

**Table 5.4** Spectral regions chosen for the detection of the 794.0  $\text{cm}^{-1}$  and 1163.0  $\text{cm}^{-1}$  bands of PAN in MIPAS-B2 channels 1 and 2 respectively.

### 5.2.3 Reference Data

To provide a reasonable first guess approximation to the true atmosphere, a simulated atmosphere must be constructed from appropriate sources for gas concentration profiles, pressure and temperature. In addition, reference spectral data for these gases should also be available. This section describes these reference data.

#### 5.2.3.1 Contaminant Gases and Aerosol

As noted earlier, the presence of other gases and aerosol having spectral influence in the window of relevance to PAN greatly complicates the detection problem. Unfortunately, both the PAN bands deemed suitable for analysis in this work lie in spectral regions dominated by a large number of other gases. Many of these contaminant gases (e.g. HCFCs) are relatively heavy molecules and hence exhibit broad spectral bands, which make them hard to separate from similar PAN signatures. The concentrations and spectroscopy of other gases therefore need to be known accurately in order to obtain an accurate spectral fit to the measurements.

Gases that are expected to have significant contributions to the spectral radiance in spectral windows described in Table 5.4 are listed in Table 5.5 below.

	Window 1: 750-850 $\text{cm}^{-1}$	Window 2: 1120-1330 $\text{cm}^{-1}$
Gas Formula	H <sub>2</sub> O, CO <sub>2</sub> , C <sub>2</sub> H <sub>2</sub> , C <sub>2</sub> H <sub>6</sub> , CCl <sub>4</sub> , COF <sub>2</sub> , NH <sub>3</sub> , NO <sub>2</sub> , O <sub>3</sub> , HNO <sub>3</sub> , HNO <sub>4</sub> , F113, CH <sub>3</sub> Cl, ClO, F22, F11, ClONO <sub>2</sub> , OCS, Aerosol, CH <sub>3</sub> C(O)CH <sub>3</sub> , PAN	H <sub>2</sub> O, CH <sub>4</sub> , CO <sub>2</sub> , COF <sub>2</sub> , N <sub>2</sub> O, NH <sub>3</sub> , O <sub>3</sub> , SO <sub>2</sub> , H <sub>2</sub> O <sub>2</sub> , HNO <sub>3</sub> , F113, F114, F115, F12, F13, F14, F22, ClONO <sub>2</sub> , N <sub>2</sub> O <sub>5</sub> , CH <sub>3</sub> C(O)CH <sub>3</sub> , Aerosol, PAN

**Table 5.5** Gases known to have spectral influence in the spectral windows of interest to PAN detection.

Such gases were identified by a search of spectral reference databases including HITRAN 2000 (see below) and Hanst and Hanst [1993]. All gases simulated to have a radiance contribution above the average noise level at any spectral point (for a simulated 10 km atmospheric spectrum) were included. Spectral data for the majority of

these gases is sourced from the HITRAN 1996 database described by Rothman [1992] and Rothman *et al.* [1998a, 1998b]. The updated HITRAN 2000 database [Rothman *et al.*, 2003] is also used where important updated spectral parameters were included. The updated HITRAN 2004 database became available at the time of writing this thesis although the results in this work do not use these reference data.

In addition, cross-sections for PAN were obtained in this thesis and a high-resolution absorption cross-section for acetone was taken from work by Waterfall [2004]. Furthermore, an extinction profile derived from previous retrievals using MIPAS-B2 data by Waterfall [2004] was used for initial aerosol extinction; assumed to be constant over the simulated spectral region. This assumption is unlikely to hold for large spectral ranges as extinction varies slowly with wavenumber, although it is reasonable for the small spectral windows considered here.

A search of the Hanst and Hanst [1993] database revealed the possibility of a further three gaseous species (methyl nitrite, trichlorophenol and dimethyl sulphate) that may be present in trace quantities in the atmosphere. Although these gases are known anthropogenic compounds, mainly from industry and fossil fuel emissions, no reported information could be found on their abundance or chemistry. It is likely that these compounds exist in such small quantity as to contribute very little spectral radiance. In the absence of any further information, these gases were not included in simulated atmospheres calculated here.

### **5.2.3.2 Atmospheric Profiles**

As well as accurate reference spectral data, accurate atmospheric profiles are also required for all gases included in the simulated atmosphere along with those of pressure and temperature. This section describes the methodology in sourcing or calculating appropriate profiles for use in atmospheric simulations.

For most minor trace gases such as some of the HCFCs listed in Table 5.5, atmospheric variability is small globally and temporally due to their inherent long-lifetime and therefore well-mixed nature. For this reason, appropriately chosen profiles from climatology databases, appropriate to the geographical region of interest, usually provide an excellent first guess representation of the true profile. Profiles used in this study for such gases were taken from both a reference atmosphere for the mid-latitude region, compiled by Remedios [1999] for use in the MIPAS-Envisat operational

processor, and also those compiled for the ACECHEM study [ACECHEM, 2001]. In addition, profiles for some minor HCFCs were sourced from those originally developed as part of the Inter-comparison of Radiation Codes used in Climate Models (ICRCCM) and used by Sihra *et al.* [2001]. A full source list for all initial guess profiles used in this work is given in Table 5.6. The MIPAS reference atmosphere database used here lists profiles derived to represent a typical mid-latitude, northern hemisphere, night-time atmosphere.

Other more variable gases in the upper troposphere such as water vapour, ozone and other active chemical species as well as the ambient profiles of pressure and temperature require a more specialised approach. As these gases are also major contributors to the observed spectral radiance (described in section 5.2.3.1), accurate representations must be made prior to any attempts at detection of more minor or weakly contributing species. Where possible, such profiles are based on numerical retrievals such as those previously made by Jay [2000] from the MIPAS-B2 flight 6 dataset. Retrieved profiles for some other compounds were also obtained from the MIPAS-B2 operating group at IMK [Wiegele, Personal communication] for flight 6 and used in this study (Table 5.6). The initial gas concentration profiles used in this work are plotted in Figure 5.8-Figure 5.11.

Gas	Reference*	Gas	Reference*	Gas	Reference*
H <sub>2</sub> O	IMK	O <sub>3</sub>	Jay [2000]	CO <sub>2</sub>	MIPAS
C <sub>2</sub> H <sub>2</sub>	MIPAS	C <sub>2</sub> H <sub>6</sub>	MIPAS	CCl <sub>4</sub>	IMK
COF <sub>2</sub>	MIPAS	NH <sub>3</sub>	MIPAS	NO <sub>2</sub>	IMK
HNO <sub>3</sub>	IMK	HNO <sub>4</sub>	ACECHEM	F113	Sihra [2001]
CH <sub>3</sub> Cl	Sihra [2001]	ClO	MIPAS	F22	IMK
F11	MIPAS	ClONO <sub>2</sub>	MIPAS	OCS	MIPAS
Acetone	Waterfall [2004]	Aerosol	Waterfall [2004]	CH <sub>4</sub>	IMK
SO <sub>2</sub>	MIPAS	F12	IMK	F114	Sihra [2001]
F115	Sihra [2001]	N <sub>2</sub> O <sub>5</sub>	IMK	F13	Sihra [2001]
F14	MIPAS	Temperature	Jay [2000]	PAN	Hauglustaine <i>et al.</i> [1998]
Pressure	Jay [2000]				

**Table 5.6** Source list for first guess concentration, pressure and temperature profiles of contaminant gases for input to simulation of true atmosphere. \*For full description of reference sources, see text.



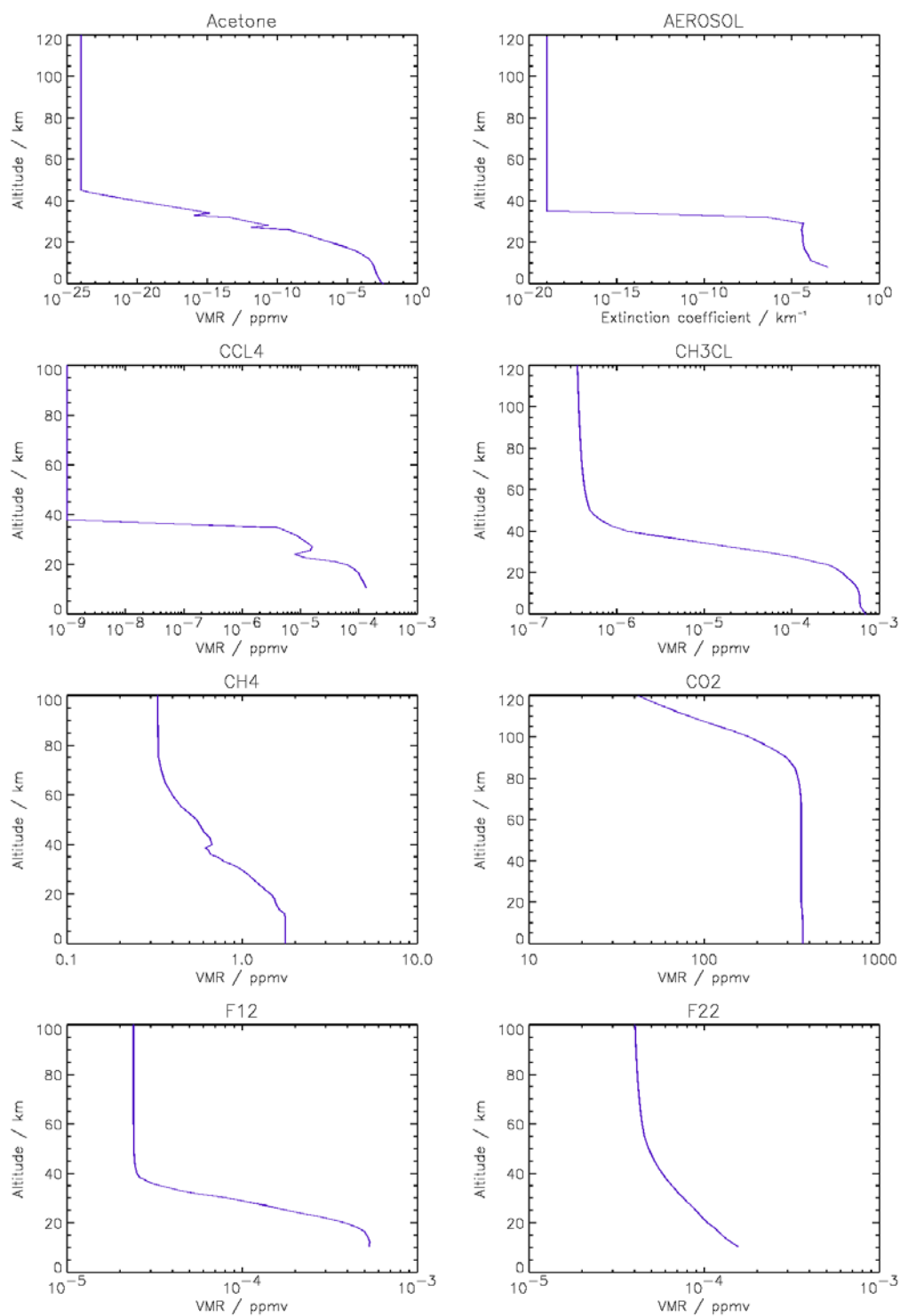


**Figure 5.8** Initial gas concentration (logarithmic scale) profiles (with altitude) for acetone, aerosol, CCl<sub>4</sub>, CH<sub>3</sub>Cl, CH<sub>4</sub>, CO<sub>2</sub>, F12 and F22 included in simulated atmospheres in this thesis.

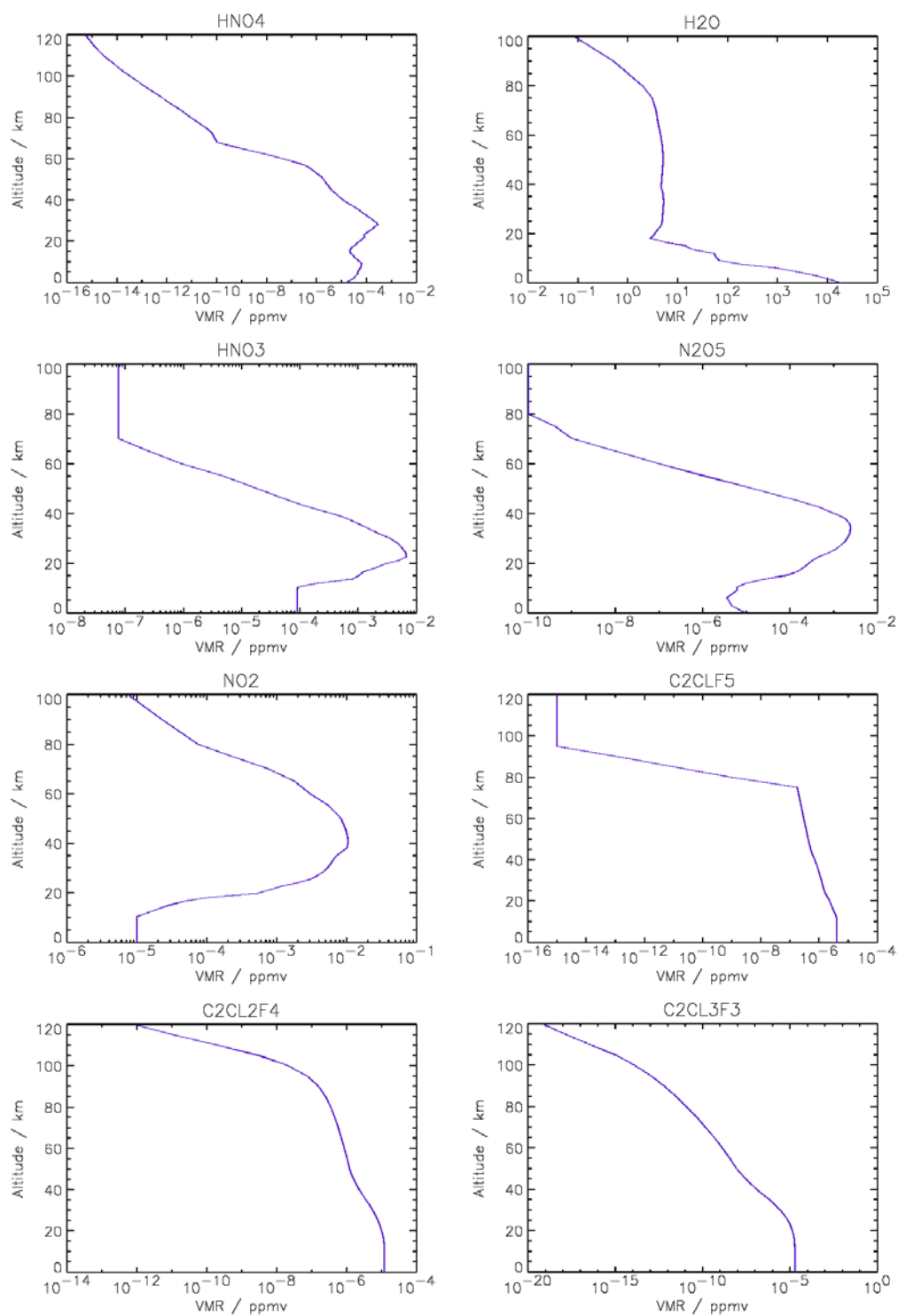


**Figure 5.9** Initial gas concentration (logarithmic scale) profiles (with altitude) for HNO<sub>4</sub>, H<sub>2</sub>O, HNO<sub>3</sub>, N<sub>2</sub>O<sub>5</sub>, NO<sub>2</sub>, C<sub>2</sub>ClF<sub>5</sub>, C<sub>2</sub>Cl<sub>2</sub>F<sub>4</sub> and C<sub>2</sub>Cl<sub>3</sub>F<sub>3</sub> included in simulated atmospheres in this thesis.

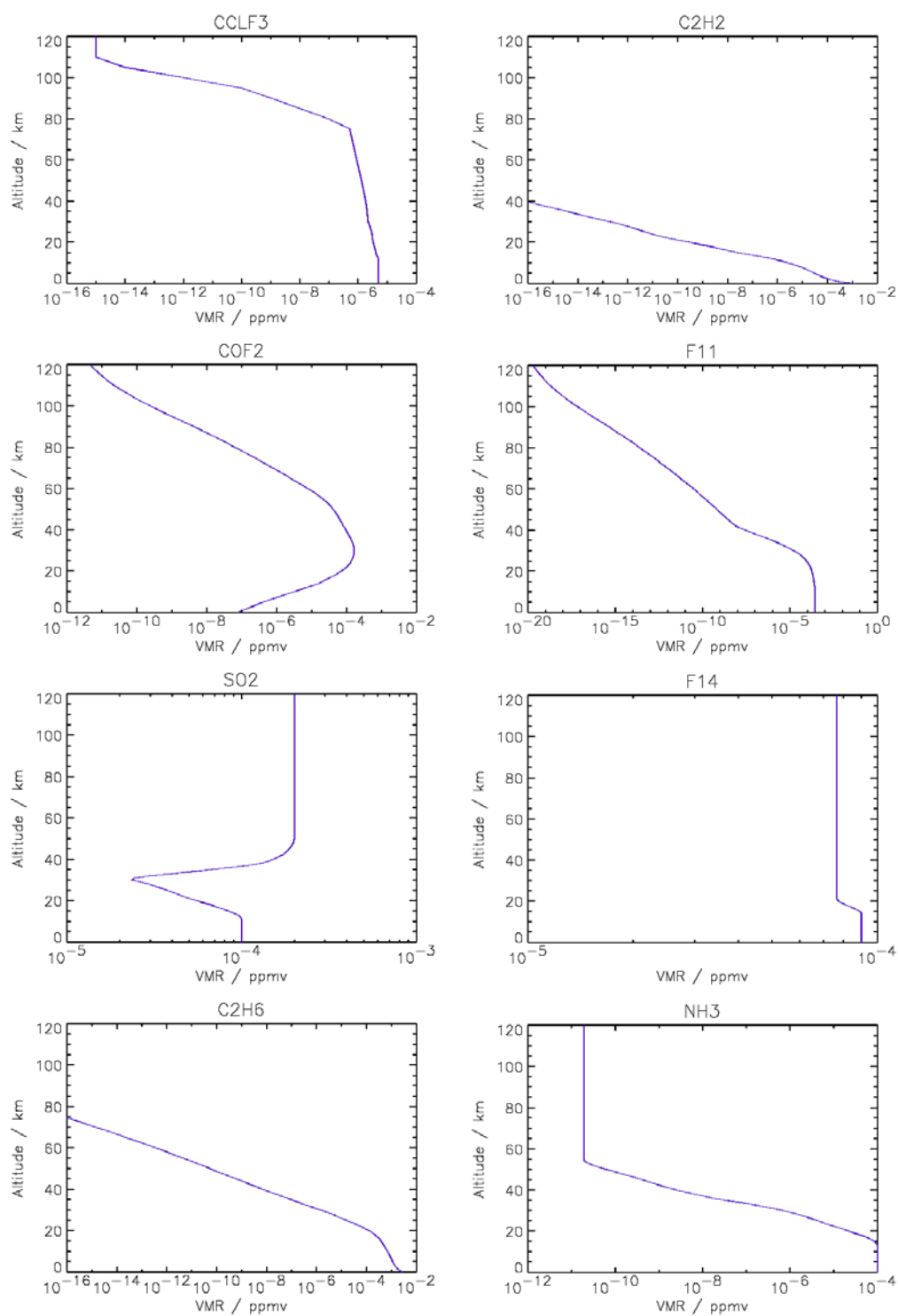


**Figure 5.10** Initial gas concentration (logarithmic scale) profiles (with altitude) for CClF<sub>3</sub>, C<sub>2</sub>H<sub>2</sub>, COF<sub>2</sub>, F11, SO<sub>2</sub>, F14, C<sub>2</sub>H<sub>6</sub> and NH<sub>3</sub> included in simulated atmospheres in this thesis.

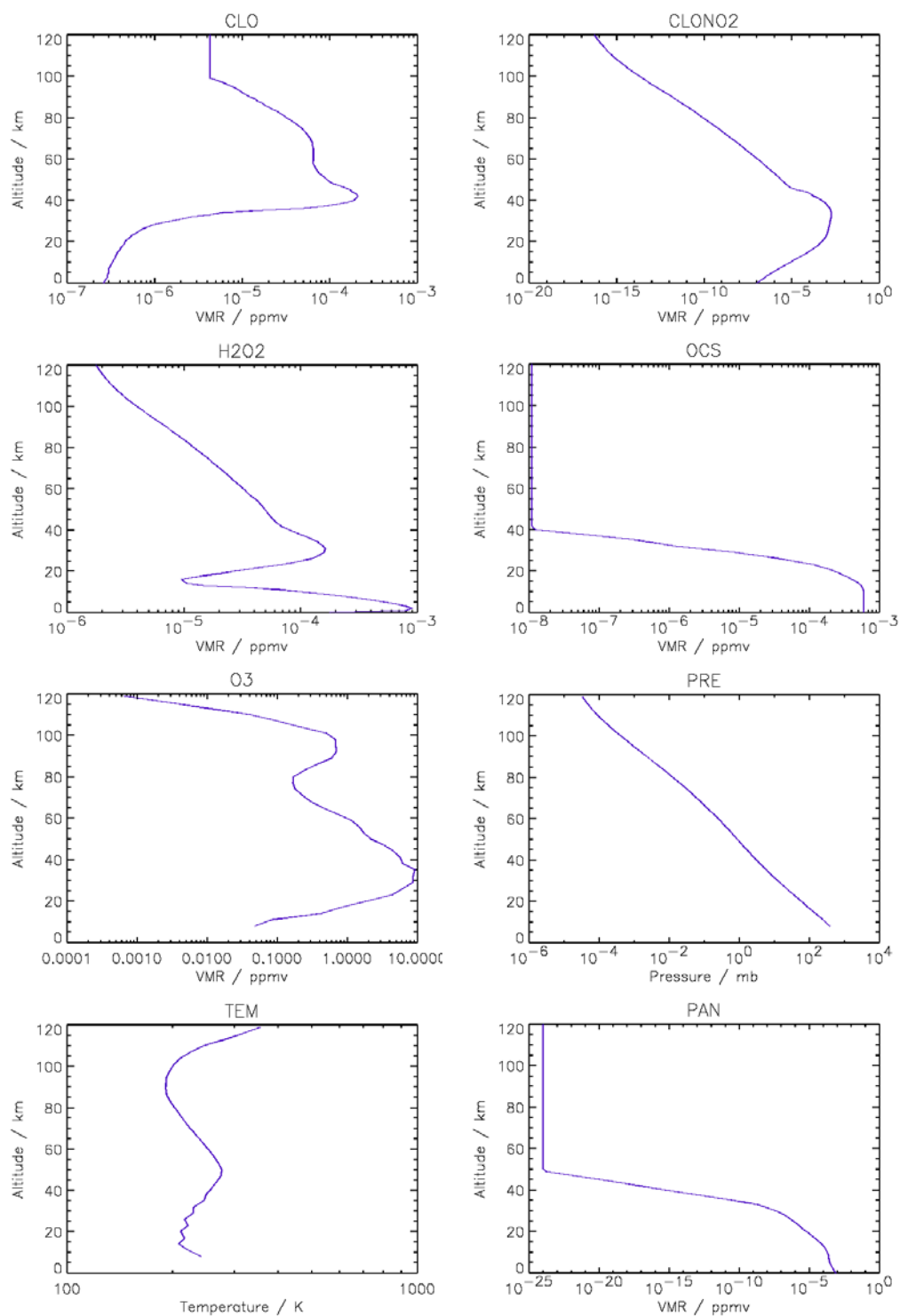


**Figure 5.11** Initial gas concentration (logarithmic scale) profiles (with altitude) for CIO, ClONO<sub>2</sub>, H<sub>2</sub>O<sub>2</sub>, OCS, O<sub>3</sub> and PAN and profiles for pressure and temperature included in simulated atmospheres in this thesis.

## 5.2.4 Spectral Fitting and Jacobian Analysis

Comparing the PAN radiance contributions for the chosen bands (see Figure 5.7) with the total simulated spectrum (Figure 5.6), we see that it is not possible to observe spectral features of PAN in the total spectrum directly. Detection is therefore based here on the analysis of spectral “residuals”. Residual spectra are defined as difference spectra of a total measured or simulated spectrum and another simulated atmospheric spectrum that excludes PAN in its simulated atmosphere. A measured residual spectrum,  $\Delta X$ , is defined here as:

$$\Delta X(\tilde{\nu}) = R_x(\tilde{\nu}) - R_{y-PAN}(\tilde{\nu}) \quad (5.1)$$

where  $\Delta X$  is the measured residual spectrum as a function of wavenumber,  $\tilde{\nu}$ , and  $R_x$  and  $R_y$  are the measured and simulated spectra respectively. The  $R_{y-PAN}$  term describes a simulated spectrum with PAN excluded from the simulated atmosphere. A simulated residual spectrum,  $\Delta Y$ , is also defined here as:

$$\Delta Y(\tilde{\nu}) = R_y(\tilde{\nu}) - R_{y-PAN}(\tilde{\nu}) \quad (5.2)$$

Hence we see that for a perfect measurement with no associated error and for a numerically perfect simulation with accurate reference data and prior knowledge of all other influencing gas concentrations, then  $\Delta X = \Delta Y$ . In practice, however, this is not possible due to many sources of measurement error as well as errors due to the forward model. In addition,  $\Delta Y$  will not be perfect because of errors in spectroscopic data, uncertainties in the profiles of other gases and as well as approximations in the forward model.

This method can also be adopted in calculating the expected contributions to total spectral radiance from other gases. Simulated spectral radiance contributions ( $\Delta Y$ ) at 10.4 km, calculated for each gas listed in Table 5.4, are plotted for each spectral region in Figure 5.12-Figure 5.14 and Figure 5.15-Figure 5.17 respectively. The  $\Delta Y$  spectrum for PAN is shown as the first plot in each of the figures. We see from such spectra that the characteristic broadband shape of the PAN band in each channel is simulated to be clearly visible above the average noise level (shown as the dashed lines

in all plots). The points of low radiance contribution within each PAN band are due to strong absorption by sharp spectral lines of other trace gases. For channel 1, these lines are noted to be due to ozone, carbon dioxide and water vapour, whilst in channel 2, they are noted to be due to ozone, nitrous oxide and water vapour.

Such  $\Delta Y$  spectra for each gas are useful in the analysis of  $\Delta X$ , since any residual spectral feature in  $\Delta X$  seen to resemble a  $\Delta Y$  spectral feature for a particular gas is likely to be due to that gas. Such a feature would therefore represent an under or overestimate of that gas in the simulation depending on whether the residual is positive or negative with respect to the spectral baseline respectively.

Along with simulated radiance spectra, it is also possible to calculate Jacobian perturbation spectra using the RFM. Here, Jacobian spectra are calculated as a difference spectrum at some tangent altitude calculated for a change of  $\pm 1\%$  in the gas concentration at a specified profile altitude. For pressure and temperature, such Jacobian spectra represent a  $\pm 1$  mb and  $\pm 1$  K change respectively, whilst for aerosol, such spectra represent a change of  $\pm 1 \times 10^{-4} \text{ km}^{-1}$  in the extinction coefficient. It may be possible to improve the  $\Delta X$  spectral fit by adding or subtracting such perturbation spectra and use the magnitude of such perturbation to approximate the inaccuracy in corresponding parameters used in simulated atmospheres for the original forward calculation of the spectrum.

This information can then be used to modify the simulated atmosphere before calculation of a new spectrum. Such a process may be repeated iteratively to obtain the best spectral fit between  $\Delta X$  and  $\Delta Y$ . The fitted state parameters at the highest altitude are then used as the initial guess to successively lower altitudes. In performing such a spectral fit over such a large spectral region iteratively for successively lower tangent altitudes, this method is analogous to a combination of the global fitting and onion peeling retrieval methods described in Section 2.3; with the exception that the convergence criterion here is based on the visual inspection of spectral residuals. This is necessary as automated methods cannot easily handle a global fit of such a large spectral region for a weak spectral signal such as that from PAN. In the remainder of this chapter, the detection of PAN is based on this principle.

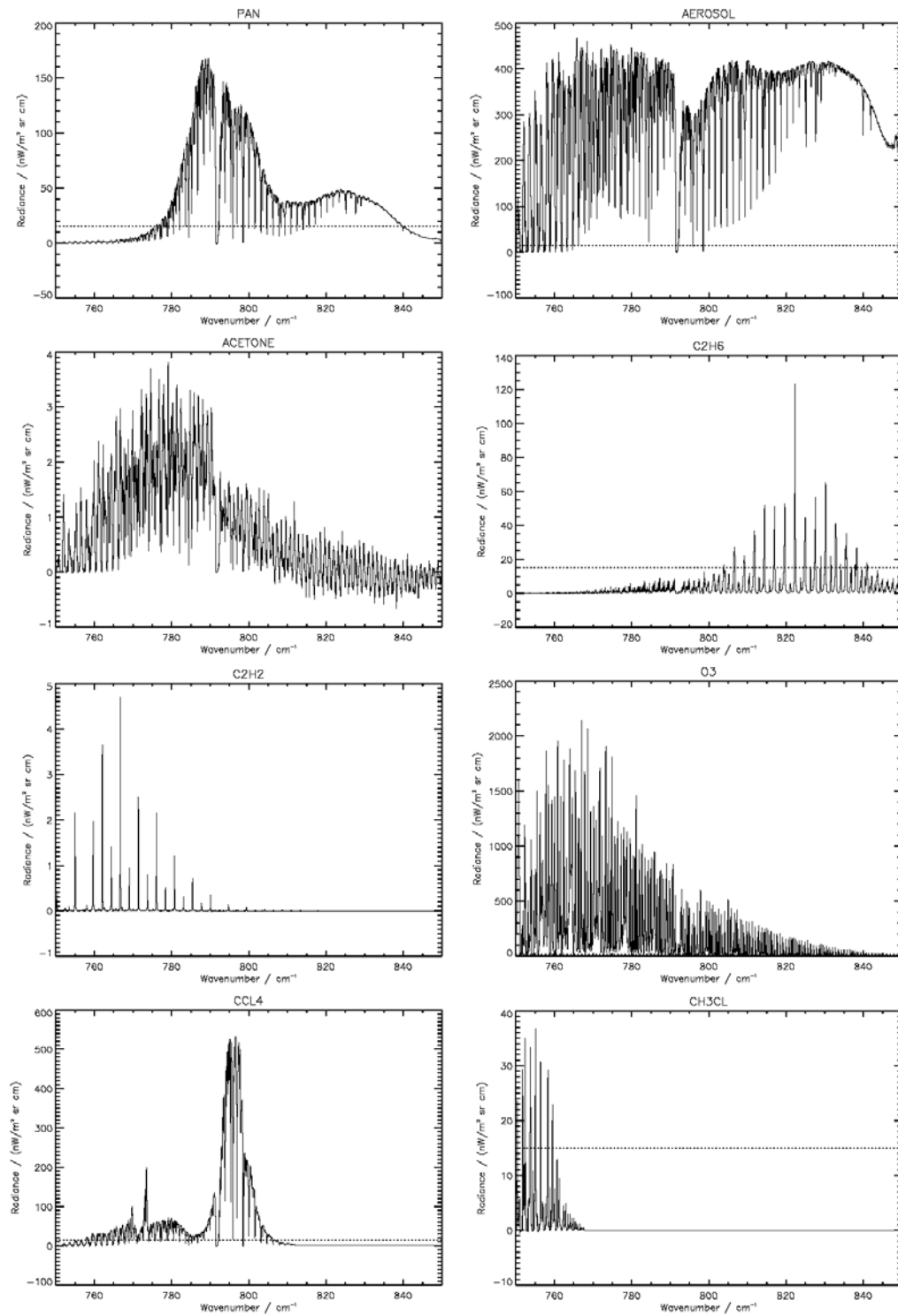


**Figure 5.12** Simulated contributed radiance for: PAN, aerosol, acetone, ethane, ethyne, ozone,  $\text{CCl}_4$  and  $\text{CH}_3\text{Cl}$ , to total limb-emission spectrum at 10.4 km simulated for MIPAS-B2- channel 1 over spectral window of interest for the 794  $\text{cm}^{-1}$  PAN band. Plots show  $\Delta Y$  spectra calculated for each gas included in the simulated atmosphere.

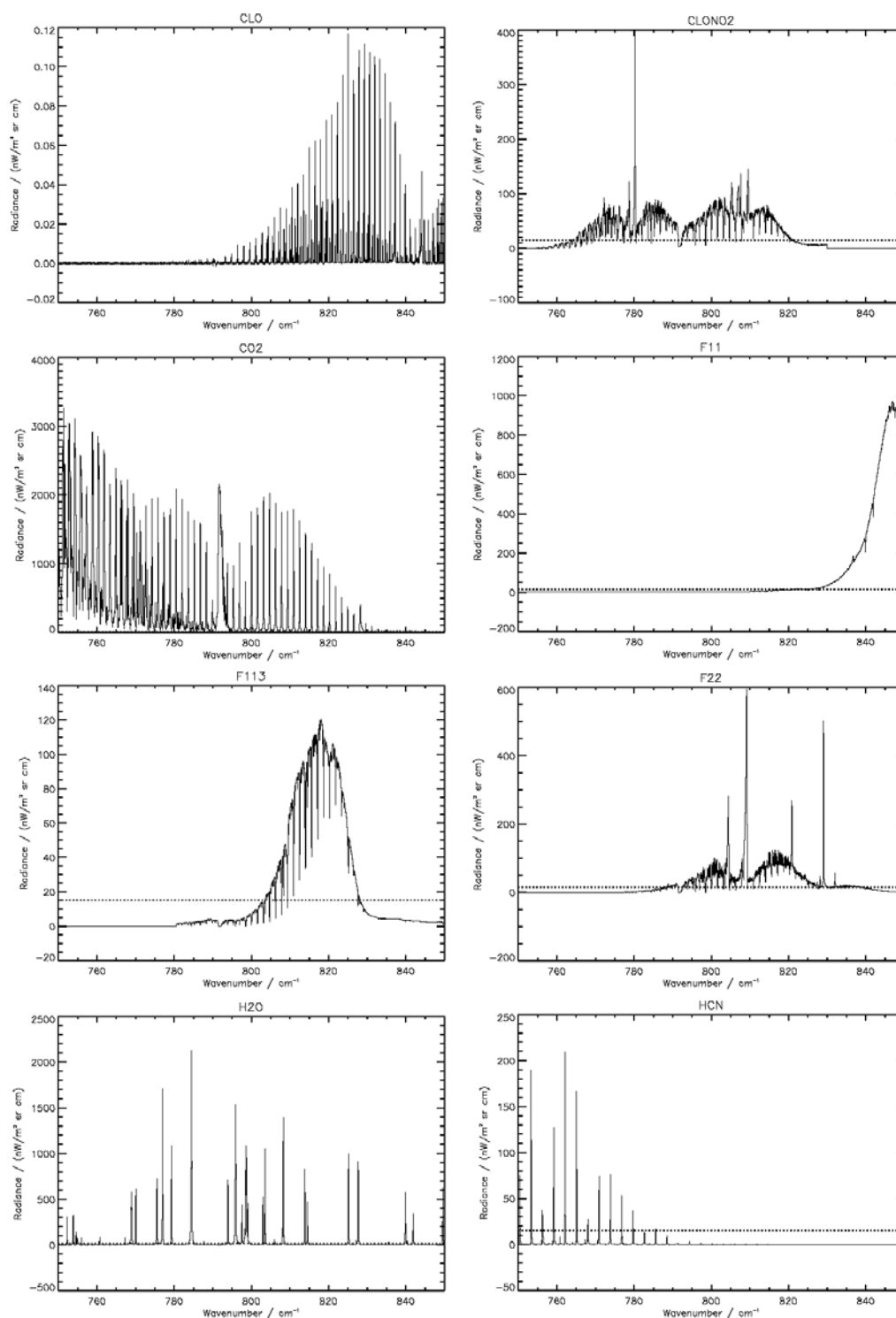


**Figure 5.13** Simulated contributed radiance for: CIO, CIONO<sub>2</sub>, CO<sub>2</sub>, F11, F113, F22, H<sub>2</sub>O and HCN, to total limb-emission spectrum at 10.4 km simulated for MIPAS-B2-channel 1 over spectral window of interest for the 794 cm<sup>-1</sup> PAN band. Plots show  $\Delta Y$  spectra calculated for each gas included in the simulated atmosphere.



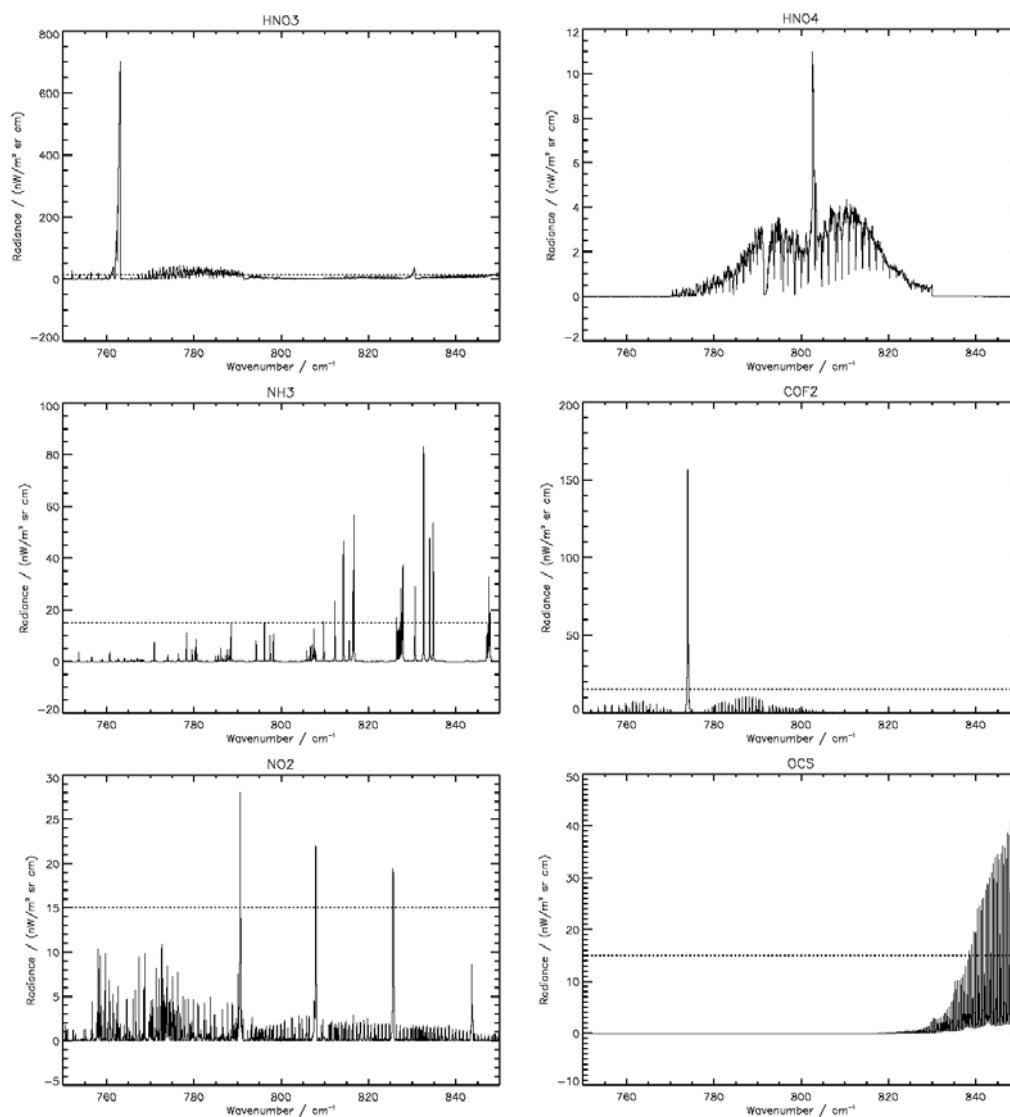


**Figure 5.14** Simulated contributed radiance for:  $\text{HNO}_3$ ,  $\text{HNO}_4$ ,  $\text{NH}_3$ ,  $\text{COF}_2$ ,  $\text{NO}_2$  and  $\text{OCS}$ , to total limb-emission spectrum at 10.4 km simulated for MIPAS-B2- channel 1 over spectral window of interest for the  $794\text{ cm}^{-1}$  PAN band. Plots show  $\Delta Y$  spectra calculated for each gas included in the simulated atmosphere.

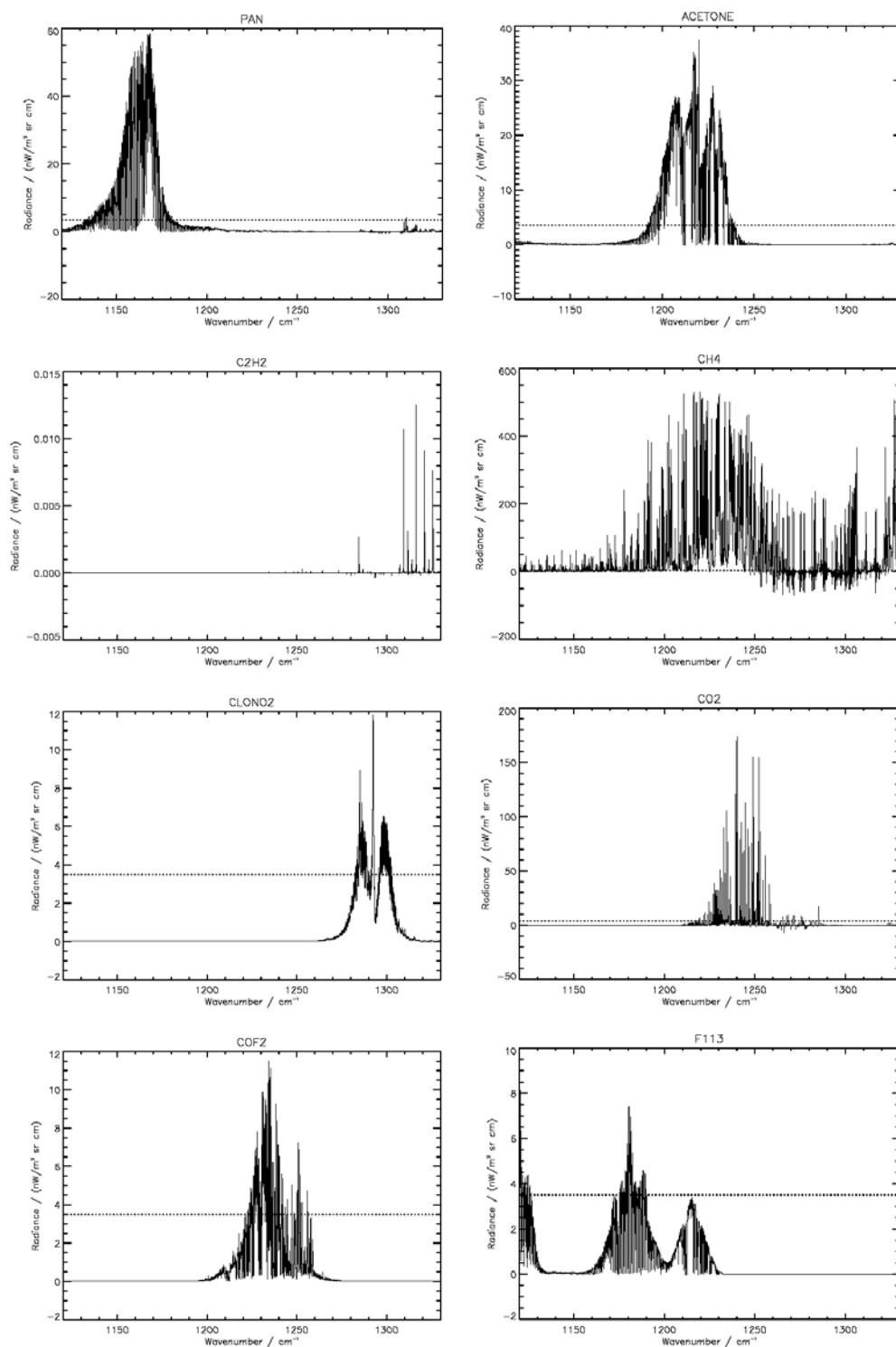


**Figure 5.15** Simulated contributed radiance for: PAN, acetone, ethyne, methane,  $\text{ClONO}_2$ ,  $\text{CO}_2$ ,  $\text{COF}_2$  and F113 to total limb-emission spectrum at 10.4 km simulated for MIPAS-B2- channel 1 over spectral window of interest for the 1163  $\text{cm}^{-1}$  PAN band. Plots show  $\Delta Y$  spectra calculated for each gas included in the simulated atmosphere.

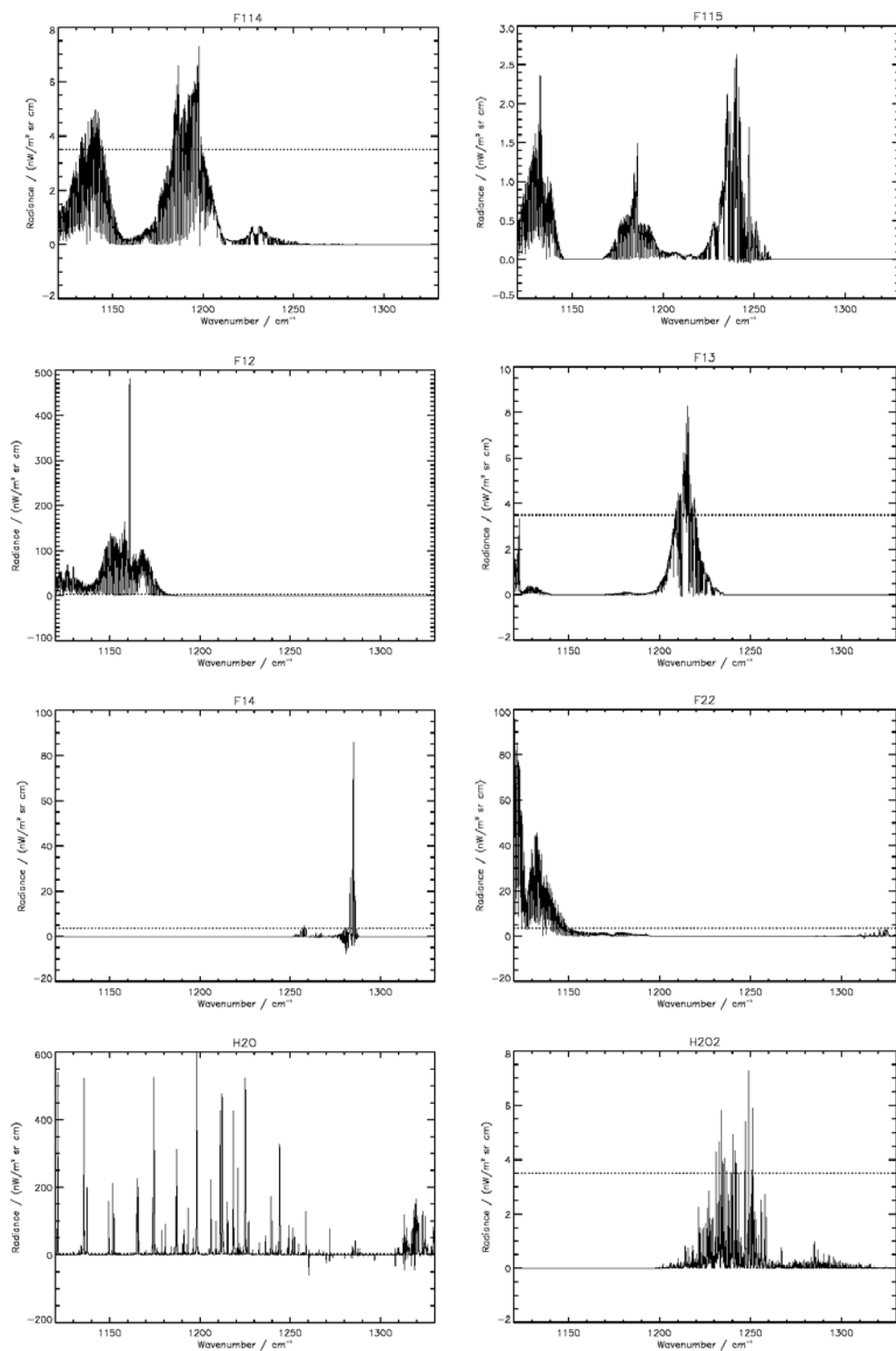


**Figure 5.16** Simulated contributed radiance for: F114, F115, F12, F13, F14, F22, H<sub>2</sub>O and H<sub>2</sub>O<sub>2</sub>, to total limb-emission spectrum at 10.4 km simulated for MIPAS-B2- channel 2 over the spectral window of interest for the 1163 cm<sup>-1</sup> PAN band. Plots show  $\Delta Y$  spectra calculated for each gas included in the simulated atmosphere.

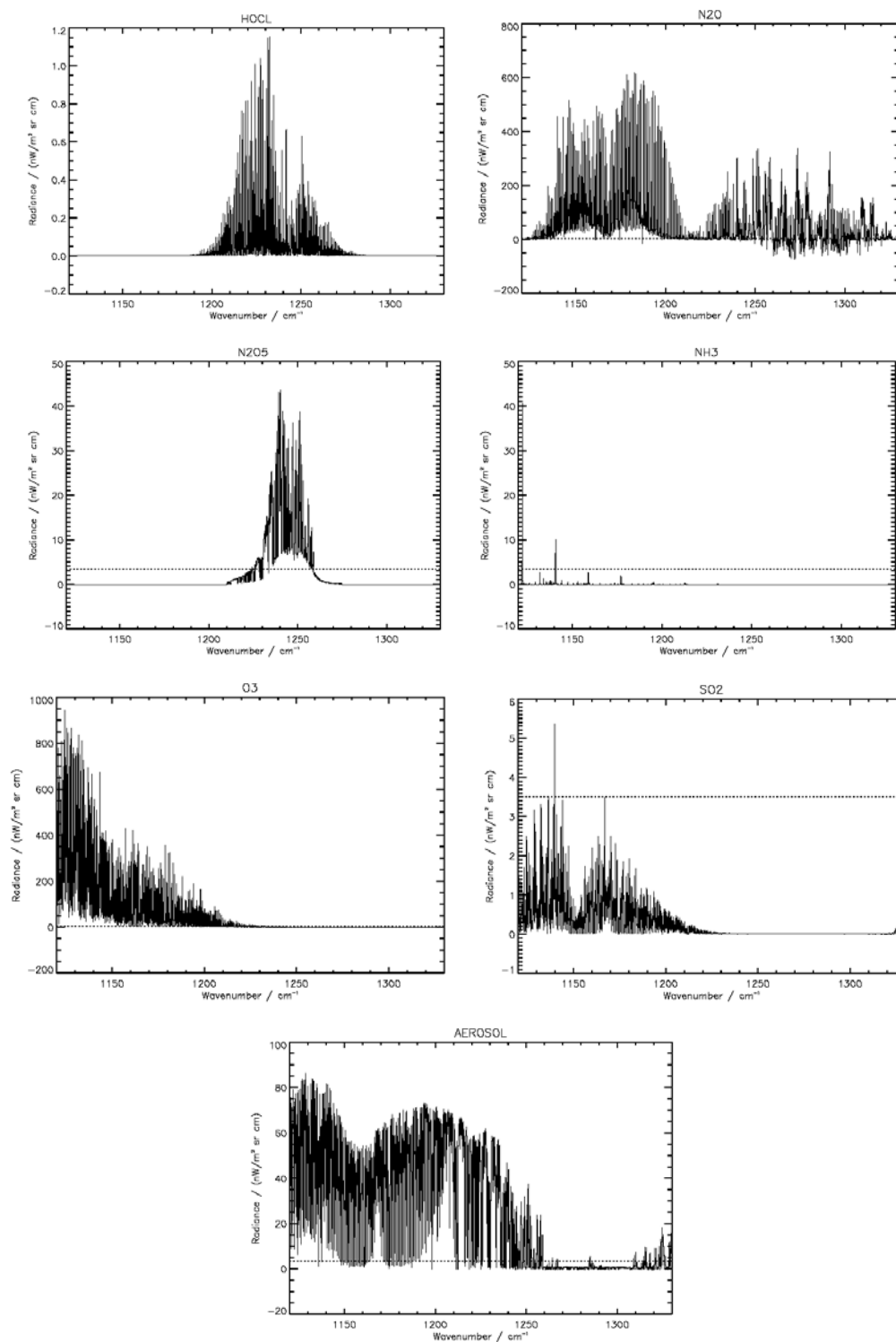


**Figure 5.17** Simulated contributed radiance for: HOCl, N<sub>2</sub>O, N<sub>2</sub>O<sub>5</sub>, NH<sub>3</sub>, O<sub>3</sub>, SO<sub>2</sub> and aerosol, to total limb-emission spectrum at 10.4 km simulated for MIPAS-B2- channel 2 over the spectral window of interest for the 1163  $\text{cm}^{-1}$  PAN band. Plots show  $\Delta Y$  spectra calculated for each gas included in the simulated atmosphere.

### 5.2.5 Wavenumber Shift

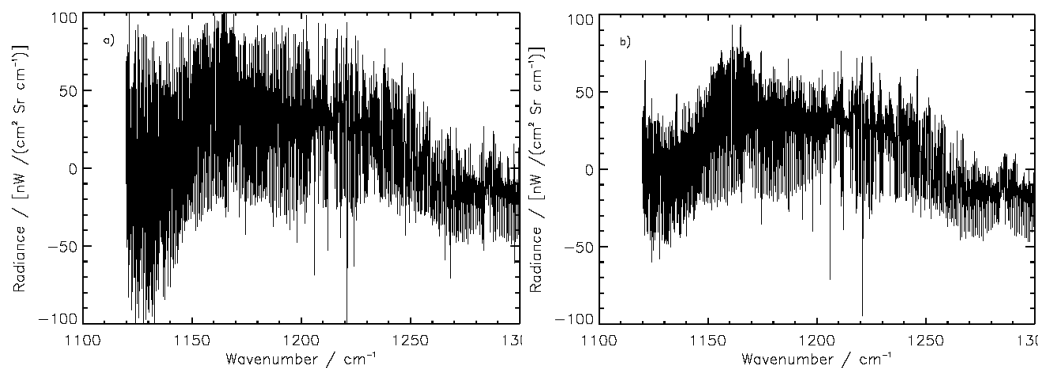
In the flight 6 spectral dataset, data processing by IMK determined and corrected for any wavenumber shift in the delivered spectra. However, this was not performed for the flight 8 spectra obtained for this thesis. Although, such spectral shift is small (found to be around half the spacing of adjacent spectral points), the potential error in residual spectra is found to be significant. Figure 5.18 illustrates the improvement in a typical spectral residual for channel 2 with a wavenumber shift correction made to the original spectral data. If uncorrected, this additional spectral “interference” would obscure any PAN signal.

The shift in wavenumber was estimated and corrected for by comparisons of uncorrected measured spectra with simulated spectra. Simulated spectra calculated with a spectral resolution of  $0.0005\text{ cm}^{-1}$ , and sampled at  $0.025\text{ cm}^{-1}$  intervals (equivalent to measured spectra), were subtracted from measured spectra. The required shift correction was then found by minimising the difference between the two spectra over spectral regions of interest. The magnitude of the shift was found to be similar at all altitudes (variation less than  $0.001\text{ cm}^{-1}$ ).

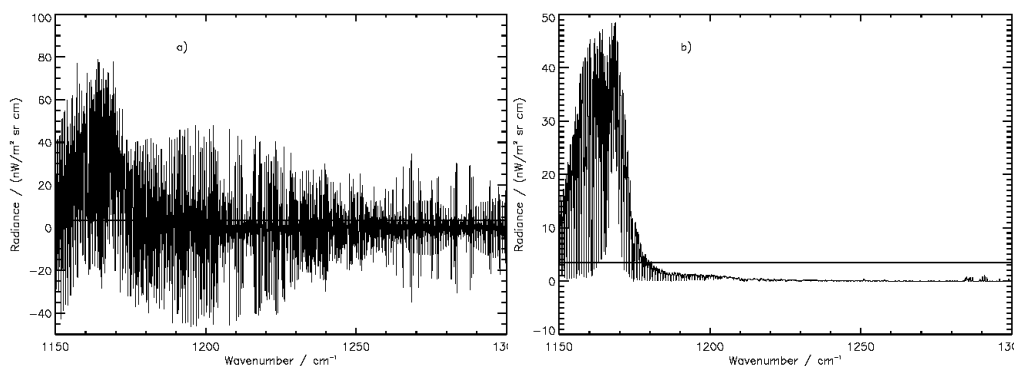
The magnitude of the wavenumber shift was found to vary as a function of wavenumber ( $0.002\text{ cm}^{-1}$  over  $200\text{ cm}^{-1}$  in channel 2 of flight 8). Therefore, the calculated wavenumber shift was calculated and applied to the flight 8 dataset in five equal spectral windows over the range of channel 2.

Figure 5.19 shows the difference between two simulated spectra; one with a simulated spectral shift of  $0.0075\text{ cm}^{-1}$ ; and the other unshifted. The large difference between Figure 6.12a and Figure 6.12b is similar to the difference seen in Figure 5.18 between real data with and without the same shift applied indicating that the shift applied to measured spectra is reasonable.

This method was also used to investigate the accuracy of the flight 6 wavenumber calibration, with no observable shift detected (less than  $0.0005\text{ cm}^{-1}$ ).



**Figure 5.18** An example of initial residual spectra for MIPAS-B2 flight 8 in channel 2 a) without wavenumber shift correction and b) with wavenumber shift correction of  $-0.0075 \text{ cm}^{-1}$ .



**Figure 5.19** Simulated PAN residual spectrum for flight 8 channel 2 with a) A  $-0.0075 \text{ cm}^{-1}$  wavenumber shift applied to the simulated spectrum and b) the simulated residual with no shift applied for comparison. Typical noise is also plotted. This simulates the spectral error of a comparison made with a poorly calibrated measured spectrum.

## 5.2.6 Results

This section presents the results of spectral fits and residual analysis of atmospheric limb spectra for MIPAS-B2 flight campaigns 6 and 8 in turn. Evidence for the detection and possibility of retrieving PAN from such analysis is also discussed. The accuracy of PAN concentrations retrieved using this method is discussed later in Section 5.4.

### 5.2.6.1 Flight 6 Channel 1

The optimised spectral fits and corresponding residual spectra, calculated from the Flight 6 dataset for channel 1 are shown in Figure 5.20 – Figure 5.22 for the three lowest measured tangent altitudes where PAN is expected to exist in sufficient quantity to be measurable above instrumental noise (determined from the initial PAN profile; see Figure 5.11). Residual and simulated spectra for channel 1 are both shown in these figures for comparison.

The top panel in each figure shows the measured spectrum (black) with the simulated spectrum (red). The fact that they are not easily resolved against each other is indicative of the excellent quality of the fit, with the difference between these spectra seen to approach the baseline noise level at all altitudes (plotted as a dashed line in the middle and lower plots in each figure).

Residual spectra, plotted in the central panel of Figure 5.20 – Figure 5.22, show the comparison of  $\Delta X$  (black) with  $\Delta Y$  (red) at each altitude for the full spectral range of channel 1. The characteristic PAN absorption band expected in  $\Delta Y$  is clearly observed in  $\Delta X$  around  $794.0\text{ cm}^{-1}$  at all altitudes.

At 13.5 km,  $\Delta X$  is seen to agree with  $\Delta Y$  to within the noise level ( $\pm 15\text{ nW}$  around  $\Delta Y$ ). At lower altitudes, with an increasing PAN radiance contribution, the signal to noise ratio of the PAN feature is greatly increased, although there is evidence of some sharper spectral features in  $\Delta X$  varying by as much as  $\pm 150\text{ nW}$  around  $\Delta Y$  for which it was not possible to improve further using the method described in this thesis. Such variations are clearly greater than the noise level and therefore attributable to some error in the fit for one or a number of other gases or parameters in the simulated atmosphere. The increased total radiance and the increased variability in all trace gases and aerosol in the troposphere, make accurate simulations of the atmosphere extremely difficult at lower altitudes with the potential also for scattering of radiation into the field of view of the instrument, which cannot be simulated here. However, although the fitting of spectra becomes more problematic at lower altitudes, the increase in the PAN radiance contribution does allow its spectral influence to be more readily observed.

In addition, it was found that initial profiles of pressure, temperature and some gases were not fitted accurately, although the iterative use of a Jacobian spectral analysis of residuals (see Section 5.2.4) yielded the excellent fits seen in each of the figures. In most cases, changes to the simulated atmosphere were required for aerosol

extinction as expected due to its high atmospheric variability, whilst changes to temperature and pressure profiles were typically small (1 K for temperature, 3 mb for pressure at 8.5 km).

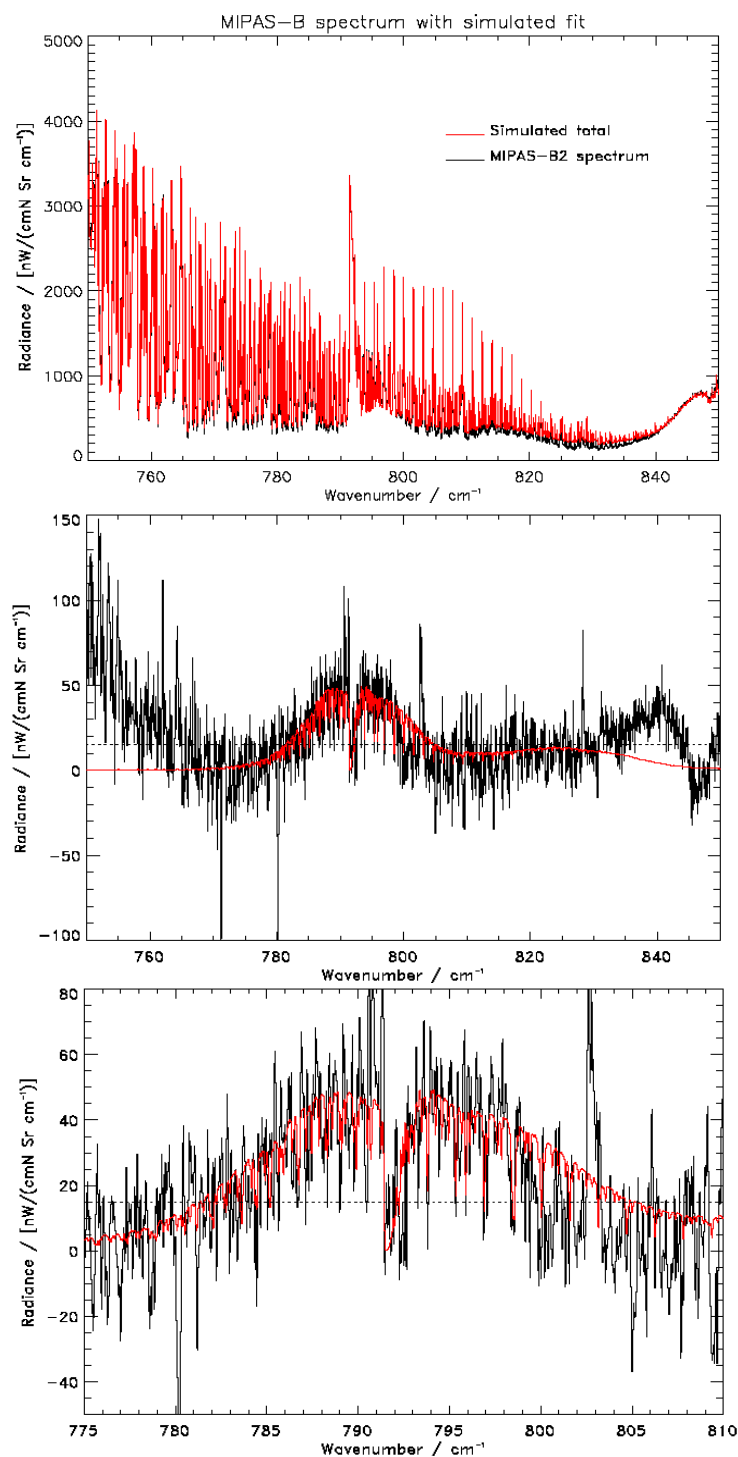


**Figure 5.20** Comparison of: top) simulated total (red) with measured (black) spectrum; middle)  $\Delta X$  (red) with  $\Delta Y$  (black); bottom) close-up of the 775-810 cm<sup>-1</sup> region, for channel 1 of Flight 6 at 13.5 km tangent altitude. PAN residual represents 70 pptv at 13.5 km.



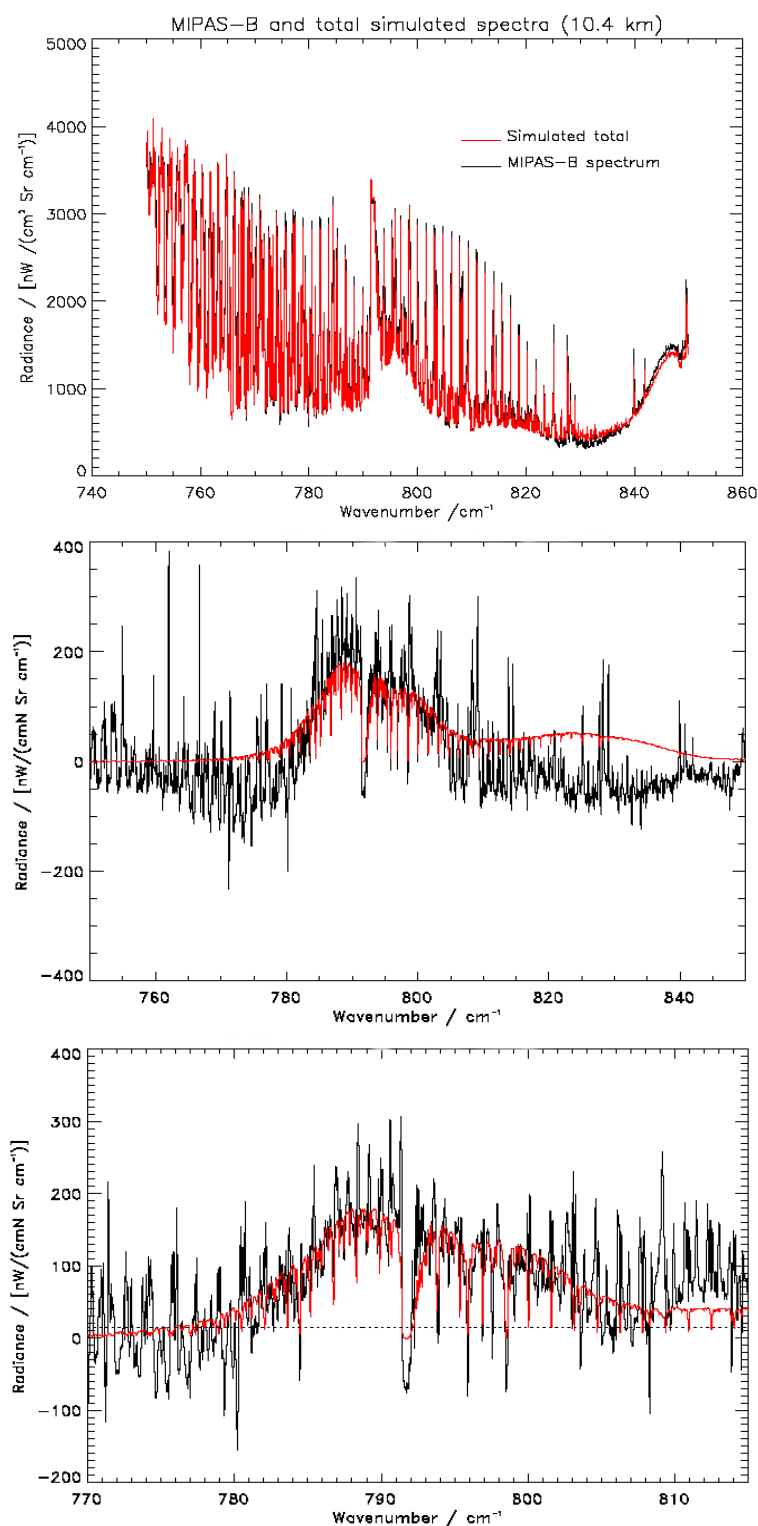


**Figure 5.21** Comparison of: top) simulated total (red) with measured (black) spectrum; middle)  $\Delta X$  (red) with  $\Delta Y$  (black); bottom) close-up of the 775-810  $\text{cm}^{-1}$  region, for channel 1 of Flight 6 at 10.4 km tangent altitude. PAN residual represents 180 pptv at 10.4 km tangent height.

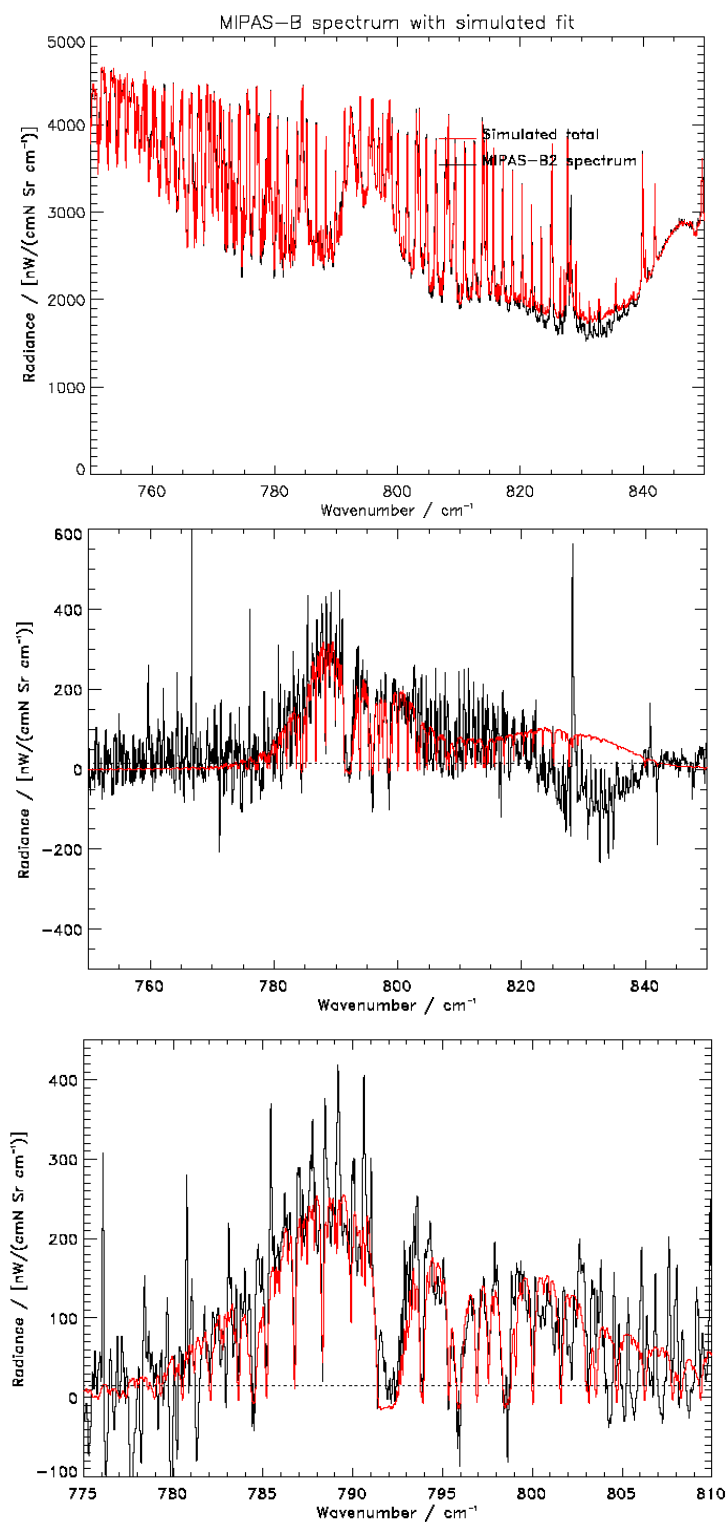


**Figure 5.22** Comparison of: top) simulated total (red) with measured (black) spectrum; middle)  $\Delta X$  (red) with  $\Delta Y$  (black); bottom) close-up of the 775-810  $\text{cm}^{-1}$  region, for channel 1 of Flight 6 at 8.5 km tangent altitude. PAN residual represents 260 pptv at 8.5 km tangent height.

An analysis of spectral features in Jacobian spectra compared to poorly fitted residual features can help to identify which parameters may be poorly fitted. Some residual features seen in the baseline of  $\Delta X$  in Figure 5.20 – Figure 5.22 are easily identified. Sharp spectral lines seen at all altitudes, with increasing intensity at lower altitudes are noted to be due to poorly fitted water vapour spectral lines. The intensities of such lines are a function of pressure, temperature and concentration. No improvement could be made on the fitting of these lines at these tangent altitudes using the water vapour spectral parameters in the HITRAN 2000 database. It is expected that the failure to completely fit these lines is due to small compound errors of water vapour spectral parameters as well as pressure, temperature and the water vapour concentration profile itself.

The fit within the region of interest for PAN ( $770\text{--}810\text{ cm}^{-1}$ ), displayed in the lower panels of Figure 5.20 – Figure 5.22, shows little evidence of any anomalous features with only a few poorly fitted water vapour lines and a small difference at 10.4 km in the fitting of the Q-branch of the  $\text{CO}_2$  ( $\nu_2$ ) hot band centred at  $791.5\text{ cm}^{-1}$ . Radiative transfer modelling of this feature is noted to be difficult, with the best results seen by using a Chi line shape for  $\text{CO}_2$  with line mixing included in radiative transfer calculations [Brown, personal communication]. Such parameters were used in this simulation and fitting of this feature was improved relative to the use of a Voigt line shape (see Section 2.4.1.4) without line mixing.

Furthermore, a notable artefact of the fitting process was that the  $\text{CCl}_4$  concentration profile had to be significantly increased from that assumed of the reference atmosphere described in Section 5.2.3.2. Fitted  $\text{CCl}_4$  concentrations at 8.5 km were increased to 125 pptv from 110 pptv. The  $\text{CCl}_4$  spectrum has a significant “broad band” feature across the same spectral range of the  $794\text{ cm}^{-1}$  PAN band, peaking at  $796\text{ cm}^{-1}$  (See Figure 5.7). Therefore care must be taken to accurately fit this feature in order to obtain an accurate fit for PAN, which could otherwise be easily masked. The  $\text{CCl}_4$  species is a controlled gas under the Montreal protocol [1987] and as a result, its concentration in the atmosphere has been steadily dropping since 1990 as a result of reduced anthropogenic emissions. The initial reference atmospheres used here for  $\text{CCl}_4$  were calculated in the year 2000 and therefore are expected to be less than those at the time of the Flight 6 campaign in 1998. The perturbed  $\text{CCl}_4$  concentration at 8.5 km used here compares exactly with that reported for 1998 by Montzka *et al.* [1999], which

charts the decrease in concentration of the gas over the time period of 1990-2000. The absence of any residual features of  $\text{CCl}_4$  in the  $780\text{ cm}^{-1}$  region in Figure 5.20 – Figure 5.22, where no influence from PAN exists, provides further proof that  $\text{CCl}_4$  has been well fitted.

In order to obtain the best agreement between  $\Delta X$  and  $\Delta Y$ , the original PAN concentration profile plotted in Figure 5.11 was perturbed by a scaling factor of 1.08. A comparison of these profiles is plotted below in Figure 5.23. The fitted PAN concentration at each altitude was that used in the simulated atmosphere to obtain the optimum correlation between  $\Delta X$  and  $\Delta Y$  over the range  $775\text{--}810\text{ cm}^{-1}$  at successively lower altitudes. These PAN concentrations were 260, 180 and 70 pptv at 8.5, 10.4 and 13.5 km respectively.

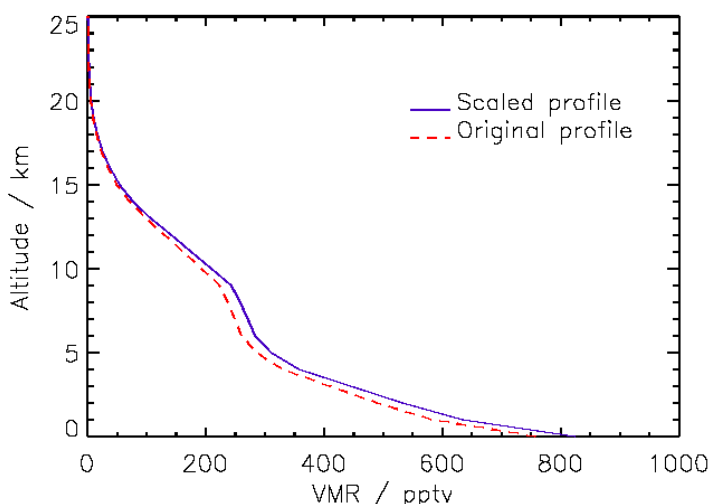


**Figure 5.23** PAN profile used to obtain the best simulated fit to MIPAS-B2 flight 6 data (blue), shown with a comparison to the original reference profile (red).

As noted in Section 5.2.3.1, the channel 1 spectral window includes radiance contributions from twenty-one gaseous species as well as aerosol. Due to strong (near saturated) absorption by species such as ozone and carbon dioxide, the spectrum in this region is also very sensitive to small changes in temperature and pressure, as well as aerosol. This is clearly evident by the high radiance and spectrally complex Jacobian spectra calculated for pressure, temperature and aerosol plotted in Figure 5.24, showing that relatively small differences in the accuracy of these parameters will cause large differences in simulated spectra and hence complex residual features. The quality of fits made in this study reflects the accuracy of such parameters used in these simulations.

The modified aerosol extinction profile is determined by a fit to the spectral baseline. Accurate determination of aerosol extinction is extremely difficult due to the prerequisite accuracy in retrievals of pressure, temperature and concentrations of many other gases. Such residual evidence of poorly fitted aerosol is not seen in this investigation through careful fitting, although the importance of aerosol is noted to be a key problem in detecting trace gases at lower altitudes. Due to the steep decreasing gradient in aerosol extinction in the upper troposphere, this effect is expected to be less significant at higher altitudes. Furthermore, such fitting of the aerosol “continuum”, essentially accounts for any baseline offset that may be present due to instrumental error.

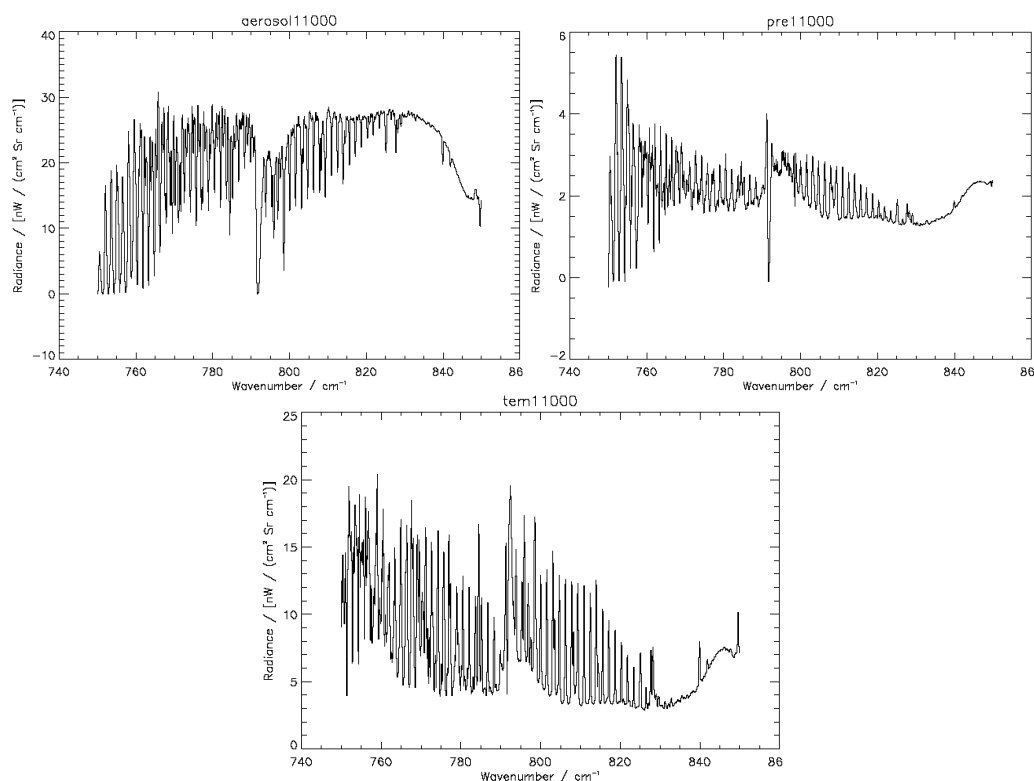


**Figure 5.24** Jacobian perturbation spectra at 10.5 km for a change at 11km level of: upper-left)  $1 \times 10^{-4}$  increase in extinction for aerosol; upper-right) 1 mb change in pressure; and lower) 1 K change in temperature.

In summary, this method provides strong evidence for the successful detection of PAN at all altitudes studied in channel 1 for flight 6. The small, but significantly greater than NESR, simulated radiance contribution ( $60 \text{ nW cm}^{-1} \text{ sr}^{-1} \text{ cm}^{-1}$ ) due to PAN at 13.5 km shows that it may be possible to detect PAN at typical concentrations (assumed here to be 70 pptv) at this altitude in the Northern Hemisphere mid-latitudes.

However, the small relative PAN radiance contribution to the total measured radiance (approximately 4% to at 13.5 km), illustrates the necessity for accurate retrieval or prior knowledge of all other atmospheric state profiles. This is also true for lower altitudes with radiance contributions for PAN of only 10% at 10.4 km and around 5% at 8.5 km.

#### **5.2.6.2 Flight 6, Channel 2**

The perturbed PAN profile, optimised for spectral fitting in channel 1 was then used for simulations of channel 2 spectra for the same three tangent altitudes. Figure 5.25 to Figure 5.27 show spectral fits and corresponding residuals similar to those plotted for channel 1 in the previous section. The fits between measured and simulated spectra are again seen to be excellent at all altitudes, reflected by good baselines in  $\Delta X$  with primarily only measurement noise.

In general, the quality of fits for channel 2 over the wider spectral region (1130-1330  $\text{cm}^{-1}$  in the centre plot of each figure) is a little better than for channel 1 at all altitudes. Although the PAN feature is not distinguished at 13.5 km (see Figure 5.25) due to an extremely weak contribution in this channel, the modelled spectral fit at this altitude is seen to be well fitted, with only residual baseline noise seen in  $\Delta X$  (lower panel of Figure 5.27). However, the weaker PAN radiance contribution to Channel 2 relative to Channel 1 at this altitude, make any residual feature of PAN extremely hard to distinguish from background noise at all altitudes.

However, a clear spectral feature of PAN is observed in residual spectra at tangent altitudes of 10.4 and 8.5 km (where PAN concentration is sufficiently high) in the centre and lower panels of Figure 5.26 and Figure 5.27 respectively. The  $\Delta X$  feature is in good agreement with the fitted  $\Delta Y$  for the 1163  $\text{cm}^{-1}$  PAN band at both altitudes. In addition to the general agreement between  $\Delta X$  and  $\Delta Y$  at lower altitudes, the magnitude (radiance) of the PAN feature is also in excellent agreement for the same PAN concentrations fitted for channel 1.

The repeated detection of a spectral feature that closely matches that of PAN in two independent measurement channels using the same PAN concentration profile is convincing evidence of its detection. In addition, the match between the strength of the residual and measured PAN feature for both channels (using the same PAN concentration profile) also reflects the quality of the reference PAN spectrum and show that the detected concentration is highly consistent.

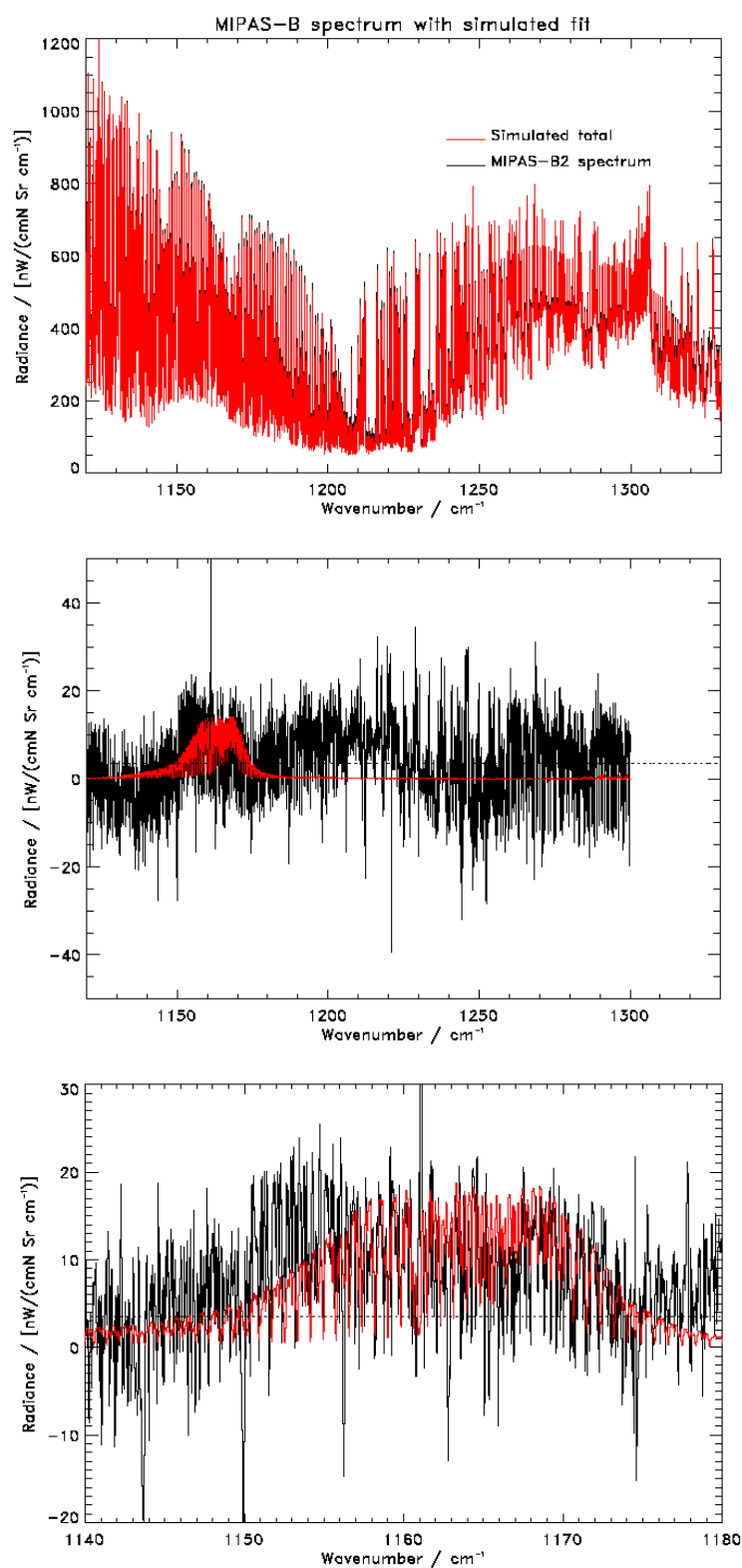


**Figure 5.25** Comparison of: top) simulated total (red) with measured (black) spectrum; middle)  $\Delta X$  (red) with  $\Delta Y$  (black); bottom) close-up of the 1140-1180  $\text{cm}^{-1}$  region, for channel 2 of flight 8 at 13.5 km tangent altitude. PAN residual represents 70 pptv at 13.5 km tangent height.

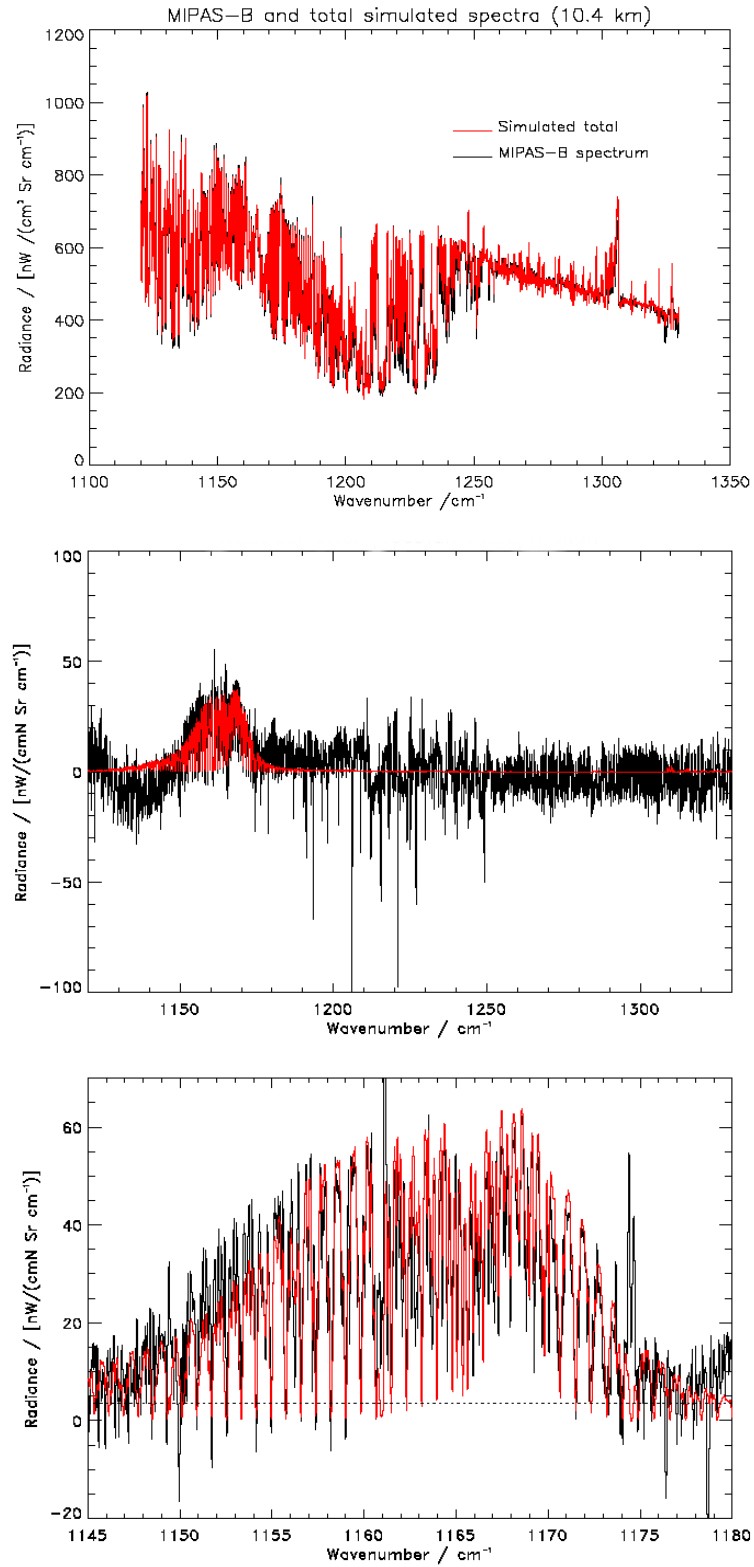


**Figure 5.26** Comparison of: top) simulated total (red) with measured (black) spectrum; middle)  $\Delta X$  (red) with  $\Delta Y$  (black); bottom) close-up of the 1140-1180  $\text{cm}^{-1}$  region, for channel 2 of flight 8 at 10.4 km tangent altitude. PAN residual represents 180 pptv at 10.4 km tangent height.



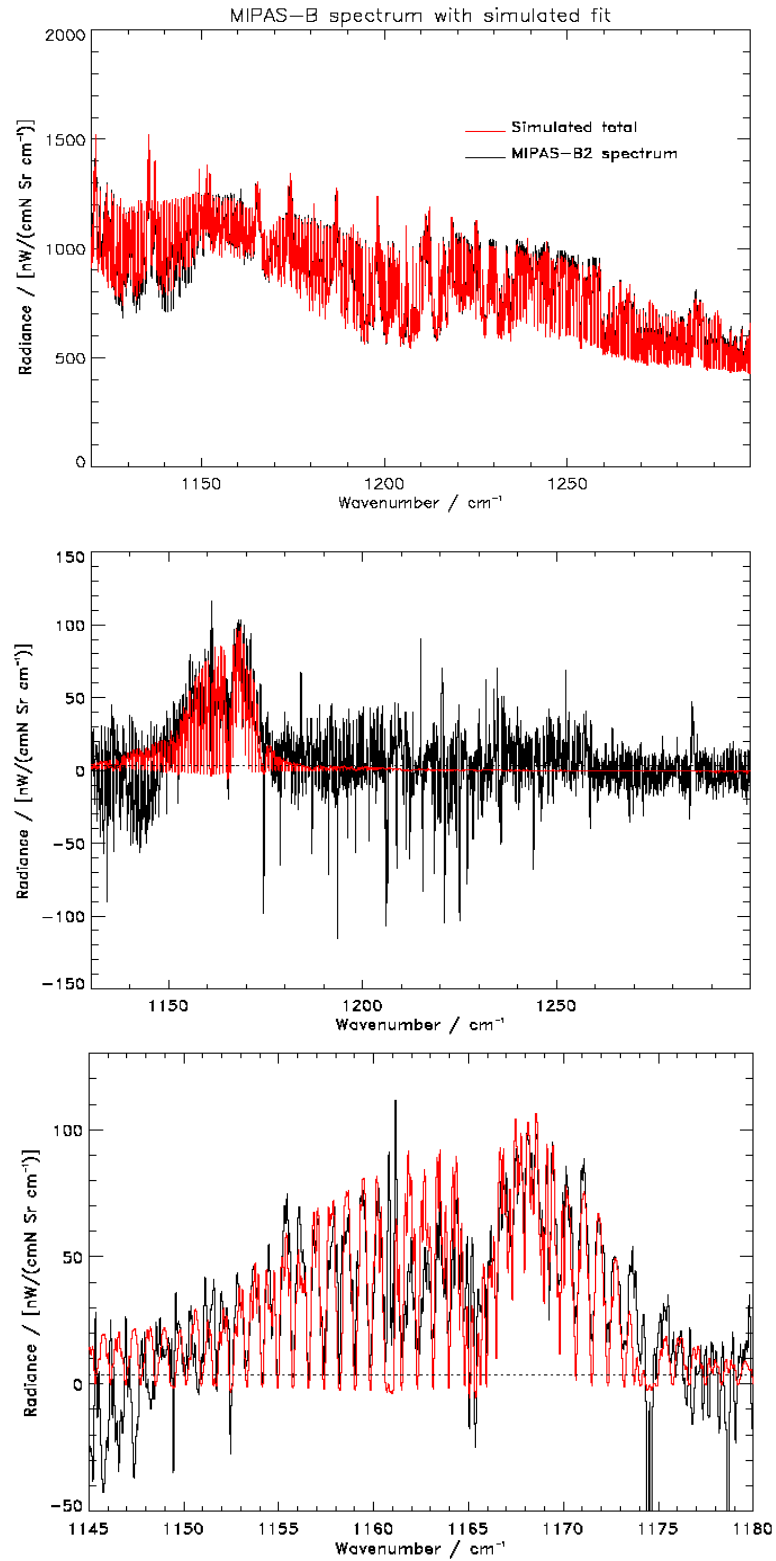


**Figure 5.27** Comparison of: top) simulated total (red) with measured (black) spectrum; middle)  $\Delta X$  (red) with  $\Delta Y$  (black); bottom) close-up of the 1140-1180  $cm^{-1}$  region, for channel 2 of flight 8 at 10.4 km tangent altitude. PAN residual represents 260 pptv at 8.7 km tangent height.

The spectral window chosen for channel 2 is less problematic than that of channel 1 for many reasons. Firstly, spectral noise in channel 2 is significantly lower with an average NESR of  $3.5 \text{ nW sr}^{-1} \text{ cm}^{-2} \text{ cm}^{-1}$ , compared to  $15 \text{ nW cm}^{-2} \text{ sr}^{-1} \text{ cm}^{-1}$  in channel 1. Also, the number of interfering gases is reduced and the spectral signatures of such gases do not significantly mask the  $1163 \text{ cm}^{-1}$  PAN band.

The sharp line features observed in the  $1170 - 1250 \text{ cm}^{-1}$  region at 10.4 and 8.5 km are again due to water vapour and can not be improved further for the same reasons discussed earlier for channel 1. However, these water lines do not significantly influence the  $1163 \text{ cm}^{-1}$  PAN band, which is clearly observed against the excellent baseline.

In summary, the smaller radiance contributions of PAN at typical concentrations in channel 2, relative to channel 1 at all altitudes, make detection of PAN using the  $1163 \text{ cm}^{-1}$  PAN band more difficult than using the  $794.0 \text{ cm}^{-1}$  band, although this spectral region may be easier to fit spectroscopically.

### **5.2.6.3 Flight 8, Channel 2**

This same analysis was performed for the flight 8 dataset for the available data in channel 2 with similar results to those observed for flight 6. Three flight 8 measurements with tangent altitudes of 8.6, 10.7 and 13.7 km were chosen here for consistent analysis with those in Flight 6 with additional tangent altitudes measured during flight 8 at 9.6 and 11.7 km.

Comparing flight 8 spectral fits in Figure 5.28 to Figure 5.32 with corresponding spectral fits for flight 6 in Figure 5.25 to Figure 5.27 shows that the quality of baseline fits for flight 8 are marginally poorer than those seen in flight 6 with apparent baseline noise of around 20 nW compared with around 10 nW in flight 6. This is possibly due to error introduced in using a constant spectral shift where, in reality, there may be small variations in the spectral shift with wavenumber (see Section 5.2.5) as well as an increased NESR for flight 8.

Similar problems with fitting water vapour lines are also seen with increasing significance at lower altitudes although these do not significantly influence the  $1163 \text{ cm}^{-1}$  PAN feature, which is clearly seen against the surrounding baseline and spectral noise at altitudes below 11.7 km. However, the increased baseline noise, coupled with

low PAN radiance contribution at 11.7 and 13.7 km make the PAN feature indistinguishable from the residual background at these heights.

Although spectral fits at higher altitudes are generally improved due to better characterisation of other gases, detection of PAN at these altitudes in this spectral range would require a spectrometer with noise levels significantly below that of the PAN residual, which is around 5 nW at 13 km.

Excellent residual fits are seen at altitudes of 10.7, 9.6 and 8.6 km in Figure 5.30, Figure 5.31 and Figure 5.32 respectively, supporting previous results for flight 6 that the  $1163\text{ cm}^{-1}$  PAN band is suitable for PAN detection only at lower altitudes.

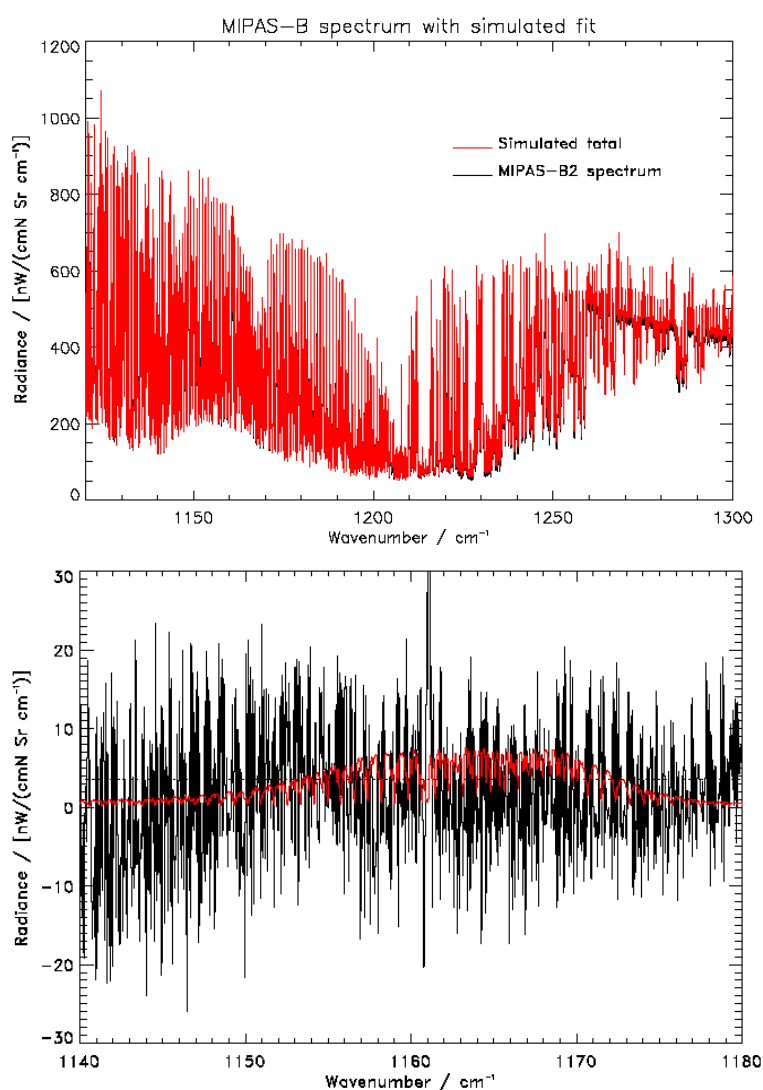


**Figure 5.28** Comparison of: top) simulated total (red) with measured (black) spectrum; bottom) close-up of the  $1140\text{--}1180\text{ cm}^{-1}$  region, for channel 2 of flight 8 at 13.7 km tangent altitude. PAN residual represents 90 pptv at 13.7 km tangent height.

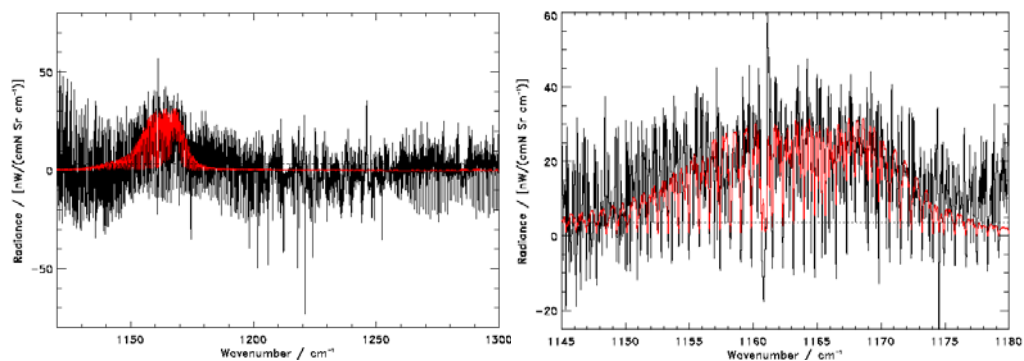


**Figure 5.29** Comparison of: left) simulated total (red) with measured (black) spectrum; right) close-up of the 1140-1180  $\text{cm}^{-1}$  region, for channel 2 of flight 8 at 11.7 km tangent altitude. Simulated PAN residual represents 170 pptv at 11.7 km tangent height.

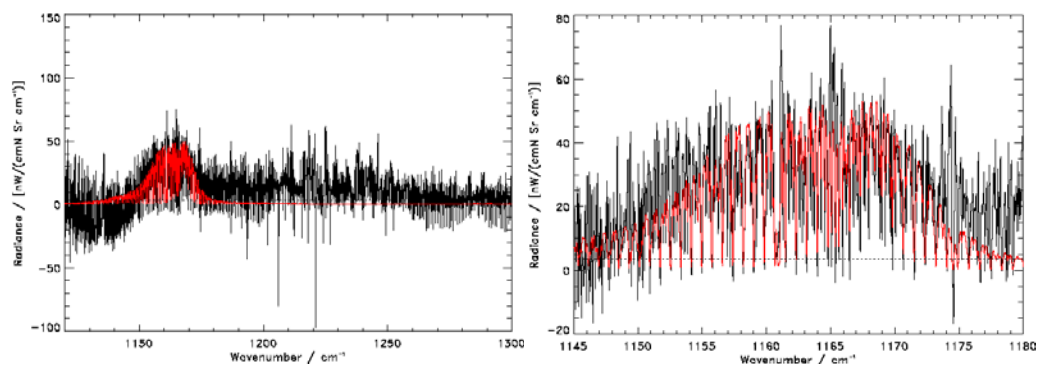


**Figure 5.30** Comparison of: left) simulated total (red) with measured (black) spectrum; right) close-up of the 1140-1180  $\text{cm}^{-1}$  region, for channel 2 of flight 8 at 10.7 km tangent altitude. PAN residual represents 230 pptv at 10.7 km tangent height.

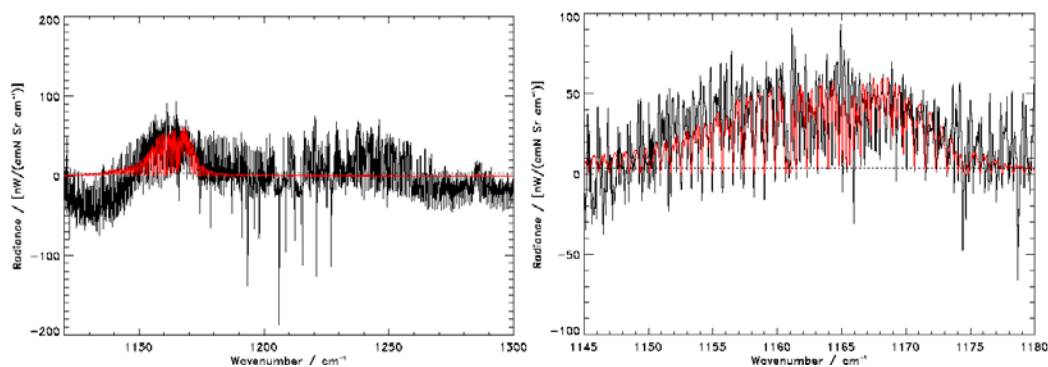


**Figure 5.31** Comparison of: left) simulated total (red) with measured (black) spectrum; right) close-up of the 1140-1180  $\text{cm}^{-1}$  region, for channel 2 of flight 8 at 9.6 km tangent altitude. PAN residual represents 310 pptv at 9.6 km tangent height.

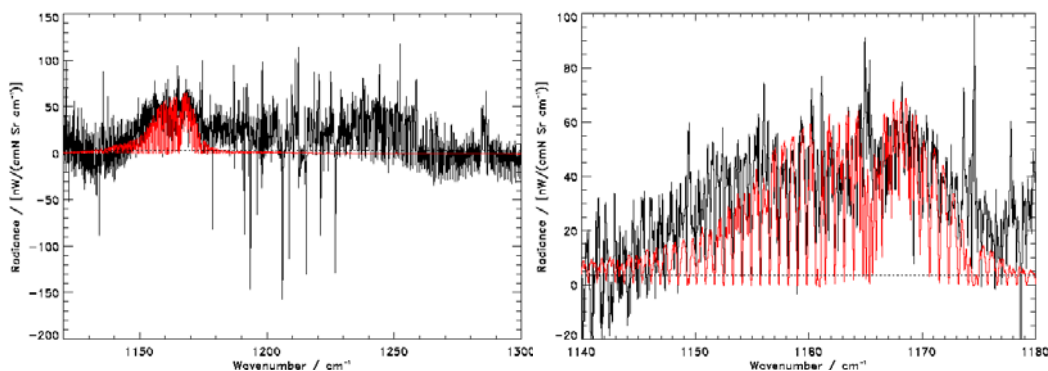


**Figure 5.32** Comparison of: left) simulated total (red) with measured (black) spectrum; right) close-up of the 1140-1180  $\text{cm}^{-1}$  region, for channel 2 of flight 8 at 8.5 km tangent altitude. PAN residual represents 350 pptv at 8.5 km tangent height.

The stronger residual associated with the fitted PAN feature at lower altitudes suggests a stronger true PAN concentration. In order to achieve the optimised fit to these data, the assumed PAN profile here was perturbed significantly from the reference profile (see Figure 5.33), indicating that the concentration of PAN in the atmosphere for this campaign was stronger than that inferred earlier for flight 6 in May 1998.

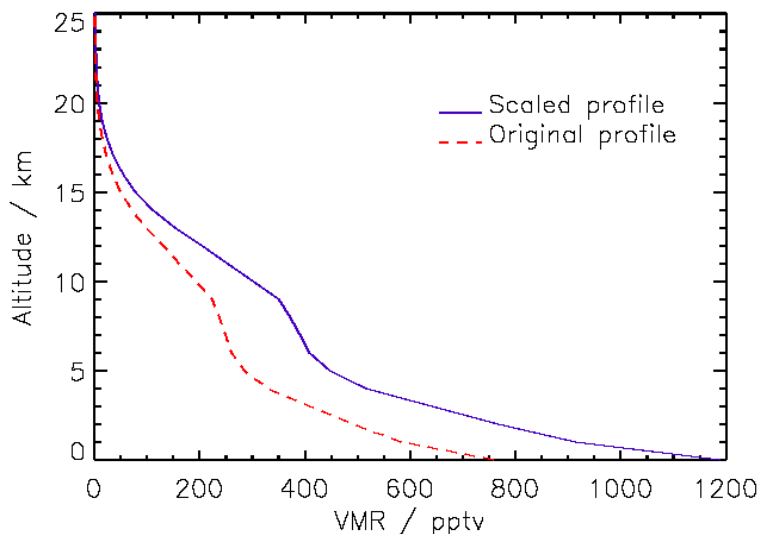


**Figure 5.33** PAN profile used to obtain the best simulated fit to MIPAS-B2 flight 8 data (blue), shown with a comparison to the original chosen characteristic profile (red).

PAN profile concentrations used at 8.5, 9.6, 10.7, 13.7 and 11.7 km in this simulation were 350, 310, 230, 170 and 90 pptv respectively. This is considerably larger than those fitted for flight 6, although not particularly extreme, with maximum values

predicted by Lelieveld [2002] of up to 500 pptv at 8 km in the nearby Eastern Mediterranean region during UT pollution episodes.

### **5.3 Further Evidence and Considerations for the Detection of PAN**

The analysis of residual spectra described in the previous section, provides a strong indication of the presence of PAN in upper tropospheric balloon spectra. However, the existence of other very weak residual spectral signatures, arising from contributions from other gases, imperfectly known atmospheric conditions, as well as spectroscopic and instrumental errors, require further characterisation to allow the most accurate retrieval of PAN concentrations using this method. In this section, further evidence in support of the detection of PAN, as well as possible problems with its identification, which have not yet been resolved, are discussed.

#### **5.3.1 Shape of the PAN Band**

As seen in many of the figures in the previous section, the residual features present in MIPAS-B2 spectra correlate very well with the expected PAN signature for both spectral channels. This is reflected by the way the shape of the PAN band simulated in  $\Delta Y$  is observed in  $\Delta X$  with increasing confidence at lower altitudes. The characteristic shape of the PAN band is clearly seen in the figures in the previous section when considering the broader shape of both the 794 and 1163  $\text{cm}^{-1}$  PAN bands at lower altitudes (less than 12 km). It should be noted that the apparent fine structure in the simulated residuals does not represent structure in the PAN reference spectrum, but rather illustrates the saturation effects of other gases in the same spectral region, principally  $\text{CO}_2$ ,  $\text{O}_3$  and  $\text{H}_2\text{O}$ . Wherever stronger absorbing gases have influence, the radiance contribution of PAN is reduced.

A test for the goodness of fit, or correlation, between fits of  $\Delta X$  to  $\Delta Y$ , is complicated by such saturation effects, making it difficult to distinguish such effects from poorly fitted spectral lines, for example. One way to assess the quality of the fit would be to neglect spectral regions exhibiting saturation and calculate the goodness of fit over the reduced range, thus only taking into account the broader shape of the PAN

band. However, such a method would not include any uncertainty due to poorly fitted lines of species causing saturation.

Another possibility that should be discussed in the context of band shape is the existence of other atmospheric trace gases not included in the forward model, which might have the same broad band spectral feature and peak as PAN. As discussed in section 5.2.3.1, three other compounds (dimethyl sulphate, trichlorophenol and methyl nitrate) were identified to have broad cross-sectional features in the region around 794.0  $\text{cm}^{-1}$  and may exist in very small quantities in the atmosphere. However, these three compounds are noted not to have an absorption feature in the region of the 1163  $\text{cm}^{-1}$  PAN band. Therefore, if such gases were to overlap with the 794.0  $\text{cm}^{-1}$  PAN feature, then there should be evidence of systematic differences between the 794 and 1163  $\text{cm}^{-1}$  residual features. Such differences were not observed, indicating that these compounds have negligible spectral influence on the 794.0  $\text{cm}^{-1}$  residual feature.

### 5.3.2 Variation with Altitude

Typical PAN concentration profiles are seen to decrease extremely rapidly with altitude through the tropopause (see Figure 5.11). This sharp decrease is observed in the previous section by a rapid decrease in the PAN residual signal between 10 and 13 km. It is possible to see this effect more clearly by differencing measured spectra and comparing them with difference spectra of simulations at two altitudes above and below the likely tropopause region using the following method:

$$[\text{MIP}_{13.5 \text{ km}} - \text{MIP}_{10.4 \text{ km}}] - [\text{SIM}_{13.5 \text{ km}} - \text{SIM}_{10.4 \text{ km}}]$$

where MIP corresponds to MIPAS-B2 measured spectra at the altitude indicated in the subscript, whilst SIM refers to simulated spectra at the same altitudes.

Figure 5.34 shows this difference, which enhances those spectral features that change rapidly between 10.4 and 13.5 km tangent altitudes. The characteristic 794  $\text{cm}^{-1}$  and 1163  $\text{cm}^{-1}$  PAN bands are seen in their respective channels indicating that PAN concentration is decreasing rapidly in line with the decrease expected using the scaled PAN profile.

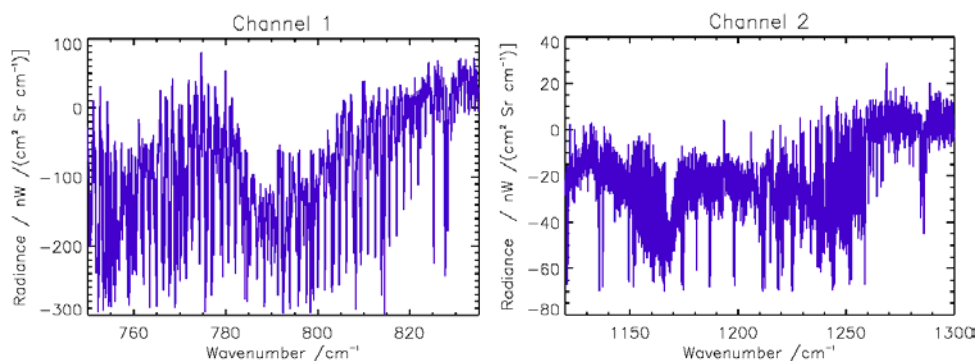


**Figure 5.34** Spectral difference plots between 11.7 and 10.4 km for a) Channel 1, b) channel 2 showing the rapid change in spectral features associated with PAN across the tropopause.

## 5.4 Retrieval Accuracy

Determining the uncertainty in concentrations used to obtain optimised spectral fits in this work requires consideration of the uncertainty in fitted state parameters such as pressure, temperature and other gas profiles as well as the accuracy of reference data and the performance of the forward model. In addition, other sources of systematic error such as inaccuracies in the instrument radiometric gain and offset calibration; and random errors such as instrument noise, must be considered.

A detailed analysis of all these sources of error has not been performed in this thesis and is not easily assessed due to the large number of covariant errors associated with the simultaneous spectral fitting of up to twenty-four independent state parameters (twenty-one gas profiles, pressure, temperature and aerosol in channel 1). Furthermore, a meaningful uncertainty for each fitted parameter taken separately cannot be calculated using the fitting method in this thesis.

For these reasons, the uncertainty in fitted PAN concentrations derived in this work is based both on the sensitivity of the fitted PAN concentration to changes in modelled state parameters (see following section) and also the uncertainty in the fitted PAN concentration due to uncertainty in the PAN reference cross-section calculated in Section 4.4.2)

Table 5.7 shows a summary of fitted PAN concentrations for MIPAS-B2 spectra in this work with an uncertainty calculated as the absolute error due to the 7% uncertainty in the 250 K reference PAN cross-section calculated in Section 4.4.2 with



the addition of an uncertainty due to the standard deviation of the NESR spectrum in each channel (see Section 5.1.2.1). The uncertainty in measured radiance used for this purpose is 15 and 3.5 ( $\text{nW sr}^{-1} \text{cm}^{-2} \text{cm}$ ) for channel 1 and 2 respectively.

Campaign	Tangent altitude / km	Ch. 1 Fitted PAN concentration /pptv	Ch. 2 Fitted PAN concentration /pptv
Flight 6	7.5	$260 \pm 33$	$260 \pm 21$
	10.4	$180 \pm 28$	$180 \pm 17$
	13.6	$70 \pm 20$	$70 \pm 14$
Flight 8	8.5	-	$350 \pm 29$
	9.6	-	$300 \pm 25$
	10.7	-	$230 \pm 20$
	11.7	-	$170 \pm 18$
	13.7	-	$90 \pm 10$

**Table 5.7** Summary of fitted PAN concentrations for MIPAS-B2 spectra. The quoted uncertainty represents the absolute error in the fit due to a 7% uncertainty in the 250 K PAN reference cross-section. Note: Channel 1 data for Flight 8 was not available.

### 5.4.1 Fit Sensitivity

This section discusses the sensitivity of fitted PAN concentrations to small changes in simulated parameters that were noted to most affect the fits made in Section 5.2.6. These were aerosol, pressure, temperature, water vapour and  $\text{CCl}_4$  (in order of importance for channel 1). Such an analysis provides a useful indication of the feasibility of accurate retrieval of PAN in the atmosphere and its limitations. Although such perturbations do not improve the spectral fits in this work, any difference in the fitted profiles of these parameters does affect the quality of the fit for PAN residual spectra and hence the inferred concentration. Such sensitivity for measurement channel 1 is shown in Table 5.8.

Aerosol is seen to have the largest influence with small changes in extinction coefficient causing large deviations in PAN fitting. Such large aerosol extinction is decreased at higher altitudes. Differences in pressure and temperature cause less

significant differences, with an increasing dependence with temperature at higher altitudes.

It should be noted that such error in pressure, temperature and aerosol in simulated spectra would be immediately obvious on inspection of  $\Delta X$  due to a clear offset in the zero baseline. Therefore, such a large error in  $\Delta Y$  would be mostly corrected for in spectral fits. However, this sensitivity analysis illustrates the need for a good initial guess or prior knowledge of such profiles in order to consider this spectral fitting method for use in retrieving PAN concentrations.

Parameter	Perturbation	Altitude		
		7.5 km	10.4 km	13.7 km
Temperature	+ 1 K	+ 5	+ 6	+ 15
	- 1 K	- 5	- 6	- 15
Pressure	+ 1 mb	+ 3	+ 3	+ 3
	- 1 mb	- 3	- 3	- 3
Aerosol*	+ $1 \times 10^{-4}$	+30	+ 25	+ 30
	- $1 \times 10^{-4}$	- 23	- 20	- 30
Water Vapour	+ 8 pptv	+ 10	0	0
	- 8 pptv	- 10	0	0
CCl <sub>4</sub>	+ 1.1 pptv	+5	+5	+5
	- 1.1 pptv	-5	-5	-5

**Table 5.8** Sensitivity of fitted PAN concentration (pptv) in channel 1 to perturbations in otherwise optimised profiles of temperature, pressure, aerosol, water vapour and CCl<sub>4</sub>. The values represent the change in the fitted PAN concentration for the quoted change in each parameter. \* Aerosol perturbation refers to a change of  $\pm 1 \times 10^{-4}$  in extinction coefficient. Changes in CCl<sub>4</sub> and water vapour represent a 1% change in concentration at 10.4 km.

In contrast, CCl<sub>4</sub> does not affect the broader spectral baseline and instead affects the shape of the PAN feature in  $\Delta X$  directly. Evidence for poorly fitted CCl<sub>4</sub> was noted in Section 5.2.6 by such a change in the shape of the PAN band around 810 cm<sup>-1</sup> and was corrected for by increasing simulated CCl<sub>4</sub> concentrations in line with correct atmospheric concentrations observed in 1998 for flight 6. Concentrations of CCl<sub>4</sub> are relatively stable globally due to its long lifetime and there is a well-characterised

decreasing trend of 1.1 pptv per year for the gas [Montzka *et al.*, 1999]. Therefore, fitted PAN concentrations should not be sensitive to such uncertainty so long as up-to-date profiles for CCl<sub>4</sub> are used.

Water vapour effects are more subtle and do not effect the broad spectral baseline significantly or the general shape of the PAN band. However, at low altitudes (8.5 km), the water vapour spectral continuum can have significant effects due to its high atmospheric variability. Saturation effects by strong water vapour lines can also reduce the quality of the fit. Therefore, the sensitivity to uncertainty in water vapour is likely to be large at low altitude, indicating the need for accurate water vapour data at such altitudes. The rapid decrease in water vapour concentrations in the UT suggests that this may be less of a problem at higher altitudes.

## 5.5 Conclusions

The evidence presented in this chapter strongly indicates the detection of PAN by its infrared emission signature for the MIPAS-B2 spectra examined in this thesis. The simultaneous observation of residual spectral features in both independent spectral channels, which correlate closely with expected features for both the 794.0 and 1163 cm<sup>-1</sup> PAN bands, gives high confidence in its detection in the upper troposphere.

Retrieved PAN concentrations were found in the range 70 to 350 pptv, with the highest PAN concentrations found at 8.5 km in flight 8 and the lowest for flight 6 at 13.5 km. Furthermore, the PAN profile retrieved in these simulations is characteristic of the expected range of PAN concentrations seen in the Mediterranean region. The expected sharp decrease in PAN concentration is also observed through the tropopause region.

The 794.0 cm<sup>-1</sup> PAN band was seen to be more suitable for detection and retrieval of PAN at typical concentrations in the UT at all altitudes due to its stronger radiance contribution, making it confidently observable above spectral noise. Conversely, the 1163 cm<sup>-1</sup> band is less well observed at typical concentrations although may be useful in conjunction with spectra of the 794 cm<sup>-1</sup> region, for high PAN concentrations.

Furthermore, the 794 cm<sup>-1</sup> spectral region is noted to be more complex to simulate than the 1163 cm<sup>-1</sup> region due to increased sensitivity to temperature and pressure, although it is possible to achieve a good spectral fit with the forward model

using a good knowledge of appropriate state parameters. The most important of these parameters are:

- Precise spectral and radiometric calibration.
- Good characterization of spectral noise.
- The best possible reference data (profiles and spectroscopic data) for all spectrally interfering gases.
- Accurate optimized retrievals of pressure and temperature profiles.
- Accurate optimized joint profile retrievals of all gases, especially water vapour, carbon dioxide, ozone and CCl<sub>4</sub>, which are critical in spectral regions of interest to PAN.
- A good knowledge of the aerosol extinction profile, appropriate to the spectral region of interest.

# Chapter 6

## 6 Detection of PAN in MIPAS- Envisat Spectra

The space-borne MIPAS-ENVISAT (MIPAS-E) instrument, launched as part of the European Space Agency's Envisat mission in March 2002, is capable of recording infrared emission spectra of the Earth's limb down to the upper troposphere ( $\sim 6$  km) at high spectral resolution ( $0.025\text{ cm}^{-1}$  unapodised).

This chapter investigates the possibility of detecting PAN in MIPAS-E spectra using a similar method to that described in the previous chapter, where the successful detection of PAN was achieved (using new reference spectral data for PAN described earlier in this thesis) from spectra recorded by the MIPAS-B2 instrument.

### 6.1 The ENVISAT Mission

The European Space Agency's (ESA) ENVironment SATellite (ENVISAT), described by Louet [2001], is a polar-orbiting Earth observation satellite hosting a total of ten scientific instruments, together providing measurements of the atmosphere, ocean, land and ice over a nominal five year lifetime. The payload of the satellite is ambitious and innovative but also aims to ensure the continuity of similar measurements made by the ESA ERS-1 and ERS-2 satellites. Its observations will be important for further understanding, modelling and predicting environmental and climatic changes. Further details to those given in this section regarding the ENVISAT mission can be found at <http://envisat.esa.int/>.

A schematic of the ENVISAT satellite is shown in Figure 6.1. ENVISAT travels in a sun-synchronous polar orbit with a mean altitude of 799.8 km. The repeat cycle of the reference orbit is thirty-five days and for most sensors with a wide swath

range, complete global coverage is achieved within one to three days. The satellite crosses the equator southwards at 10 am local solar time (MLST) at a 98.55-degree inclination and has a payload mass of over 2000 kg, with a total mass of 8000 kg.

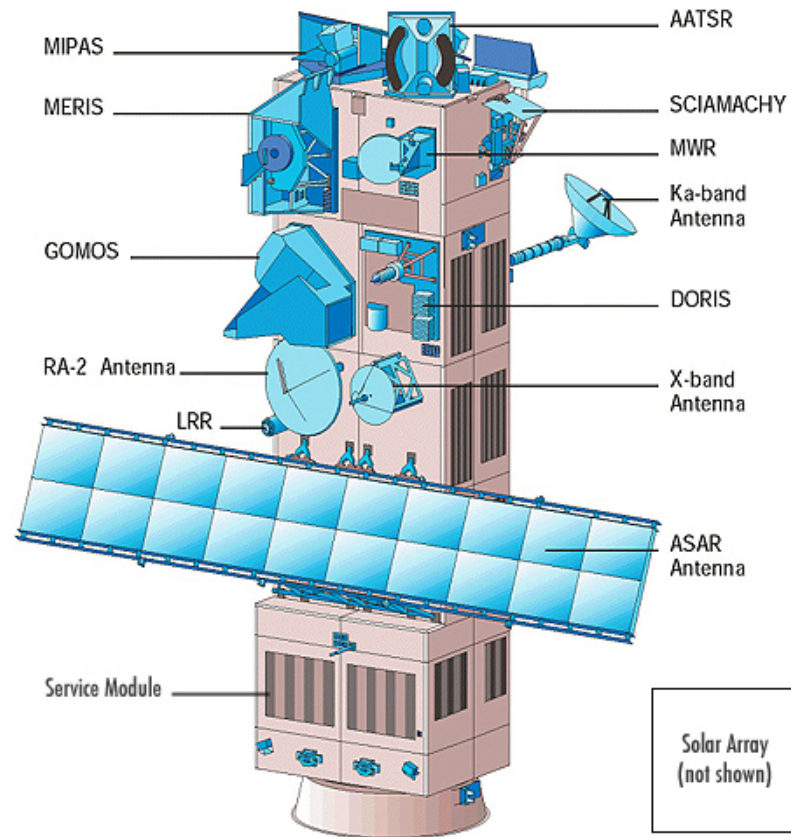


**Figure 6.1** An illustration of the ENVISAT satellite showing the various positions of the scientific payload (picture courtesy of ESA).

To make near real time (NRT) data products available to the user within three hours, ENVISAT stores complete orbits of data for most instruments before downloading to the main ESA ground stations directly or via the ARTEMIS relay satellite.

## 6.2 The MIPAS-E Instrument

The MIPAS-E instrument, described by Nett [2001], shown schematically in Figure 6.2, has been designed to measure infrared radiance emission spectra of the Earth's limb with an approximate vertical resolution of 3 km in the upper troposphere and

stratosphere and covers the altitude range 6 to 68 km. The MIPAS-E operationally retrieved NRT data (Level 2) product includes pressure, temperature and concentrations of water vapour (H<sub>2</sub>O), ozone (O<sub>3</sub>), methane (CH<sub>4</sub>), nitrous oxide (N<sub>2</sub>O), nitric acid (HNO<sub>3</sub>) and nitrogen dioxide (NO<sub>2</sub>). Measurement of this suite of molecules contributes to an improved understanding of stratospheric chemistry, atmospheric dynamics and upper tropospheric chemistry.

In addition, information about a large number of other trace gases (up to twenty-one), as well as the atmospheric distribution of aerosol particles, tropospheric cirrus clouds and the properties and occurrence of polar stratospheric clouds (PSCs), can also be derived from MIPAS-E spectral (Level 1B) data.

### 6.2.1 Interferometer and Optics

MIPAS-E is a rapid scanning FTS based on the same principles already described of such spectrometers in Chapter 2.5. The input telescope collects radiation within the instrument field of view, with the viewing angle of the instrument controlled by an azimuth scan unit shown in Figure 6.2. This radiation is then collimated using a telescope apparatus and directed (using coated mirrors) to the first input port of the interferometer. The second input port is closed with a cold blackbody reference source, which is used for radiometric calibration. Blackbody reference spectra are periodically and routinely recorded during operation.

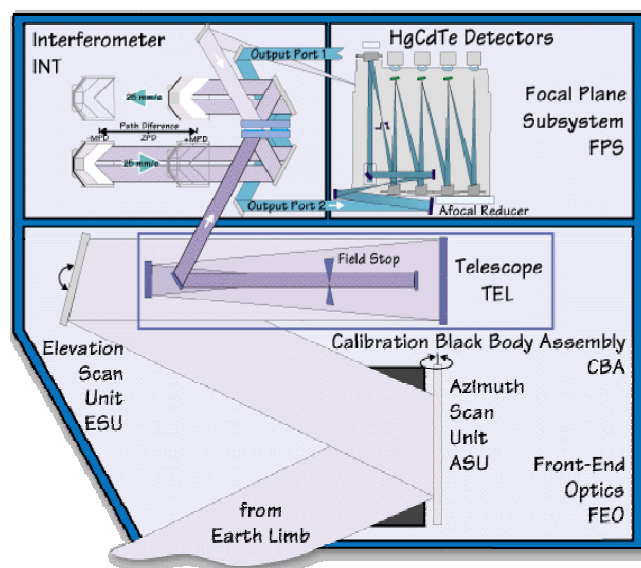


**Figure 6.2** A component overview schematic of the MIPAS-E instrument showing the optical path of radiation entering the instrument field of view (picture courtesy of ESA).

The interferometer unit illustrated in Figure 6.3 is based on a variant of the classical Michelson Interferometer, known as a *dual-slide* interferometer by virtue of its ability to simultaneously move both interferometer mirrors. This has the advantage that the maximum optical path difference is doubled relative to the classic one-mirror motion approach. Through the use of two folding mirrors also shown in Figure 6.3, mirror movement is contained along the same reference axis. Such configuration not only greatly reduces the space required for the interferometer, but the simultaneous motion of the interferometer mirrors in opposite directions along the same reference axis means that the total momentum imparted to the satellite is equally and oppositely balanced and therefore equal to zero. This property is important for the stability of the satellite as a whole.

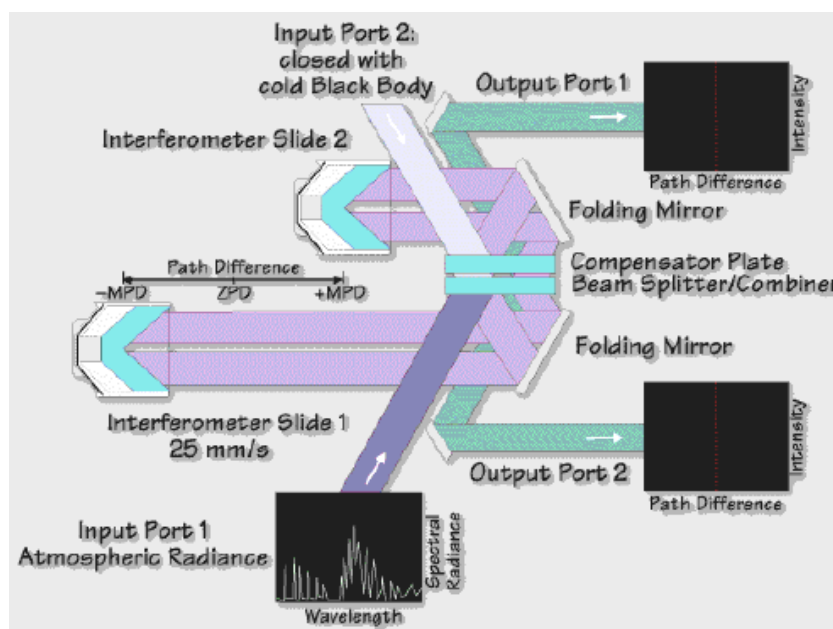


**Figure 6.3** An illustrative schematic of the MIPAS-E interferometer unit showing the optical path of a collimated beam of radiation through the interferometer (picture courtesy of ESA).

The MIPAS-E beamsplitter is a semi-transparent mirror with optical coatings designed to reflect approximately 50% of the incoming infrared radiation and transmit the remaining fraction. Both the beamsplitter transmitted and reflected beams are then reflected by two cube-corner retro-reflectors, which reflect the beams back to the beamsplitter where they are recombined. The use of cube-corner retro-reflectors ensures that the beams are reflected directly back along the same principal axis as the



incident radiation, thus removing the possibility of producing off-axis rays which may be otherwise caused by imperfections in the alignment of plane mirrors.

The recombined beam is then split again with each beam directed to an output port where radiation is focussed by the focal plane sub-system (see Figure 6.2) and directed to Mercury-Cadmium Telluride (MCT) detectors. The ability to detect radiation from both output ports not only doubles the detected signal but also allows the possibility to correct for optical imperfections in the beamsplitter and interferometer optics. The interferometer and detector sub-systems are cooled using a sterling-cycle refrigerator to a nominal operating temperature of 200 K.

## **6.2.2 Viewing Geometry**

The MIPAS-E measures limb emission from the atmosphere through a rearwards (or anti-flight) direction and occasionally in the sideways (anti-sun) direction. To achieve the greatest latitudinal coverage, including the Polar Regions, the rearward viewing geometry is employed as a nominal mode. The instrument field of view (FOV) at the tangent point can be as low as 3 km, but to collect sufficient radiance through the instrument's aperture, a 30 km wide swath is needed. For limb viewing geometry, the path length of radiation through the atmosphere can be up to 3300 km, which limits the horizontal resolution of measurements (see Figure 6.4).

Each MIPAS-E sweep represents a single recorded interferogram recorded in under 4 seconds with 0.6 seconds taken to reverse the slide mirrors. In nominal mode, one full MIPAS-E scan comprises seventeen tangent height sweeps (6 to 42 km at a step size of 3 km; and 42 to 52 at a step size of 5 km; and 52 to 68 km at a step size of 8 km), taking approximately 75 seconds to complete each profile measurement.

MIPAS-E also has the capability of operating in special modes such as those used for monitoring special atmospheric events, such as large intrusions of ash and sulphur dioxide into the stratosphere from volcanic eruptions or to observe polar vortex splitting. Upper atmospheric observation modes are also possible to observe the effects of non-local thermodynamic equilibrium (non-LTE) in the atmosphere. The most important of these modes for the purposes of this thesis is the "S6" nominal mode for the study of the upper troposphere and lower stratosphere regions.

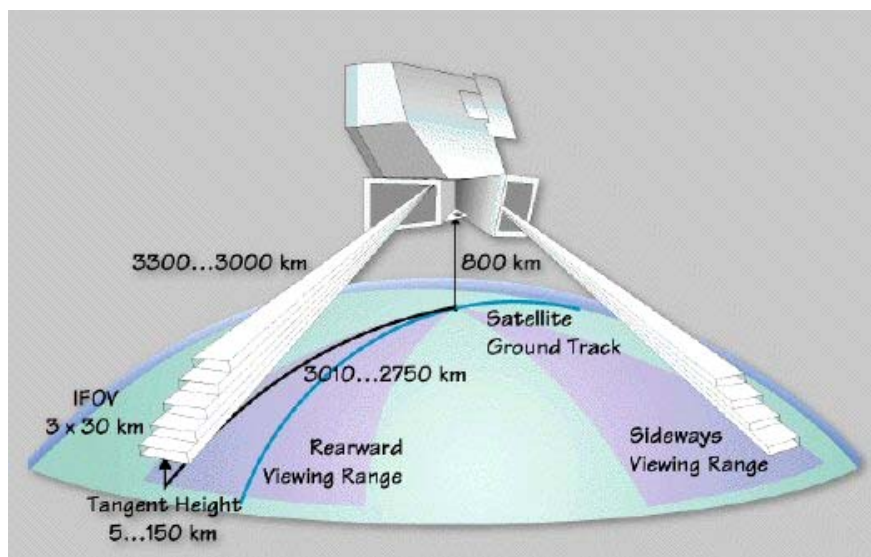


**Figure 6.4** Viewing geometry of the MIPAS-E instrument showing anti-flight and anti-sun viewing angles (picture courtesy of ESA).

### 6.2.3 Detectors and Spectral Ranges

In MIPAS-E, four detectors are placed in each of two output ports to record the interferogram. Where detectors are in common, the data recorded by each output port are coadded to increase the signal to noise ratio. This type of set-up also allows some redundancy of the measurements; a useful property in space-based instruments.

Each of the four MCT detectors is optimised for a specific spectral range. Together, the four detectors cover the spectral range 685 to 2410  $\text{cm}^{-1}$  (4.15 to 14.6  $\mu\text{m}$ ) and named arbitrarily as A, B, C and D. Detectors A, C and D of port 1 and 2 are identical, whereas detector B is different in each port allowing the eight detectors to be combined in five spectral bands (see Table 6.1).

Band	Detectors	Spectral range / $\text{cm}^{-1}$
A	A1 and A2	685-970
AB	B1	1020-1170
B	B2	1215-1500
C	C1 and C2	1570-1750
D	D1 and D2	1820-2410

**Table 6.1** Nominal pass bands of MIPAS-E spectral channels allowed by the combination of detectors in each output port.

## **6.2.4 Sampling of the Interferogram**

The interferogram is sampled in optical path difference intervals of 30 nm. The accuracy of this sampling is achieved with a monochromatic laser (1300 nm wavelength), which is also transmitted along the same optical path. The interferogram of the monochromatic laser is, in principle, a pure sine wave and detected by an interference fringe counter used to determine the optical path difference by the phase of the sine wave.

This fringe counter modulates a “clock signal” that is sent to an analogue to digital converter in the on-board signal processor electronics. Thus, the fringes trigger the sampling of the interferogram at regular intervals.

## **6.2.5 Radiometric Calibration and Gain**

Radiometric calibration is the process by which physical radiance units are attributed to the raw spectrum derived from the measured interferogram. This is achieved using measurements of well-defined calibration targets. To radiometrically calibrate spectra generated by MIPAS-E, two separate measurements are made, the first from an internal calibration blackbody at a temperature of 224 K, the second from deep space (at a tangent altitude of 235 km) where the radiance emission is assumed to be negligible.

Such calibration measurements are performed after the instrument slides have been stopped and as a result this calibration sequence is the first operation in any nominal measurement sequence.

In addition, the internal calibration blackbody is used to establish the instrument responsiveness; or gain. Gain calibration requires 1200 measurements (600 deep space sweeps and 600 internal black body measurements) at a unapodised spectral resolution of  $0.25 \text{ cm}^{-1}$ , which are then co-added after relay to ground to reduce spectral noise.

## **6.2.6 Spectral Offset Measurement**

Deep space measurements are used to determine the instrument spectral offset (the contribution that the instrument’s self-emission contributes to the signal measured). To compute this offset, a calibration is performed consisting of six measurement sweeps made at a lower spectral resolution. The process is repeated for every five fully recorded scans [Mantovani, 2003].

## 6.2.7 Instrument Noise Characterisation

Successful retrieval of trace gas species from atmospheric measurements requires a large signal to noise ratio (SNR) such that results are not limited by random noise errors. The instrument noise of MIPAS-E is calculated in terms of the Noise Equivalent Spectral Radiance (NESR). Pre-flight maximum instrument noise requirements were defined separately for each of the five spectral bands (see Table 6.2).

MIPAS-E channel	NESR / ( $\text{nW}/[\text{cm}^2 \text{ sr cm}^{-1}]$ )
A	50
AB	40
B	20
C	6
D	4.2

**Table 6.2** Pre-flight NESR (spectral noise) maxima for MIPAS-E measurement channels

The calculation of the in-flight MIPAS-E NESR from spectral measurement (on July 24<sup>th</sup> 2002) has shown that such requirements are superseded in all spectral bands, with the exception of the small spectral region below  $720 \text{ cm}^{-1}$  in band A and above  $2180 \text{ cm}^{-1}$  in band D. This is illustrated in Figure 6.5, which also shows a general decrease with altitude in the NESR.

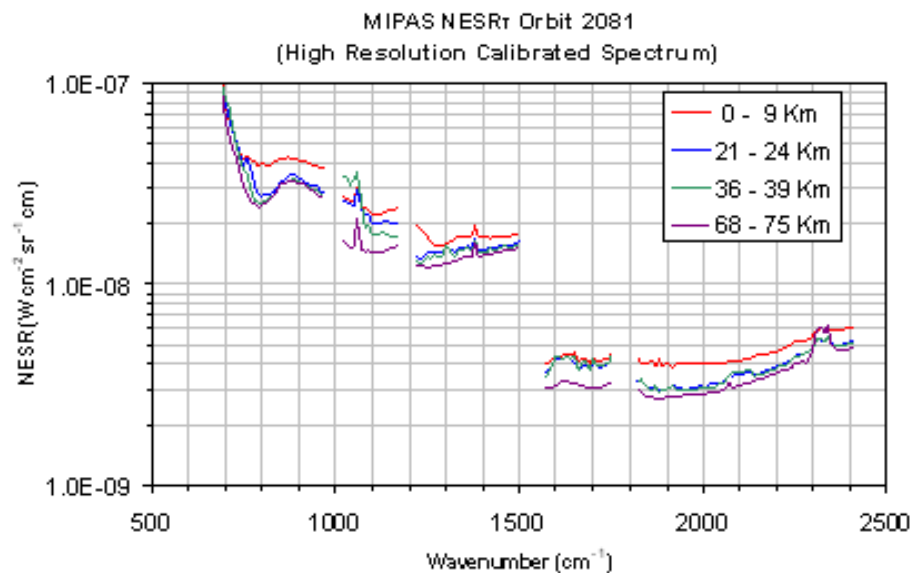


**Figure 6.5** NESR characterisation for MIPAS-E orbit 02081, July 24<sup>th</sup>, 2002. Source: Perron [2003].

Further routine characterisation of NESR has been derived many times to date. Typical noise levels plotted in Figure 6.5 are assumed in the later analysis performed in this chapter.

## 6.2.8 Spectral Calibration

MIPAS-E measurements are marginally affected by Doppler shifting caused by the relative movement of the satellite and the Earth and also from non-negligible shifts in the frequency scale from the operation of the interferometer. Calibration is performed with comparison of measured MIPAS-E spectra with synthesised spectra produced using accurate line-by-line models. This is performed in all five spectral bands using spectral lines from gases with well-known spectroscopy listed in Table 6.3.

Band	Target gas	Spectral interval (cm <sup>-1</sup> )
A	CO <sub>2</sub>	945.98 – 954.54
AB	O <sub>3</sub>	1128.75 - 1151.73
B	H <sub>2</sub> O	1399.20-1429.94
C	H <sub>2</sub> O	1616.71 - 1677.75
D	H <sub>2</sub> O	1866.38 - 1889.57

**Table 6.3** Reference lines and spectral windows used for spectral calibration and ILS retrieval (source: <http://envisat.esa.int>)

## 6.2.9 MIPAS-E Data Processing

The operational data processing chain for MIPAS-E has been defined in the following four stages and is shown schematically in Figure 6.6:

- Level 0: Reformatted, time-ordered, satellite data in binary format
- Level 1a: Reconstructed interferograms
- Level 1b: Radiometrically and spectrally calibrated emission spectra
- Level 2: Operational profiles of atmospheric pressure, temperature and trace gas constituents of six gases (see Section 6.1) along the orbit track.

The raw data received by the ground segment is known as level 0 data and have undergone a minimal amount of on board processing.

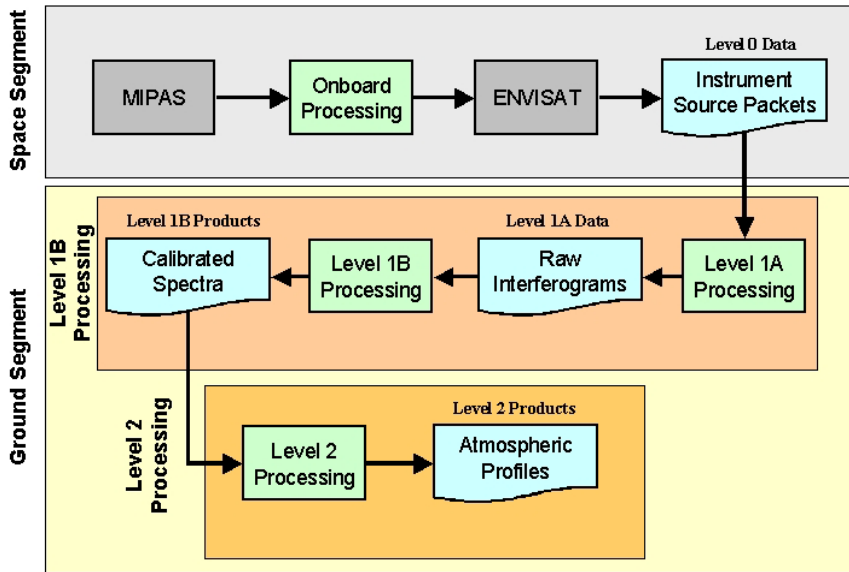


**Figure 6.6** Data processing structure for MIPAS-E (source: [envisat.esa.int/instruments/mipas/](http://envisat.esa.int/instruments/mipas/))

The ground based processing of MIPAS-E data is divided into two parts known as *level 1b* and *level 2*. Level 1b processing converts the raw interferogram into a fully calibrated and geolocated radiance spectrum. Such calibration includes the gain, offset, wavenumber, Doppler shift and detector non-linearities discussed in Section 6.2. Furthermore, the ILS and NESR spectrum are included with level 1b data along with pointing and geolocation data.

Level 2 processing converts these spectra, where possible, into vertical profiles of those parameters detailed earlier using state of the art data inversion models. A more detailed description than that given here for this forward model and the global fitting retrieval algorithm for MIPAS-E level 2 data is given by Ridolfi [2000]. As noted in Section 2.4.1.4, the measured spectral line intensity is a function of pressure and temperature (as well as of concentrations of gases); therefore, the level 2 operational processor firstly retrieves these parameters using well-known CO<sub>2</sub> lines. This is possible as CO<sub>2</sub> is a well-mixed gas in the atmosphere and its spatial distribution is relatively well known. The volume mixing ratios of other gases are then calculated using strong emission “micro-windows”, selected such that these small spectral ranges contain optimised information about the target gas but little information from

interfering species [Von Clarmann and Eehle, 1998]. Further information regarding the optimised selection of micro-windows is discussed by Dudhia [1999; 2001] and their role in MIPAS operational data processing is described by Carli *et al.* [2004].

## **6.3 Detection of PAN**

This section describes the attempted detection of PAN in MIPAS-E spectra. Such detection is based largely on the method already described for the MIPAS-B2 instrument in Chapter 6.2 and relies primarily on the process of spectral fitting and residual analysis. Given the large dataset of available MIPAS-E spectral data, a small subset of data are identified in the following section that are of interest to this study. Such data are chosen on the basis of suitability for comparison to the results obtained from MIPAS-B2 in the previous chapter and also for the probability of high PAN content.

### **6.3.1 Selecting MIPAS-E Data**

Two geographical regions were chosen for analysis. These were the Mediterranean Sea (for the purpose of comparison with the results of the previous chapter) and also an area around the East China Sea.

The East China Sea region was chosen due to the high pollution levels regularly seen in convective outflows from China that carry pollutants both from anthropogenic sources (cities) and also from biomass burning sites. High concentrations of reactive nitrogen and many volatile organic compounds (including PAN) have recently been observed, for example during the TRACE-P campaign [Crawford *et al.*, 2003], which measured Asian convective outflow in Spring 2001. PAN concentrations in the UT during this campaign have been observed to be in excess of 600 pptv (at 10 km) during aircraft studies of this region in April 2001 [Koike *et al.*, 2003] and hence this region represents a likely place to encounter high PAN concentrations.

In order to select a number of MIPAS-E profiles for comparison with results for MIPAS-B2, data were selected to conform to the geo-location criteria listed in Table 6.4. The two regions represent a portion of the East China Sea and mid to Western Mediterranean. The region selected for the East China Sea represents an area well off the coast of China where convective uplifting and so-called “warm conveyor belts”

(WCBs) have been observed to lift polluted airmasses high into the troposphere (see Chapter 1.1.1). These WCBs are associated with ascending airstreams ahead of surface cold fronts and are regularly seen in the China Sea region in Northern Hemisphere spring [Miyazaki *et al.*, 2003].

The Mediterranean region was selected to coincide as closely as possible with the geographical and seasonal location of the MIPAS-B2 flight 6 campaign for comparison with the results of the previous chapter. The wider Eastern Mediterranean region was also included to increase the likelihood of observing high levels of PAN, which have recently been associated with the Mediterranean “pollution cross-roads” reported by Holzinger *et al.* [2005].

Region	Dates	Latitude	Longitude
Mediterranean Sea	(16.04–06.05) 2003	16–35°	0–15°
East China Sea	(01.04–30.04) 2003	20–30°	130–140°

**Table 6.4** Geo-location selection criteria for MIPAS-E data

A total of thirty-four scans were found to match these initial criteria for the Mediterranean Sea, whilst eighty-two were identified for the China Sea. These data were then screened for the presence of cloud-contaminated data. Such “cloud-clearing” is simply the removal of scans that are most likely to contain a spectral influence due to scattering by cloud particles. This is determined using a chosen threshold value of 2.5 for a *cloud index* defined by Spang *et al.* [2003]. This cloud index is defined as the ratio of the integrated radiance of two spectral regions (788.2 to 796.25 cm<sup>-1</sup> and 832.3 to 834.4 cm<sup>-1</sup>) in Channel A of MIPAS-E spectra. A threshold value of 1.8 is usually sufficient for screening most cloud-contaminated data. However, the more stringent value of 2.5 is chosen here to remove even thin cloud in the UT, since the detection of PAN by the method used in this thesis is expected to be highly sensitive to the spectral influence of cloud, which is not included in the forward model chosen for spectral simulations in this study. It should be noted that a higher value for this threshold is not used, as larger values are known to be sensitive to concentrations of gases and not cloud.

Additional data were also removed from further analysis due to an unexplained ambiguity in the *validity* of level 1B data for channel A at low altitudes in some



profiles. This validity flag is included with the level 1B data product and analysis of invalidly flagged data reveals that such spectra are unrealistic and therefore unusable.

Ultimately, a total of eight MIPAS-E profiles were identified to be valid and cloud-free for the Mediterranean in April/May 2003, whilst thirteen were found for the East China Sea (April only). Level 2 profiles were also available of operationally processed data for pressure, temperature and concentrations of six trace gases. These Level 2 profiles are plotted for the Mediterranean and China Sea in Figure 6.8 and Figure 6.10 respectively. Data are plotted as a function of altitude and labelled with the time identification of the sweep recorded at the top of each profile.

The time identifications (TIDs) in Figure 6.8 represent the number of seconds elapsed since midnight on January 1<sup>st</sup> 2000 and are used to cross-reference matching level 1b and cloud index data with level 2 data.

On visual inspection, the selected profiles do not contain any anomalous or unrealistic values that would otherwise require consideration, with the exception of some anomalously high concentrations of NO<sub>2</sub> at high altitude (> 60 km) in two profiles. The influence of NO<sub>2</sub> on simulated spectra at low altitude is small and not significant for the purposes of this study.

The level 2 profiles were used to construct part of a simulated atmosphere for use in the forward model. This is described in the following section.

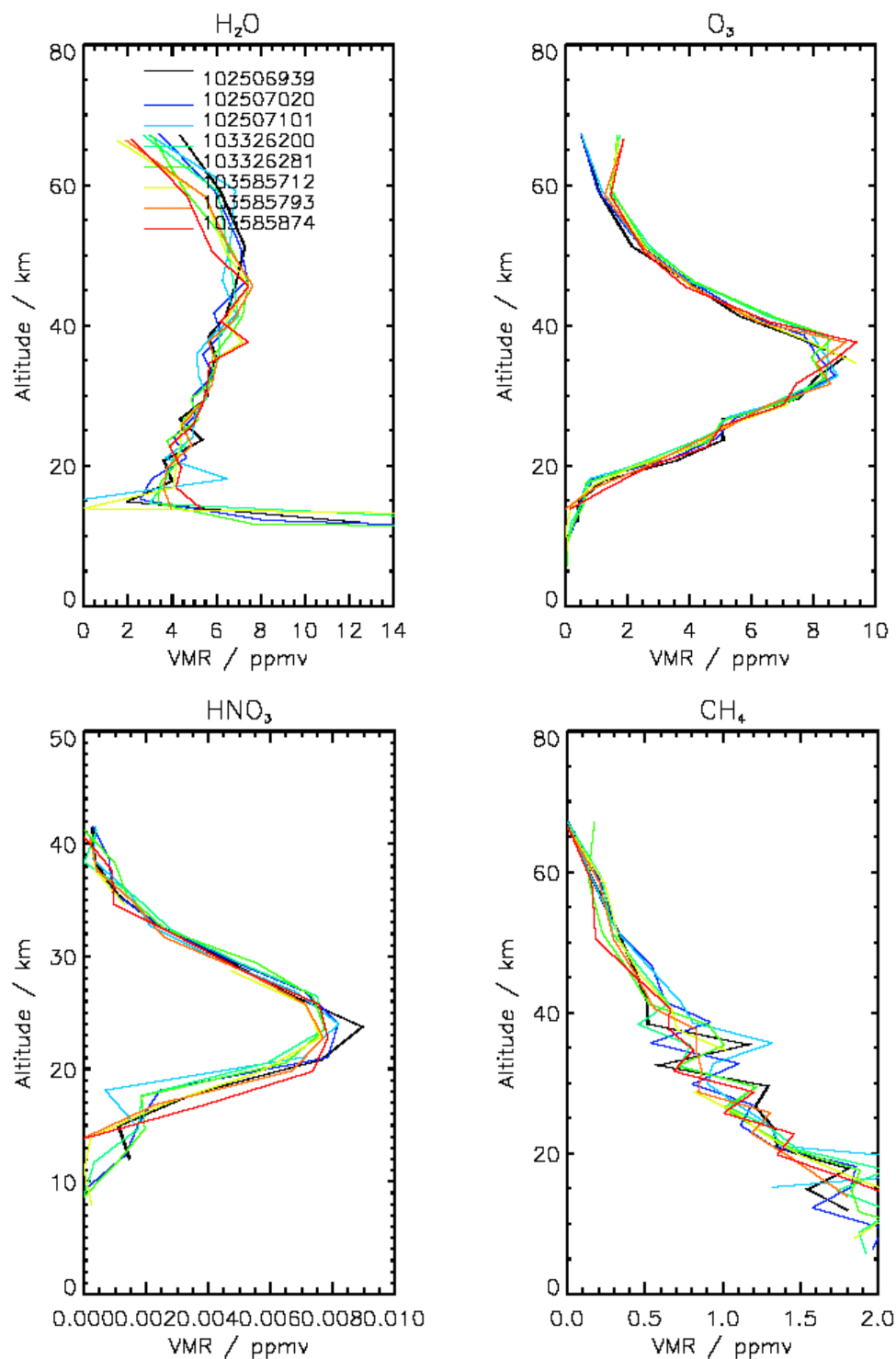


**Figure 6.7** Valid and cloud-free Level 2 profiles of MIPAS-E data for: H<sub>2</sub>O, O<sub>3</sub>, HNO<sub>3</sub> and CH<sub>4</sub>, selected for the Mediterranean Sea in April 2003. Time identifications (seconds since 01/01/2000) for colour-coded profiles are plotted with the H<sub>2</sub>O profile.

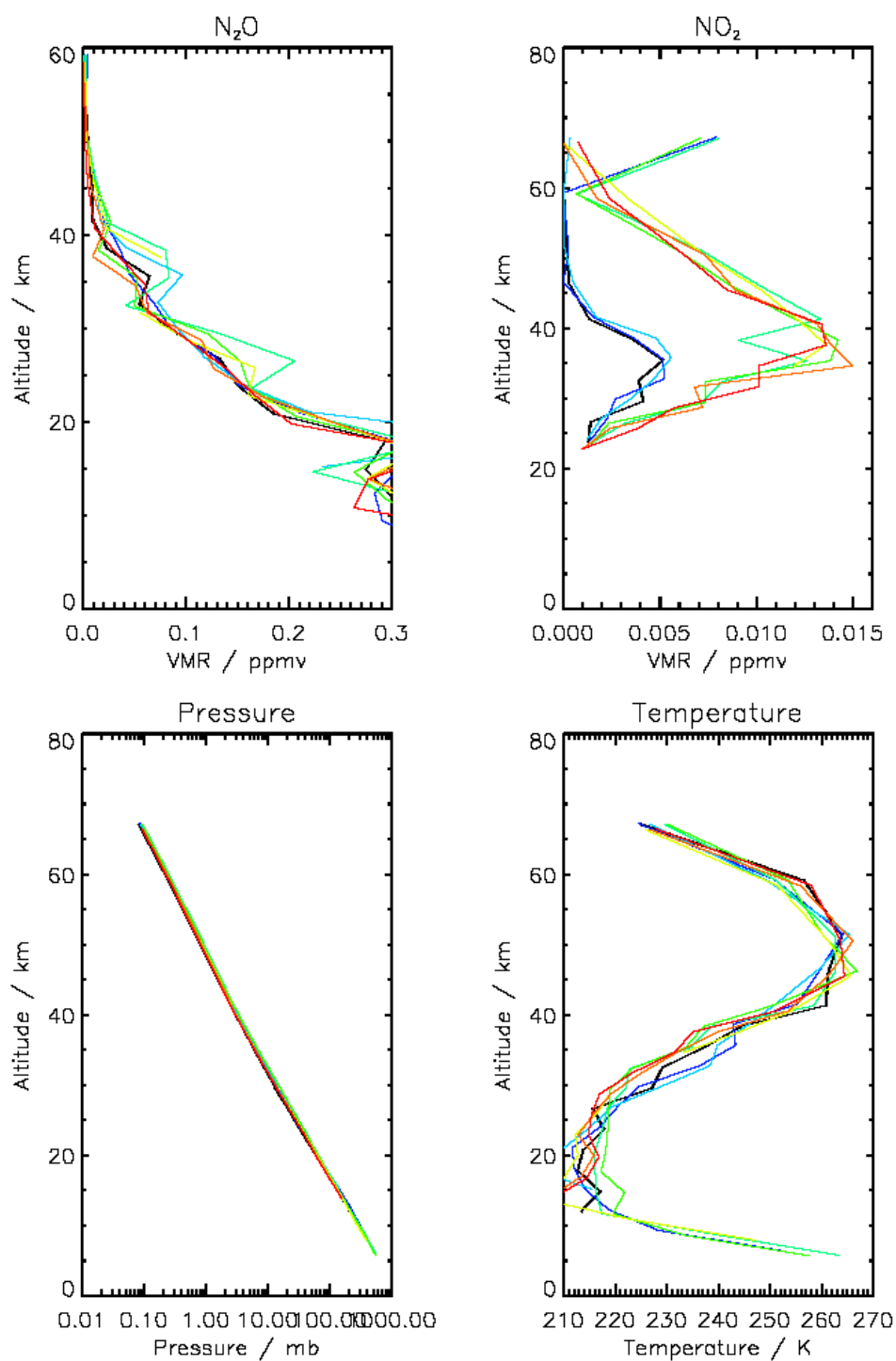


**Figure 6.8** Valid and cloud-free Level 2 profiles of MIPAS-E data for:  $N_2O$ ,  $NO_2$ , pressure and temperature, selected for the Mediterranean Sea in April 2003. Time identifications (seconds since 01/01/2000) for colour-coded profiles are plotted with the  $H_2O$  profile in Figure 6.7

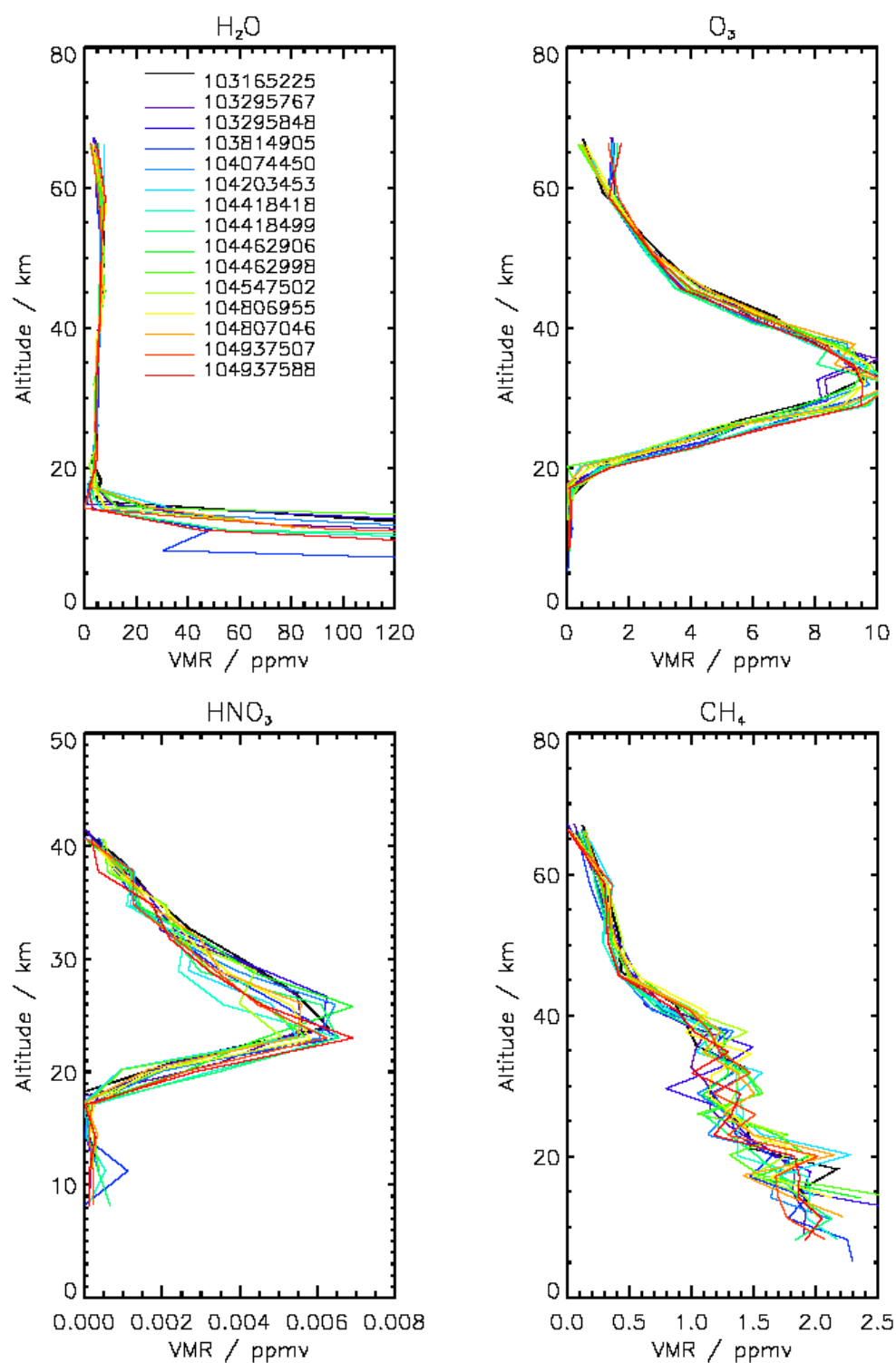


**Figure 6.9** Valid and cloud-free Level 2 profiles of MIPAS-E data for: H<sub>2</sub>O, O<sub>3</sub>, HNO<sub>3</sub> and CH<sub>4</sub> selected for the East China Sea in April 2003. Time identifications (seconds since 01/01/2000) for colour-coded profiles are plotted with the H<sub>2</sub>O profile.

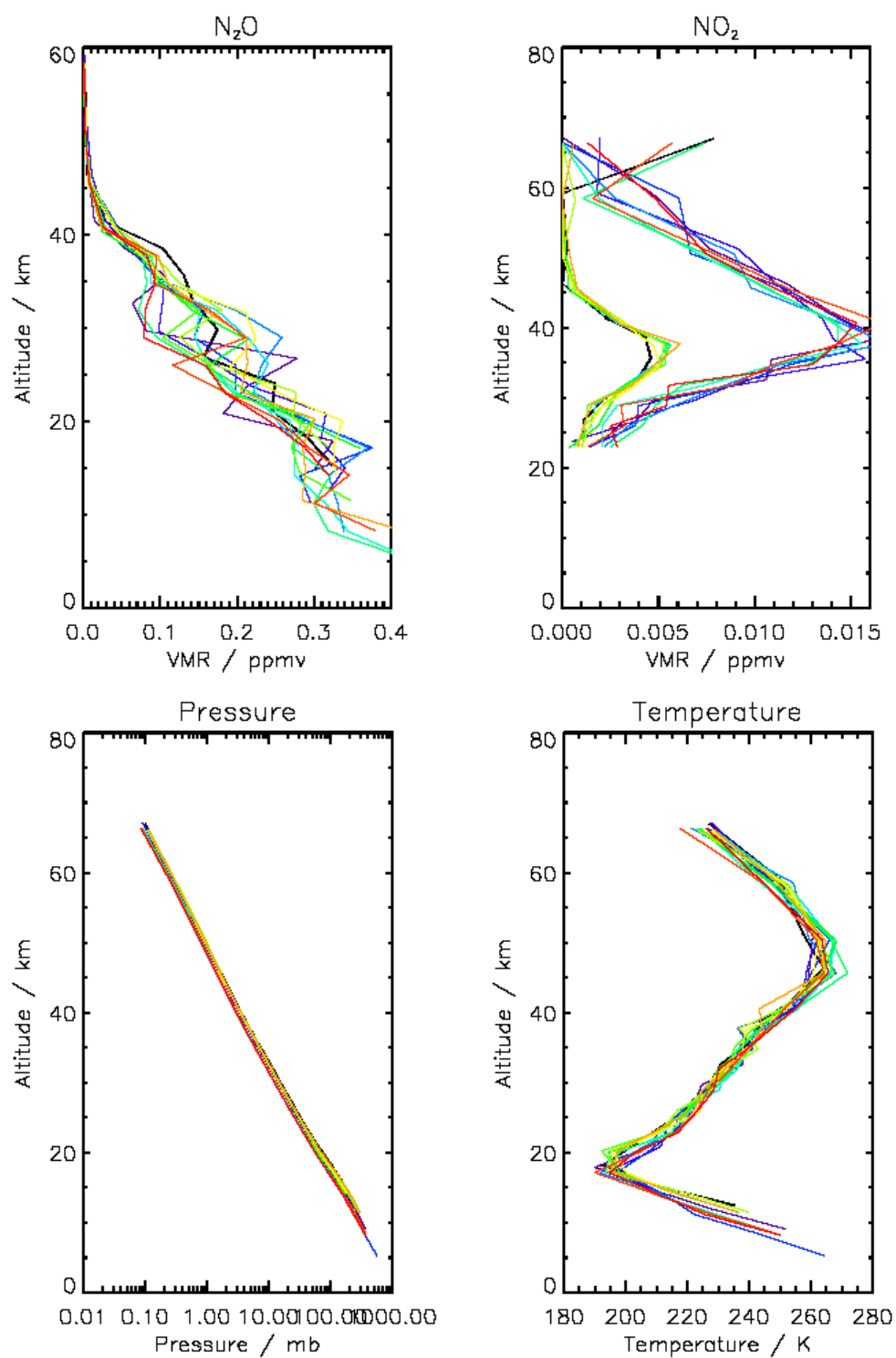


**Figure 6.10** Valid and cloud-free Level 2 profiles of MIPAS-E data for :  $N_2O$ ,  $NO_2$ , pressure and temperature, selected for the East China Sea in April 2003. Time identifications (seconds since 01/01/2000) for colour-coded profiles are plotted with the  $H_2O$  profile in Figure 6.9.

### 6.3.2 Simulated Atmospheric Profiles

In order to compile the simulated atmosphere for each MIPAS-E profile under investigation, all available level 2 profile data (see Figure 6.8) were inserted into the relevant simulated profiles. For MIPAS-E, the availability of level 2 profiles for the spectrally important concentrations of pressure, temperature, water vapour and ozone concentration provides a good initial guess of the simulated atmosphere for these parameters.

Since some level 2 data are missing (e.g. NO<sub>2</sub> below 24 km for all profiles) and since MIPAS-E data are only retrieved nominally up to 60 km, the remainder of the simulated profile between 6 and 120 km (where necessary) is filled with profile information from reference atmospheres. Such information is derived from the same sources as those listed in Table 5.6 for MIPAS-B2 simulated atmospheres. Profiles of the same additional infrared active “contaminating” gases considered for MIPAS-B2 are also included. Therefore, the simulated profiles used in forward modelling of infrared spectra used in this chapter broadly resemble those plotted in Figure 5.11, with the insertion of MIPAS-E level 2 data where available.

### 6.3.3 Simulated Spectra

As already discussed in Chapter 5.2.4, detection of PAN in this thesis relies on the clear observation of a characteristic PAN signature in residual spectra. As before, a residual spectrum ( $\Delta X$ ), is calculated as the difference of a measured spectrum with that simulated without PAN present in a simulated atmosphere. A comparison between  $\Delta X$  and a simulated difference spectrum ( $\Delta Y$ ) yields the quality of spectral fitting in general as well as the level of confidence in PAN detection and concentration. The quality of the spectral fit and hence the residual relies on the accuracy of the simulated atmosphere of infrared active species, in representing the true state of the atmosphere.

The spectral range of simulated spectra for MIPAS-E is limited by the spectral pass bands of the instrument (see Table 6.1). From these channels we see that the 794 cm<sup>-1</sup> PAN spectral band is completely measured in Channel A. However, the cut-off of Channel AB at 1170 cm<sup>-1</sup> makes observation of the 1163 cm<sup>-1</sup> PAN band difficult as this band has a FWHM of approximately 40 cm<sup>-1</sup>. Therefore, simulated residual spectra for MIPAS-E are calculated in the ranges detailed in Table 6.5. This unfortunate cut-off

in channel AB means that roughly only half of the  $1163\text{ cm}^{-1}$  PAN band can be potentially observed.

All simulated spectra are calculated at the nominal unapodised spectral resolution ( $0.025\text{ cm}^{-1}$ ) of MIPAS-E measurements using the instrument field of view (FOV) provided for the relevant channel. Spectra are then convolved with the provided MIPAS-E instrument lineshape (ILS) and corresponding level 1B data are apodised with the Norton-Beer strong apodisation function [Norton and Beer, 1976; 1977].

Channel A	Channel AB
750-850 $\text{cm}^{-1}$	1100-1169 $\text{cm}^{-1}$

**Table 6.5** Spectral range of simulated spectra appropriate for detection of PAN in MIPAS-E channels A and AB.

For reasons cited in Chapter 5.2.1, spectral line mixing is also enabled in the radiative transfer model together with the use of a *chi* lineshape for carbon dioxide.

Simulated spectra are calculated at the retrieved tangent altitudes reported in the level 2 data product for the corresponding profile. Since MIPAS-E records spectra in 3 km steps, simulated spectra are therefore calculated nominally around 6, 9, 12 and 15 km tangent altitudes. These represent the altitudes most likely to be of interest to detecting PAN in the upper troposphere.

An example of simulated MIPAS-E spectra at 11.4 km for each of the spectral ranges under investigation is plotted in Figure 6.11 together with simulated residuals for PAN at a concentration of 90 pptv. The NESR assumed for each channel (see Section 6.2.7) is plotted as a dashed line for comparison with such residuals.

Figure 6.11 shows that typical PAN concentrations at 11.4 km are expected to give a signal to noise ratio of just under 4 at the peak of the  $794\text{ cm}^{-1}$  band with a radiance contribution to the total spectrum of around 100 nW (or 5%). However, for the  $1163\text{ cm}^{-1}$  PAN band, signal to noise is reduced to less than 2 at the point of peak radiance contribution with a contribution of only 40 nW to the total (4%). This is marginally improved at 8 km, with signal to noise ratios of 6 and 3 respectively for channel A and AB, but with reduced fractional contributions to the total simulated radiance of 3% and 2% respectively.

This shows that there is the potential to observe PAN at typical concentrations in the upper troposphere from MIPAS-E in Band A, although this may be more difficult

in Band AB, where larger PAN concentrations may be required in order to conclusively detect PAN's spectral influence.

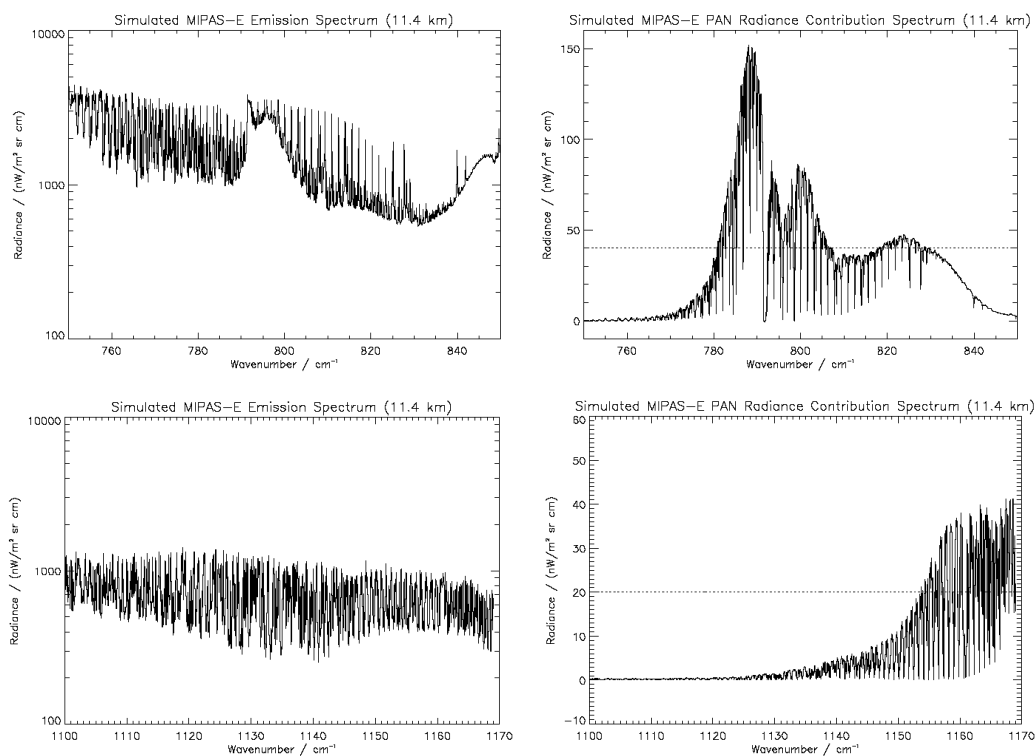


**Figure 6.11** Simulated atmospheric spectra and PAN residuals for each spectral range under investigation as observed from MIPAS-E at a tangent altitude of 11.4 km (Simulated PAN concentration at 11.4 km = 90 pptv).

As spectral ranges simulated here are similar to those studied earlier for the MIPAS-B2 instrument, the same infrared active gases are included in the simulated atmosphere here as those described for MIPAS-B2 in Table 5.5.

### 6.3.4 Comparison to Measured Spectra

This section presents the results of the comparison between simulated and measured atmospheric limb spectra for MIPAS-E over the Mediterranean and East China Sea in April 2003. Evidence for the detection and possibility of retrieving PAN concentrations from such data are also discussed.

In summary, the success of detection is again based here on the comparison of measured ( $\Delta X$ ) and simulated ( $\Delta Y$ ) residual spectra. A summary of this procedure used for each MIPAS-E profile is given below:



1. Construction of a simulated altitude grid: An altitude grid is created between 6 and 120 km in 3 km steps, with retrieved level 2 altitudes substituted in the altitude range where they are operationally reported by MIPAS-E
2. Construction of a simulated atmosphere: Level 2 profiles of pressure, temperature, O<sub>3</sub>, H<sub>2</sub>O, CH<sub>4</sub>, HNO<sub>3</sub>, NO<sub>2</sub> and N<sub>2</sub>O are used where available between 6 and 60 km. Reference atmospheres are used to fill the remainder of the simulated profile and used also for all other spectrally important gases listed in Table 5.5. Where required, reference atmosphere profile data are linearly interpolated onto the simulated altitude grid created in step 1.
3. Simulation of measured spectra: The Oxford Reference Forward Model (RFM) is used to forward model spectra at the tangent altitudes reported in the Level 2 data product in the range 6 to 15 km using the simulated atmosphere and an approximation to the instrument FOV. This is performed over the spectral ranges listed in Table 6.5 at 0.025 cm<sup>-1</sup> spectral resolution. Two such spectra are calculated, one with PAN present in the simulation and one without. Both are convolved with the relevant MIPAS-E ILS.
4. Simulation of Jacobian spectra: The RFM is also used to calculate small perturbation spectra at each tangent altitude for each simulated parameter and used in step 9.
5. Calculation of the expected residual signature for PAN ( $\Delta Y$ ): This is the difference of the two spectra calculated in step 3 at each tangent altitude.
6. Apodisation of Level 1B spectra: Level 1B spectra corresponding to those simulated in step 3 are apodised with the Norton-Beer strong function and the relevant spectral regions are extracted.
7. Calculation of the measured residual spectrum ( $\Delta X$ ) at each tangent altitude: This is the difference spectrum of the measured spectrum calculated in step 5 and the simulated spectrum in step 3 (without PAN present). This residual ( $\Delta X$ ), if perfect, includes only the PAN radiance contribution to the measured spectrum, plus some noise component.
8. Comparison between  $\Delta X$  and  $\Delta Y$ : This yields the quality of the spectral fit. If well correlated this comparison can be used to provide evidence for the detection and possible retrieval of PAN.

9. Jacobian analysis: If necessary, the fit can be improved with the addition or subtraction of relevant Jacobian spectra. If an improvement is possible, simulated atmospheres are updated with the corresponding change inferred by Jacobian fitting.
10. Iterative fitting: Such a process may be repeated iteratively until the best possible fit is achieved on the basis of minimising the difference between  $\Delta X$  and  $\Delta Y$ .
11. Sequential fitting: Fitting is first performed for the highest altitude in the desired range (usually around 15 km), with sequential fitting of the next highest altitude spectrum only when the best possible fit is achieved for the spectrum above. This is repeated down to the lowest available Level 1B spectrum in the profile.

The quality of the fit between  $\Delta X$  and  $\Delta Y$  described in step 8 is judged by eye on a number of parameters. Firstly, the  $\Delta X$  spectral baseline is fitted by perturbing  $\Delta X$  using temperature, pressure or aerosol Jacobian spectra as required. Secondly, the fit for temperature and pressure is refined further by considering the fit in  $\Delta X$  for the Q-branch feature of  $\text{CO}_2$  at  $792\text{ cm}^{-1}$ ; which is known to be sensitive to these parameters. Finally, Jacobians for other gases are considered and fitted as necessary. The simulated atmosphere is then updated with new parameters corresponding to the changes inferred by Jacobian perturbations (e.g. the addition of a Jacobian perturbation for  $\text{H}_2\text{O}$  corresponds to a 1% change in concentration at that altitude). The recalculated  $\Delta X$  is then compared again with the new  $\Delta Y$  and the process is repeated iteratively until the best possible fit is achieved.

The success of PAN detection using this method is now described for each spectral measurement channel and each geographical region.

#### **6.3.4.1 Mediterranean Sea, Spectral Band A**

Spectral fits between 7.8 and 13.9 km tangent altitude for two MIPAS-E, band A profiles in the Mediterranean Sea are plotted in Figure 6.12 to Figure 6.16. These fits represent examples for two of the eight profiles analysed. In each case, these plots show the spectral fit between modelled and observed total radiance spectra together with a comparison of  $\Delta X$  (black) and  $\Delta Y$  (red) residuals. The  $\Delta X$  residual has also been

shifted below the baseline in the lower panel of each Figure for ease of comparison with  $\Delta Y$  in the spectral region of interest for the  $794.0\text{ cm}^{-1}$  PAN band.

The overall total spectral fits at each altitude, displayed in the top panel of each figure in this altitude range are seen to be excellent at altitudes above 7.8 km for these spectra (compared to magnitude of signal). This is represented by a baseline in  $\Delta X$  around the PAN feature (where seen), consisting mostly of high frequency variation around the typical NESR level.

At altitudes between 9.1 and 13.8 km, there is a strong residual feature in  $\Delta X$ , which is seen to be in excellent agreement with the simulated  $\Delta Y$  PAN residual. This feature is strongest and gives the greatest confidence for the fit at 9.1 km (See Figure 6.13). The shape of the PAN band is also clearly defined in  $\Delta X$  at each of the higher altitudes; 10.8 km (Figure 6.14), 11.9 km (Figure 6.15) and 13.8 km (Figure 6.16). At altitudes above 13.8 km, for this region and time of year, no PAN feature is reliably observed due to the expected rapid decrease in PAN concentration across the tropopause.

At low altitude (less than 9 km), spectra become increasingly difficult to fit due to the nature of the extremely variable aerosol extinction profile and water vapour continuum. In Figure 6.12, this is reflected by a slightly poorer  $\Delta X$  baseline at 7.8 km than that seen at higher altitudes, with increased noise and some offset in the broader zero base line. This fit cannot be improved further using the iterative fitting method in this work. At low altitude, we also see that  $\Delta Y$  is comparable to the noise level at 7.8 km, even at the relatively high simulated PAN concentrations (360 pptv). This is due to the saturation effects of stronger molecules in this spectral region such as water vapour, carbon dioxide and carbon tetrachloride. The spectrum seen in the top panel of Figure 6.12 is noted to be very high in water vapour concentration (415 ppmv) on examination of the corresponding level 2 profile of water vapour in Figure 6.8. Hence, the retrieval of PAN is limited at such low altitudes with high water vapour concentrations.

The fitted PAN concentrations as well as an assessment of the accuracy of such values is given later in Section 6.5.

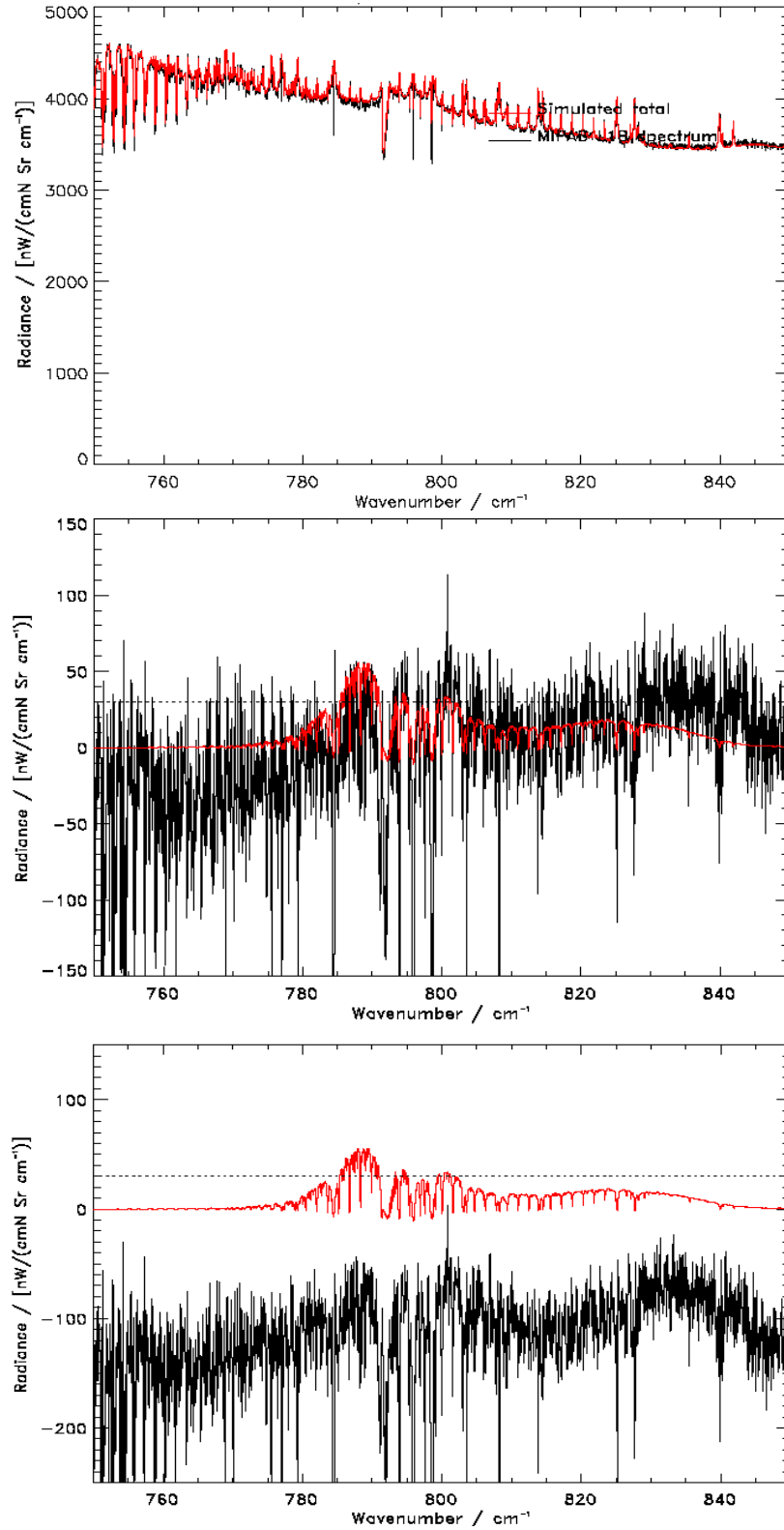


**Figure 6.12** Comparison of MIPAS-E band A (black line) and simulated spectra (red line) at 7.8 km tangent altitude (TID=102506949, 01/04/2003) between: a) total radiance spectra; b) residuals; and c) residuals with  $\Delta X$  shifted by  $-150$  nW for comparison. (Dashed line = typical noise)

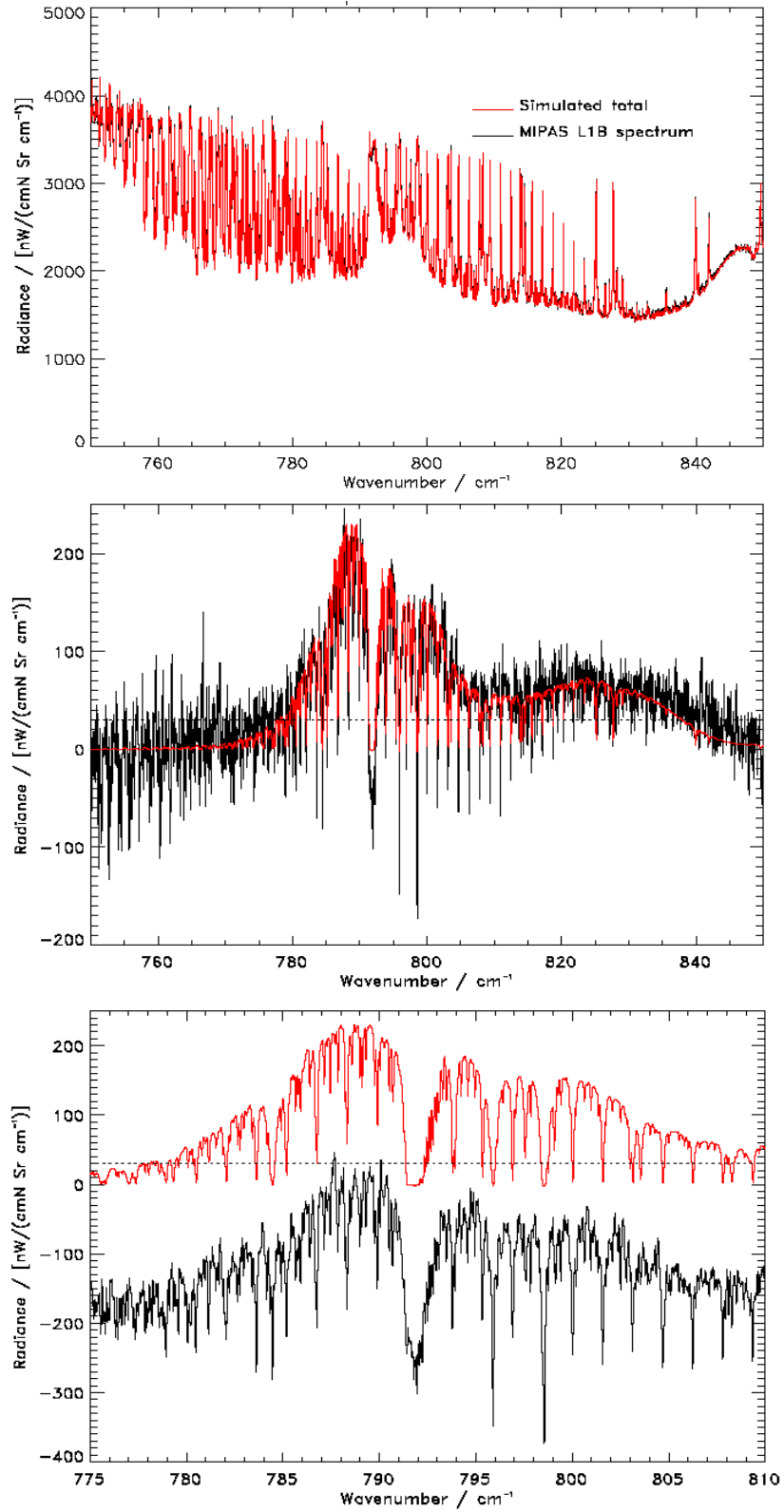


**Figure 6.13** Comparison of MIPAS-E band A and simulated spectra at 9.1 km tangent altitude (TID=102506868, 01/04/2003) for: a) total radiance spectrum; b) residuals; and c) close-up of 775-810  $\text{cm}^{-1}$  region with  $\Delta X$  shifted by  $-200$  nW for comparison. (Dashed line = typical noise)

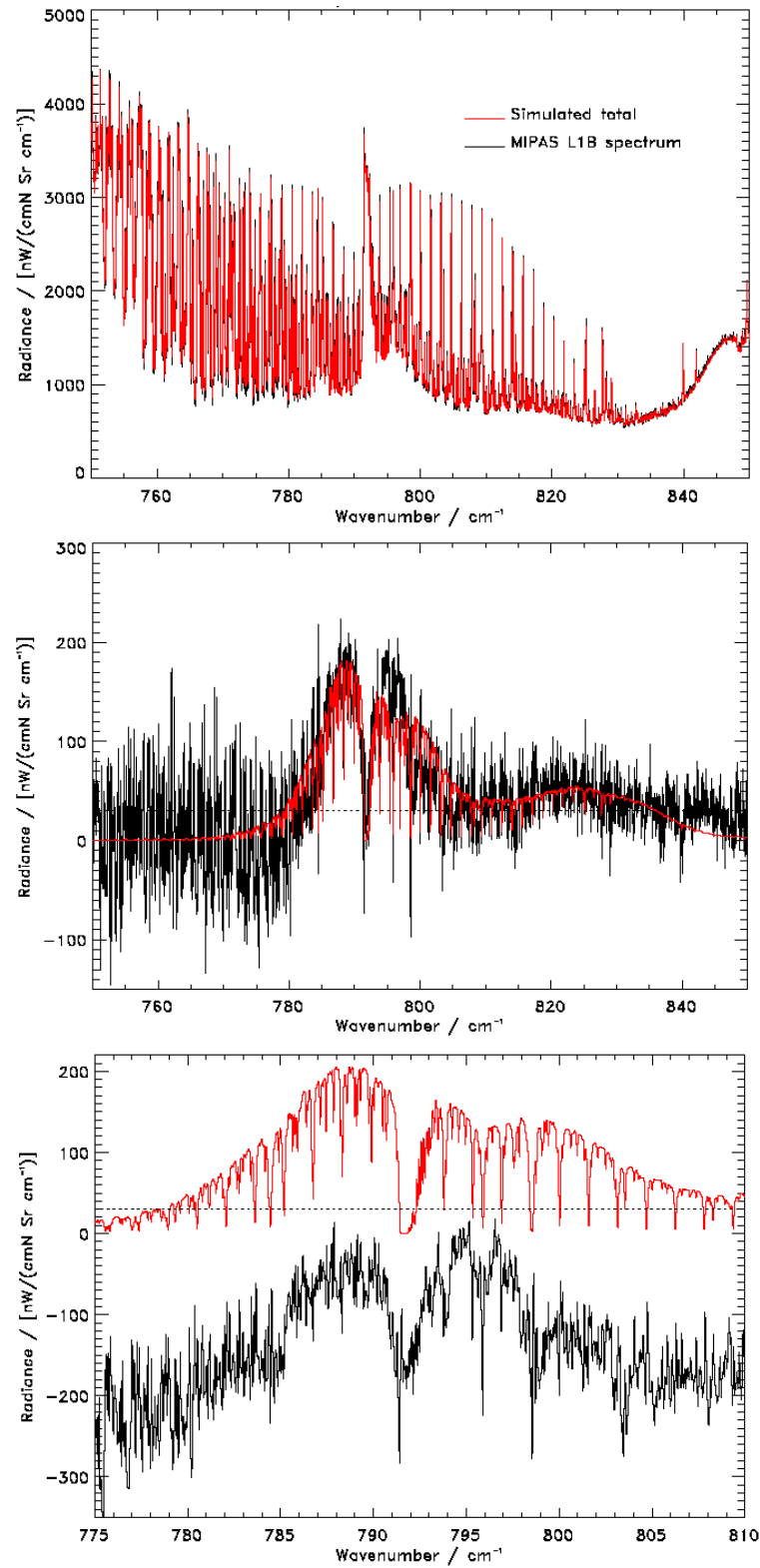


**Figure 6.14** Comparison of MIPAS-E band A and simulated spectra at 10.8 km tangent altitude (TID=105571598, 06/05/2003) for: a) total radiance spectrum; b) residuals; and c) close-up of 775-810  $\text{cm}^{-1}$  region with  $\Delta X$  shifted by  $-200$  nW for comparison. (Dashed line = typical noise)

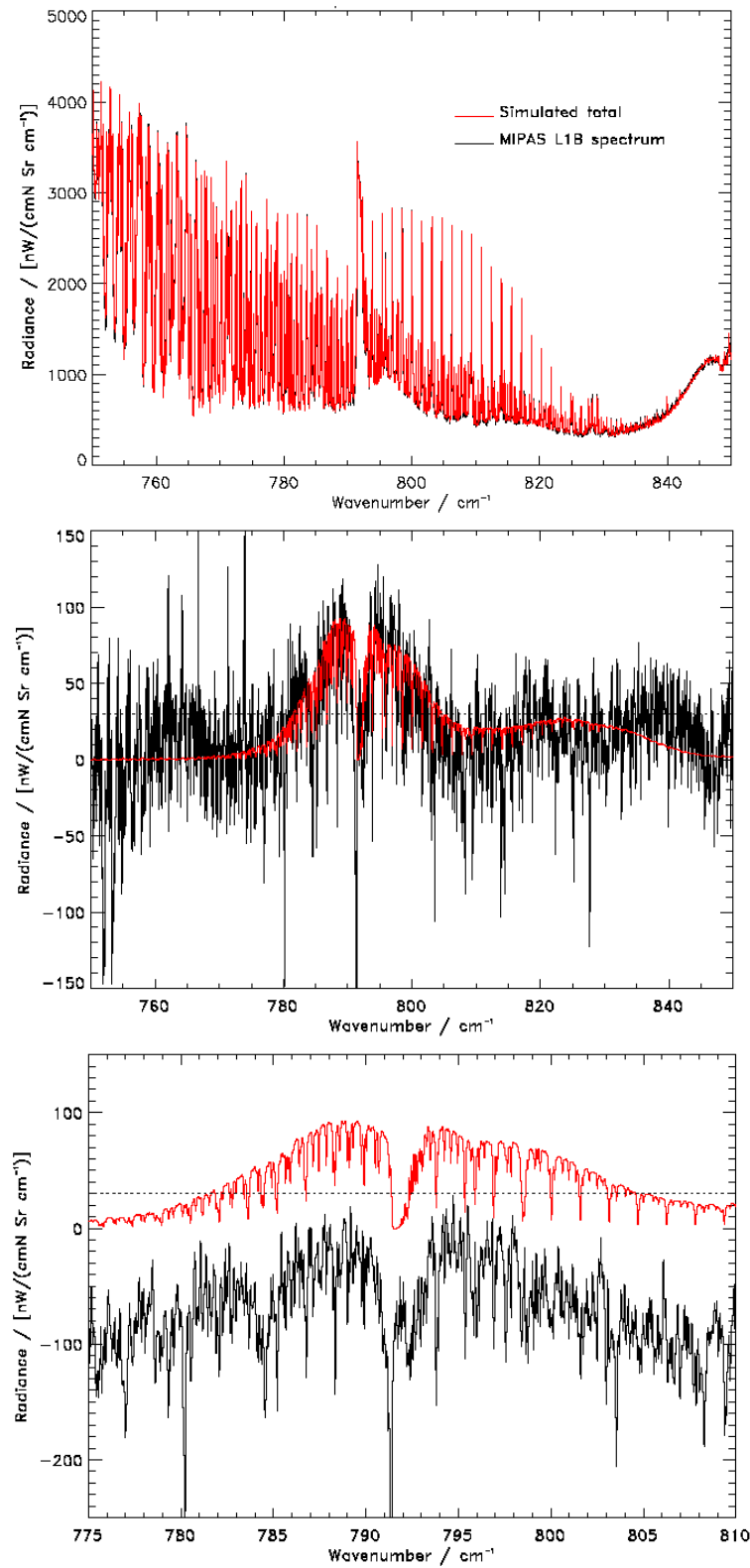


**Figure 6.15** Comparison of MIPAS-E band A and simulated spectra at 11.9 km tangent altitude (TID=102506868, 01/04/2003) for: a) total radiance spectrum; b) residuals; and c) close-up of 775-810 cm⁻¹ region with  $\Delta X$  shifted by -100 nW for comparison. (Dashed line = typical noise)

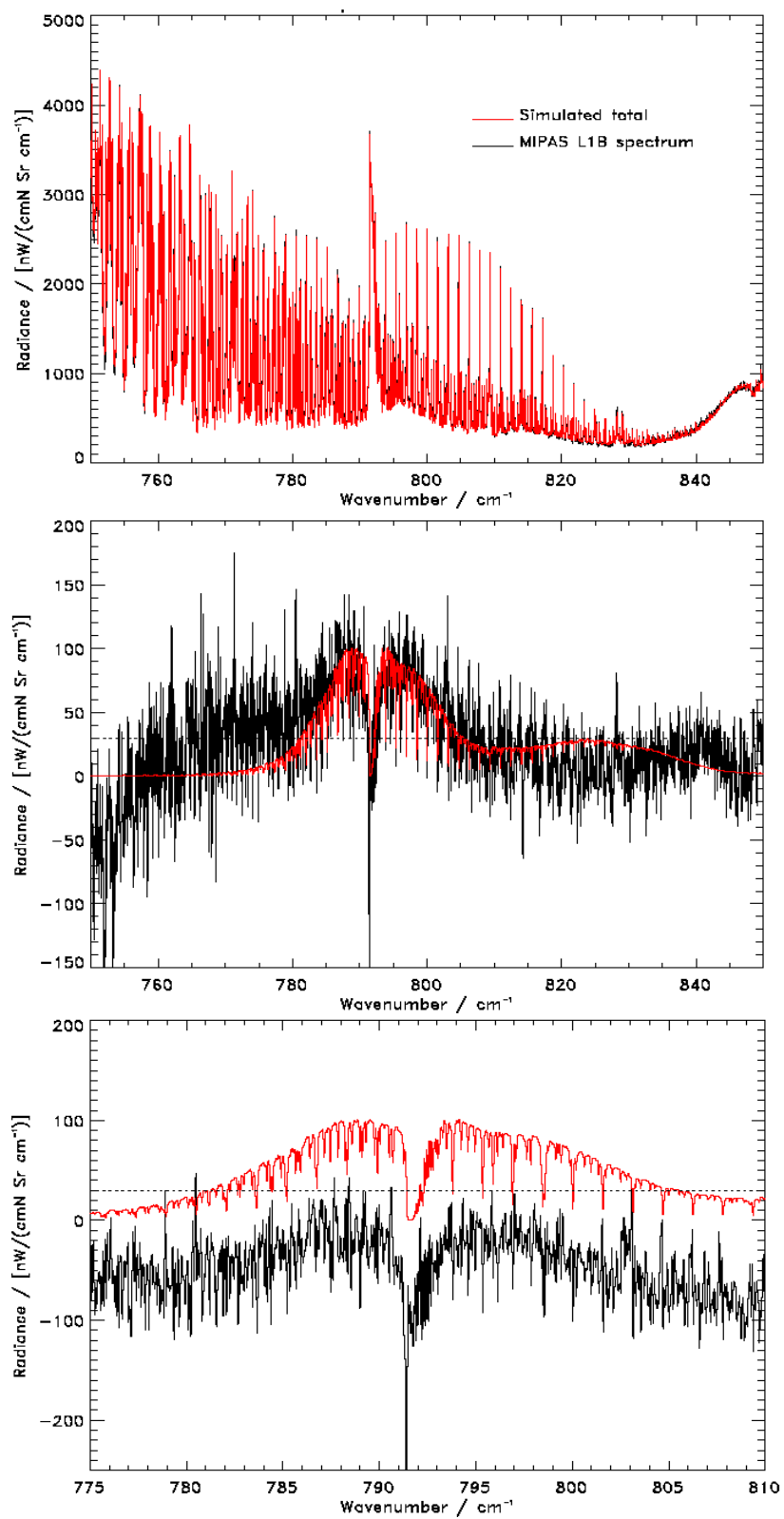


**Figure 6.16** Comparison of MIPAS-E band A and simulated spectra at 13.8 km tangent altitude (TID=1055761598, 06/05/2003) for: a) total radiance spectrum; b) residuals; and c) close-up of 775-810  $\text{cm}^{-1}$  region with  $\Delta X$  shifted by  $-50 \text{ nW}$  for comparison. (Dashed line = typical noise)



### 6.3.4.2 Mediterranean Sea, Spectral Band AB

Examples of spectral fits at 9.1 and 11.9 km tangent altitude, for the two MIPAS-E profiles considered in the previous section for band A in the Mediterranean Sea, are plotted in Figure 6.17 and Figure 6.18 respectively. In each case, these plots show the spectral fit between modelled and observed total radiance spectra together with a comparison of  $\Delta X$  (black) and  $\Delta Y$  (red) residuals. The  $\Delta X$  residual has also been shifted below the baseline in the lower panel of each Figure for ease of comparison with  $\Delta Y$ .

The simulated atmosphere used to forward model these spectra is the same as that used for Band A in the previous section, with the exception of aerosol. The aerosol extinction profile varies with wavelength and therefore different extinction profiles are necessary for each spectral region.

The general spectral fits at each altitude, displayed in the top panel of each figure in this altitude range are also seen to be excellent. This is represented by the good zero baseline in  $\Delta X$  with the remaining high frequency variation predominantly seen around the typical NESR level (dashed line) and therefore attributable to random measurement noise.

The expected residual features in this spectral region are much weaker than for Band A and only just greater than the typical NESR. This makes it difficult to observe any potential influence due to PAN in  $\Delta X$  for Band AB at these PAN concentrations. The residual spectra ( $\Delta X$ ) plotted in Figure 6.17 and Figure 6.18 do not show any clear correlation with  $\Delta Y$  at either of the altitudes considered. At altitudes higher than 12 km, the simulated residual drops well below the noise level and no PAN influence is seen in any of the profiles analysed for the Mediterranean region. Furthermore, below, 9 km,  $\Delta Y$  is also less than the noise level due to saturation effects by more dominant absorbing gases and therefore not observable.

In summary, no clear detection of PAN in the UT is possible from Band AB of MIPAS-E at the concentrations fitted for Band A in the previous section. However, this may be possible at higher concentrations such as those encountered in more polluted geographical regions. This is attempted in the following sections for the East China Sea.

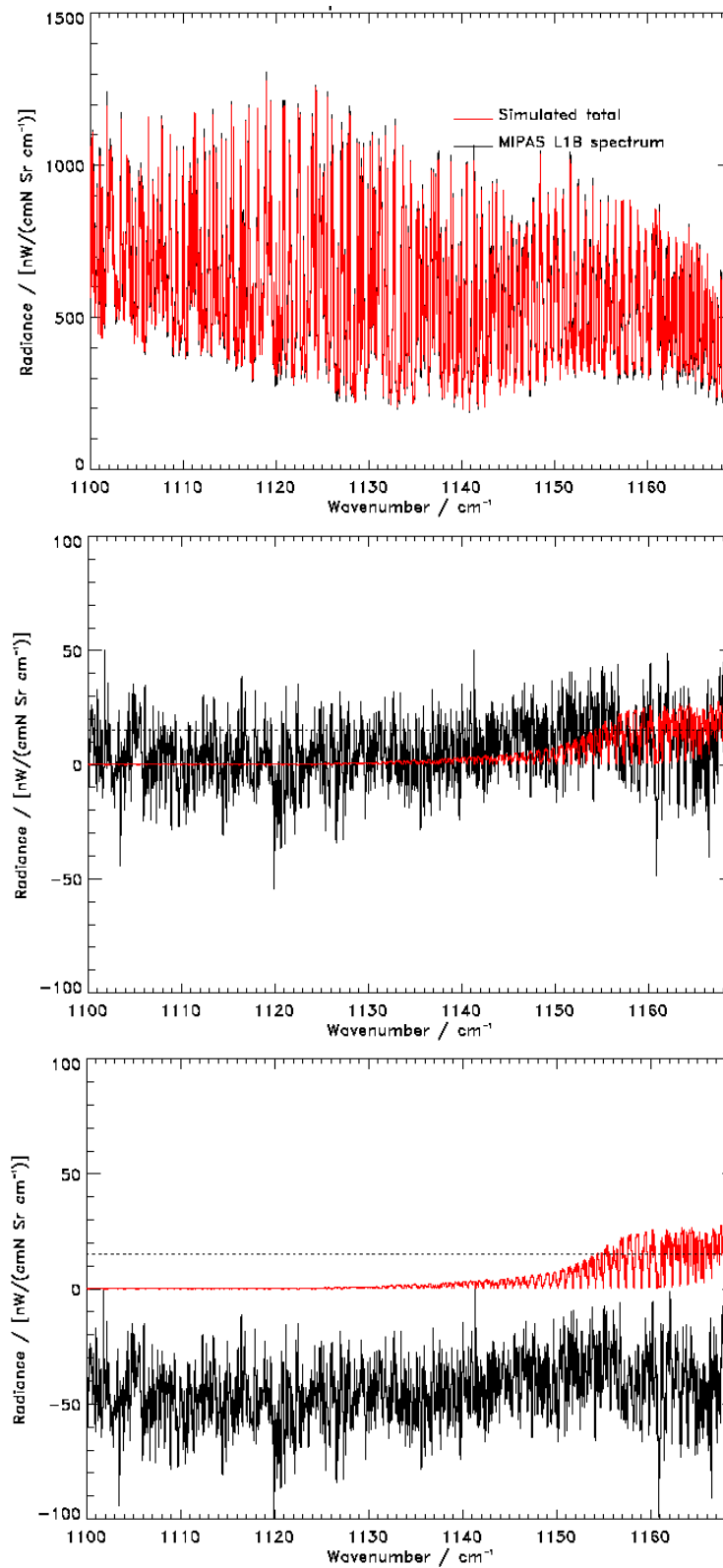


**Figure 6.17** Comparison of MIPAS-E band AB and simulated spectra at 9.1 km tangent altitude (TID=102506868, 01/04/2003) for: a) total radiance spectrum; b) residuals; and c) close-up of 775-810  $\text{cm}^{-1}$  region with  $\Delta X$  shifted by  $-50 \text{ nW}$  for comparison. (Dashed line = typical NESR)

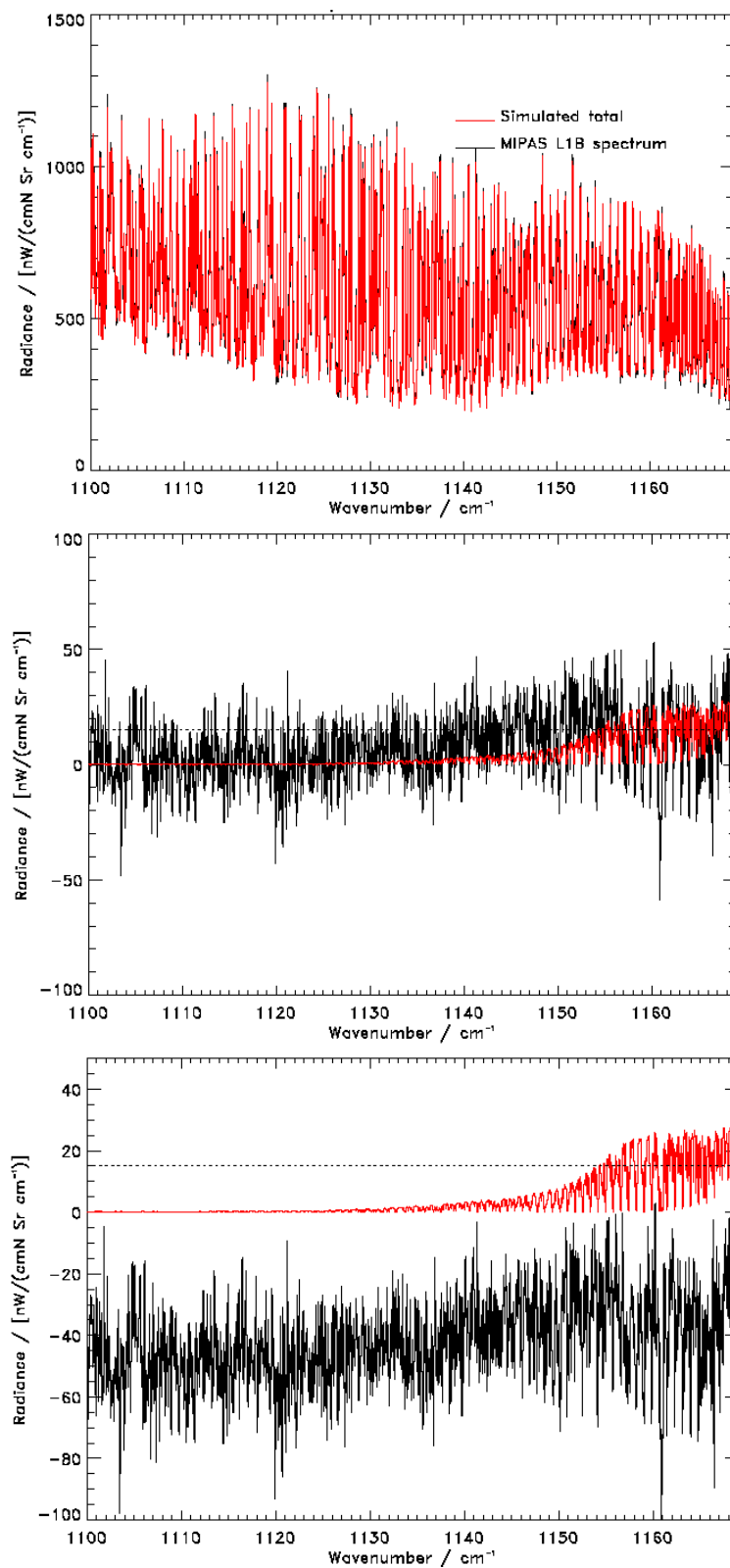


**Figure 6.18** Comparison of MIPAS-E band AB and simulated spectra at 11.9 km tangent altitude (TID=102506868, 01/04/2003) for: a) total radiance spectrum; b) residuals; and c) close-up of 775-810  $\text{cm}^{-1}$  region with  $\Delta X$  shifted by  $-50 \text{ nW}$  for comparison. (Dashed line = typical NESR)

### 6.3.4.3 East China Sea, Spectral Band A

Spectral fits and residual spectra between 9.0 and 13.9 km tangent altitude from four example MIPAS-E, band A profiles in the East China Sea are plotted in Figure 6.19 to Figure 6.23. These fits represent examples for four of the thirteen profiles analysed in this region.

The spectral fits at each altitude displayed in the top panel of each figure in this altitude range are again seen to be excellent, reflected by the excellent zero baseline in  $\Delta X$  either side of the PAN feature, with remaining high frequency variation mostly attributable to instrument noise. Fits for the other ten profiles studied in this region are also seen to be excellent.

Across the altitude range 9.0 to 12.1 km, there is a very strong residual feature in  $\Delta X$  for some profiles, which is seen to be in excellent agreement with simulated  $\Delta Y$  PAN residuals. Some of these very strong residual features correspond to very high fitted PAN concentrations (up to 688 pptv at 11.2 km). This is typical of a number of the profiles studied in this region, with fitted PAN concentrations ranging from 294 pptv to 688 pptv across the altitude range 8.2 to 12.1 km. PAN Concentrations at around 11 km were seen to be lowest on 16<sup>th</sup> April (294 pptv) with the highest concentrations seen on 10<sup>th</sup> April (688 pptv). Such concentrations are rarely observed in the UT, except during strong pollution events. This possibility as well as a full discussion of these fitted concentrations and their accuracy is given in Section 6.5.

Again, at low altitudes (less than 9 km), spectra become increasingly difficult to fit due to aerosol extinction and increased water vapour and PAN radiance contributions are decreased due to saturation; although the very high PAN concentrations do allow observation of a residual feature above the noise level.

At high altitudes (above 14 km), no residual features were observed which correlate with PAN. The expected low concentrations of PAN at this altitude again give a  $\Delta Y$  spectrum that is well below the noise level. This observation of extremely low PAN concentrations at high altitude and very high concentrations in the UT further demonstrate the success of this detection method.

The fitted PAN concentrations here are now used to investigate the possibility of detecting PAN in MIPAS-E band AB in the East China Sea.

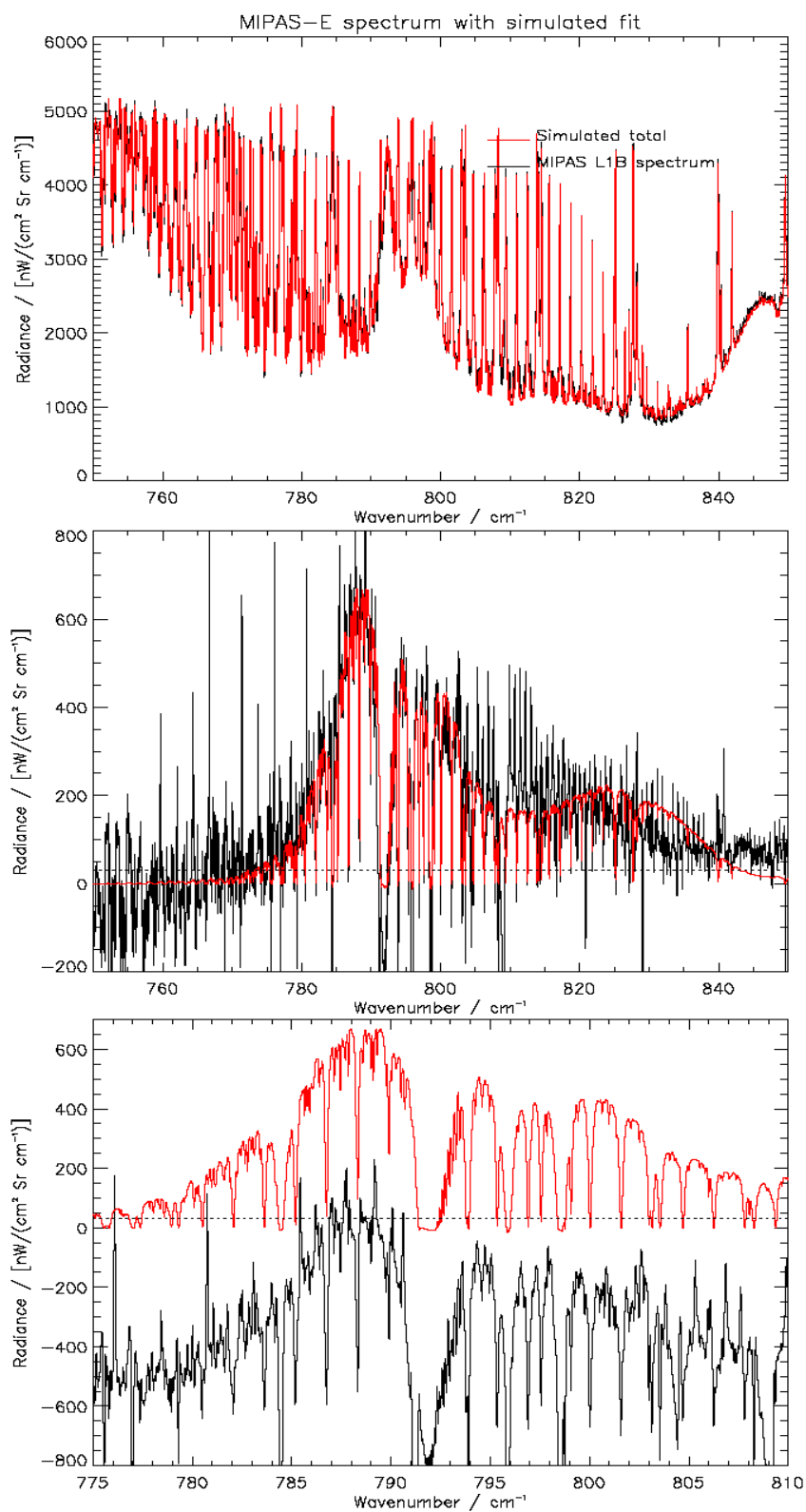


**Figure 6.19** Comparison of MIPAS-E band A and simulated spectra at 9.0 km tangent altitude (TID=103295696, 10/04/2003) for: a) total radiance spectrum; b) residuals; and c) close-up of 775-810  $\text{cm}^{-1}$  region with  $\Delta X$  shifted by  $-600$  nW for comparison. (Dashed line = typical noise)

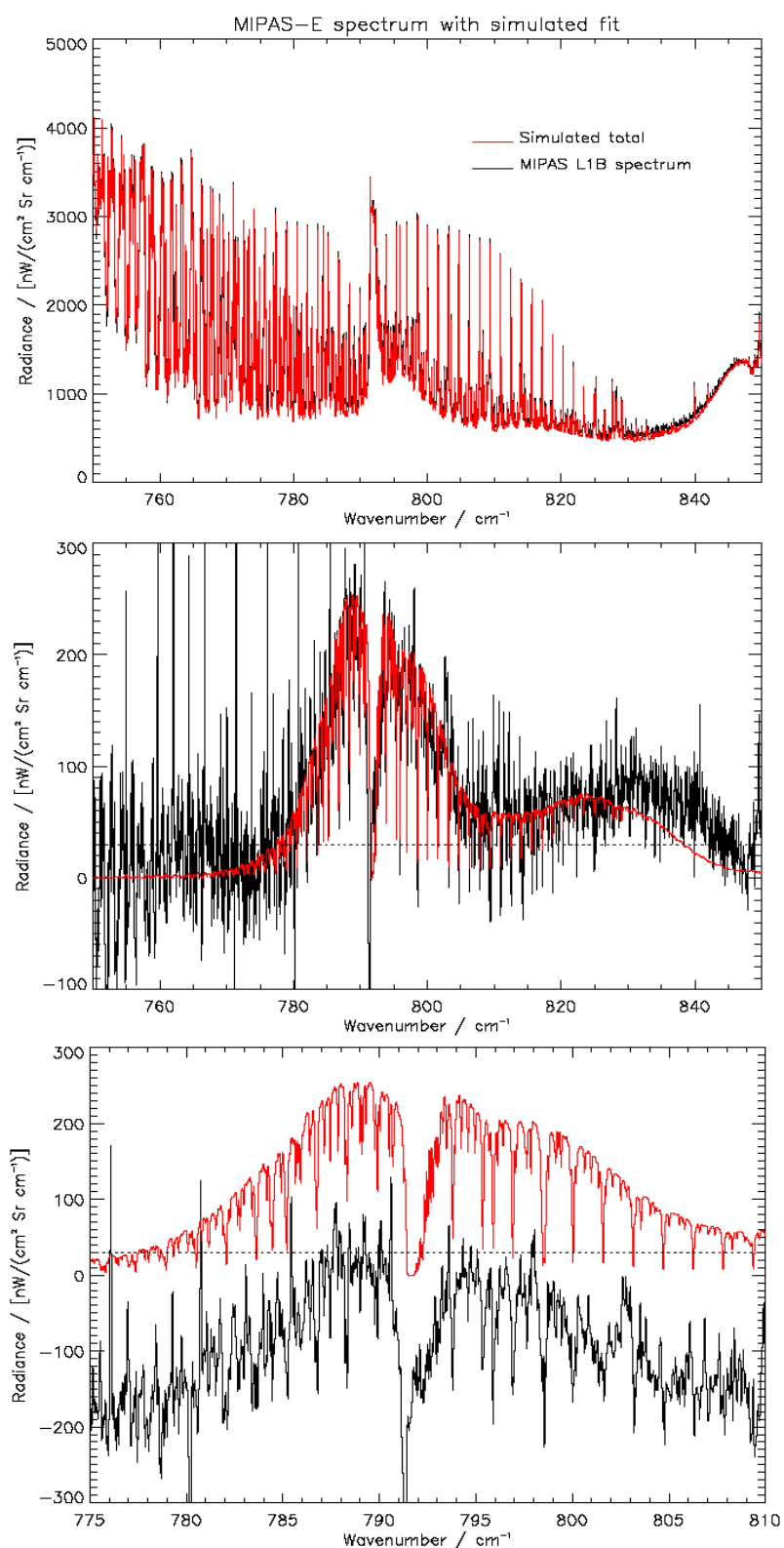


**Figure 6.20** Comparison of MIPAS-E band A and simulated spectra at 11.2 km tangent altitude (TID=103814896, 16/04/2003) for: a) total radiance spectrum; b) residuals; and c) close-up of 775-810  $\text{cm}^{-1}$  region with  $\Delta X$  shifted by  $-200$  nW for comparison. (Dashed line = typical noise)

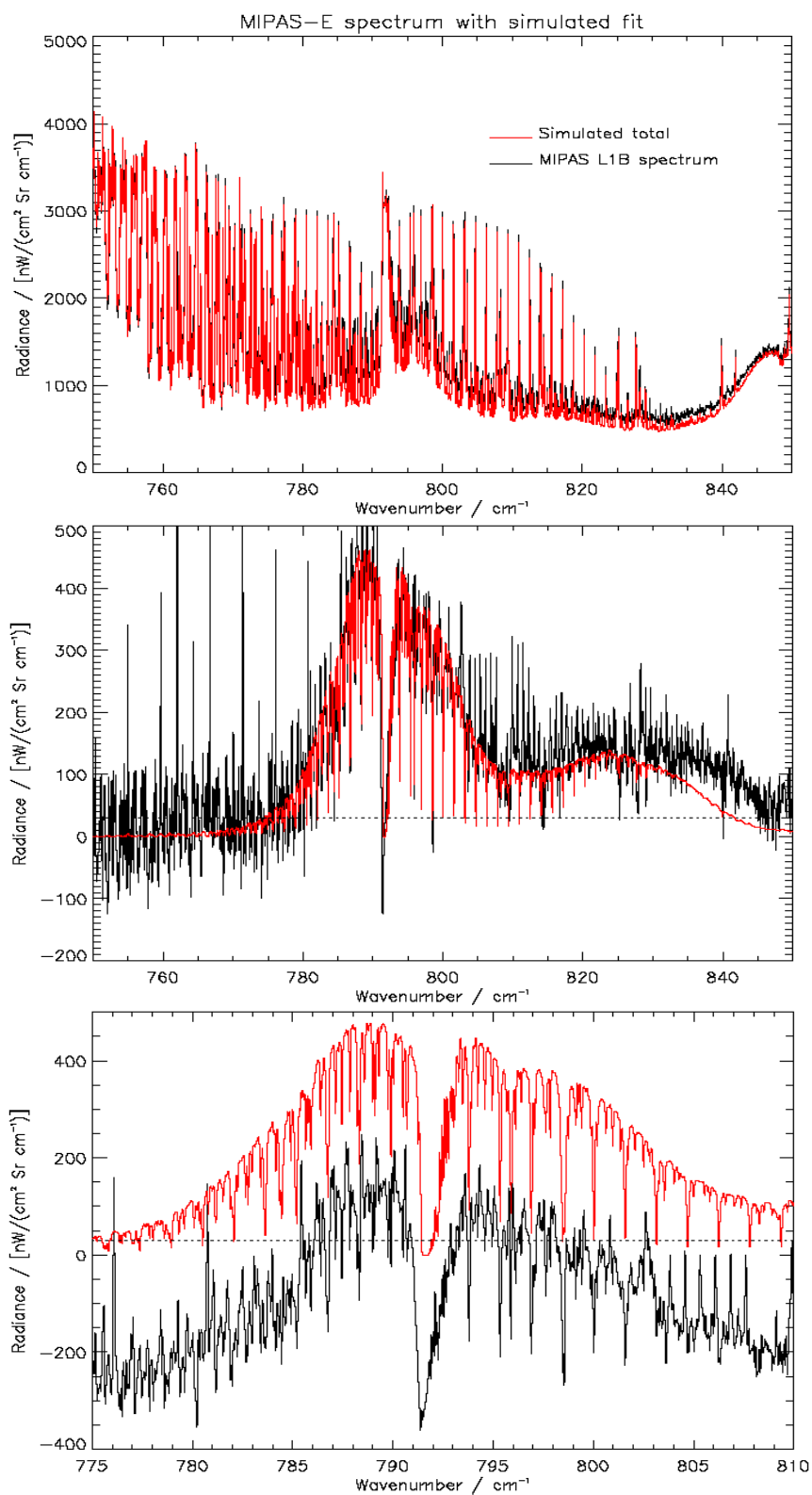


**Figure 6.21** Comparison of MIPAS-E band A and simulated spectra at 11.2 km tangent altitude (TID=104074379, 19/04/2003) for: a) total radiance spectrum; b) residuals; and c) close-up of 775 to 810 cm<sup>-1</sup> region with  $\Delta X$  shifted by -200 nW for comparison. (Dashed line = typical noise)

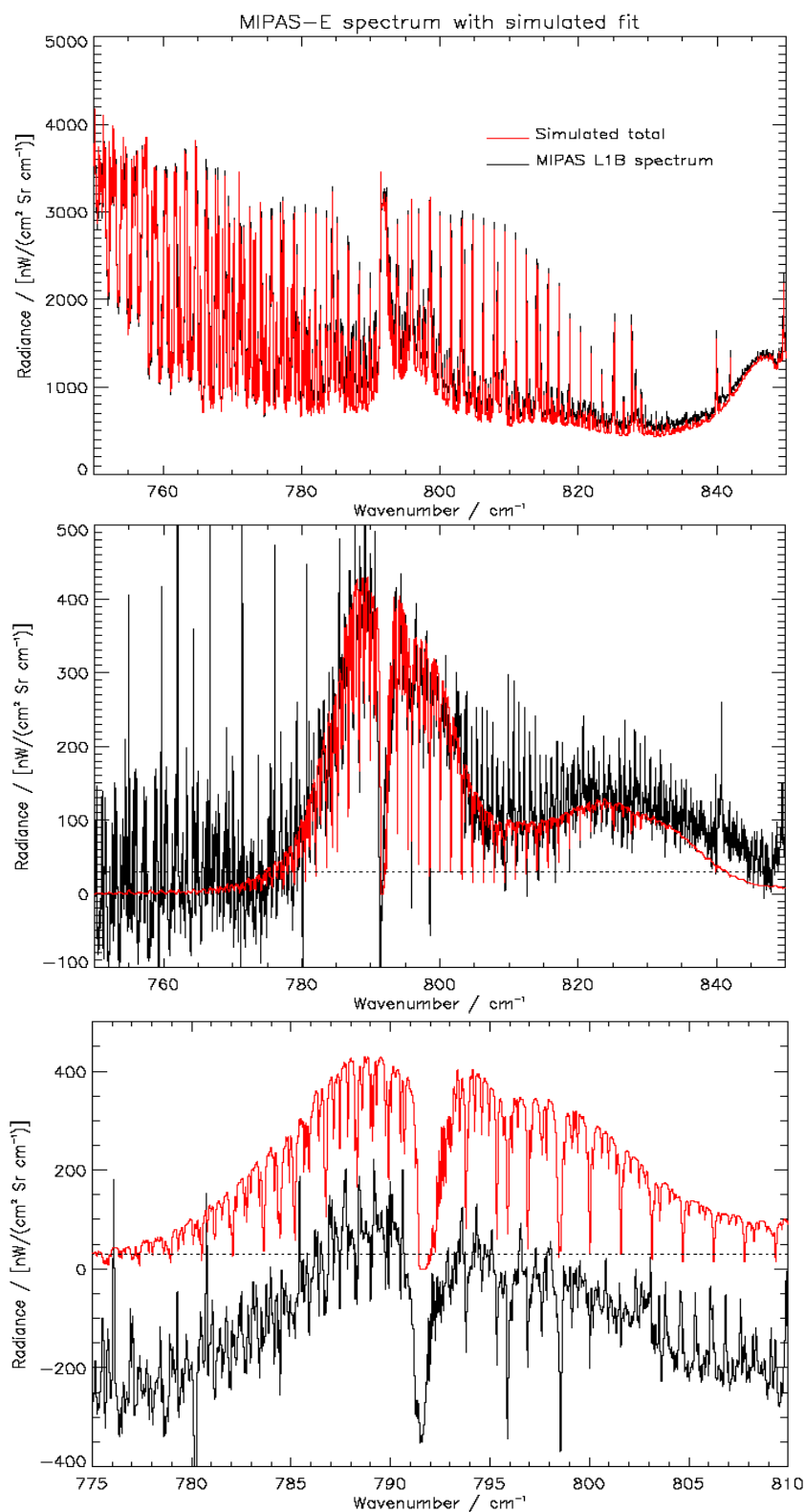


**Figure 6.22** Comparison of MIPAS-E band A and simulated spectra at 12.1 km tangent altitude (TID=103295696, 10/04/2003) for: a) total radiance spectrum; b) residuals; and c) close-up of 775 to 810  $\text{cm}^{-1}$  region with  $\Delta X$  shifted by  $-200$  nW for comparison. (Dashed line = typical noise)



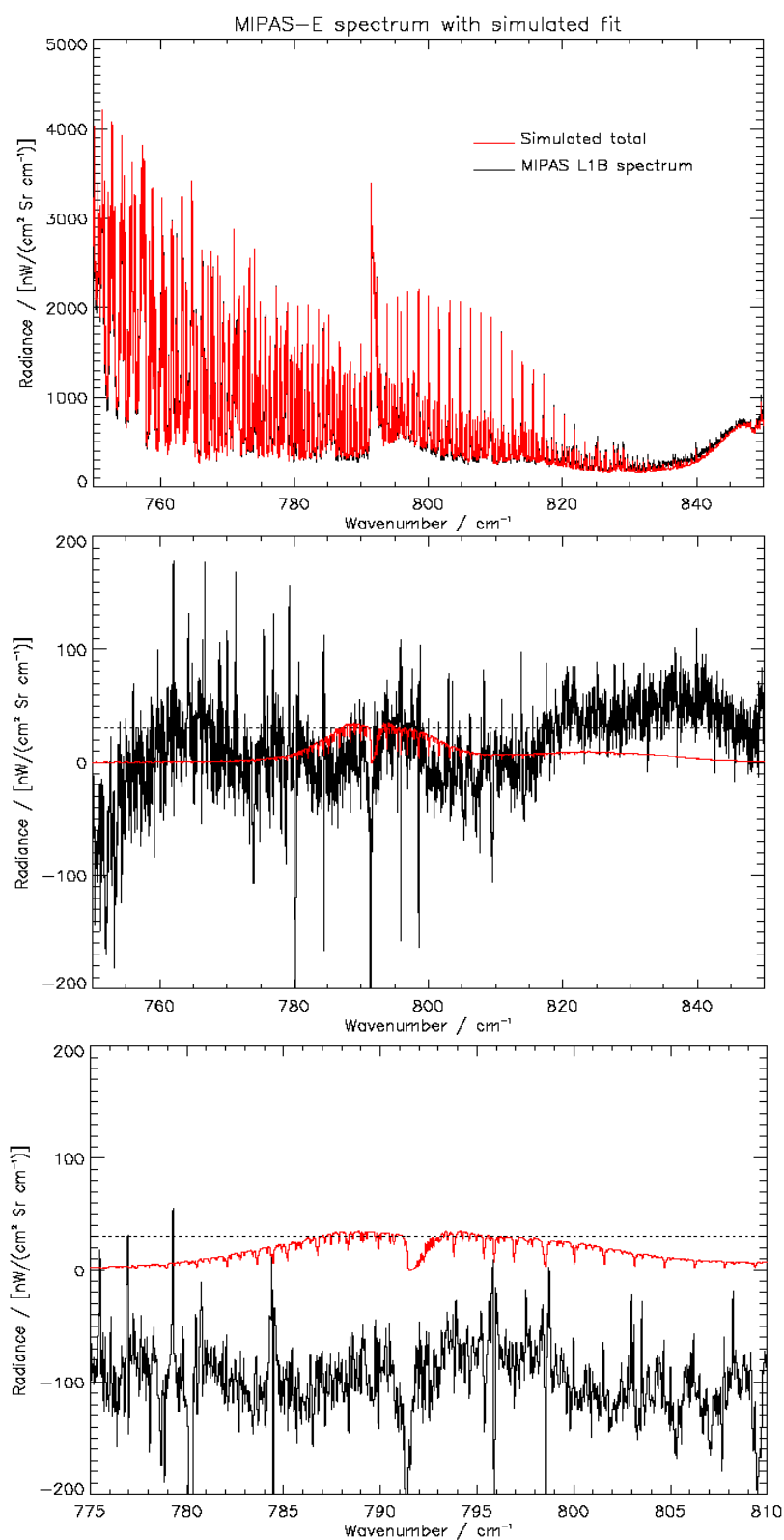


**Figure 6.23** Comparison of MIPAS-E band A and simulated spectra at 13.9 km tangent altitude (TID=104203382, 21/04/2003) for: a) total radiance spectrum; b) residuals; and c) close-up of 775 to 810  $\text{cm}^{-1}$  region with  $\Delta X$  shifted by  $-100 \text{ nW}$  for comparison. (Dashed line = typical noise)

#### 6.3.4.4 East China Sea, Spectral Band AB

Spectral fits and residual spectra between 9.1 and 12.1 km tangent altitude for two example MIPAS-E band AB profiles in the East China Sea are plotted in Figure 6.24 and Figure 6.25. These fits represent examples for two of the thirteen profiles analysed in this region.

In both figures, there is a strong residual feature in  $\Delta X$  (black), which is seen to be in excellent agreement with simulated  $\Delta Y$  PAN (red) residuals using the fitted PAN concentrations derived for Band A. This feature is readily observed for the high PAN concentrations fitted here (up to 688 pptv), although it is not easily observed at concentrations less than 300 pptv, such as those plotted earlier for the Mediterranean (see Figure 6.17).

A further strong and clear feature is also observed in  $\Delta X$  between 1100 and 1130  $\text{cm}^{-1}$ . This feature strongly resembles part of a characteristic molecular P, Q, R branching. After further investigation, this spectral feature was confidently identified to be due to formic acid  $[\text{C}(\text{O})\text{OH}]$ . Further information regarding the detection of formic acid is given in the following section.

At lower altitudes (less than 9 km), saturation effects reduce the PAN radiance contribution to well below the noise level, even at the high PAN concentrations expected here. Therefore no evidence of PAN is seen in Band AB below 9 km for those profiles considered.

At high altitudes (above 14 km), the expected low concentrations of PAN give a  $\Delta Y$  spectrum that is well below the noise level and consequently no PAN influence was observed in any of the band AB spectra considered here.

In summary, PAN is detectable in Band AB for high concentrations of PAN between 9 and 12 km and an excellent agreement is seen using concentrations inferred from band A spectral fits. Below 9 km and above 12 km, no PAN feature is observed due to spectral saturation and low concentration respectively.

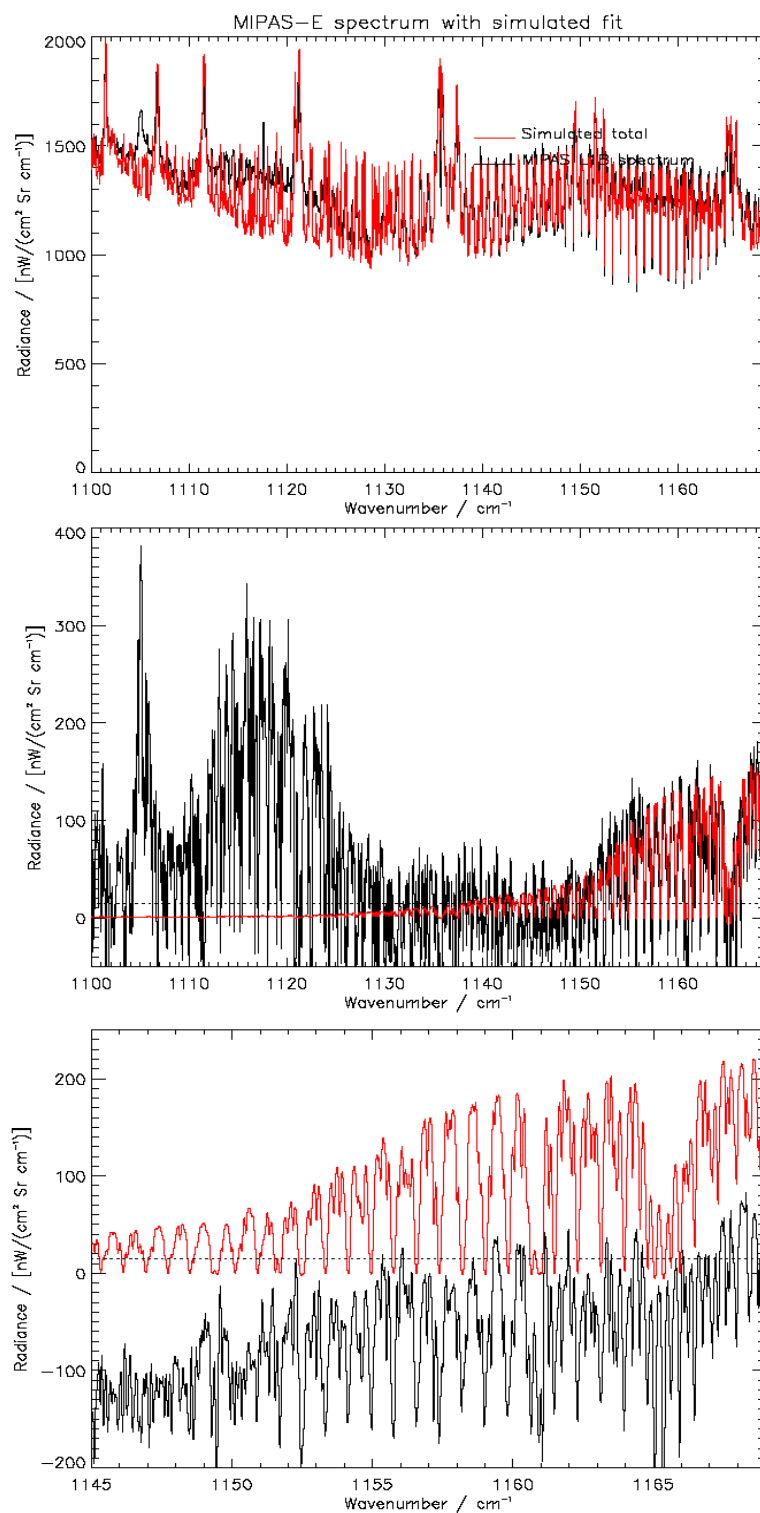


**Figure 6.24** Comparison of MIPAS-E band AB (black line) and simulated spectra (red line) at 9.1 km tangent altitude (TID=103295696, 10/04/2003) for: a) total radiance spectrum; b) residuals; and c) close-up of 1145 to 1170  $\text{cm}^{-1}$  region with  $\Delta X$  shifted by  $-150 \text{ nW}$  for comparison. (Dashed line = typical noise)

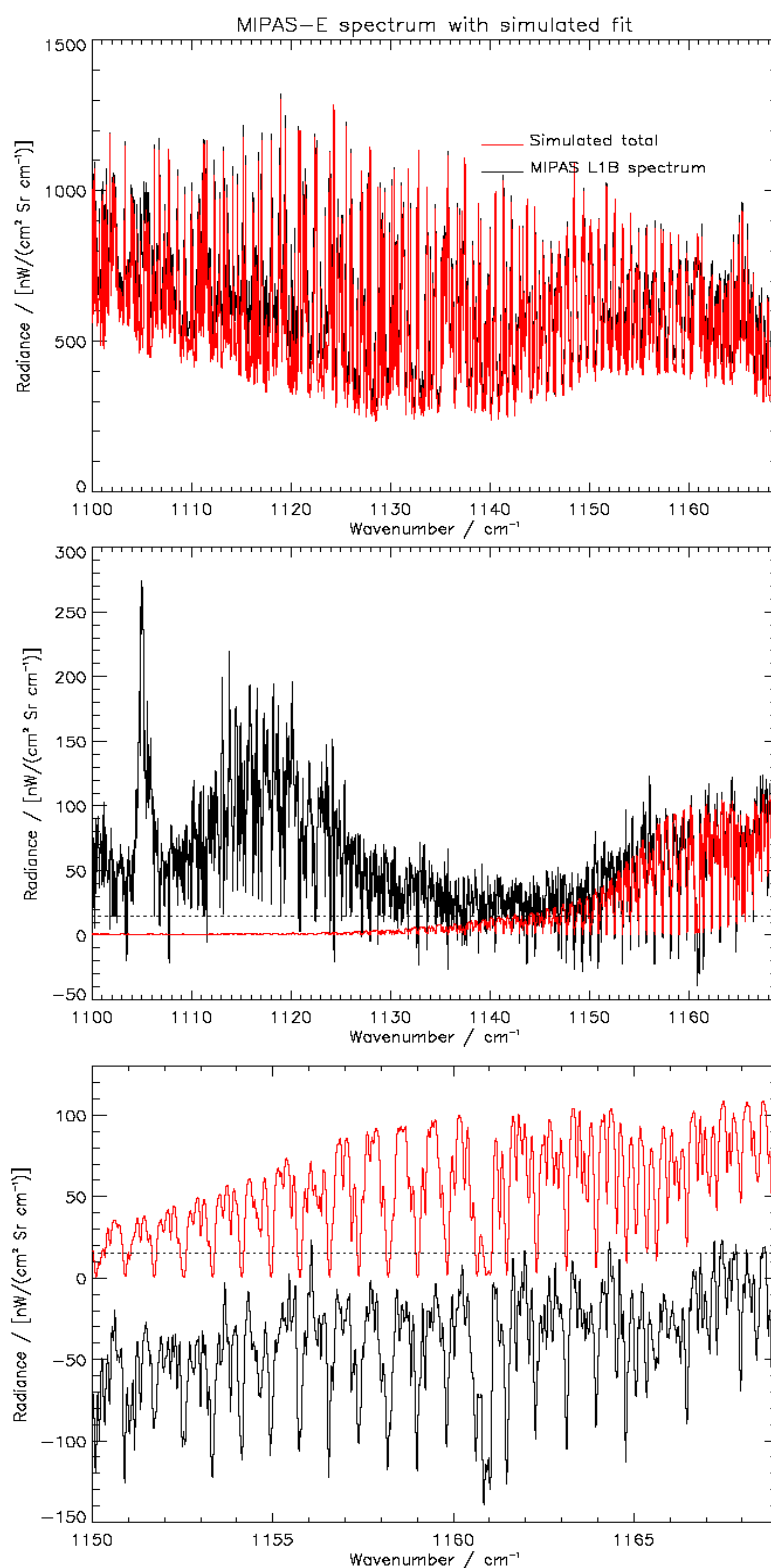


**Figure 6.25** Comparison of MIPAS-E band AB and simulated spectra at 12.1 km tangent altitude (TID=103295696, 10/04/2003) for: a) total radiance spectrum; b) residuals; and c) close-up of 1145-1170 cm<sup>-1</sup> region with  $\Delta X$  shifted by -100 nW for comparison. (Dashed line = typical noise)

## 6.4 Detection of Formic Acid

As shown in the previous section, strong residual spectral features identified to be due to formic acid [HCOOH], were observed during the course of PAN detection in MIPAS-E Band AB spectra of the East China Sea region between 9 and 11 km.

Formic acid is an organic compound that has a number of direct anthropogenic and biogenic sources as well as from biomass burning. It is also formed in the atmosphere by oxidation of hydrocarbon precursors [see Khare *et al.*, 1999, for a discussion of possible sources and sinks]. Interestingly, formic acid has been observed to be well correlated with springtime PAN concentrations [Granby *et al.*, 1997] by virtue of their common atmospheric precursors, with concentrations of up to 600 pptv for formic acid reported in the UT (7.7 to 9.8 km) by Reiner *et al.* [1999]. A full discussion of the atmospheric role and spectroscopy of formic acid is beyond the scope of this thesis, but the reader is referred to work by Waterfall [2003], which discusses the potential detection of the compound using MIPAS-B2 data.

The formic acid spectral signal detected here in the MIPAS-E data of the East China Sea greatly exceeds those inferred in the study by Waterfall [2003] for the Mediterranean region (around 100 pptv). Concentrations of formic acid retrieved using the data considered in this thesis have been found to be higher than 1000 pptv at 11.9 km [Waterfall, private communication]; although this retrieval is noted to be subject to considerable uncertainty at the time of writing. A simulated residual spectrum for the retrieved formic acid concentration found from data plotted in Figure 6.24, is plotted with the measured MIPAS-E residual in Figure 6.26. The simulated residual using the retrieved formic acid concentration is seen to be in excellent agreement with the measurement residual.

Such high concentrations of formic acid, if accurate, may represent some of the highest known observed concentrations of formic acid in the UT and are seen here to be coincident with very high inferred PAN concentrations. The implications of this observation for chemical process studies of the atmosphere is beyond the scope of this work although such observation may prove a useful tool for such work with further development. This possibility is further discussed in the next chapter.

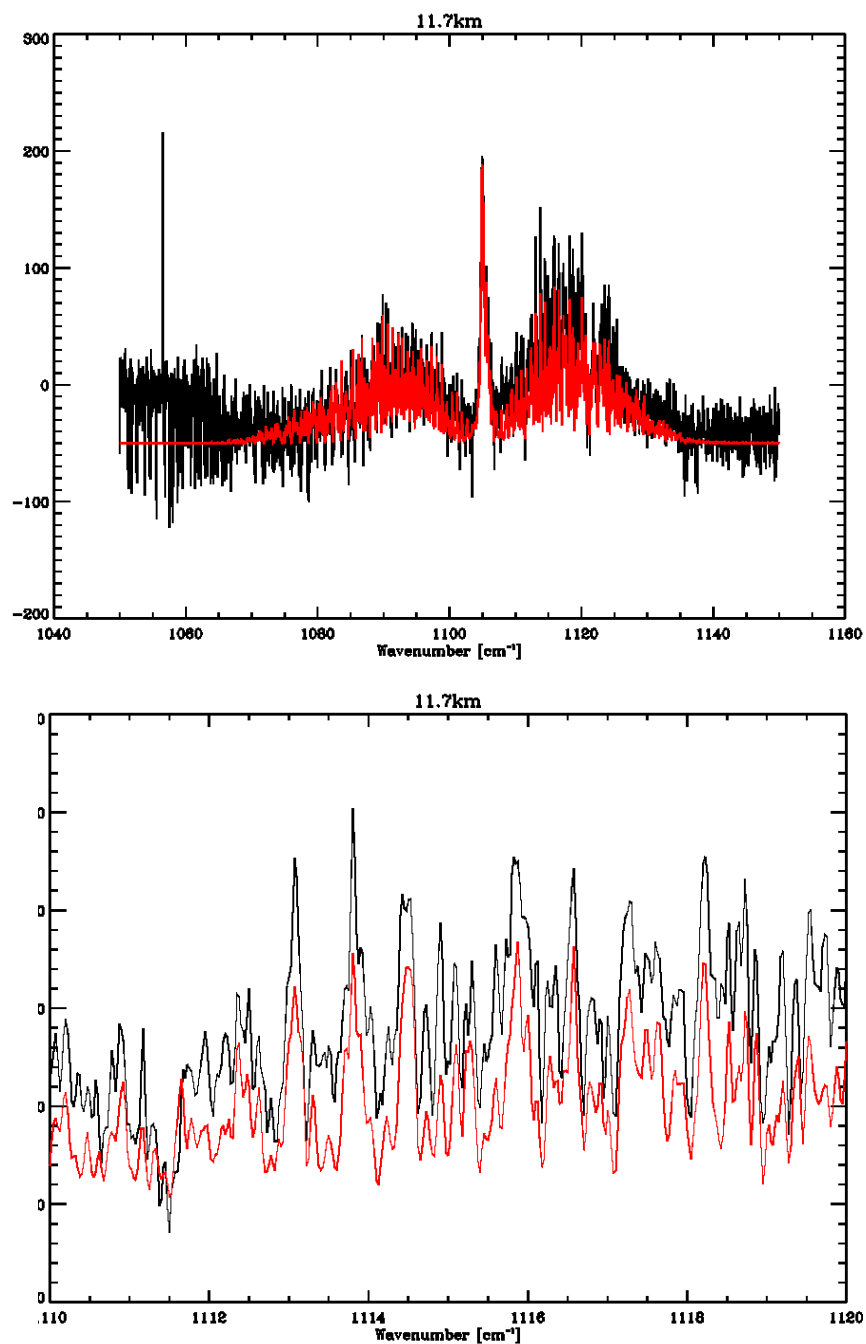


**Figure 6.26** Comparison of residual spectra for MIPAS-E (black) and simulated residual for formic acid (red) using retrieved concentration of formic acid (1000 pptv), Waterfall [personal communication]) for MIPAS-E profile time ID:103295696 at 11.7 km. (Top: 1050-1150  $\text{cm}^{-1}$  spectral region; Bottom: close-up of the 1110-1120  $\text{cm}^{-1}$  region).

## 6.5 Retrieval Accuracy

The fitted PAN concentrations for profiles studied in the previous sections are given in Table 6.6 for both geographical regions studied in the altitude ranges 8 to 9.2 km and 11 to 12.3 km.

Region	Time ID and (day)	Tangent Altitude range	
		(8.0-9.2 km) Fitted PAN conc. /pptv	(11.0-12.3 km) Fitted PAN conc. /pptv
Mediterranean Sea	102506868 (01)	$322 \pm 23$	$131 \pm 10$
	102506949 (01)	-	$90 \pm 7$
	103585641 (13)	-	$86 \pm 6$
	103845186 (16)	$259 \pm 18$	$143 \pm 10$
	103929970 (17)	-	$120 \pm 9$
	105571598 (06)	$177 \pm 13$	$84 \pm 6$
	106006102 (11)	$268 \pm 18$	$77 \pm 6$
East China Sea	103165159 (09)	-	$315 \pm 23$
	103295696 (10)	$780 \pm 55$	$590 \pm 42$
	103295777 (10)	$743 \pm 53$	$575 \pm 41$
	103814901 (16)	-	$668 \pm 47$
	104074379 (19)	$815 \pm 58$	$628 \pm 44$
	104203382 (21)	-	$608 \pm 43$
	104418346 (23)	$596 \pm 42$	$540 \pm 38$
	104418427 (23)	$622 \pm 44$	$565 \pm 40$
	104462835 (24)	-	$350 \pm 25$
	104462926 (24)	-	$325 \pm 24$
	104547430 (25)	-	$450 \pm 32$
	104806884 (28)	$630 \pm 44$	$350 \pm 25$
	104806975 (28)	$650 \pm 46$	$390 \pm 27$
	104937436 (29)	-	$590 \pm 42$

**Table 6.6** Fitted PAN concentrations for MIPAS-E profiles studied in this thesis with uncertainty due to spectroscopic error. Note: “day” corresponds to the date in April 2003.

The uncertainty quoted in Table 6.6 represents the uncertainty in the fit due to the uncertainty in the 250 K PAN reference cross-section (7%) at  $794\text{ cm}^{-1}$  calculated in Chapter 4.

It should be noted that this uncertainty does not include the many other potential sources of uncertainty, both systematic and random. Systematic errors may include spectral offset and gain calibration errors as well as errors in the spectroscopy of contaminant gases. In addition, random error sources such as a baseline shift caused by incorrect temperature, pressure, water vapour and aerosol concentrations, may be present. This uncertainty therefore represents an underestimate of the absolute error if all other parameters are perfectly fitted.

Further insight into the potential influence of such poorly fitted parameters is considered in the following section.

### 6.5.1 Fit Sensitivity

An analysis of the sensitivity of fitted PAN concentrations to small changes in pressure, temperature and other gas concentrations provides a useful indication of the feasibility of accurate retrieval of PAN in the atmosphere and its limitations. Such analysis was performed using Jacobian spectra of temperature, pressure, aerosol, water vapour and  $\text{CCl}_4$  (parameters that are noted to be of the greatest significance in the region of the  $794.0\text{ cm}^{-1}$  PAN band).

Although such perturbations do not improve the spectral fits in this work, any difference in the fitted profiles of these parameters does affect the quality of the fit for PAN residual spectra and hence the inferred concentration. The difference in fitted PAN concentrations for profiles perturbed in this way for MIPAS-E Band A are shown in Table 6.7.

Aerosol is seen to have the biggest influence with small changes in extinction coefficient causing large deviations in the fitted PAN concentration. Such large aerosol extinction is typically decreased at higher altitudes, suggesting that this source of uncertainty is less significant in the high UT. Small changes in pressure and temperature cause less significant changes in fitted PAN concentration, with an increasing dependence with temperature at higher altitudes.

It should be noted that perturbations in spectra induced by changes in aerosol, temperature, or pressure profiles are visible as a baseline shift in  $\Delta X$  and therefore such



perturbations would be corrected for using the spectral fitting method in this thesis. In addition, the nature of such perturbations to spectral features such as the CO<sub>2</sub> Q-branch at 792 cm<sup>-1</sup> (which is sensitive to pressure and temperature) can also indicate the cause of such an offset in the baseline and therefore allow its correction.

Parameter	Perturbation	Altitude		
		9.0 km	12.0 km	15.0 km
Temperature	+ 1 K	+ 6	+ 10	+ 18
	- 1 K	- 6	- 10	- 18
Pressure	+ 1 mb	+ 6	+ 9	+ 3
	- 1 mb	- 6	- 9	- 3
Aerosol*	+ 1×10 <sup>-4</sup>	+40	+ 35	+ 20
	- 1×10 <sup>-4</sup>	- 29	- 26	- 20
Water Vapour	+ 8 pptv	+ 10	0	0
	- 8 pptv	- 10	0	0
CCl <sub>4</sub> <sup>†</sup>	+ 1.1 pptv	+5	+5	+5
	- 1.1 pptv	-5	-5	-5

**Table 6.7** Sensitivity of fitted PAN concentration (pptv) to perturbations in otherwise optimised profiles of temperature, pressure, aerosol and CCl<sub>4</sub>. The values represent the change in the fitted PAN concentration for the quoted change in each parameter. \* Aerosol perturbation refers to a change of  $\pm 1 \times 10^{-4}$  in extinction coefficient. † A change of 1.1pptv in CCl<sub>4</sub> represents a 1% change in CCl<sub>4</sub> concentration at 12.0 km.

CCl<sub>4</sub> is seen to have a systematic and small effect on the fitted PAN concentration, although CCl<sub>4</sub> concentrations in the atmosphere are relatively homogeneous in the troposphere due to its long lifetime and therefore should not pose a significant problem so long as a recent measurement of the compound's concentration is used in the simulated atmosphere.

This sensitivity (especially to aerosol and temperature) demonstrates the need for accurate knowledge of all profiles in order to obtain an accurate retrieval of PAN concentration.

## 6.5.2 Limit of Detection

The detection limit for PAN from MIPAS-E is calculated here as the minimum PAN concentration required to give a spectral radiance signal greater than the typical NESR at the point of peak PAN radiance contribution for both the 794 and 1163  $\text{cm}^{-1}$  PAN bands. These limits are given in Table 6.8.

Band	9 km	12 km
A	65	56
AB	210	115

**Table 6.8** Theoretical limits of detection for PAN (pptv) in measurement bands A and AB for MIPAS-E at nominal altitudes of 9 and 12 km.

Saturation effects and increased measurement noise at 9 km increase the detection limit at this altitude relative to 12 km. At altitudes less than 9 km, increased water vapour and other gases reduce PAN radiance contributions to well below the noise level and no reliable limit of detection can be calculated. Above the tropopause, PAN is expected to be present in very small concentrations and is therefore undetectable; although, should PAN be present, limits of detection at higher altitude remain similar to those calculated here at 12 km.

## 6.6 Back Trajectory Analysis

This section attempts to investigate the origin of airmasses observed to be high in PAN content (using the spectral fitting method in this thesis) over the East China Sea.

As noted in Section 6.3.4.3, very high PAN concentrations were fitted to spectra in the UT on occasion in the East China Sea. Lower, more typical background concentrations were seen at other times. Such high concentrations may be indicative of a recent pollution event such as the convective outflow of pollutants from the polluted Asian boundary layer or the lifting of pollutants into the upper troposphere by so-called warm-conveyor belts (WCBs). Both clean lifted [Grant *et al.*, 2000] and heavily polluted [Stohl and Trickl, 1999] airmasses have been observed in the UT due to such lifting depending on location. WCBs have been seen to originate with high frequency in

the boundary layer over the warm water pools in East Asia, based on trajectory calculations [Stohl, 2001].

The fitted concentrations of PAN between 11 and 12 km are plotted according to geographical location in Figure 6.27 showing the high concentrations seen in the East China Sea.

In order to investigate the possibility that airmasses seen to have high PAN content may have been subject to frontal uplifting, a number of back-trajectories were calculated using the HYSPLIT model described by Draxler and Rolph [2003]. This well-used Lagrangian model, developed by National Oceanic and Atmospheric Agency (NOAA), is capable of calculating single-particle trajectories reversed from a nominal time and location using available meteorological data recorded from a range of stations near to the region of interest. A discussion of the relative merits and limitations of this and other such models is beyond the scope of this thesis but further information can be found at the NOAA-HYSPLIT website ([www.arl.noaa.gov/ready/hysp\\_info.html](http://www.arl.noaa.gov/ready/hysp_info.html)).

Three-day back trajectories were calculated from the nominal geolocation and times reported for MIPAS-E spectra that were seen here to contain the highest and lowest PAN concentrations. These were spectra recorded on 16<sup>th</sup> April 2003 at 11.2 km (TID = 103814901, 668 pptv PAN) and on 9<sup>th</sup> April 2003 at 12.4 km (TID = 104462835, 315 pptv PAN) respectively. These back trajectories are plotted in Figure 6.28 and Figure 6.29 respectively.

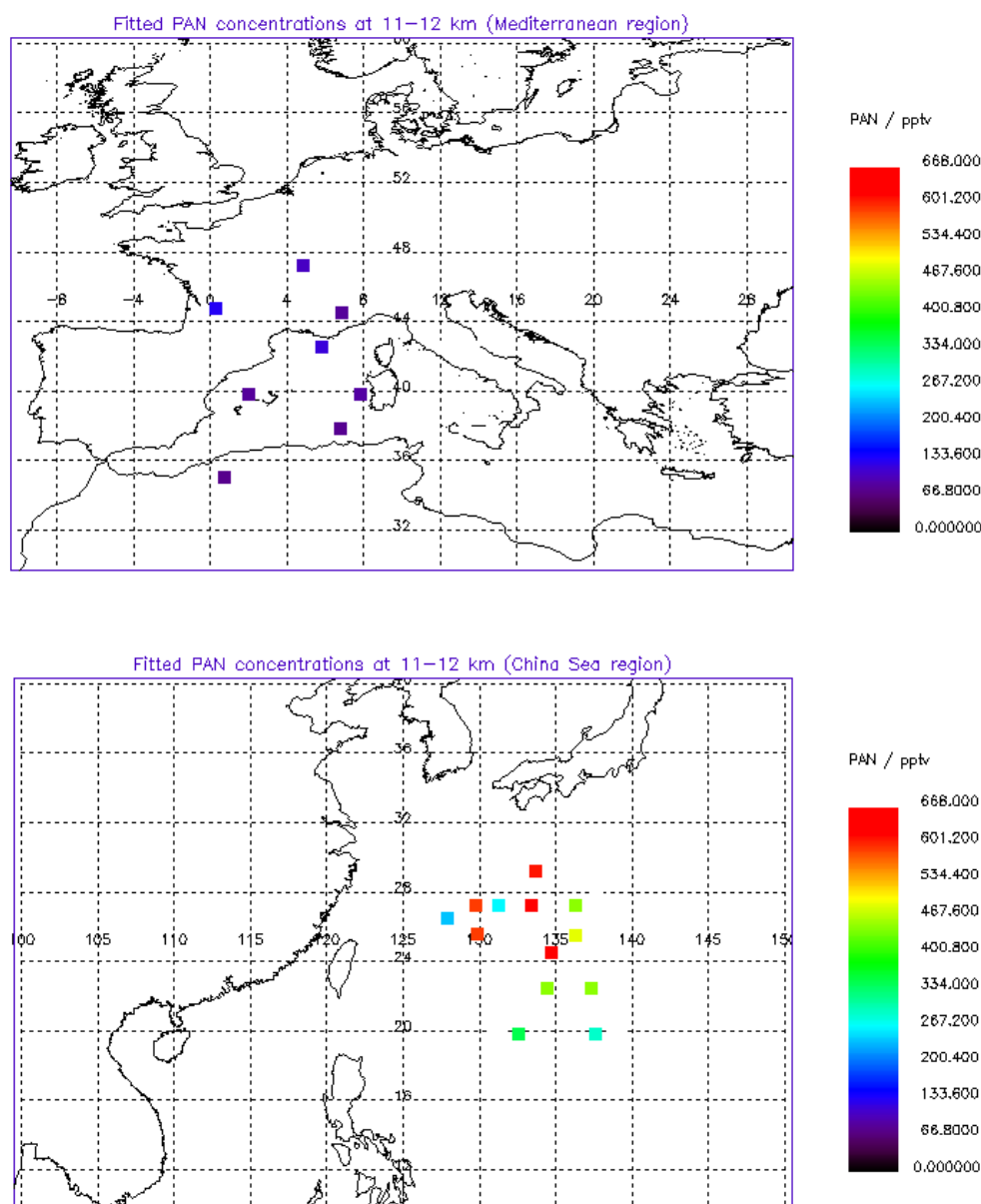


**Figure 6.27** Fitted PAN concentrations between 11 and 12 km for April 2003 in the a) Mediterranean Sea; b) East China Sea showing some very high concentrations of PAN in the China Sea.

Figure 6.28 shows seventy-two hour back trajectories from the point of the MIPAS-E scan observed to have the highest PAN content at 11 km. Back trajectories calculated at 11.2, 8.2 and 3.0 km clearly show the uplift of air from 3 km to the upper troposphere over the coast of China. This vertical motion is characteristic of trajectories reported by Miyazaki *et al.* [2003], which are known to be associated with uplifting by WCBs. Furthermore, this uplifting is seen to occur over mainland China in the region of high

population centres including Shanghai, before being lifted to higher altitudes over the East China Sea at the point of measurement. It is therefore reasonable to postulate that the airmass sensed by MIPAS-E at this location is high in PAN content due to a recent lifting of heavily polluted air into the UT from Chinese outflow.

Conversely, Figure 6.29 shows back trajectories for the lowest fitted PAN concentration around 12 km in this region. Back trajectories, calculated at 1.0, 4.0 and 10.0 km show no evidence of the uplifting seen in Figure 6.28 and air at lower altitudes seen simply to pool over the ocean over this three-day period. The spectrum recorded by MIPAS-E at this location is therefore not expected to sample an airmass of recently polluted air.

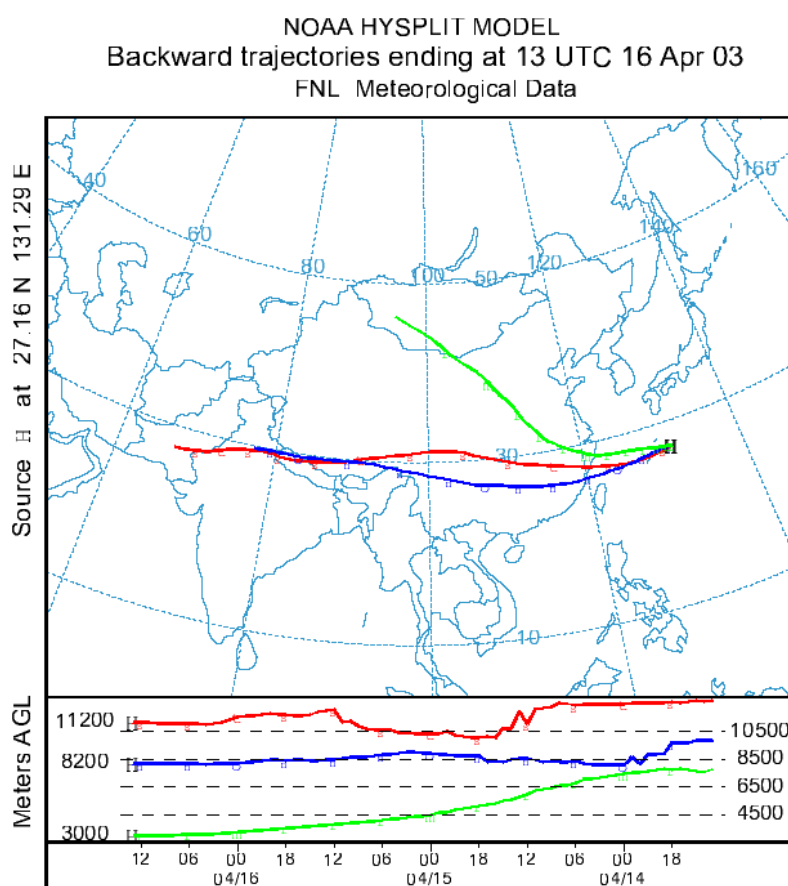


**Figure 6.28** 72-hour HYSPLIT single-particle back trajectories at 11.2, 8.2 and 3.0 km originating from nominal geolocation for MIPAS-E sweep TID: 103814901, 11.2 km on 16/04/2003. Ascent of lower tropospheric air (green trace) indicates probable WCB activity and lifting of polluted air from China (fitted PAN concentration = 668 pptv). Figure courtesy of NOAA. Note: AGL signifies Above Ground Level.

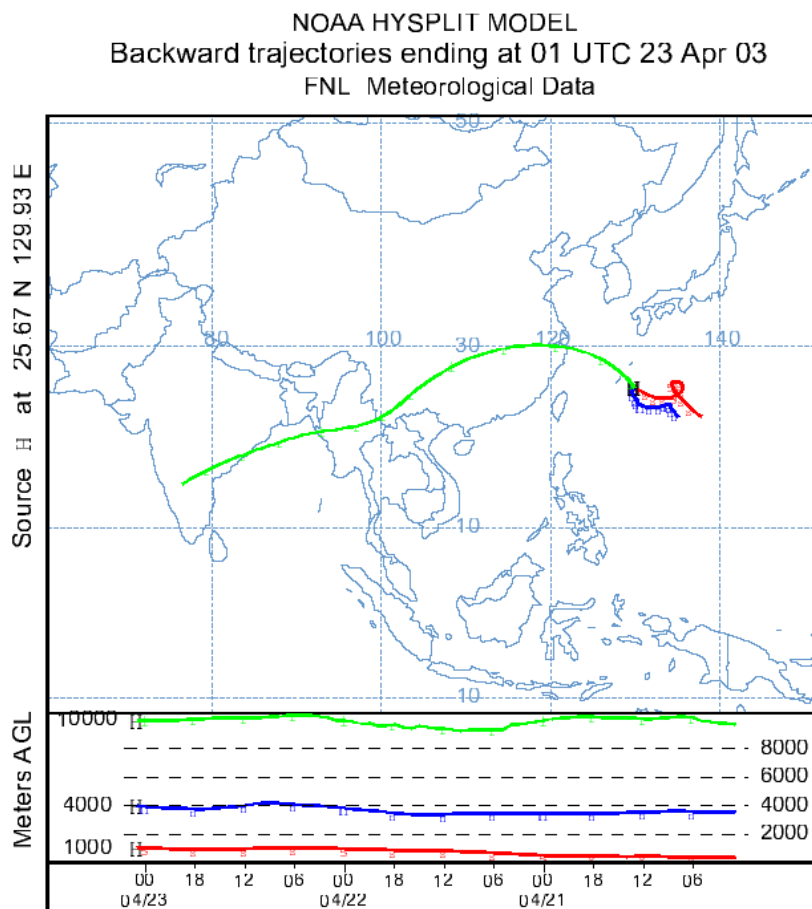


**Figure 6.29** 72-hour HYSPLIT single-particle back trajectories at 10.0, 4.0 and 1.0 km originating from nominal geolocation for MIPAS-E sweep TID: 10316519, 12.4 km on 09/04/2003. Lower tropospheric air is seen to pool for 3 days over the clean ocean (fitted PAN concentration = 315 pptv). Figure courtesy of NOAA. Note: AGL signifies Above Ground Level.

This short analysis of the modelled back-trajectories for MIPAS-E sampled airmasses shows that high PAN content may well be seen in pollution outflow events such as those seen during TRACE-P.

## 6.7 Conclusions

The evidence presented in this chapter strongly indicates the detection of PAN by its infrared signature for the MIPAS-E spectra examined in this thesis for both the Mediterranean Sea and the East China Sea during April 2003 in the upper troposphere. The simultaneous observation of residual spectral features in both MIPAS-E spectral

channels A and AB, which correlates closely with expected features for both the 794.0 and 1163  $\text{cm}^{-1}$  PAN bands, gives high confidence in its detection.

The nature of spectrally interfering gases in the spectral regions of interest for PAN and their variability in the atmosphere make the 794.0  $\text{cm}^{-1}$  PAN band more suitable for detection at all altitudes (by virtue of the stronger intensity of this PAN band relative to that at 1163  $\text{cm}^{-1}$ ).

Spectral fitting and detection of PAN was achieved for a number of profiles over both geographical regions between 9 and 12.4 km for cloud-free spectra with a range of fitted PAN concentrations.

Expected limits of detection for PAN from MIPAS-E at 9 and 12 km (such that the simulated PAN signal exceeds typical random measurement noise) are calculated to be 40 and 28 pptv respectively for band A and 215 and 110 pptv respectively for Band AB.

Detection and fitting become increasingly difficult at altitudes less than 8 km due to spectral saturation by high concentrations of stronger infrared absorbers such as water vapour, reducing the expected signal for PAN to well below the noise level at 6 km.

Detection at higher altitudes (greater than 13 km) has not been made, despite accurate spectral fitting at such altitudes. This is probably due to the expected low concentrations of PAN at such high altitude, which is expected to give a spectral signal well below the noise level.

Concentrations of PAN inferred using this spectral fitting method are seen to be highly sensitive to the accuracy of other parameters such as pressure, temperature and aerosol extinction profiles. The high variability of aerosol at lower altitudes has shown that this may be the most important consideration at altitudes between 8 and 10 km whilst temperature accuracy is important at all altitudes.

Concentrations of PAN inferred using this spectral fitting method are seen to be of the order of those previously reported for the Mediterranean. Evidence for a number of very high PAN concentrations (up to 668 pptv) at 12 km was seen in spectral fits for the East China Sea. Back trajectory analysis of airmasses showing spectra with high PAN content revealed that this could be due to the uplifting of polluted boundary layer air over China by a characteristic warm-conveyor belt. Back trajectories of airmasses with possible lower PAN content revealed no evidence of such uplifting and instead shows the pooling of lower troposphere air over the ocean.

Despite the high concentrations of PAN detected here, the relatively small radiance contributions of PAN to the total measured radiance in both spectral channels, requires that accurate knowledge of many other parameters be obtained prior to spectral fitting for PAN. The most important of these parameters are:

- Precise spectral and radiometric calibration
- Good characterization of spectral noise.
- The best possible reference spectroscopic data for all gases
- Accurate optimized retrievals of pressure and temperature profiles.
- A good fit of the aerosol extinction profile, appropriate to the spectral region of interest.
- Accurate optimized profile retrievals of all gases, especially water vapour, carbon dioxide, ozone and  $\text{CCl}_4$ , which are very important in spectral regions of interest to PAN.



# Chapter 7

## 7 Conclusions and Further Work

This chapter summarises the work undertaken in this thesis and the conclusions drawn from its results. In addition, a number of possible avenues for future work will be identified related to the detection of peroxyacetyl nitrate (PAN) and other organic compounds in the upper troposphere using infrared remote sensing.

In this thesis, novel mid-infrared laboratory reference cross-sections for PAN have been obtained at a range of pressures and temperatures at high spectral resolution. These new reference data are now publically available through the HITRAN reference spectral database (<http://cfa-www.harvard.edu/HITRAN/>).

The new reference data were applied to the investigation of the potential to detect and retrieve PAN concentrations in the upper troposphere from atmospheric limb spectra recorded by both the MIPAS-B2 and MIPAS-E infrared remote-sensing platforms. This investigation yielded positive results, suggesting that PAN may be retrieved at typical concentrations in the UT by careful and detailed analysis of spectral residuals.

The detection of high concentrations of PAN in MIPAS-E data over the East China Sea and the subsequent analysis of single-particle back trajectories suggest that the high concentrations of PAN observed may be due to the convective outflow of boundary layer pollutants from mainland China in characteristic warm conveyor belts. The coincident detection of high concentrations of formic acid using this method serves to reinforce the potential for infrared remote sensing as a tool to detect organic compounds in polluted airmasses.

These conclusions are now summarised further in the following sections.

## 7.1 New Laboratory Cross-sections for PAN

New laboratory reference cross-sections for PAN vapour at nominal spectral resolutions of  $0.03\text{ cm}^{-1}$  and  $0.25\text{ cm}^{-1}$  were calculated from a total of fourteen spectra covering the mid-infrared spectral range of  $550$  to  $2200\text{ cm}^{-1}$  at  $295$  and  $250\text{ K}$  with further cross-sections calculated at  $0.25\text{ cm}^{-1}$  resolution in the range  $550$ - $1400\text{ cm}^{-1}$  at  $273\text{ K}$ .

A general increase in peak infrared absorptivity and integrated band intensities was observed with decreasing temperature with a range of  $17$  to  $25\%$  relative difference observed in band intensities for the  $1163\text{ cm}^{-1}$  and  $794.0\text{ cm}^{-1}$  bands respectively between  $295$  and  $250\text{ K}$ .

No evidence of nitrogen induced broadening was observed in any of the PAN bands studied up to a nitrogen partial pressure of  $400\text{ mb}$ .

Peak cross-sections at  $295\text{ K}$  of the five principal PAN absorption nominal band centres were calculated to be  $0.95(\pm 0.02)$ ,  $1.21(\pm 0.03)$ ,  $0.92(\pm 0.02)$ ,  $2.39(\pm 0.06)$  and  $0.74(\pm 0.03)$  ( $\times 10^{-18}\text{ cm}^2\text{ molecule}^{-1}$ ) for the  $794$ ,  $1163$ ,  $1302$ ,  $1741$  and  $1842\text{ cm}^{-1}$  PAN bands respectively.

The  $794$  and  $1163\text{ cm}^{-1}$  PAN absorption band absorptivities were calculated with good accuracy at all temperatures in this study ( $<7\%$  relative uncertainty for both bands at the  $95\%$  confidence level).

The good agreement between this study and the results of Tsalkani and Toupance [1989] for PAN Integrated band intensities at room temperature support these results rather than those of Gaffney *et al.* [1984]. The integrated intensity of the  $1163\text{ cm}^{-1}$  PAN band is noted to show the greatest inconsistency between previously reported datasets.

Furthermore, the good agreement between this study and the results of Tsalkani and Toupance [1989] suggest that a large and systematic difference in a previously reported PAN cross-section by Hanst and Hanst [1993] may be indicative of an error in those results.

The nature of a large difference in the integrated band intensities reported for the  $1741\text{ cm}^{-1}$  band between all previously reported datasets remains unresolved although it is proposed here that contamination by acetone in this band may be a source

of error in previous measurements. Such contamination may have resulted in an overestimation of the reported integrated intensity for the  $1741\text{ cm}^{-1}$  band in previously reported data. In addition, probable contamination from small concentrations of water vapour and carbon dioxide were not considered or removed in calculations of previously reported PAN data. Spectral fitting and partial pressure correction of contaminants in the Gaffney *et al.* [1984] and Tsalkani and Toupance [1989] datasets are imperative if these data are to be considered in quantitative applications. Without access to previous datasets it is difficult to confirm the effects of contamination on those results.

New integrated band intensities and band centre absorptivities have also been reported in this thesis for the weak PAN absorption bands centred at 606, 930, 990, and  $1055\text{ cm}^{-1}$  for the first time.

The requirement for remote sensing applications is the confirmation of absorption cross-section data with estimated errors. This has been achieved for PAN at room temperature for the first time. Furthermore, cross-sections have also been derived at lower temperatures (down to 250 K) allowing a more accurate investigation of PAN at the typically cold temperatures of the upper troposphere.

## **7.2 PAN Detection in MIPAS-B2 Spectral Data**

Spectral data, recorded during flight campaigns 6 and 8 of the Michelson Interferometer for Passive Atmospheric Sounding Balloon-borne version 2 (MIPAS-B2) over the Mediterranean Sea in May 1998 and April 1999 respectively, were used to investigate the detection of PAN in such spectra over an altitude range of 7 to 15 km.

The analysis and spectral fitting of spectral residuals calculated using data measured by the MIPAS-B2 instrument in conjunction with a line-by-line radiative transfer forward model (the Oxford RFM), strongly indicates the presence of PAN by its characteristic infrared emission signature for spectra examined in this thesis.

The simultaneous observation of residual spectral features in two independent spectral measurement channels (1 and 2), which correlates closely with simulated spectral features for both the  $794.0$  and  $1163\text{ cm}^{-1}$  PAN bands, gives high confidence in the detection of PAN in the upper troposphere. This is further illustrated by the

excellent agreement between simulated and measured residuals for PAN using the same simulated PAN concentration in both measurement channels at all altitudes.

The fitted PAN profile found in these simulations is characteristic of the expected range of PAN concentrations seen in the Mediterranean region during April-May. The expected sharp decrease in PAN concentration is also observed through the tropopause region.

The nature of spectrally interfering gases in the region of interest for PAN and their variability in the atmosphere make the  $794.0\text{ cm}^{-1}$  PAN band more suitable for its detection at all altitudes where water vapour saturation effects are less significant, so long as PAN spectral radiance contributions remain sufficiently high (by virtue of the stronger intensity of this PAN band) so as to be observable above instrumental noise. The weaker intensity of the  $1163\text{ cm}^{-1}$  PAN band does not permit reliable observation of spectral presence above instrumental noise at altitudes greater than 10 km due to expected lower concentrations of PAN.

The relatively small radiance contribution of PAN to the total measured radiance in both spectral channels at the typical concentrations inferred in this work, requires that an accurate knowledge of many other parameters be obtained in order to retrieve accurate and reliable PAN concentrations. Such parameters are also required for detection of PAN from MIPAS-E data and are listed in the following section.

### **7.3 PAN Detection in MIPAS-E Spectral Data**

Selected cloud-free spectral data, recorded during April and May 2003 over the Mediterranean and East China Sea, by the Michelson Interferometer for Passive Atmospheric Sounding on Envisat (MIPAS-E), were used to investigate the detection of PAN in such spectra over an altitude range of 6 to 15 km.

In similarity to the findings of the MIPAS-B2 study, the simultaneous observation of residual spectral features in both MIPAS-E spectral channels A and AB, which correlate closely with simulated spectral features for both the  $794.0$  and  $1163\text{ cm}^{-1}$  PAN bands, gives high confidence in its detection.

The stronger spectral influence of the  $794.0\text{ cm}^{-1}$  PAN band relative to the  $1163\text{ cm}^{-1}$  PAN band, indicates that the  $794.0\text{ cm}^{-1}$  band may be more suitable for its detection at all altitudes.

Successful spectral fitting and detection of PAN was achieved for a number of profiles over both geographical regions between 9 and 12.4 km for cloud-free MIPAS-E spectra, with a range of fitted PAN concentrations.

Theoretical limits of detection for PAN from MIPAS-E at 9 and 12 km (such that the simulated PAN signal exceeds typical random measurement noise) are calculated to be 40 and 28 pptv respectively for band A and 215 and 110 pptv respectively for Band AB.

Detection and fitting become increasingly difficult at altitudes less than 8 km due to spectral saturation by high concentrations of stronger infrared absorbers such as water vapour, reducing the expected signal for PAN to well below the noise level at 6 km.

Detection of PAN at higher altitudes (greater than 13 km) has not been made, despite accurate spectral fitting at such altitudes. This is expected to be due to the low concentrations of PAN at such high altitude, which is expected to give a spectral signal well below the noise level.

Concentrations of PAN inferred using this spectral fitting method were seen to be highly sensitive to the accuracy of other parameters such as pressure, temperature and aerosol extinction profiles. The high variability of aerosol has shown that this may be the most important consideration at altitudes between 8 and 10 km whilst temperature accuracy is important at all altitudes.

Concentrations of PAN inferred using this spectral fitting method are seen to be of the order of those previously reported for the Mediterranean and similar to those fitted in MIPAS-B2 data. Evidence for a number of very high PAN concentrations (up to 668 pptv) at 12 km were seen in spectral fits for the East China Sea. Back trajectory analysis of airmasses showing spectra with high PAN content revealed that this could be due to the uplifting of polluted boundary layer air over China by a characteristic warm-conveyor belt. Back trajectories of airmasses with possible lower PAN content revealed no evidence of such uplifting and instead shows the pooling of lower troposphere air over the ocean with little convective activity.

Despite the high concentrations of PAN detected here, the relatively small radiance contributions of PAN to the total measured radiance in both spectral channels of MIPAS-E, requires that accurate knowledge of many other parameters be obtained prior to spectral fitting for PAN. The most important of these parameters are:

- Precise spectral and radiometric calibration
- Good characterization of spectral noise.
- A good knowledge or retrieval of the aerosol extinction profile, appropriate to the spectral region of interest.
- The best possible reference spectral data for all “contaminant” gases.
- Accurate optimized retrievals of pressure and temperature profiles.
- Well-known profiles of all gases through optimized retrievals or well-known references, especially for water vapour, carbon dioxide, ozone and CCl<sub>4</sub>, which are critical in the spectral regions of interest to the remote-sensing of PAN in the mid-infrared.

## 7.4 Future Work

### 7.4.1 Laboratory Measurements

The laboratory absorption cross-sections for PAN calculated in this thesis were recorded down to a temperature of 250 K. The measurement of colder temperatures was prevented in the experimental setup used here due primarily to the very low saturation vapour pressure of PAN at such temperatures. With the cell pathlength used here (26.0 cm), such pressures yield very low spectral absorption and problems with uncertainty in inferred PAN concentrations in the gas cell (due to pressure measurement and cell leakage).

Consequently, the absorption cross-section dataset derived in this thesis does not cover the complete temperature range seen in the upper troposphere (as low as 190 K). If future quantitative measurements of PAN in the upper troposphere are possible using infrared remote sensing, additional measurements to extend the dataset to lower temperatures would be desirable. This would require a much longer pathlength absorption cell and an improvement in the measurement of cell pressure at low temperature. This is further complicated by the dangerous nature of handling PAN, especially in its pure frozen form as well as cell adsorption and reaction. All such considerations would be necessary before further low temperature measurement is attempted.

## 7.4.2 PAN Detection and Retrieval at High Spectral Resolution

The detection of PAN in this thesis requires the careful analysis and fitting of residual spectra. Such a method is computationally and labour intensive although such a method does show the potential for the retrieval of PAN at typical concentrations in the UT.

Global observations of PAN, such as those potentially offered by the high spectral resolution MIPAS-E dataset as well as from other current and planned infrared remote-sensing platforms in space (e.g. TES on EOS-AURA described by Beer [1999]), would be a significant contribution to the fields of atmospheric chemistry and climate science and could also provide a useful tool for atmospheric process studies (e.g. to study pollution outflow events). This possibility requires the development of an automated retrieval scheme for PAN tailored to the analysis of large datasets. Such a scheme may be achievable with the consideration of those parameters seen to be of importance in the spectral regions identified for PAN detection (see Section 7.3) in the UT.

Future work to develop such a scheme includes:

- The optimised retrieval of, or use of otherwise well-known profiles of all contaminant gases as well as pressure and temperature and aerosol extinction profiles using the best possible available laboratory reference spectral data. A good fit for all these parameters is required in order to accurately retrieve PAN concentrations from the typically weak PAN radiance contribution to the total measured radiance.
- An investigation of the possible presence of other unknown infrared active trace species in the atmosphere that may influence the infrared region of interest to PAN. A tentative observation of additional weak spectral features in the  $820\text{ cm}^{-1}$  region seen in some spectra in this thesis illustrates the need for such analysis. As well as improving the accuracy of retrieved PAN concentrations, this may also lead to the detection of other trace species using this method.
- The computationally expensive retrieval of PAN concentration using the full spectral range of the  $794\text{ cm}^{-1}$  PAN feature could be improved using a number of spectral “micro-windows” chosen to maximise PAN information content, whilst minimising the contributions of other gases.

- Alternatively, a large spectral dataset could be screened for high PAN content on the basis of some pre-defined sensitivity index. This could be defined simply as a ratio of two spectral regions; one containing high PAN information content and the other containing little PAN content with spectral influence due mostly to a well-known and well-mixed gas (e.g. CO<sub>2</sub>). Such spectra could then be marked for further analysis.
- Furthermore, computational retrieval could be performed on a spectral dataset recorded at, or degraded to, a lower resolution.

### 7.4.3 PAN Detection and Retrieval at Lower Spectral Resolution

Given the broad cross-sectional nature of PAN bands in the infrared, it may be possible to perform an atmospheric retrieval of PAN from infrared measurements at a lower or degraded spectral resolution. This possibility could be important for the consideration and planning of future space missions in infrared remote sensing such as those currently being debated under the European Space Agency CAPACITY study for Global Monitoring for Environment and Security (GMES; see <http://www.gmes.info/> for further information).

The possibility for retrieval of PAN at lower spectral resolution can be investigated by degrading an existing high spectral resolution dataset to lower resolutions. This is carried out here for selected data from MIPAS-E, where the accuracy of the spectral fitting method at lower spectral resolutions can be compared with that made at higher resolution. Figure 7.1 and Figure 7.2 shows a comparison between spectral fits made earlier at 0.025 cm<sup>-1</sup> and a fit made using the same methodology with MIPAS-E data degraded to 0.1 cm<sup>-1</sup>.

Spectral resolution was degraded here by taking the fast Fourier Transform of unapodised Level 1B data and truncating the resulting interferogram to obtain a sampling interval of 0.1 cm<sup>-1</sup> in the new spectrum; which is then obtained by taking the inverse fast Fourier Transform. For comparison purposes between measured and simulated spectra, the same process was carried out on RFM spectra that were first calculated at 0.025 cm<sup>-1</sup> resolution and convolved with the high resolution MIPAS-E instrument lineshape.



This comparison using the same fitting method at both resolutions yields exactly the same result, with fitted PAN concentrations of 590 pptv at both resolutions. No improvement in the fit was achieved using the minimum 1% jacobian spectrum for PAN at either resolution at 11.9 km. This suggests that the agreement in inferred PAN concentration between fits at both spectral resolutions is within 5.9 pptv.

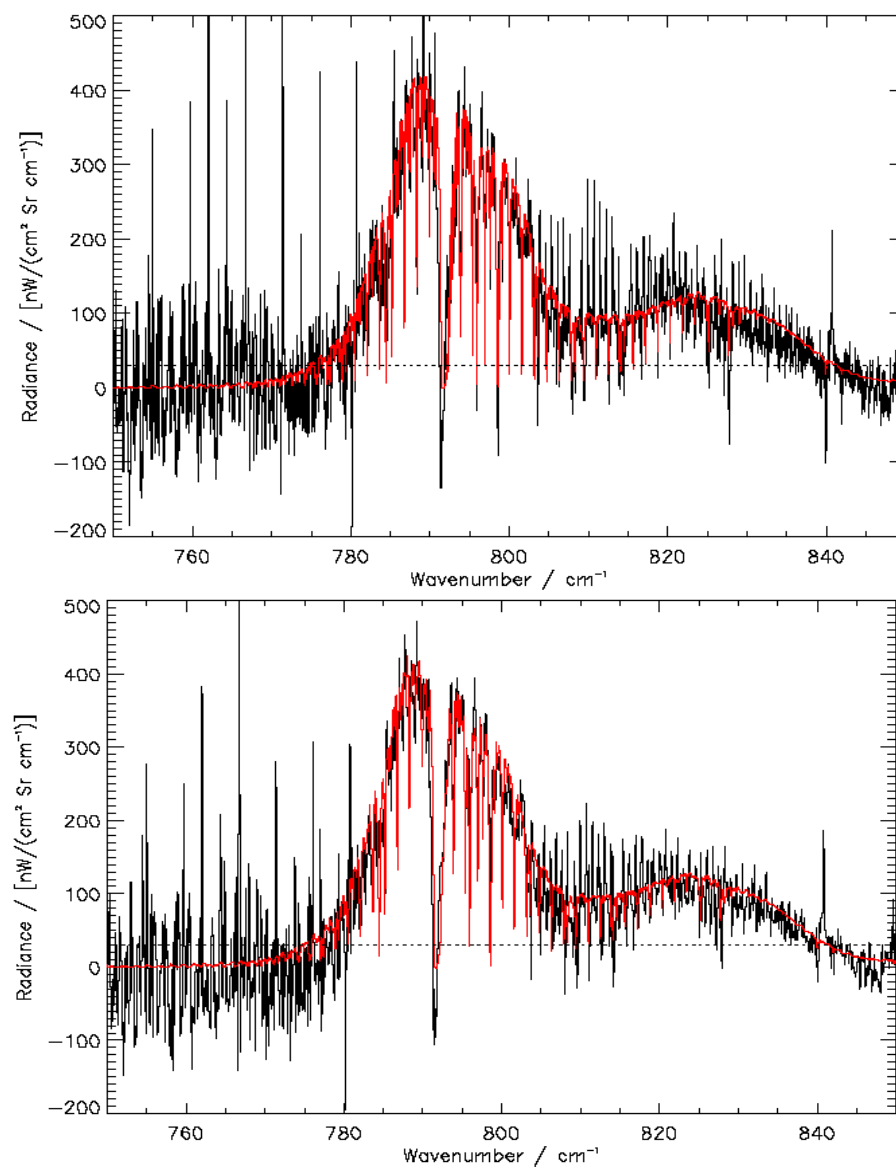


**Figure 7.1** Comparison of spectral fits between fitted simulated PAN residual (red) and MIPAS-E measured residual (black) at spectral resolutions of: top)  $0.025 \text{ cm}^{-1}$  unapodised; and bottom) MIPAS-E data degraded to  $0.1 \text{ cm}^{-1}$  unapodised. Fitted PAN concentration is 590 pptv in both plots.

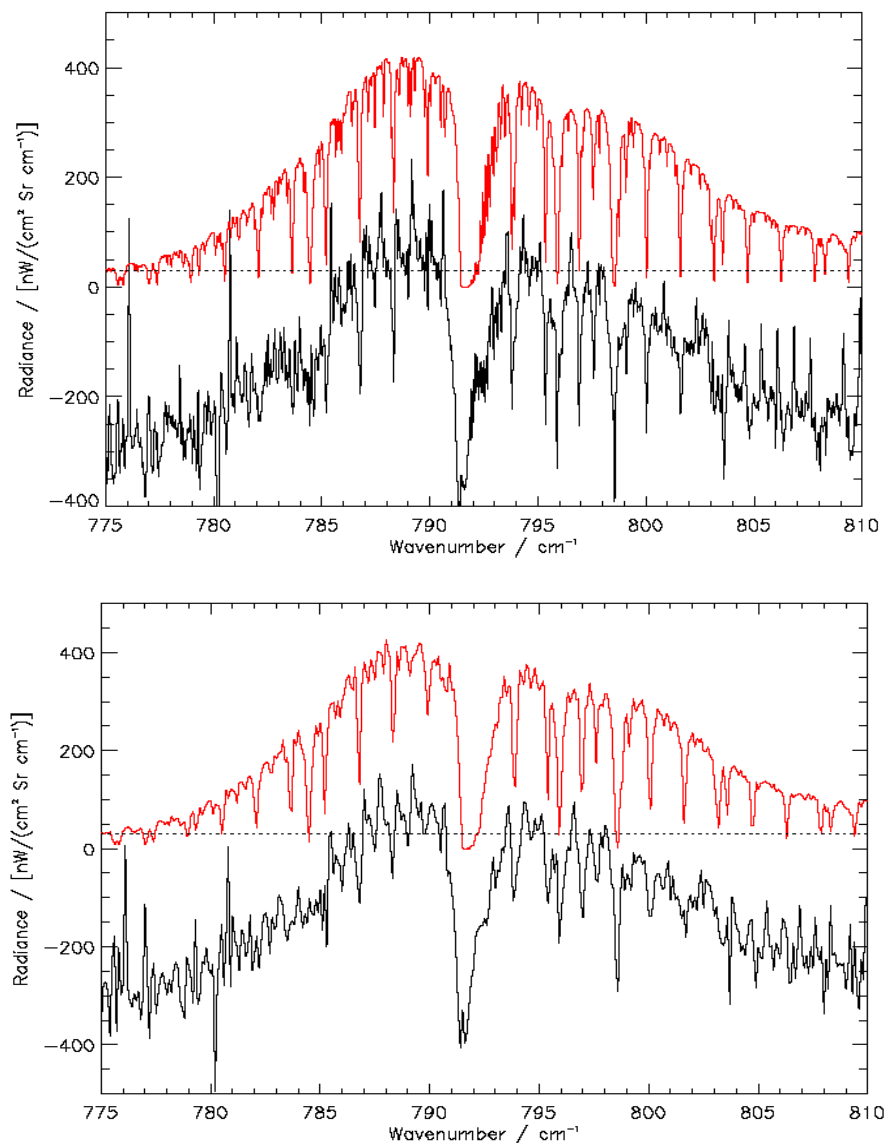


**Figure 7.2** A close up between 775-810  $\text{cm}^{-1}$  comparing of spectral fits between fitted simulated PAN residual (red) and MIPAS-E measured residual (black) at spectral resolutions of: top) 0.025  $\text{cm}^{-1}$  unapodised; and bottom) MIPAS-E data degraded to 0.1  $\text{cm}^{-1}$  unapodised. Fitted PAN concentration is 590 pptv for both plots.

A point of note is that the simulated atmosphere used at both resolutions uses the same level 2 profiles of spectrally important pressure, temperature, ozone and water vapour that were retrieved optimally from the high-resolution dataset. Therefore the success of such fitting at low resolution relies again on accurate profiles of these parameters. This possibility could be further investigated by comparing the difference in retrievals of such parameters at different resolutions and the resulting differences in fitted spectra.

As discussed in Chapters 5 and 6, fitted PAN concentrations are seen to be highly sensitive to biases in temperature and pressure (e.g. 5 pptv K<sup>-1</sup> at 9 km).

In summary, the sensitivity to the detection and retrieval of PAN is similar between spectral resolutions of 0.1 and 0.025 cm<sup>-1</sup> and retrieval may be possible from existing or future planned remote-sensing missions given accurate knowledge of other important parameters, especially pressure and temperature profiles.

#### **7.4.4 Validation**

In order to gauge the accuracy of detected PAN concentrations using infrared remote sensing, it is important that results for PAN using this method are compared with results from independent coincident measurements of PAN in the atmosphere. This could be achieved by the analysis of MIPAS-E spectra that are closely coincident with existing or planned aircraft measurements of PAN in the UT for example. Such validation would give greater confidence in the accuracy of inferred concentrations.

#### **7.4.5 Other Organic Compounds**

Formic acid was accidentally detected using the method in this thesis, confirming the findings of Waterfall [2004]. An analysis of a more extended spectral region of the MIPAS-E dataset could yield the detection of a number of other important tropospheric trace species, including organic compounds using the same method. Such work may also require the use of improved laboratory reference spectral data for such molecules.

# Bibliography

ACECHEM: Definition of mission objectives and observational requirements for an atmospheric chemistry explorer mission. ESA contract: 14048/98/NL/GD, 2001.

Andreae, M. O., and Merlet, P.: Emission of trace gases and aerosols from biomass burning, *Global biogeochemical cycles*, 15(4), 955-966, 2001.

Armstrong, B. H.: Spectrum Line Profiles: The Voigt Function. *J. Quant. Spectrosc. Radiat. Transfer* **7**, 61-88, 1967.

Arnold, F., Burger, V., Droste-Fanke, B., Grimm, F., Krieger, A., Schneider, J., and Stilp, T.: Acetone in the upper troposphere and lower stratosphere: Impact on trace gases and aerosols. *Geophys. Res. Lett.* **24**, 3017-3020, 1997.

Baird, C.: Environmental chemistry, 2<sup>nd</sup> edition, *W. H. Freeman and co.* 1999.

Ballard, J., Remedios, J. J., and Roscoe, H. K.: Sample emission effect on spectral parameters, *J. Quant. Spect. Radiat. Transfer*, **48**, 733-741, 1992.

Ballard, J., Knight, R. J., Newnham, D. A., Vander Auwera, J., Herman, M., Lonardo, G., Masciarelli, G., Nicolaisen, F. M., Beukes, J. A., Christensen, L. K., McPheat, R., Duxbury, G., Freckleton, R., and Shine, K. P.: An inter-comparison of laboratory measurements of absorption cross-sections and integrated absorption intensities for HCFC-22, *J. Quant. Spect. Radiat. Trans.*, **66** (2), 109-128, 2000.

Beer, R. H.: Remote sensing by Fourier Transform Spectroscopy. *Wiley.* 1992

Beer, R: TES Scientific Objectives & Approach, Goals & Requirements *Revision 6.0*, JPL document: D-11294, April 14, 1999.

- Birch, J. R., and Clarke, J. J.: Fifty categories of ordinate error in Fourier Transform spectroscopy. *Spectroscopy Europe* (7/4), 16-22, 1995.
- Bridier, I., Caralp, F., Loirat, H., Lesclauxm, R., Veyret, B., Becker, L. H., Reimer, A., and Zabel, F.: Kinetic and Theoretical Studies of the Reaction  $\text{CH}_3\text{C}(\text{O})\text{OO} + \text{NO}_2 + \text{M} \leftrightarrow \text{CH}_3\text{C}(\text{O})\text{O}_2\text{NO}_2 + \text{M}$  between 248 and 393 K and between 30 and 760 Torr, *J. Phys. Chem.*, 95, 3594-3600, 1991.
- Bruckmann, P. W., and Willner, H.: Infrared spectroscopic study of peroxyacetyl nitrate (PAN) and its decomposition products. *Envir. Sci. Tech.*, 17, 352-357, 1983.
- Bruhl, C., Poschl, U., Crutzen, P. J., *et al.*, Acetone and PAN in the upper troposphere: Impact on ozone production from aircraft emissions, *Atmos. Env.*, 34, 3931-3938, 2000.
- Carli, B, Alpaslan, D., Calotti, M., and Castelli, S.: First results of MIPAS/ENVISAT with operational Level 2 code, *Adv. Space. Res.*, 2004.
- Carroll, M. A., Thompson A. M.: Aircraft measurements of  $\text{NO}_x$  over the Eastern Pacific and continental United States and implications for ozone production, *J. Geophys. Res.*, 95, 10205-10233, 1990.
- Chase, D. B.: Nonlinear detector response in FT-IR. *Applied Spectroscopy*, 38(4), 491-494, 1984.
- Chipperfield, M. P.: Multiannual simulations with a three-dimensional chemical transport model. *J. Geophys. Res.*, 104, 1781-1806, 1999.
- Chu, P. M., Grunther, F. R., Rhoderick, G. C., and Lafferty, W. J.: The NIST quantitative infrared database. *J. Res. Nat. I*, 104(1), 59-81, 1999
- Clerbaux, C., Coheur, P. F., Turquety, S., and Hadji-Lazaro, J.: Capabilities of infrared sounder observations for monitoring atmospheric composition and chemistry applications, EUMETSAT contract EUM/CO/O3/1127/SAT, 2003.
- Crawford, J., Olson, J., Davis, D., Chen, G., Barrick, J., Shetter, R., Lefer, B., Jordan, C., Anderson, B., Clarke, A., Sachse, G., Blake, D., Singh, H. B., Sandolm, S., Tan, D., Kondo, Y., Avery, M., Flocke, F., Eisele, F., Mauldin, L., Zondlo, M., Brune, W.,

- Harder, H., Martinez, M., Talbot, R., Bandy, A. and Thornton, D.: Clouds and trace gas distributions during TRACE-P, *J. Geophys. Res.*, 108, D21, 8818-8831, 2003.
- Crutzen, P. J.: Photochemical reaction initiated by and influencing ozone in unpolluted tropospheric air, *Tellus*, 26, 45-55, 1974.
- Crutzen, P. J.: The role of NO and NO<sub>2</sub> in the chemistry of the troposphere and stratosphere, *Ann. Rev. Earth Planet. Sci.*, 7, 443-472, 1979.
- Dinelli, B. M. and Carloti, M.: MIPAS-B2 Flight 6 data analysis using Oxford MWs data base selected for satellite measurements delivered on February 2001, Technical report by IMK, Forschungszentrum, Karlsruhe.. ESA contract No. 11717/95/NL/CN, 2001.
- Draxler, R.R. and Rolph, G.D.: HYSPLIT (HYbrid Single-Particle Lagrangian Integrated Trajectory) Model access via NOAA ARL READY Website (<http://www.arl.noaa.gov/ready/hysplit4.html>). NOAA Air Resources Laboratory, Silver Spring, MD, 2003.
- Dudhia, A.: A multi-layer Technique for Micro-window Selection, ESA Contract No. 11886/96/NL/GS, 1999.
- Dudhia, A.: MIPAS Micro-window Processing Scheme (MWPROC), ESA contract No. 11886/96/NL/GS, 2001.
- Duxbury, G.: Infrared vibration-rotation spectroscopy: from free radicals to the infrared sky, *Wiley*, 1999.
- Emmons, L. K., Carroll, M. A., Hauglustaine, D. A., Brasseur, G. P., Atherton, C., Penner, J., Sillman, S., Levy II, H., Rohrer, F., Wauben W. M. F., van Velthoven, P. F. J., Wang Y., Jacob, D. J., Bakwin, P., Dickerson, R., Doddridge, B., Gerbig, C., Honrath, R., Hubler, G., Jaffe, D., Kondo, Y., Munger, J. W., Torres, A., and Volz-Thomas, A.: Climatologies of NO<sub>x</sub> and NO<sub>y</sub>: a comparison of data and models. *Atmos. Envir.*, 31, 1851–1903, 1997.
- Emmons L. K., Hauglustaine, D. A., Muller, M. A., Carroll, M. A., Brasseur, G. P., Brunner, D., Staehelin, J., Thouret, V., and Marenco, A.: Data composites of airborne

- observations of tropospheric ozone and its precursors, *J. Geophys. Res.*, 105, 20497-20538, 2000.
- Finlayson-Pitts, J.: Chemistry of the upper & lower atmosphere. *Academic press*, 2000.
- Fischer, H., and Oelhaf, H.: Remote sensing of vertical profiles of atmospheric trace constituents with MIPAS limb-emission spectrometers. *Appl. Optics*, 35, 2787-2796, 1996.
- Folkins, I., and Chatfield, R.: Impact of acetone on ozone production and OH in the upper troposphere at high NO<sub>x</sub>. *J. Geophys. Res.*, 105, 11585-11589, 2000.
- Friedl-Vallon, F., *et al.*: MIPAS-B Flight report: Flight #6 of 7/8.5.98 from Aire sur l'Adour / France. Revision 1 of 22.12.1999. Technical report, IMK, Forschungszentrum, Karlsruhe, ESA contract No. 12078/96/NL/GS, 1999a.
- Friedl-Vallon, F., *et al.*: The balloon-borne Michelson Interferometer for Passive Atmospheric Sounding (MIPAS-B2) – instrument and results. A. M. Larar, editor, *Optical spectroscopic techniques and instrumentation for atmospheric and space research III*, volume 3756 of Proceedings of the Society of Photo-optical instrumentation engineers, 9-16, 1999b.
- Friedl-Vallon, F., *et al.*: Design and characterization of the balloon-borne Michelson Interferometer for Passive Atmospheric Sounding (MIPAS-B2), *Appl. Optics*, 43, 3335-3355, 2004.
- Gaffney, J. S., Fajer, R., and Senum, G. I.: An improved procedure for high purity gaseous peroxyacetyl nitrate production: Use of heavy lipid solvents. *Atmos. Envir.*, 18, 215-218, 1984.
- Gaffney, J. S., Marley, N. A., and Prestbo, E. W.: Peroxyacyl nitrates (PANs): Their physical and chemical properties, in the Handbook of Environmental Chemistry, vol. 4, part B, edited by O. Hutzinger, 1-38, *Springer-Verlag, New York*, 1989.
- Granby, K., Egelov, A. H., Nielsen, T., and Lohse, C.: Carboxylic acids: Seasonal variation and relation to chemical and meteorological parameters. *Atmos. Env.*, 28, 195-207, 1997

- Grant, W. B. *et al.*: A case study of transport of tropical marine boundary layer and lower tropospheric airmasses to the northern midlatitude upper troposphere. *J. Geophys. Res.*, 105, 3757-3769, 2000.
- Guelachvili, G.: Distortions in Fourier spectra and diagnosis. Spectroscopic techniques. Volume II. *Academic press*, 1983.
- Hanst, P. L. and Hanst, S. T.: Database and atlas: Infrared spectra for qualitative analysis of gases, *Infrared Analysis Inc.*, Anaheim, Calif., 1993.
- Hauglustaine *et al.*: Mozart: a global chemical transport model for ozone and related chemical tracers 2. model results and evaluation. *J. Geophys. Res.*, 103, 28291-28335, 1998.
- Heald, C. L., Jacob, D. J., Fiore, A. M. *et al.*: Asian outflow and trans-Pacific transport of carbon monoxide and ozone pollution: An integrated satellite, aircraft and model perspective, *J. Geophys. Res.*, 108, 4804, 2003.
- Horowitz, L. W., Walters, S., Mauzerall, D. L., *et al.*: A global simulation of tropospheric ozone and related tracers: Description and evaluation of MOZART, version 2, *J. Geophys. Res.*, 108, 4784, 2003
- Hollas, J. M.: Modern Spectroscopy, Third edition. *John Wiley & sons*, Chichester, UK. 1997.
- Holton, J. R., Haynes, P. H., McIntyre, M. E., Douglass, A. R., Rood, R. B., and Pfister, L.: Stratosphere-Troposphere Exchange, *Rev. Geophys.*, 33, 403-439, 1995.
- Holzinger, R., Williams, J., Salisbury, G., Klupfel, T., de Reus, M., Traub, M., Crutzen, P. J., and Lelieveld, J.: Oxygenated compounds in aged biomass burning plumes over the Eastern Mediterranean: evidence for strong secondary production of methanol and acetone, *Atm. Chem. Phys.*, 5, 39-46, 2005.
- IPCC Third Assessment Report – Climate change 2001: Impacts, adaptation and vulnerability, 2001.



- Jacob, D. J.: The oxidizing power of the atmosphere. Chapter for the Handbook of Weather, Climate and Water, ed. by T. Potter, B. Colman, and J. Fishman, *Mc-Graw Hill*, 2000.
- Jacob, D. J. *et al.*: Atmospheric budget of acetone. *J. Geophys. Res.* 101, 2001.
- Jacob, D. J., Crawford, J. H., Kleb, M., M., Connors, V. S., Bendura, R. J., Rpaer, J., L., Sachse, G. W., Gille, J. C., Emmons, L., and Heald, C., L.: Transport and Chemical Evolution over the Pacific (TRACE-P) aircraft mission: Design, execution, and first results, *J. Geophys. Res.*, 108, 9000-9019, 2003.
- Jacobi, H. W., Weller, R., Bluszech, T., and Schrems, D.: Latitudinal distribution of peroxyacetyl nitrate (PAN) over the Atlantic Ocean, *J. Geophys. Res.*, 104, 26901-26912, 1999
- Jacquinet-Husson, N. *et al.*: The 2003 edition of the GEISA/IASI spectroscopic database, Submitted to *J. Quant. Spec. Rad. Trans*, July, 2004.
- Jaeglé, L., Jacob, D. J., Brune, W. H., Faloona, I. C., Tan, D., Kondo, Y., Sachse, G. W., Anderson, B., Gregory, G. L., Vay, S., Singh, H. B., Blake, D. R., and Shetter, R.: Ozone production in the upper troposphere and the influence of aircraft during SONEX: Approach of NO<sub>x</sub>-saturated conditions, *Geophys. Res. Lett.*, 26, 3081-3084, 1999a.
- Jaeglé, L., Jacob, D. J., Brune, W. H., Faloona, I. C., Tan, D., Kondo, Y., Sachse, G. W., Anderson, B., Gregory, G. L., Vay, S., Singh, H. B., Blake, D. R., and Shetter, R.: Photochemistry of HO<sub>x</sub> in the upper troposphere at northern mid-latitudes, *G. Geophys. Res.*, 1999b.
- Jaeglé, L., Jacob, D. J., Brune, W. H., Wennberg, P. O.: Chemistry of HO<sub>x</sub> radicals in the Upper Troposphere, *Atm. Env.*, 35, 469-489, 2000.
- Jaffe, D. A., Bernsten, T. K. and Isaksen, I. S. A.: A global three-dimensional chemical transport model: Nitrogen oxides and nonmethane hydrocarbons results, *J. Geophys. Res.*, 102, 21821-21296, 1997.

- Jay, V.: Remote sounding of the atmosphere by high-resolution spectroscopy, DPhil thesis, *Oxford University*, 2000.
- Johns, J. W. C.: High-resolution and the accurate measurement of intensities, *Mikrochimica Acta*, 3(1-6), 171-188, 1987.
- Johnson, T. J., Sams, R. L., Blake, T. A., Sharpe, S. W., and Chu, P. M.: Removing aperture-induced artefacts from Fourier Transform infrared intensity values, *Applied Optics*, 41, 2831-2839, 2002.
- Kames, J., Schweighoeffer, S., and Schurath, U.: Henry's Law Constant and Hydrolysis of Peroxyacetyl Nitrate. *J. Atmos. Chem.*, 12, 169-180, 1991.
- Kashibatla, P. S., Levy II, H., and Moxim, W. J.: Global NO<sub>x</sub>, HNO<sub>3</sub>, PAN, and NO<sub>y</sub> distributions from fossil fuel combustion emissions: A model study, *J. Geophys. Res.*, 98, 7165-7180, 1993.
- Kelly, K., Proffitt, M. H., Chan, K. R., Loewenstein, M., Podolske, J. R., Strahan, S. E., Wilson, J., and Kley, D.: Water vapour and cloud water measurements over Darwin during the STEP 1987 tropical mission, *J. Geophys. Res.*, 98, 8713-8723, 1993.
- Khare, P. *et al.*: Atmospheric formic and acetic acids: an overview. *Reviews of geophysics*, 37(2), 227-248, 1999.
- Kirchener, F., Mayer-Figge, A., Zabel, F., and Becker, K. H.: Thermal stability of peroxy nitrates. *Int. Journal. Chem. Kinetics.*, 31, 127-144, 1999.
- Kleindienst, T. E.: Recent developments in the chemistry and biology of peroxyacetyl nitrate. Research on Chemical intermediates, *Atm. Res.*, 20, 335-384, 1994.
- Koike M., Kondo Y., Kita K., Takegawa N., and Masui, Y.: Export of anthropogenic reactive nitrogen and sulfur compounds from the East Asia region in spring, *J. Geophys. Res.*, 108(D20), 8789-8812, 2003.
- Kotchenruther, R. A., Jaffe, D. A., and Jaegle, L.: Ozone photochemistry and the role of peroxyacetyl nitrate in the springtime northeastern Pacific troposphere: Results from the Photochemical Ozone Budget of the Eastern North Pacific Atmosphere (PHOBEA) campaign. *J. Geophys. Res.*, 106, 2001.

- Krause, A. B., Rohrer, F., Grobler, E. S., and Ehhalt, D. H.: The global tropospheric distribution of NO<sub>x</sub> estimated by a three-dimensional chemical tracer model, *J. Geophys. Res.*, 18,587-18,604, 1996.
- Kritz, M., S. W. Rosner, E. F. Danielsen, and H. B. Selkirk: Air mass origins and troposphere-to-stratosphere exchange associated with mid-latitude cyclogenesis and tropopause folding inferred from <sup>7</sup>Be measurements, *J. Geophys. Res.*, 96, 17405-17414, 1991.
- Lelieveld *et al.*: Global air pollution crossroads over the Mediterranean. (Research Articles), *Science*, 298, 794-796, 2002.
- Levy II, H., Moxim, W. J., Klonecki, A. A., and Kasibhatla, P. S.: Simulated tropospheric NO<sub>x</sub>: Its evaluation, global distribution and individual source contributions. *J. Geophys. Res.-A*, 104, 26279-26306, 1999.
- Lide, D. R.: Handbook of chemistry and physics: a ready-reference book of chemical and physical data, *CRC Press*, 1996.
- Liu, S. C., Trainer, M., Fehensfeld, F. C., Parish, D. D., Williams, E. J., Fahey, D. W., Hubler, G., and Murphy, P. C.: Ozone production in the rural troposphere and the implications for regional and global ozone distributions, *J. Geophys. Res.*, 92, 4191-4207, 1987.
- Louet, J.: The Envisat mission and system. ESA Bulletin – European Space Agency. (106) 11-25, 2001.
- Kames, J., Schweighoeffer, S., and Schurath, U.: Henry's Law Constant and Hydrolysis of Peroxyacetyl Nitrate. *J. Atmos. Chem.*, 12, 169-180, 1991.
- Kotchenruther, R. A., Jaffe, D. A. and Jaeglé, L.: Ozone photochemistry and the role of peroxyacetyl nitrate in the springtime northeastern Pacific troposphere: Results from the Photochemical Ozone Budget of the Eastern North Pacific Atmosphere (PHOBEA) campaign, *J. Geophys. Res.*, 106, 2001.
- Mantovani, R.: Envisat MIPAS technical note, ESA document: ENVI-SPPA-EOPG-TN-05-0012, 2003.

- Marti, J. K. and Mauersberger, A.: Survey and new measurements of ice vapour pressure at temperatures between 170 and 250K, *Geophys. Res. Lett.*, 20(5), 363-366, 1993.
- McFadyen, G. G., and Cape, J. J.: Spring-time sources and sinks of Peroxyacetyl Nitrate in the UK and its contribution to acidification and nitrification of cloud water, *Atm. Res.*, 50, 359-371, 1999.
- Moxim, W. J., Levy II, H., and Kashibatla, P. S.: Simulated global tropospheric PAN: Its transport and impact on NO<sub>x</sub>, *J. Geophys. Res.* 101, 12621-12638, 1996.
- Miller, C. E., Lynton, J. I., Keevil, D. M., and Francisco, J. S.: Dissociation pathways of Peroxyacetyl Nitrate (PAN). *J. Phys. Chem. A*, 103, 11451-11459, 1999.
- Miyasaki, Y., Kondo, Y., Koike, M., Fuelberg, H. E., Kiley, C. M., Kita, K., Takegawa, N., Sachse, G. W., Flocke, F., Weinheimer, A. J., Singh, H. B., Eisele, F. L., Zondlo, M., Talbot, R. W., Sandholm, S. T., Avery, M. A., and Blake, D. R.: Synoptic-scale transport of reactive nitrogen over the Western Pacific on spring. *J. Geophys. Res.*, 108, D20, 8788-8802, 2003.
- Montzka, S. A., Butler, J. H., Elkins, J. W., Thompson, T. M., Clarke, A. D., and Lock, L. T.: Present and future trends in the atmospheric burden of ozone-depleting halogens, *Nature*, 398, 690-694, 1999.
- Montreal protocol, Protocol on Substances That Deplete the Ozone Layer, treaty signed on Sept. 16, 1987.
- Nett, H., Frerick, J., Paulsen, T., and Levrini, G.: The atmospheric instruments and their applications: GOMOS, MIPAS and SCIAMACHY. ESA Bulletin – European Space Agency, 106, 77-87, 2001.
- Newell, R. E., and Gould-Stewart, S.: A stratospheric fountain?, *J. Atmos. Sciences*, 38, 2789-2796, 1981.
- Newnham, D. A. and Knight, R. J.: Report on Accident in the RAL Molecular Spectroscopy Facility (MSF) on Thursday 23 May 2002.

- Nielsen, T.: A convenient method for preparation of pure standards of peroxyacetyl nitrate for atmospheric analyses. *Atmos. Envir.*, 16, 2447-2450, 1982.
- Niki, H., Maker, P. D., Savage, C. M., and Breitenbach, L. P.: An FTIR spectroscopic study of the reactions  $\text{Br} + \text{CH}_3\text{CHO} \rightarrow \text{HBr} + \text{CH}_3\text{CO}$  and  $\text{CH}_3\text{C(O)OO} + \text{NO}_2 \leftrightarrow \text{CH}_3\text{C(O)OONO}_2$  (PAN). *Int. Journal. Chem. Kinetics.*, 17, 525-534, 1985.
- Norton, R. H., and Beer, R.: New apodising functions for Fourier spectrometry, *J. Opt. Soc. A.* 66, 259, 1976.
- Norton, R. H., and Beer, R.: New apodising functions for Fourier spectrometry – Erratum. *J. Opt. Soc. A.*, 67, 419, 1977.
- Offersgaard, J. F. and Öjelund, H.: Correction of Non-linear Effects in Absorbance Measurements, *Applied Spectroscopy*, 56(4), 2002.
- Olszyna, K. J., Bailey, E. M., Simonaitis R., and Meagher, J. F.:  $\text{O}_3$  and  $\text{NO}_y$  relationships at a rural site. *J. Geophys. Res-A.*, 99, 14557-14563, 1994.
- Orlando, J. J., Tyndall, G. S., and Calvert, J. G.: Thermal decomposition pathways for peroxyacetyl nitrate (PAN): Implications for atmospheric methyl nitrate levels. *Atmos. Env.*, 17, 3111-3118, 1992.
- Penkett, S. A., and Brice, K. A.: The spring maximum in photo-oxidants in the Northern Hemisphere troposphere, *Nature*, 319, 655-657
- Penner, J. E., Bergmann, D. J., Walton, J. J., and Kinnison D.: An evaluation of upper troposphere  $\text{NO}_x$  with two models, *J. Geophys. Res.*, 103 (D17), 22097-22106, 1998.
- Perron G.: NESRT verification, MIPAS: Quality Working Group meeting (QWG#3), Frascati, March 2003.
- Poisson, N., Kanakidou, M., and Crutzen, P. J.: Impact of Non-Methane Hydrocarbons on Tropospheric Chemistry and the Oxidizing Power of the Global Troposphere: 3-Dimensional Modelling Results, *J. Atmos. Chem.*, 36, 157 – 230, 2000.
- Press, W.: Numerical recipes in Fortran 77: The art of scientific computing. 2<sup>nd</sup> edition. Volume 1 of Fortran Numerical Recipes, *Cambridge University Press*, 2001.

- Rahmelow, K.: Electronic influences on an infrared detector signal: nonlinearity and amplification. *Applied Optics*, 36(10), 2123-2132, 1997.
- Reiner, T., Mohler, O., and Arnold, F.: Measurements of acetone, acetic acid and formic acid in the northern midlatitude upper troposphere and lower stratosphere. *J. Geophys. Res.*, 104(D11), 13943-13952, 1999.
- Remedios, J. J.: Extreme atmospheric constituent profiles for MIPAS, *Proceedings of the European Symposium on atmospheric measurements from space*, Vol. 2, ESTEC, Noordwijk, Netherlands, 20-22<sup>nd</sup> Jan, 779-783, 1999.
- Richardson R. L., Yang H., and Griffiths P. R.: Effects of Detector Nonlinearity on Spectra Measured on Three Commercial FT-IR Spectrometers. *Appl. Spectroscopy*, 52(4), 572-578, 1998.
- Ridolfi, M., Carli, B., Carlotti, M., von Clarmann, T., Dinelli, B. M., Dudhia, A., Flaud, J-M., Hopfner, M., Morris, P. E., Raspollini, P., Stiller, G., and Wells, R. J.: Optimised forward modelling and retrieval scheme for MIPAS near-real-time data processing, *Applied Optics*, 39, 1323-1340, 2000.
- Roberts, J. M.: The atmospheric chemistry of organic nitrates, *Atmos. Environ., Part A*, 24A, 243-287, 1990.
- Roberts, J. M., Flocke, F., Chen, G., *et al.*: Measurement of peroxy-carboxylic nitric anhydrides (PANs) during the ITCT 2K2 aircraft intensive experiment, *J. Geophys. Res.*, 109, D23S21, 2004.
- Rodgers, C. D.: Inverse methods for atmospheric sounding: Theory and practice (Series on atmospheric, oceanic and planetary physics). *World Scientific Publishing*, 2000.
- Rothman, L. S.: The HITRAN database. *J. Quan. Spect. Radiat. Transfer*, 48, 469-507, 1992.
- Rothman, L. S., *et al.*: The HITRAN molecular spectroscopic database and HAWKS (HITRAN atmospheric workstation): 1996 edition. *J. Quant. Spectrosc. Radiat. Transfer*, 60(5), 665-710, 1998a.

- Rothman L. S., Goldman, A., Rinsland, C. P.: HITRAN – Preface, *J. Quant. Spectrosc. Radiat. Transfer*, 60(5): 661-661, 1998b
- Rothman, L. S., Barbe, A., Benner, D.C., Brown, L. R., Camy-Peyret, C., Carleer, M. R., K. Chance, K., Clerbaux, C., Dana, V., Devi, V. M., Fayth, A. Flaud, J.M., Gamache, R. R., Goldman, A., Jacquemart, D., Jucks, K. W., Lafferty, W. J., Mandin, J.-Y., Massie, S. T., Nemtchinov, V., Newnham, D. A., Perrin, A., Rinsland, C. P., Schroeder, J., Smith, K. M., Smith, M. A. H., Tang, K., Toth, R. A., Vander Auwera, J., Varanasi, P., and Yoshino, K.: The HITRAN molecular spectroscopic database: edition of 2000 including updates through 2001. *J. Quant. Spect.*, 82(1-4): 5-44, 2003.
- Rothman, L. S., Jacquemart, D., Barbe, A., Benner, D. C., Birk, M., Brown, L. R., Carleer, M. R., Chackerian, C., Chance, K., Coudert, L. H., Dana, V., Devi, V. M., Flaud, J-M., Gamache, R. R., Goldman, A., Hartmann, J-M., Jucks, K. W., Maki, A. G., Mandini, J.Y., Massie, S. T., Orphal, J., Perrin, A., Rinsland, C. P., Smith, M. A. H., Tennyson, J., Tolchenov, R. N., Toth, R. A., Vander Auwera, J., Varanasi, P., and Wagner, G.: The *HITRAN* 2004 Molecular Spectroscopic Database, Submitted to *J. Quant. Spect.*, Oct, 2004.
- Sakai, H.: High resolving power Fourier spectroscopy. Spectrometric techniques. Volume I. *Academic press*.1983.
- Schrumpf, W. *et al.*: Dry deposition of peroxyacetyl nitrate (PAN) Determination of its deposition velocity at night from measurements of the atmospheric PAN and <sup>222</sup>Radon concentration gradient, *Geophys. Res. Lett.*, 23, 2599-3602, 1996.
- Senum, G. I., Fajer, R., and Gaffney, J. S.: Fourier Transform Infrared Spectroscopic study of the Thermal Stability of Peroxyacetyl nitrate, *J. Phys. Chem.*, 90, 152-156, 1986.
- Sharpe S. W., Sams R. L., Johnson T. J., and Chu P. M.: Intensity artefacts in gas phase FTIR spectroscopy: Focus on the aperture, *Fourier Transform Spectroscopy, Technical digest, OSA trends in optics and photonics*, 51, 123-126, 2001.

- Sihra, K., Hurley, M. D., Shine, K. P., and Wallington, T. J.: Updated radiative forcing estimates of 65 halocarbons and nonmethane hydrocarbons. *J. Geophys. Res.*, 106(D17), 2001.
- Sillman S., Logan J. A., and Wofsy S. C.: The sensitivity of ozone to nitrogen oxides and hydrocarbons in regional ozone episodes, *J. Geophys. Res.*, 95(D2), 1837–1851, 1990.
- Singh, H. B., and Hanst, P. L.: Peroxyacetyl nitrate (PAN) in the unpolluted atmosphere: An important reservoir for nitrogen oxides, *Geophys. Re. Lett.*, 8, 941-944, 1981.
- Singh, H. B., and Salas, L. J.: Peroxyacetyl nitrate in the free troposphere, *Nature*, 302, 326-328, 1983
- Singh, H. B., Salas, L. J., and Viezee, W.: Global distribution of peroxyacetyl nitrate, *Nature*, 321, 588-591, 1986.
- Singh, H. B.: Reactive nitrogen in the troposphere - chemistry and transport of NO<sub>x</sub> and PAN. *Envir. Sci. Technol.*, 21, 320-327, 1987
- Singh, H. B., *et al.*: Peroxyacetyl nitrate measurements during CITE 2: Atmospheric distribution and precursor relationships, *J. Geophys. Res.*, 95, 10163-10178, 1990.
- Singh, H. B., *et al.*: Atmospheric measurements of peroxyacetyl nitrate and other organic nitrates at high latitudes: Possible sources and sinks, *J. Geophys. Res.*, 97, 16511-16522, 1992a
- Singh, H. B., Herlth, D., O'hara, D., Zahnle, K., Bradhsaw, J. D., Sandholm, S. T., Talbot, R., Crutzen, P. J., and Kanakidou, M.: Relationship of peroxyacetyl nitrate to active and total odd nitrogen at northern high latitudes: Influence of reservoir species of NO<sub>x</sub> and O<sub>3</sub>, *J. Geophys. Res.*, 97, 16523-16530, 1992b.
- Singh, H. B., *et al.*: Summertime distribution of PAN and other reactive nitrogen species in the northern high-latitude atmosphere of eastern Canada. *J. Geophys. Res.*, 99, 1821-1835, 1994.



- Singh H. B., Herlth D., Kolyer R., Chatfield R., Viezee W., Salas L. J., Chen Y., Bradshaw J. D., Sandholm S. T., Talbot R., Gregory G. L., Anderson B., Sachse G. W., Browell E., Bachmeier A. S., Blake D. R., Heikes B., Jacob D, and Fuelberg, H. E.: Impact of biomass burning emissions on the composition of the South Atlantic troposphere: Reactive nitrogen and ozone. *J. Geophys. Res.* 101 (D19): 24203-24219, 1996.
- Smith K. M., Duxbury G., Newnham D. A., and Ballard J.: A High-Resolution Analysis of the  $\nu_3$  and  $\nu_9$  Absorption Bands of Difluoromethane, *J. Mol. Spect.* 193(1), 166-173, 1999.
- Spang, R. H., Remedios, J. J., and Barkley, M. P.: Colour indices for the detection and differentiation of cloud types in infra-red limb emission spectra, *Adv. Space. Res.* 2003.
- Stephens, E. R., Hanst P. L., Dörr, R. C, and Scott, W. E.: Reactions of nitrogen dioxide and organic compounds in air, *Ind. Eng. Chem.*, 48, 1498, 1956.
- Stephens, E. R.: The formation, reactions and properties of peroxyacetyl nitrates (PAN) in photochemical air pollution, *Adv. Environ. Sci. Technol.*, 1, 119-146, 1969.
- Stohl, A., and Trickl, T.: A textbook example of long-range transport: Simultaneous observation of ozone maxima of stratospheric and North American origin in the free troposphere over Europe, *J. Geophys. Res.*, 104, 30,445-30,462, 1999.
- Stohl, A.: A 1-year Lagrangian “climatology” of airstreams in the Northern Hemisphere troposphere and lowermost stratosphere. *J. Geophys. Res.*, 106, 7263-7279, 2001.
- Talukdar, R. K., Burkholder, J. B., Schmoltner, A., Roberts, J. M., Wilson, R. R., and Ravishankara, A. R.: Investigation of loss processes for peroxyacetyl nitrate in the atmosphere: UV photolysis and reaction with OH. *J. Geophys. Res.*, 100, 14163-14173, 1995.
- Tanimoto, H., Hirokawa, J., Kajii, Y., and Akimoto, H.: A new measurement technique at parts per trillion by volume levels: Gas chromatography/negative ion chemical ionization mass spectrometry, *J. Geophys. Res.*, 104, 21343-21354, 1999.

- Trainer, M., Buhr, M. P., Curran, C. M., Fehsenfeld, F. C., Hsie, E. Y., Liu, S. C., Norton, R. B., Parrish, D. D., Williams, E. J., Gandrud, B. W., Ridley, B. A., Shetter, J. D., Allwine, E. J., and Westberg, H. H.: Observations and modelling of reactive nitrogen photochemistry at a rural site, *J. Geophys. Res.*, 96, 3045-3063, 1991.
- Trieschmann, O.: Level 0 to 1b Data Processing of the MIPAS-B2 balloon-borne Fourier Transform Spectrometer, revision 1.0 of 10.04.2000. Technical report, IMK, Forschungszentrum, Karlsruhe, ESA contract No. 112078/96/NL/GS, 2000.
- Tsalkani, N., and Toupance, G.: Infrared absorptivities and integrated band intensities for gaseous peroxyacetyl nitrate (PAN). *Atmos. Env.*, 23, 1849-1854, 1989.
- Tsalkani, N., Perros, P., Dutot, A. L., and Toupance, G.: One year measurements of PAN in the Paris basin: effect of meteorological parameter. *Atmos. Env.*, 25A, 1941-1949, 1991.
- Von Ahsen S, and Willner H.: Thermal decomposition of peroxyacetyl nitrate  $\text{CH}_3\text{C}(\text{O})\text{OONO}_2$ . *J. Chem. Phys.*, 121, 2048-2057, 2004.
- Von Clarmann, T. and Echle, G.: Selection of optimized micro-windows for atmospheric spectroscopy, *Applied Optics*, 37, 7661-7669, 1998.
- Wang Y., Jacob, D. J., Bakwin, P., Dickerson, R., Doddridge, B., Gerbig, C., Honrath, R., Hubler, G., Jaffe, D., Kondo, Y., Munger, J. W., Torres, A., and Volz-Thomas, A.: Climatologies of  $\text{NO}_x$  and  $\text{NO}_y$ : a comparison of data and models. *Atmos. Envir.*, 31, 1851–1903, 1997.
- Wang, W. F., Stevenson, A., Reuter, D. C., and Sirota, J. M.: Absolute band intensities of acetone  $[(\text{CH}_3)_2\text{CO}]$  in the infrared region of  $830 - 3200 \text{ cm}^{-1}$  at low and room temperatures. *Spectrochimica Acta*, 57, 1603-1610, 2001.
- Waterfall, A. M.: Measurement of organic compounds in the upper troposphere using remote sensing, DPhil thesis, *Oxford University*, 2003.
- Wayne, R.P.: *Chemistry of Atmospheres*, 2<sup>nd</sup> Ed., Oxford University Press, Oxford, 1991.
- Zalicki, P., and Zare, R. N.: Cavity ring-down spectroscopy for quantitative absorption measurements, *J. Chem. Phys.*, 102, 2708-2717, 1995.